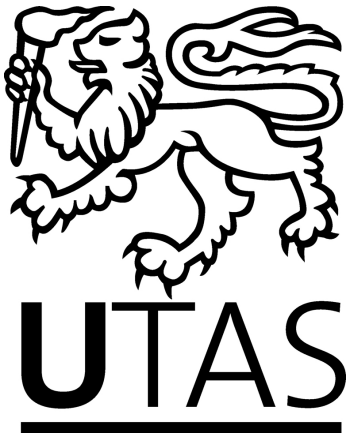

University of Tasmania
School of Mathematics and Physics

Cosmic Evolution of Radio Sources in ATLAS

Minnie Yuan Mao
B.Sc. (Hons.)

October 2012

Submitted in fulfilment of the requirements for the Degree of
Doctor of Philosophy

I declare that this thesis contains no material which has been accepted for a degree or diploma by the University or any other institution, except by way of background information and duly acknowledged in the thesis, and that, to the best of my knowledge and belief, this thesis contains no material previously published or written by another person, except where due acknowledgement is made in the text of the thesis.

Signed: 

Date: 15 Oct 2012

Signed: 

Date: 15 Oct 2012

Statement of Co-Authorship

The following people contributed to the publication of the work undertaken as part of this thesis:

Chapter 3: *The Australia Telescope Large Area Survey: Spectroscopic Catalogue and Radio Luminosity Functions*, submitted to MNRAS on March 23, 2012

Minnie Yuan Mao (75%), Rob Sharp (5%), Ray Norris (5%), Andrew Hopkins (2.5%), Nick Seymour (2.5%), Elaine Sadler (2.5%), remaining coauthors (7.5%)

Chapter 4: *Wide-angle tail galaxies in ATLAS*, 2010, MNRAS, 406, 2578

Minnie Yuan Mao (80%), Rob Sharp (5%), Dhruba Saikia (5%), Ray Norris (5%), remaining coauthors (5%)

Chapter 5: *No Evidence for Evolution in the Far-Infrared-Radio Correlation out to z ∼ 2 in the ECDFS*, 2011, ApJ, 731, 79

Minnie Yuan Mao (80%), Minh Huynh (10%), Ray Norris (5%), remaining coauthors (5%)

Details of the Authors' roles are provided at the beginning of each chapter.

We the undersigned agree with the above stated "proportion of work undertaken" for each of the above published and submitted peer-reviewed manuscripts contributing to this thesis.

Signed: _____ _____

Jim Lovell	**John Dickey**
Supervisor	Head of School
School of Mathematics and Physics	School of Mathematics and Physics
University of Tasmania	University of Tasmania

Date: _____

Abstract

The Australian Telescope Large Area Survey (ATLAS) observes seven square degrees of sky down to 10 μJy beam^{-1} at 1.4 GHz using the Australia Telescope Compact Array. The survey covers two fields to minimise cosmic variance; the Chandra Deep Field South (CDFS) and the European Large Area ISO Survey - South 1 (ELAIS). My PhD focusses specifically on the cosmic evolution of radio sources in ATLAS. We have used the AAOmega spectrograph on the Anglo-Australian Telescope (AAT) to measure 466 new spectroscopic redshifts in ATLAS. We have used both the spectra obtained from the AAT, and other multi-wavelength ancillary data available in these fields to discriminate between star-forming galaxies and AGN. Using these data we have studied the radio luminosity function for both star-forming galaxies and AGN. We have also identified and analysed wide-angle tailed galaxies in ATLAS and discovered a ~12 Mpc large-scale structure associated with a wide-angle tailed galaxy in ELAIS at z~0.2. Using deep far-infrared data from the Far-Infrared Deep Extragalactic Legacy Survey (FIDEL) we were able to study the far-infrared radio correlation in the Extended-CDFS and we found no evidence for evolution out to redshifts of ~3.

Acknowledgements

The work presented in this thesis could not have been achieved without the guidance and support of a great number of people. I am so lucky to have been surrounded by the wonderful people that have made my PhD experience so enjoyable.

It's imperative that I acknowledge my simply superb supervisory team, **Ray Norris, Rob Sharp and Jim Lovell**. Ray, Rob and Jim worked tirelessly to guide me through my PhD life and have assisted me in all stages of my PhD. I especially enjoyed the fact that my supervisors all have such different approaches to science leading to many interesting (and occasionally heated) discussions where I learned so much, not in the least including how science actually works.

Being Ray Norris's student has been so much fun and I can't count how many jealous PhD students have wistfully told me how much they wished their relationship with their supervisors could be as wonderful as mine is with Ray.

Ray, working with you has been such an absolute pleasure. I'm going to miss arguing about work with you all the time, scribbling equations on paper tablecloths, learning about bird calls in Narrabri and proudly announcing to people that I'm Ray Norris's PhD student. It makes me so sad to think that I'll no longer be your student, but I hope that we will always remain collaborators, and of course, good friends.

Rob Sharp took on the role of my "pseudo" summer project supervisor in late 2007 and I enjoyed working with him so much that I asked Ray if Rob could co-supervise me. While Ray and I "get" each other so easily, I'm not sure there could be two personalities further apart than Rob and me. It's fantastic! Rob points out things that I wouldn't and couldn't have seen without him and he is excellent at focussing and grounding me (which I've been told isn't easy!). Rob, thank you so much for "putting up" with me over the last four years. I really hope I haven't been too much of a pain and I've really enjoyed working with you and am so

grateful you agreed to take me on as a student!

Jim Lovell is my "University" supervisor and on top of supervising my science, Jim has also had to play tie-breaker when Ray and Rob disagree. Jim has always been super supportive and is a gun at pulling references out of his brain! Jim, I've really enjoyed being your student and have learned so much from you, especially the importance of capitalising letters in emails!

I was awarded an IPAC Graduate Research Fellowship at the end of 2009 for which I must sincerely thank my IPAC supervisor **Minh Huynh**. Minh opened my eyes to the far-infrared regime and lead me to see how fascinating the far-infrared radio correlation is. Minh also forced me to learn IDL and, although I griped about it at the time, I'm really pleased that I did. While mentioning IPAC I need to thank **Phil Appleton** who organised the fellowship program and also sent me to Palomar to see the famous Hale Telescope.

I have also been fortunate with my collaborators, many of which have taken me under their wing and become "pseudo" supervisors to me. In particular, I want to thank **Andrew Hopkins, Elaine Sadler and Dhruba Saikia**. Andrew Hopkins has always made time to answer my questions and spent many hours on the phone explaining astronomical concepts to me. Andrew is also my go-to person for alcoholic beverage ideas. Elaine Sadler worked through my radio luminosity function data when I became hopelessly stuck and helped me to understand RLFs and (finally!) construct them correctly. Dhruba Saikia ("Sykes") rescued the WATs in ATLAS paper from the bin and convinced me that it was worth pushing on when I decided it wasn't good enough. It's now one of the pieces of work I'm most proud of.

The entire **ATLAS team** have been so nice and supportive and, sad as it sounds, I actually look forward to the Tuesday 4pm ATLAS meetings so I can see everyone. In particular I need to thank fellow ATLAS student **Kate Randall** for being there to bounce ideas off, for the laughs, support, chocolate and origami mice. You rock Katiekate and I'm so lucky to be friends with you.

My visits to the ATNF were considerably brightened by stimulating conversations with many knowledgeable people including **Ron Ekers**, **Bjorn Emonts**, **Nick Seymour**, **Andrew Walsh**, **Liz Mahony**, **Justin Bray** and especially **Vicki** and **Elsa** for sorting out my accommodation in Sydney!

I have spent many happy weeks observing and being Duty Astronomer at the ATCA in Narrabri. I am so grateful to **all the staff at the ATCA**. My time at the ATCA wouldn't have been the same without walks with **Robin**, being fed sausage

rolls and icecream by **Clarrie**, asking **Marg** to bring chocolate for me from town and being cooked for by **Meg**, **Chris** and **Pam**. In particular I wish to thank senior systems scientist and one of my best friends **Jamie Stevens**. Jamie has not only taught me almost everything I know about the ATCA, he has also always been there to discuss my research with. Jamie is hands-down the best programmer I know and this thesis style is his design. I don't know how I'd live without you Jamie!

On the subject of telescopes I need to thank **all the staff at the AAT** in Coonabarabran, in particular **Kristin Fiegert** and **Steve Lee** for their observing support and for making the cold cloudy nights so much fun, and **Donna Burton** for making us a splendid Christmas Dinner when we were stuck observing over the holiday season.

I need to thank all the wonderful people in the School of Maths and Physics. **Simon Ellingsen**, **John Dickey**, **Stas Shabala** and **Jo Dawson** have always been there to answer "just another quick question". **Barry Gardner** who always has a silly joke to make me laugh and a new type of tea to try. And I absolutely have to thank **Karen Bradford** who has been my Hobart "mum". Karen always looks out for me and has provided me with so many opportunities including taking telescope tours, painting faces and even being on TV. Thank you Karen!!

I've been so lucky to have so many fellow PhD students and wonderful friends supporting me through my PhD journey. I shared an office and later a house with **Shari Breen** and countless evenings after working late I'd come home to find dinner waiting for me. Shari was also there for me to constantly ask "how-to" PhD questions and provided me with the template for this thesis. **Anita Titmarsh**, my gym buddy and planking motivator. Anita is responsible for making my office pink in my last few months of PhD. I swear fluorescent pink is the most motivating colour! **Melissa Humphries**, my current officemate who has seriously, the most amazing laugh. Listening to Mel laugh always brightens my day. **Jay Blanchard**, who's one of my favourite people in the world. During my time in Hobart, Jay has driven me around, fed me and given in to my most irrational demands (I eat the icing, you can have the cake).

It would be impossible to thank everyone individually and I'm so terribly sorry if I've left you off the list, so to everyone that has made this thesis what it is today, thank you.

Finally, I need to thank **Mum** and **Dad**, and of course **the dog**. I love you.

Contents

List of Figures

List of Tables

Our whole universe was in a hot dense state,
Then nearly fourteen billion years ago expansion started, wait...
The Earth began to cool,
The autotrophs began to drool,
Neanderthals developed tools,
We built a wall (we built the pyramids),
Math, science, history, unravelling the mysteries,
That all started with the big bang!

Barenaked Ladies - The History of Everything

1

Introduction

It is generally accepted that the Universe began with the Big Bang, almost 14 billion years ago. Tiny quantum fluctuations occurring in the first instants after the Big Bang (10^{-30} of a second) seeded small density inhomogeneities, which grew in time giving rise to the structure of the Universe that we see today.

One of the most enduring questions of modern astronomy however, is how galaxies have formed and evolved since the Big Bang. The "best guess" model suggests galaxies take billions of years to form as they are built hierarchically from the small density inhomogeneities seeded soon after the Big Bang. So why do we see large galaxies in existence within the first billion years (e.g Zheng et al. 2012)?

In order to understand how the Universe has changed and how galaxies have formed and evolved, many astronomers are using data from large astronomical surveys to study the Universe. Well-defined large deep surveys are required to understand galaxy evolution.

This thesis presents the optical spectroscopy follow-up of the Australia Telescope Large Area Survey (ATLAS), and science resulting from these observations. The remainder of this Chapter is dedicated to summarising our current knowledge of the Universe today, focussing specifically on the radio emission from

galaxies. This chapter ends with a brief review of radio surveys, giving context to the importance of ATLAS.

1.1 Astronomy

Astronomy[1] is one of the oldest natural sciences. People have observed the motions of visible celestial objects to determine agricultural calendars and ritual events. The spectacular night sky has fascinated people for millennia and ancient monuments such as Stonehenge and the Egyptian pyramids appear to be aligned with astronomical events.

Astronomy is the study of all celestial objects. It is the study of the Moon, the Sun and the Solar System, the stars, the Milky Way and other galaxies. In short, astronomy is the study of everything in the Universe, including how the Universe began and how it shall ultimately end. However, astronomy was not always such a broad science.

Ptolemy proposed a geocentric Universe (Ptolemy 150BC) and this was more or less accepted until Copernicus proposed a heliocentric Universe (Copernicus 1543). At this point, the Universe comprised only the Earth, the Moon, the Sun, the planets and the stars.

The stars we see in the night sky are grouped into 88 "official", International Astronomical Union recognised, constellations and the majority of these come from the constellations defined by Ptolemy over two thousand years ago (Ptolemy 150BC). The earliest recorded star catalogues however were created in the 4th Century BC by Chinese astronomers Shi Shen and Gan De. Most of the stars that can be seen with the naked eye reside within our galaxy, the Milky Way.

Even less than a hundred years ago, the Universe was believed to be composed of only the Milky Way. In 1926 two prominent astronomers, Harlow Shapley and Heber Curtis, debated whether the spiral nebulae that had been observed (e.g Herschel 1786) were relatively small and resided within the Milky Way, or large distant galaxies beyond the Milky Way. This came to be known as the Great De-

[1]There is some confusion between the terms "astronomy" and "astrophysics". Although historically "astrophysics" required the application of physics to understand astronomy, most astronomy today cannot be done without physics so the terms are now very much interchangeable. Astronomy is also often confused with astrology. While astrology is generally viewed with derision in modern times, in the past it was strongly believed that the motion of the stars and planets could affect one's life. Historically, many now-famous astronomers were also astrologers. It is interesting to remember that Galileo and Kepler were regarded not only as leading astronomers, but also as astrologers!

bate. The debate was settled when Edwin Hubble[2] identified Cepheid variables[3] in the Andromeda galaxy and found them to be too distant to be within the Milky Way (Hubble 1925). Thus extragalactic astronomy was born.

Hubble also devised a system of classifying galaxies based on their optical morphology in an attempt to understand their relation to each other (Hubble 1926). The varied optical morphology of galaxies led to studies attempting to understand the formation of galaxies and what mechanisms triggered the different morphologies. Determining how galaxies have formed and evolved remains one of the hottest topics in modern astronomy.

1.2 Modelling the Universe

The best estimate of the age of the Universe is 13.75 ± 0.11 billion years (Jarosik et al. 2011), within the ΛCDM model. ΛCDM is an abbreviation for Lambda-Cold Dark Matter, and this model is frequently referred to as the standard model of big bang cosmology. In broad terms, the ΛCDM model explains away anomalies in gravitational effects by invoking the presence of cold dark matter and dark energy.

Dark energy is a hypothetical form of energy that explains the acceleration of the expansion of the Universe. Although dark energy appears to have been detected (e.g. Blake et al. 2011), the physics behind it is not understood. Currently, dark energy is believed to make up 73% of the energy density of the Universe.

The rest of the Universe is composed of two types of matter: the matter that we can see and interact with, including the stuff of planets, stars and galaxies, and the matter that we cannot see and interact with. On large-scale structures the observed gravitational effects cannot be accounted for by the quantity of observable matter. For example, galaxy rotation curves suggest that there is far more matter at the edges of galaxies than is observed. This led to the prediction of cold dark matter (Blumenthal et al. 1984). This matter is described as "cold" because the particles move slowly, and "dark" as they do not interact with electromagnetic

[2]Although the discovery of the expansion of the Universe, and indeed Hubble's Law is commonly attributed to Edwin Hubble, it was actually the Belgian astronomer, Georges Lemaitre, who first proposed these (Lemaître 1927). However, his article was not widely read on account of it being published in a lower-impact journal.

[3]The relationship between a Cepheid variable's luminosity and pulsation period was discovered by Henrietta Swan Leavitt (Leavitt 1908). Henrietta Swan Leavitt was employed as a "computer" at the Harvard College Observatory. Women were hired because they could be paid less than half the wage of men!

radiation. Cold dark matter is believed to make up 23% of the energy density of the Universe. That is to say, the baryonic matter that we can detect makes up less than 5% of the Universe.

The ΛCDM model assumes that the Universe is flat. This means that gravitational effects shall never overcome the expansion of the Universe and the Universe can expand forever. This is supported by results from the Wilkinson Microwave Anisotropy Probe (WMAP Spergel et al. 2003) and the 2dF Galaxy Redshift Survey (2dFGRS Colless et al. 2001; Tegmark et al. 2002). In an attempt to understand the fate of the Universe, two independent teams used type 1a Supernovae[4] as distance indicators and found the expansion of the Universe to be accelerating (Schmidt et al. 1998; Perlmutter et al. 1999). This work led to the 2011 Nobel Prize in Physics being awarded to Saul Perlmutter, Adam Riess, and Brian Schmidt.

The ΛCDM model predicts that structure grows hierarchically ("bottom-up"). Smaller objects coalesce into larger objects to form larger and more massive structures. In other words, stars are bound into clusters, that are bound into galaxies, that are bound into clusters of galaxies, that are bound into superclusters. While simulations of galaxy formation relying on the ΛCDM model broadly agree with the observed Universe (e.g. Springel et al. 2005), there are a number of problems with the hierarchical theory. For example, simulations predict orders of magnitudes more dwarf satellites than are actually detected (Moore et al. 1999). Moreover, giant galaxies take billions of years to form under the hierarchical theory, yet many of the largest galaxies have already formed early in the Universe (Glazebrook et al. 2004). Questions like these fuel studies into the formation and evolution of galaxies.

Prior to the dominance of the ΛCDM model, one explanation for the expansion of the Universe was given by the Steady State Theory (Hoyle 1948). The Steady State Theory proposed an infinitely old, unevolving Universe that is continuously creating matter as the Universe expands so as to maintain a constant energy density. Although this model makes cosmological calculations much simpler, observational results have largely discredited it.

[4]Type 1a Supernovae are powerful "standard candles" because they all have the same peak luminosity.

1.3 Radio Astronomy

Karl G. Jansky was the first person to detect extraterrestrial radio waves, and is considered one of the pioneers of radio astronomy. In 1928, Jansky was hired by Bell Laboratories as a radio engineer to investigate sources of static that might cause interference with radio voice transmissions at 20.5 MHz. He identified static from local and distant thunderstorms and a steady hiss of unknown origin. Although he initially attributed the hiss to the Sun, over time he noticed the time-scale of variation was a sidereal day, leading to the conclusion that these radio waves originated from beyond the Solar System (Jansky 1933). He was later able to pinpoint the origin of the radio waves to the centre of the Milky Way (Jansky 1935). Kraus (1966) refers to Jansky (1935) as "the first observational paper on radio astronomy", and notes that although this was a very significant historic occasion, the presentation of this work attracted little attention with "scarcely two dozen persons in Jansky's audience". Jansky wished to continue with his work but this was during the Great Depression and the lack of funding and conservative outlook of observatories made it impossible. Jansky did no more work in the field of astronomy, although his name lives on as the unit of radio flux density with 1 Jansky = 10^{-26} W m^{-2} Hz^{-1}.

Jansky's work piqued the interest of another radio engineer, Grote Reber, who is also considered to be one of the pioneers of radio astronomy. Reber applied for a job at Bell Laboratories so that he could work with Jansky, but was turned down as there were no jobs available at the time. Reber took matters into his own hands and constructed a 9 m radio dish in his backyard in Illinois, USA. With this telescope, observing at 160 MHz, he produced the first radio map of the Milky Way (Reber 1944). Reber subsequently moved to Tasmania in 1957 where he constructed an array in Bothwell to study low-frequency radio emissions and lived there until his death in 2002. The Grote Reber Museum is a museum dedicated to his life and works and is located on the site of the University of Tasmania operated Mt Pleasant Radio Observatory. The museum was opened in 2008 by Professor Ken Kellermann.

After World War II, radio astronomy rose to prominence with many radio telescopes being constructed predominately in the UK and Australia. The Cambridge Interferometer was built in the early 1950s in the UK (Ryle and Hewish 1955) and would later be used to produce the famous 2C and 3C radio catalogues, many sources of which are still referred to by their "3C" names.

Due to the low resolution of radio images at the time, identification of the optical hosts was difficult and the true nature of radio sources, often referred to as "radio frequency noise" or "cosmic noise", was unknown. Bolton and Stanley (1948) used the sea interferometer at Dover Heights in Sydney to measure Cygnus A and found that it had an angular diameter of less than eight arcminutes. Narrowing down the size of the radio source enabled others to identify its optical host and eventually determine that Cygnus A lies at a distance of ~ 600 Mly (Baade and Minkowski 1954)[5]. From this, the radio power of Cygnus A was calculated to be $\sim 10^{28}$ W Hz^{-1}. In comparison, the Andromeda galaxy at a distance of ~ 2.6 Mly has a radio power of only $\sim 10^{21}$ W Hz^{-1}. This large discrepancy led to extragalactic radio galaxies being separated into "normal galaxies" and "radio galaxies". Nowadays we know that the radio emission from "normal galaxies" is predominately powered by star-formation, and that the radio emission from "radio galaxies" is predominately powered by the presence of Active Galactic Nuclei (AGN).

1.4 Radio Emission from Galaxies

Extragalactic radio emission from galaxies can be attributed to either star-formation or the presence of AGN. This section presents an introduction to both AGN and star-forming (SF) galaxies. Both emit non-thermal synchrotron emission at radio frequencies.

Synchrotron Emission

The radio emission from galaxies follows a non-thermal spectrum and is often polarised. The predominant form of emission from radio galaxies is synchrotron emission, which results from highly relativistic electrons spiralling in a magnetic field. The frequency of rotation for the relativistic electron is known as the gyrofrequency and is defined as

$$\nu_g = \frac{e\mathbf{B}}{2\pi\gamma m_0} \tag{1.1}$$

[5]This corresponds to a redshift of z ~ 0.06. Redshift is defined as $z = \frac{\lambda_{obs}-\lambda_{emit}}{\lambda_{emit}} = \frac{\nu_{emit}-\nu_{obs}}{\nu_{obs}}$, where λ_{emit} and λ_{obs} are the emitted and observed wavelengths and ν_{emit} and ν_{obs} are the emitted and observed frequencies.

and

$$\gamma = \frac{1}{\sqrt{1 - \frac{v^2}{c^2}}}, \tag{1.2}$$

where v_g is the gyrofrequency, e is the change of the electron, **B** is the magnetic field strength, γ is the Lorentz factor, m_0 is the rest mass of the electron, v is the speed of the electron and c is the speed of light.

The acceleration due to circular motion causes synchrotron emission. The synchrotron photons are emitted at a constant pitch angle and are highly beamed with a radial width of

$$\phi = \frac{1}{\gamma} \tag{1.3}$$

where ϕ is the radial width of the beamed cone of synchrotron emission. As the electron loses energy, its speed will decrease thus increasing the radial width.

Calculating Radio Luminosity

The luminosity of a source is the amount of energy produced per unit frequency. We can calculate this by multiplying the flux density at the given frequency by the total surface area of a sphere with radius D_L, the distance of the source. That is,

$$\mathrm{L}_\nu = 4\pi \mathrm{D}_L^2 \mathrm{S}_\nu \tag{1.4}$$

where L_ν is the luminosity in W Hz^{-1} at the frequency ν, D_L is the luminosity distance in metres, and S_ν is the flux density in W m^{-2} Hz^{-1} and the frequency ν.

When we observe a source at a particular redshift, z, we are measuring the flux density at the observing frequency for a bandwidth that is set by the observer. However, due to the expansion of the Universe, the frequency we are observing at is lower than the emitting frequency. That is,

$$\frac{\nu_{emit}}{\nu_{obs}} = 1 + z \tag{1.5}$$

where ν_{emit} is the emitting frequency, ν_{obs} is the observing frequency, and z is the redshift.

Furthermore, the bandwidth with which we are observing corresponds to a wider bandwidth at the emitting frequency.

$$\frac{B_{emit}}{B_{obs}} = \frac{\Delta\nu_{emit}}{\Delta\nu_{obs}} = 1 + z \tag{1.6}$$

However, energy is conserved so the radiated power is equal to the observed power and thus,

$$S_{obs} \times B_{obs} = S_{\nu emit} \times B_{\nu emit} \tag{1.7}$$

where S_{obs} is the observed flux density at the observing frequency, B_{obs} is the observing bandwidth, $S_{\nu emit}$ is the emitted flux density at the emitting frequency, and $B_{\nu emit}$ is the bandwidth at the emitting frequency,

Rearranging the above equation gives

$$S_{\nu emit} = S_{obs}\frac{B_{obs}}{B_{\nu emit}} = \frac{S_{obs}}{1+z} \tag{1.8}$$

This gives the the flux density at the emitting frequency, but we need to calculate the flux density at the observing frequency.

$$\frac{S_{\nu obs}}{S_{\nu emit}} = (\frac{\nu_{emit}}{\nu_{obs}})^{\alpha} = (1+z)^{\alpha} \tag{1.9}$$

where $S_{\nu obs}$ is the flux density at the observing frequency, and α is the spectral index where spectral index is defined as $S \propto \nu^{\alpha}$, due to the non-thermal nature of synchrotron emission.

Rearranging the above equation for $S_{\nu obs}$,

$$S_{\nu obs} = S_{\nu emit}(1+z)^{-\alpha} = \frac{S_{obs}}{(1+z)^{1+\alpha}} \tag{1.10}$$

Substituting this into Equation 1.4 gives

$$L_{\nu} = \frac{4\pi D_L^2 S_{obs}}{(1+z)^{1+\alpha}} \tag{1.11}$$

1.4.1 Active Galactic Nuclei

AGN are found in the central regions of galaxies, and can be highly luminous over some parts of the electromagnetic spectrum. AGN are caused by the accretion of matter onto a super massive black hole (SMBH). Nowadays, it is widely accepted that all galaxies have a SMBH in their centre[6], but not all of these are

[6]With the exception of dwarf galaxies such as the Magellanic Clouds. The centre of the Milky Way hosts a 4.2×10^6 $M_{\odot}$ SMBH (e.g Schödel et al. 2002; Ghez et al. 2008; Gillessen et al. 2009).

AGN (although all of these may be AGN at some point in their life-cycle). An AGN requires matter to be accreting onto the SMBH to make it "active".

The general model of AGN consists of an accretion disk of cold material around a SMBH, which is also ionising gas clouds in the vicinity. The clouds that are closest to the SMBH are dense and have very high velocities ($\sim$ thousands of $\mathrm{km\,s^{-1}}$) so the clouds do not fall into the SMBH. Consequently the emission lines from these clouds are very broad and this region is referred to as the Broad Line Region (BLR). The BLR provides valuable information about the SMBH due to its proximity. The full extent of the BLR is $\sim$ 1 pc. The clouds further from the SMBH have a lower density and relatively lower velocities ($\sim$ hundreds of $\mathrm{km\,s^{-1}}$). Consequently emission lines from these clouds will be narrower and this region is referred to as the Narrow Line Region (NLR). The NLR is typically $\sim$ 1 kpc from the SMBH. Just beyond the BLR exists a dusty torus that lies in the same plane as the accretion disk. Finally, some AGN display jets emerging from the the SMBH.

The best evidence we have to date for the existence of SMBHs in AGN is the presence of water megamasers associated with the accretion disk around the SMBH (e.g. Miyoshi et al. 1995). The correlation between black hole mass and the luminosity of the galaxy's bulge (Magorrian et al. 1998) and the strong correlation between the velocity dispersion of a galaxy's bulge and the mass of the SMBH at the galaxy's centre (M-sigma relation, Gebhardt et al. 2000; Ferrarese and Merritt 2000; Gültekin et al. 2009) indicate that the formation of galaxies is closely related to the formation of SMBHs (Richstone et al. 1998).

Historically, AGN have been broadly classed as "radio-loud" and "radio-quiet" (e.g. Kellermann et al. 1989), although there is evidence that all AGN, including those deemed "radio-quiet", have radio emission at some level. Moreover, the presence of radio emission cannot be predicted from optical spectra alone (Dunlop et al. 2003). There is much debate over whether the distribution of radio luminosity is bimodal or not, with some studies (e.g. Kellermann et al. 1989; Ivezić et al. 2002) finding evidence for bimodality and others (e.g White et al. 2000; Cirasuolo et al. 2003) not. This is often referred to as the "radio-loud/radio-quiet dichotomy" (e.g Broderick and Fender 2011), and despite numerous studies in this area a firm conclusion has not yet been reached. Recent results from the EVLA suggest that the radio luminosity function for quasars has components from both radio emission from the AGN and star-formation in the quasar host galaxy (Kimball et al. 2011). It is important to resolve this dichotomy

to fully understand black hole accretion and feedback modes.

The "radio-loud" AGN include radio-loud quasars, blazars and radio galaxies and the "radio-quiet" AGN include Seyfert galaxies, radio-quiet quasars[7] and LINERs. The nomenclature of AGN is somewhat confusing as the distinctions between different classes reflect historical differences in how objects were first identified or initially classified, rather than physical differences.

Types of AGN

Carl Seyfert, after whom Seyfert galaxies are named, was the first to identify the class of galaxies whose optical spectra showed high-excitation nuclear emission lines (Seyfert 1943). The emission lines tend to be very broad and the hydrogen lines were even broader than the other emission lines. Morphologically, Seyfert galaxies look like normal spiral galaxies with a star superimposed on the centre.

The bright nuclei of Seyfert galaxies were measured to be less than 100 pc in size (Woltjer 1959). The broad emission lines indicate high velocity dispersions within the nucleus thus the mass of the nucleus must be very high. This was the first evidence that Seyferts contained nuclear AGN (although they were often termed "monsters" at this time).

A few decades later, Khachikian and Weedman (1974) noticed that there were two subclasses of Seyfert galaxies. The optical spectra of Seyfert 1 galaxies contain both broad and narrow[8] emission lines, while the spectra of Seyfert 2 galaxies contain only narrow emission lines. The broad emission lines only occur for permitted transitions. This implies that the broad-line gas is of very high density thus forbidden transitions are collisionally suppressed. Conversely, the narrow forbidden lines indicate that the ionised gas is of very low-density. Figure 1.1 provides an example of Seyfert 1 and Seyfert 2 galaxy spectra.

There is much overlap between Seyfert 1 and Seyfert 2 galaxy spectra leading Osterbrock (1981) to introduce Seyfert 1.5, 1.8 and 1.9. This is further evidence that as opposed to two classes of Seyfert galaxy, we are actually seeing a continuum of sources.

Low-ionisation nuclear emission-line region galaxies (LINERs) were first

[7] Quasars were first identified from their radio counterparts, but it soon became apparent that there existed many similar sources that did not emit at radio wavelengths. These were subsequently termed quasi-stellar objects or QSOs, and only $\sim 10\%$ of QSOs have detected radio emission. Nowadays, the terms QSOs and quasars are often used interchangeably. For clarity, we refer to radio-loud and radio-quiet quasars.

[8] Although termed "narrow" emission lines, the line widths correspond to velocities of several hundred $\mathrm{km\,s^{-1}}$ and are still broader than emission lines due to star formation.

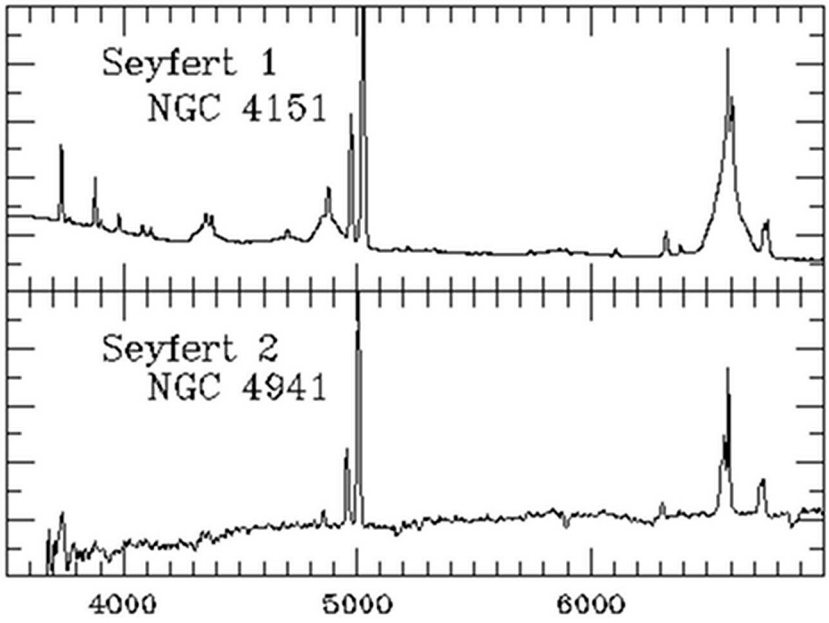

Figure 1.1: An example of the optical spectrum of a Seyfert 1 galaxy (top) and a Seyfert 2 galaxy (bottom). The Seyfert 1 galaxy spectrum has characteristically broad emission lines. Image courtesy of Bill Keel.

identified by Heckman (1980). They are defined by their optical spectra, similar to Seyfert 2 galaxies, but with relatively strong emission from low-ionisation lines (such as [OI] and [NII]) and relatively weak emission from high-ionisation lines (such as [OII]). LINERs are very common making up approximately a third of all galaxies in the local volume (Ho et al. 1997).

Quasars are likely to be the high-luminosity equivalent of Seyfert galaxies. Aside from their more luminous nature, quasars are also distinguished from Seyfert galaxies by their optical hosts. When they were first discovered, the sensitivity of optical telescopes was such that quasar hosts were unresolved and looked like bright stars. In modern times, many of these host galaxies have been resolved and appear to be a range of galaxy types. Quasar hosts are likely to have close companions (e.g Bahcall et al. 1997; Letawe et al. 2010). The optical spectra of quasars are very similar to those of Seyfert galaxies and Figure 1.2 shows the average spectrum of quasars from Peterson (1997). The term quasar is a contraction of "quasi-stellar radio source" and was coined by Chiu (1964), who abbreviated their "clumsily long name" for convenience.

Blazars are among the most energetic phenomena in the Universe. They display short time-scale variability indicating very small angular sizes. The optical

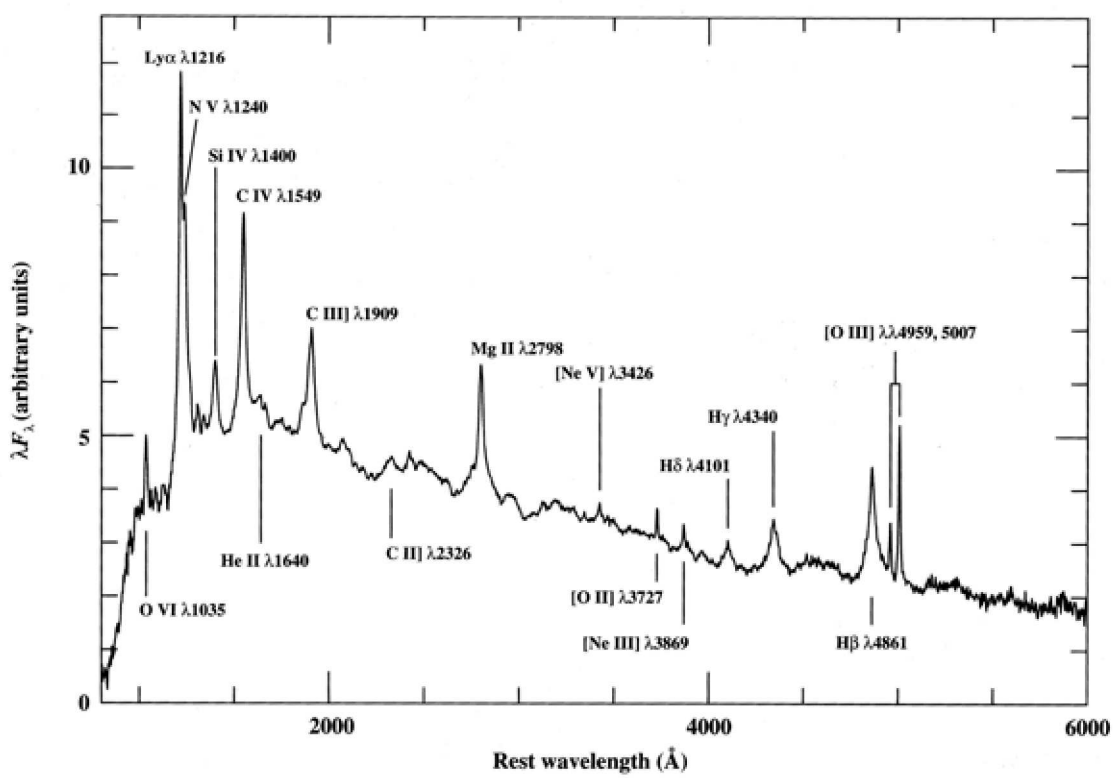

Figure 1.2: The mean quasar spectrum formed by averaging a large number of quasars from the Large Bright Quasar Survey (Francis et al. 1991). Image credit: Peterson (1997)

spectra of blazars often show only continuum emission with no strong emission or absorption lines making the redshifts of these sources difficult to attain. Very high signal-to-noise spectra however, can often detect weak spectral features. The radio jets emanating from blazars often display superluminal motion.

Finally, there exist strong radio sources that are hosted by giant elliptical galaxies (e.g. M87). These are confusingly termed "radio galaxies" There exist both broad-line radio galaxies (BLRGs) and narrow-line radio galaxies (NLRGs), and these are thought to be the radio-loud rendition of Seyfert 1 and 2s. There are also radio galaxies that have early-type hosts and whose spectra do not show any emission lines (e.g. Sadler et al. 2002).

1.4.2 The Unification Models of AGN

Unification models of AGN propose that the different species of AGN are the same type of physical object observed under different conditions. Astronomers have been attempting to unify the different classes of AGN for many decades (For an in-depth review see Antonucci 1993). The currently accepted model that unifies AGN is that of Urry and Padovani (1995). In this model, the apparent differences between the classes are simply attributed to the orientation of the source to the observer.

Osterbrock (1978) suggested that Seyfert 2 galaxies may be physically similar to Seyfert 1 galaxies but viewed in such a way that the BLR is obscured. Figure 1.3 shows how Seyfert 2 galaxies are being viewed side-on with the dusty torus obscuring the BLR. Similarly, NLRGs are being viewed in such a way that the dusty torus is obscuring the BLR.

The luminous nature of blazars may be explained as radio sources aligned to our line-of-sight.

While the unified model of AGN does not yet account for the "radio loud" and "radio quiet" sub-classes of AGN, it seems feasible that these are the brightest and faintest manifestations of the phenomena and the only difference between Seyfert 1 and 2 galaxies, and quasars and blazars, is the luminosity of the AGN. Kellermann et al. (1994) found that many "radio quiet" quasars had similar properties to "radio loud" quasars and concluded that at least some "radio quiet" quasars were powered in a similar way to their "radio-loud" counterparts.

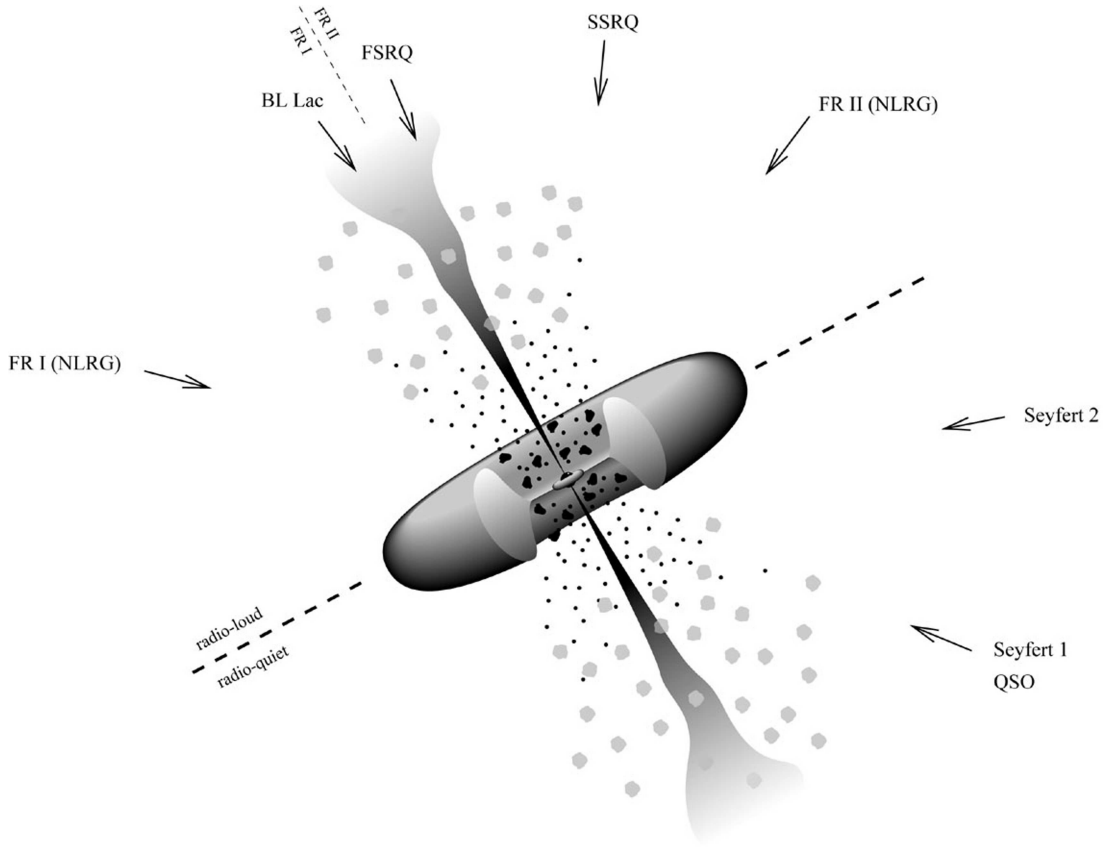

Figure 1.3: A schematic of the general AGN model, showing the central SMBH surrounded by the accretion disk. Also shown are the dusty torus and the jets. The arrows show how the orientation of the AGN affects the observer. For example, observing close to the plane of the torus would obscure the BLR resulting in the observation of a Seyfert 2 galaxy or a NLRG. Classifications above the dotted line are for radio-loud AGN while classifications below the line are for radio-quiet AGN. Image credit: Urry and Padovani (1995)

1.4.3 Radio Emission from AGN

Radio emission from AGN can be compact or extended. Extended radio emission tends to have very characteristic morphologies with a radio "core", coincident with the SMBH, and radio "lobes" corresponding to the medium disturbed by the AGN jet. High resolution radio images sometimes also show the highly collimated radio "jet". Radio lobes typically display a steep power law spectrum while radio cores can have flat spectra, indicative of synchrotron self-absorption (e.g Ker et al. 2012).

Fanaroff and Riley (1974) separated extended radio emission into what are now known as FRI and FRII types based on the morphology of the radio source. FRI galaxies have very bright cores and fainter radio lobes (Figure 1.4) while FRII galaxies are edge-bright with a fainter core (Figure 1.5). FRII galaxies tend to be more luminous than FRI galaxies (e.g Auriemma et al. 1977) and they reside in different environments, with FRIs often associated with clusters of galaxies.

Any of the above classes of AGN may host compact radio emission. Only quasars, blazars and radio galaxies have been associated with FRI and FRII radio sources.

Some radio galaxies display a "C" or "V" shaped morphology and these are known collectively as Head-Tail Galaxies (Miley et al. 1972). Head-tail galaxies can be further separated into narrow-angle tail galaxies (NATs) and wide-angle tail galaxies (WATs) (Owen and Rudnick 1976). Both WATs and NATs tend to be associated with clusters of galaxies and the peculiar morphology of NATs and WATs is attributed to the strong intra-cluster winds caused by interactions such as merging clusters. Venkatesan et al. (1994) suggest that NATs are caused by their host galaxies having high peculiar velocities while WATs tend to reside near the centres of dynamical, non-relaxed clusters (Burns 1998). Chapter 4 describes WATs in more detail.

Accretion Modes

As discussed in Section 1.4.1, radio-loud AGN hosts may display either emission-line spectra with strong high-excitation lines, either broad or narrow depending on orientation (e.g. Antonucci 1993), or early-type spectra (e.g Sadler et al. 2002). Sources with high-excitation lines are said to be undergoing "cold-mode" accretion while sources without high-excitation lines are said to be undergoing "hot-mode" accretion (Hardcastle et al. 2007; Croton et al. 2006). The radiatively

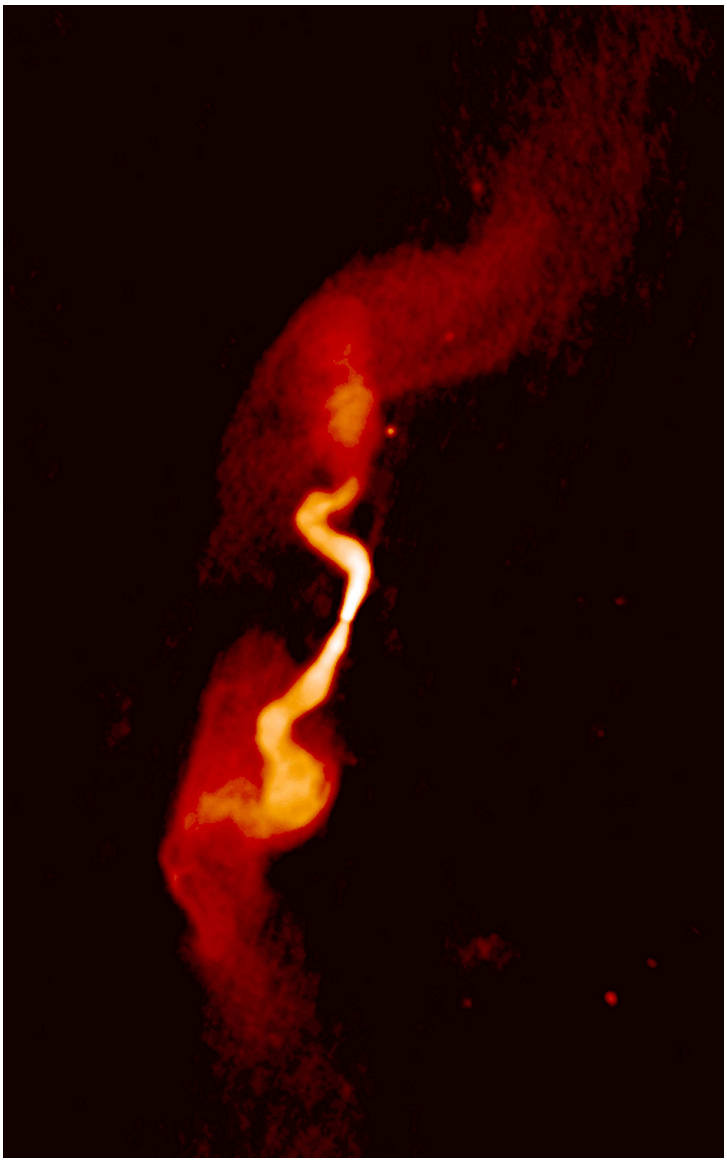

Figure 1.4: The FRI galaxy 3C31 observed using the VLA at 1.4 GHz. Image courtesy of NRAO/AUI.

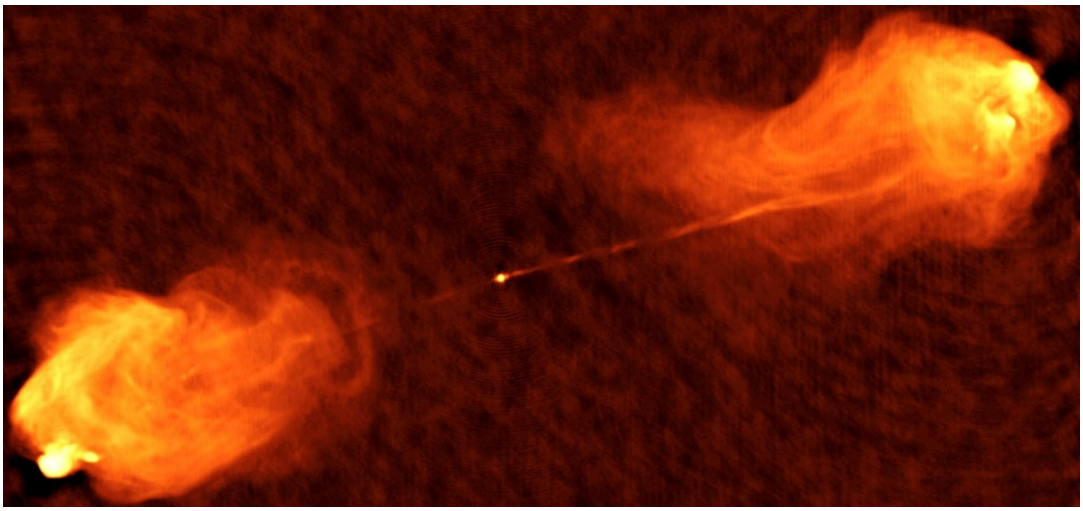

Figure 1.5: Cygnus A, the archetypal FRII galaxy, observed using the VLA at 5 GHz. Image courtesy of NRAO/AUI.

efficient "cold-mode" accretion is fuelled by cold gas and results in an geometrically thin, optically thick accretion disk within a hot broad-line region, and a narrow-line region further out, consistent with the standard model for AGN. Conversely the radiatively inefficient "hot-mode" accretion is fuelled by hot gas and results in a geometrically thick, optically thin accretion disk. Recently Best and Heckman (2012) suggested that the varying fractions of "hot" and "cold" mode sources with redshift could explain the luminosity dependence of the AGN radio luminosity function.

1.4.4 Star-Forming Galaxies

The radio emission from star-forming galaxies is predominately non-thermal synchrotron emission from cosmic ray electrons that are accelerated by supernovae shocks (e.g Condon 1992). There is also a minor contribution by a thermal component that arises from free-free emission from ionised hydrogen in HII regions. Figure 1.6 shows the observed radio and infrared spectral energy distribution (SED) for M82.

The far-infrared emission from star-forming galaxies is dominated by thermal radiation from dust. van der Kruit (1971) was the first to notice the correlation between far-infrared and radio emission from star-forming galaxies in the local Universe. This correlation is known as the far-infrared radio correlation (FRC) and is one of the tightest and most universal correlations known among global

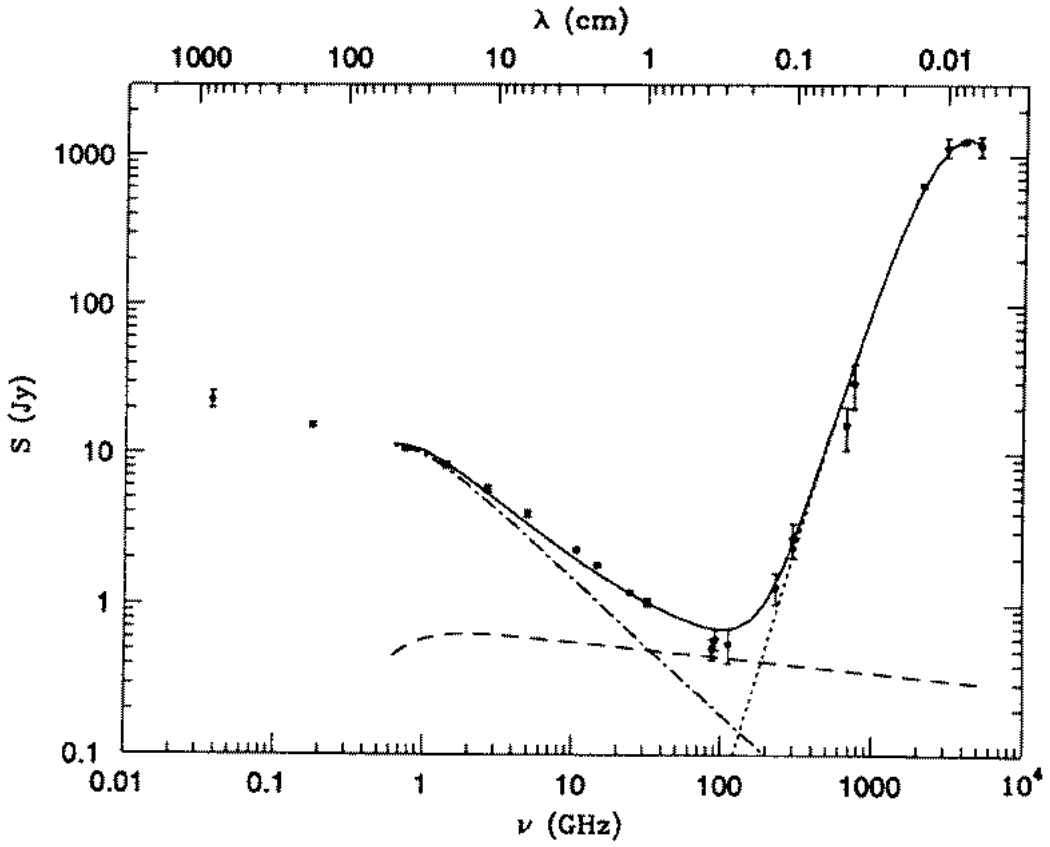

Figure 1.6: The observed far-infrared and radio SED of M82. Synchrotron emission is denoted by the dot-dash line, free-free emission is denoted by the dashed line and thermal emission from dust is shown by the dotted line. The solid line is the sum of these components. Image credit: Condon (1992)

parameters of galaxies (Helou and Bicay 1993). The correlation is believed to arise due to the presence of young, high-mass stars. The young massive stars emit UV radiation that is absorbed by dust and subsequently reradiated at infrared wavelengths. The radio emission is dominated by supernovae shocks accelerating cosmic ray electrons, which emit synchrotron emission. Chapter 5 presents a study of the FRC to $z \sim 2$.

The optical spectra we see for star-forming galaxies are made up of direct emission from stars as well as emission features due to gas being heated and then re-radiated at specific wavelengths. The short-lived, young, hot OB stars emit most of the ionizing photons ($E > 13.6\,eV$) that energize the surrounding HII regions. The most prominent spectral lines include the forbidden lines [OII] (3726 Å, 3729 Å), [OIII] (4959 Å, 5007 Å) and [NII] (6548 Å, 6583 Å), as well as the Balmer series (6563 Å, 4851 Å, 4340 Å, ...). The first detection of [OIII] was proposed to be a new element termed "Nebulium" by William Huggins in 1864. This was because the forbidden nature of this transition means that it can only occur in extremely low density environments. Bowen (1927) correctly identified Nebulium as the forbidden transition, [OIII]. SF galaxy spectra also include absorption features due to the older, underlying stellar population.

1.4.5 Radio Surveys

This section will summarise the current status of radio surveys and emphasise the need for a deep and wide survey such as the Australia Telescope Large Area Survey, the data from which the remainder of this thesis relies.

Until recently, most radio surveys concentrated on detecting only AGN, and radio emission from star-forming galaxies could only be detected in the very nearby Universe. As telescope technology has improved, deeper radio surveys are detecting radio emission from progressively fainter populations. One of the most confounding issues in radio astronomy in recently times is the nature of the sub-milliJansky radio population. Radio source count plots show a distinct "upturn" below 1 mJy beam^{-1} (Figure 1.7) and some studies attribute this to evolution of the SF galaxy radio luminosity function (e.g. Hopkins et al. 1998), others attribute this to a higher number density of low-luminosity AGN (e.g Huynh et al. 2007). The lack of consensus regarding the relative distribution of SF galaxies and AGN at low flux densities is likely due to the small areas of sky surveyed at these sensitivities.

The famous 3C and 3CR catalogues (Edge et al. 1959; Bennett 1962) presents

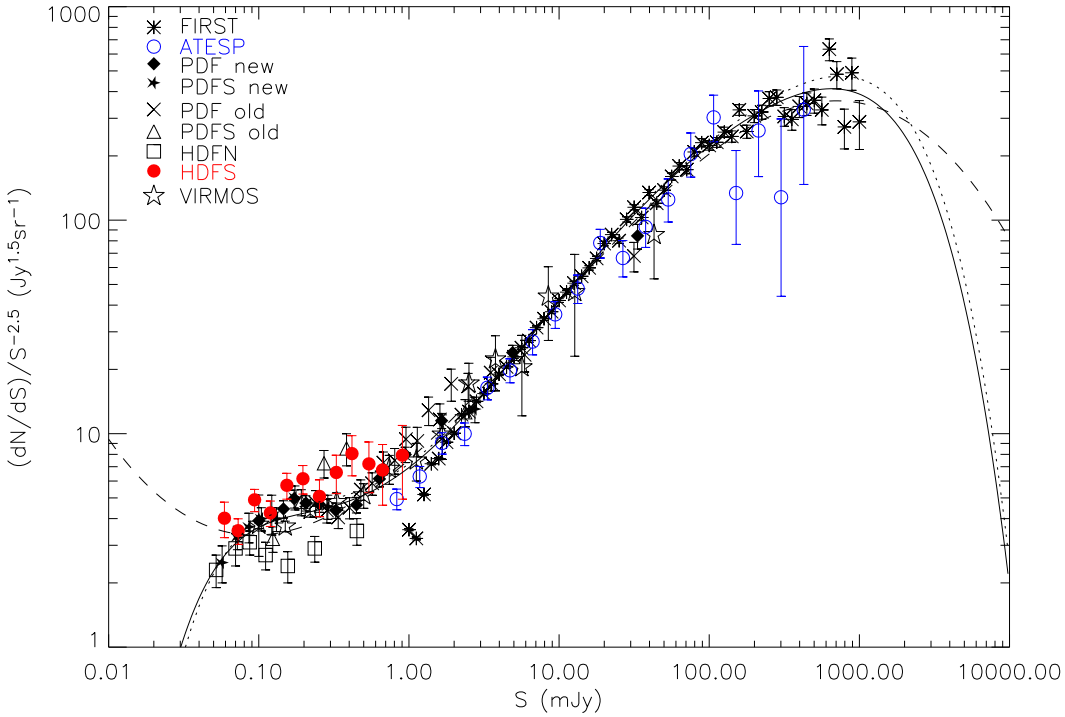

Figure 1.7: Normalized 1.4 GHz differential radio source counts for the Hubble Deep Field South compared with other radio surveys. Image credit: Huynh et al. (2005)

radio sources at 158 MHz and 178 MHz respectively down to a limiting flux density of 9 Jy beam^{-1}. Interestingly, the flux density limit was not based on telescope sensitivity, but on confusion due to the poor angular resolution of the telescope. The PKS catalogue (Ekers 1969) presents radio sources observed with the Parkes radio telescope to 4 Jy beam^{-1} at 408 MHz. Needless to say, at these flux density limits, most detected sources were radio-loud AGN, with the notable exceptions of the centre of the Milky Way and the Crab Nebula.

The NRAO VLA Sky Survey (NVSS) was conducted using the Very Large Array at 1.4 GHz detecting all radio sources brighter than 2.5 mJy beam^{-1} (Condon et al. 1998) and covered the northern sky. The Southern hemisphere equivalent, the Sydney University Molonglo Sky Survey (SUMSS) was completed a few years later at 843 MHz (Mauch et al. 2003). These surveys were able to detect large numbers of star-forming galaxies in the local Universe and were subsequently used to probe the cosmic evolution of radio sources, both SF galaxies and AGN, to faint flux density levels (e.g Sadler et al. 2002; Best et al. 2005; Mauch and Sadler 2007).

The current deepest radio surveys reach rms levels of $< 10\mu$Jy beam^{-1}, but cover only very small areas on the sky (e.g Owen and Morrison 2008).

In order to understand the μJy-radio population it is imperative that sensitive surveys are conducted over large areas on the sky. The large areas ensure the volumes of the Universe probed are truly representative, and also mitigate the effects of cosmic variance (Moster et al. 2011). Deep radio survey data combined with sensitive multi-wavelength ancillary data will enable the formation and evolution of radio sources to be investigated.

A number of teams are working with this goal in mind including the Cosmic Evolution Survey (COSMOS Scoville et al. 2007). Figure 1.8 plots the area against sensitivity for a number of radio surveys. With the aim of imaging seven square degrees down to 10 μJy beam^{-1}, the Australia Telescope Large Area Survey will produce the widest deep radio image at 1.4 GHz to date with the major goal of probing the formation and evolution of radio galaxies.

Spectroscopic Redshifts and the importance of multi-wavelength ancillary data

In order to determine the cosmic evolution of radio sources it is important to know their distance measure, or redshift. Unfortunately determining the red-

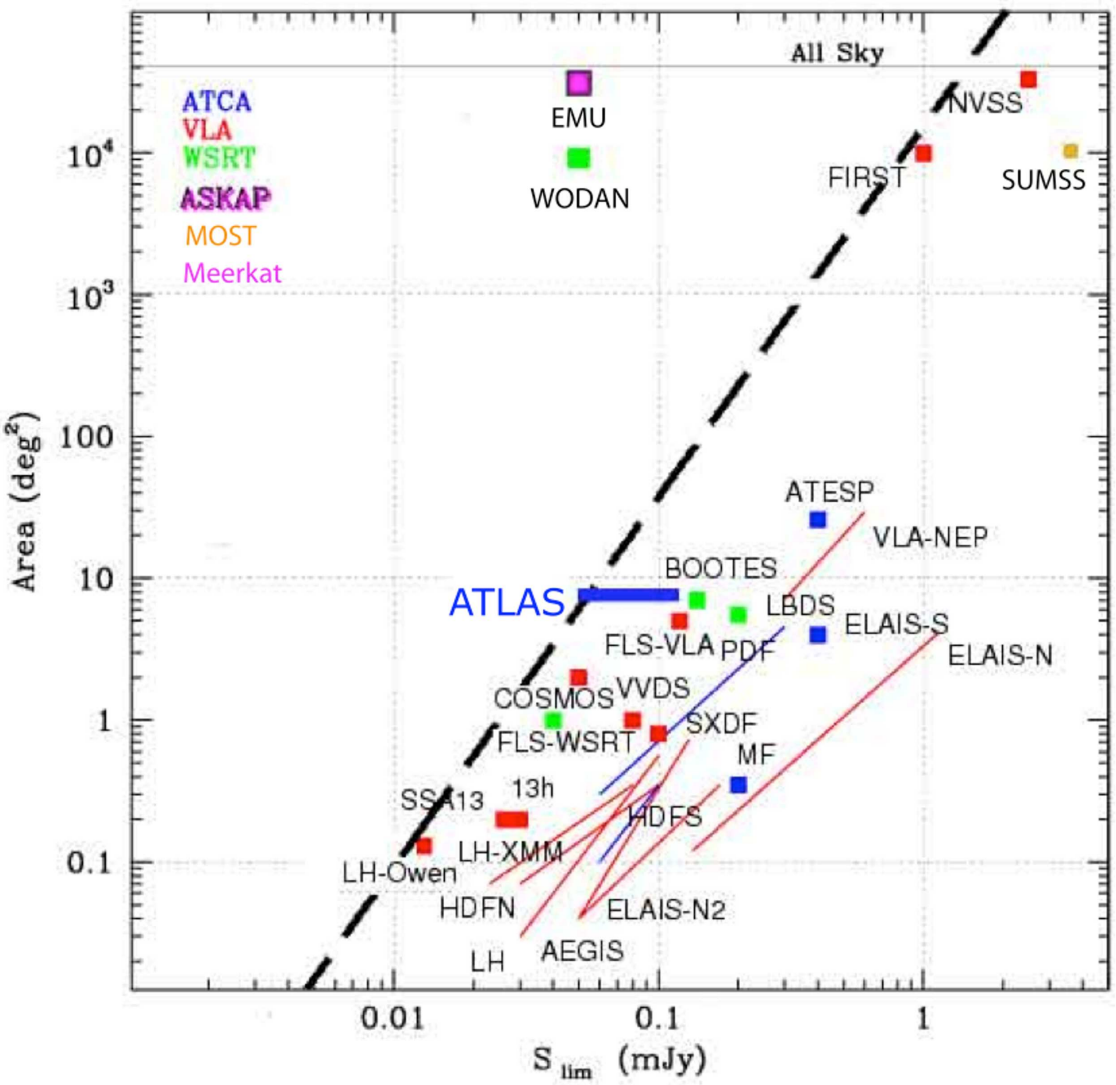

Figure 1.8: The area and sensitivity of current 1.4 GHz radio surveys. The dashed line shows the limit of conventional radio telescopes with the shallowest all-sky surveys appearing the top right corner and the deepest, albeit small, surveys appearing in the bottom left. Also shown are the EMU (Norris et al. 2011a) and WODAN (Röttgering et al. 2011) surveys that will utilise the next generation radio telescopes ASKAP and WODAN. EMU is so far left of the dashed line due to ASKAP's phased-array feed, which will enable survey speeds $\sim 30\times$ faster than current-generation telescopes, despite comparable integration times per field. Image courtesy of Ray Norris.

shift is difficult from radio continuum emission alone[9]. Consequently, radio surveys with the aim of understanding cosmic evolution are of little value without redshift data. These surveys are further enhanced by multi-wavelength ancillary data. Multiwavelength data contribute valuable information about the radio sources, including the ability to help differentiate between star-forming galaxies and AGN.

As the primary science goal of ATLAS is to determine the cosmic evolution of radio sources, obtaining redshifts for these sources is imperative. Photometric redshifts rely on the shape of the galaxy continuum emission and are very accurate for bright sources in the local Universe, but less accurate at higher redshifts. Photometric data can be thought of as very low resolution spectra. Photometric redshifts are derived from matching template spectra with the "photometric spectrum". For spectra with strong continuum features, such as the 4000Åbreak in early-type spectra, photometric redshifts can be very accurately determined. Conversely, late-type spectra have much weaker continuum features until the Lyman-alpha line is redshifted into optical bands at higher redshifts. Moreover, the continuum emission for late-type spectra is strongly related to the age of the underlying stellar population and the presence of dust can severely "redden" a spectrum. For these reasons, photometric redshifts for late-type hosts can be less accurate. Radio sources may be hosted by a wide-range of galaxy types and may contain both AGN and star-forming components so the inaccuracies with photometric redshifts are compounded.

We note here that much work is being undertaken to improve the accuracy of photometric redshifts (e.g Salvato et al. 2009). In ATLAS we choose to rely solely on spectroscopic redshifts, which are highly accurate and very reliable, but are much more time consuming to obtain.

1.5 This Thesis

The background provided in this Chapter sets the scene for this thesis, which presents work that has resulted from the optical spectroscopy of ATLAS radio sources from data release 1. Chapter 2 presents a summary of the ATLAS radio survey, and briefly describes the telescopes used during this thesis.

In the remainder of this thesis I explore three issues as steps towards under-

[9]Yun and Carilli (2002) have developed a technique to derive photometric redshifts using the radio-to-far-infrared SED.

standing the cosmic evolution of galaxies.

1. How does the radio luminosity function evolve with redshift?

2. Can we use wide-angle tail radio sources to trace the clustering of galaxies to high redshifts?

3. Does the far-infrared radio correlation change with redshift?

The radio luminosity function (RLF) plots the number density of sources as a function of radio luminosity. Understanding how the RLF evolves with redshift is integral to studies of galaxy evolution. While the RLF is well defined in the local Universe (e.g. Mauch and Sadler 2007), it is less well understood at higher redshifts where the sources appear fainter. ATLAS's depth and breadth allows us to study the RLF for low-luminosity radio sources to moderate redshifts. Furthermore, the relative fraction of star-forming galaxies and AGN may be investigated as a function of radio luminosity. For example, a recent study by Kimball et al. (2011) suggests that the radio luminosity function of quasars is dominated by the AGN component at high luminosities and star-formation in the host galaxy at low-luminosities. Chapter 3 presents the ATLAS spectroscopic catalogue including spectroscopic classifications and the radio luminosity function.

WATs may be used as probes for clusters of galaxies (e.g. Blanton et al. 2001). In Chapter 4 we report the detection of six WATs in ATLAS and investigate whether WATs may be detected to high redshifts and hence be used as probes for high-redshift clusters. It is important to calibrate how well we can detect WATs to high redshifts, as next-generation surveys such as EMU will likely detect tens of thousands to hundreds of thousands of WATs and hence clusters. The detection of high-redshift clusters will contribute significantly to research into areas such as the evolution of clusters of galaxies, the formation of massive elliptical galaxies and the relationship between massive ellipticals and SMBHs (e.g Blanton et al. 2003; Chiaberge et al. 2009).

The FRC holds for a wide range of galaxy types and is remarkably tight over five orders of magnitude of bolometric luminosity. Understanding how it evolves with redshift will place constraints on how properties such as magnetic field strength and metallicity evolve with redshift. For example, evolution of the magnetic field strength should affect measured radio flux densities, and evolution in dust properties and metallicity should affect measured infrared flux densities, both of which may be expected to affect the FRC, especially at higher redshifts

(e.g Murphy 2009; Amblard et al. 2010). The FRC has been used to distinguish between star-forming galaxies and radio-loud AGN (e.g. Norris et al. 2006), and Carilli and Yun (1999) has used the FRC to estimate distances to submillimetre galaxies without optical counterparts. Thus it is very important to determine whether the FRC holds at high redshifts. Chapter 5 presents our study into the evolution of the FRC in to $z \sim 2$.

Chapter 6 summarises and concludes this thesis.

2

ATLAS and the telescopes

2.1 ATLAS

The Australia Telescope Large Area Survey (ATLAS) is the widest deep-field radio survey attempted to date at 1.4 GHz, with the aim of imaging seven square degrees to 10 μJy beam^{-1} rms using the Australia Telescope Compact Array (ATCA) (Norris et al. 2006; Middelberg et al. 2008). ATLAS is observed over two fields to minimise the effects of cosmic variance[1]: the Chandra Deep Field South (CDFS) and the European Large Area ISO Survey–South 1 (ELAIS-S1). These fields are chosen for their wealth of multi-wavelength data and have both been observed extensively in the infrared as part of the Spitzer Wide-field InfraRed Extragalactic survey (SWIRE Lonsdale et al. 2003) and the Spitzer Extragalactic Representative Volume Survey (SERVS Lacy and SERVS Team 2009).

Deep radio surveys are invaluable for understanding the formation and evolution of galaxies, especially because radio emission can penetrate obscuring dust.

[1] Cosmic variance in the context of this thesis is taken to mean the presence of large-scale structures in the Universe (Moster et al. 2011). The only method of avoiding the effects of cosmic variance is to survey a sufficiently large volume of the Universe so that it is fairly represented.

2.1.1 CDFS

The Chandra Deep Field South (CDFS) was initially observed as a single field (∼16 × 16 arcminutes) with the ACIS (AXAF CCD Imaging Spectrometer) on the Chandra X-ray Observatory for 1Ms (Giacconi et al. 2002). The CDFS now contains the deepest X-ray observations (Xue et al. 2011) having been observed for 4Ms. The CDFS is probably the most intensely studied region of the sky and incorporates the Southern field of the Great Observatories Origins Deep Survey (GOODS-South, Dickinson et al. 2003), which also includes the *Hubble* Ultradeep Field (HUDF, Beckwith et al. 2006).

Prior to Norris et al. (2006), the CDFS had been observed with the ATCA at 1.4 GHz by Koekemoer et al. (2003). These observations reached a similar rms to Norris et al. (2006), over a smaller area (Figure 2.1). Kellermann et al. (2008) and Miller et al. (2008) have also observed the quarter of a square degree extended-CDFS at 1.4 GHz with the Very Large Array (VLA) down to ∼8 μJy beam^{-1} rms.

2.1.2 ELAIS-S1

The European Large Area ISO Survey (ELAIS) imaged 12 square degrees of sky at 15 and 90 μm using the Infrared Space Observatory (ISO) (Rowan-Robinson et al. 1999), including the South-one field. ELAIS was the largest project undertaken with ISO. Subsequently ELAIS-S1 has been observed as part of both the SWIRE and SERVS infrared surveys. ELAIS-S1 is also the subject of optical follow-up as part of the ESO-Spitzer Imaging extragalactic Survey (ESIS Berta et al. 2006). At the time of writing this thesis, the ESIS data has not yet been fully released.

Prior to Middelberg et al. (2008), the ELAIS-S1 had been observed with the ATCA at 1.4 GHz by Gruppioni et al. (1999). These observations were a factor of three lower in sensitivity, albeit over a slightly larger area.

2.1.3 ATLAS Science Goals

The broad scientific goals of ATLAS are to understand the formation and evolution of galaxies since the beginning of time. The specific science goals of ATLAS include

1. Determining the relative contribution of star-forming galaxies and AGN at faint radio flux densities. "Hybrid" sources are of particular interest, that

is, sources with radio emission originating both from the star-forming disc and the AGN.

2. Tracing the radio luminosity function to high redshifts.

3. Determining whether the far-infrared radio correlation changes with redshift.

4. Searching for overdensities of ultra-luminous infrared galaxies (ULIRGs) at high redshifts, which are likely to be signposting the positions of proto-clusters in the early Universe.

5. Exploring a region of uncharted parameter space that would enable us to discover rare but important objects.

ATLAS radio observations were carried out with the Australia Telescope Compact Array (ATCA, Project ID C1241) from 2004–2008 using the old ATCA correlator, and from 2008–2011 using the Compact Array Broadband Backend (CABB Wilson et al. 2011). The first data release (Data Release 1, or DR1) consists of the preliminary data from the old correlator and reaches an rms sensitivity of $\sim 30\mu$Jy beam^{-1} (Norris et al. 2006; Middelberg et al. 2008). The final ATLAS data release (DR3, Banfield et al. in preparation) will include the additional CABB data and is expected to reach an rms sensitivity of $\sim 10\mu$Jy beam^{-1}. Unless specified otherwise, all ATLAS radio data in this thesis are from DR1. This is because at the time of writing this thesis future data releases had not been finalised.

The radio data from DR1 comprised 173 hours on CDFS, or 8.2 hours per pointing, and 231 on ELAIS-S1, or 10.5 hours per pointing. There are 2018 radio sources in ATLAS within a total area of 7.65 square degrees. The ATLAS radio fields are shown in Figures 2.1 and 2.2.

2.1.4 ATLAS Science Results

ATLAS data have yielded a number of science results including the discovery of infrared faint radio sources, extending the infrared-radio correlation to lower flux densities and the discovery of a large population of obscured AGN with AGN-like radio morphologies but star-forming spectral energy distributions (e.g Mao et al. 2010a).

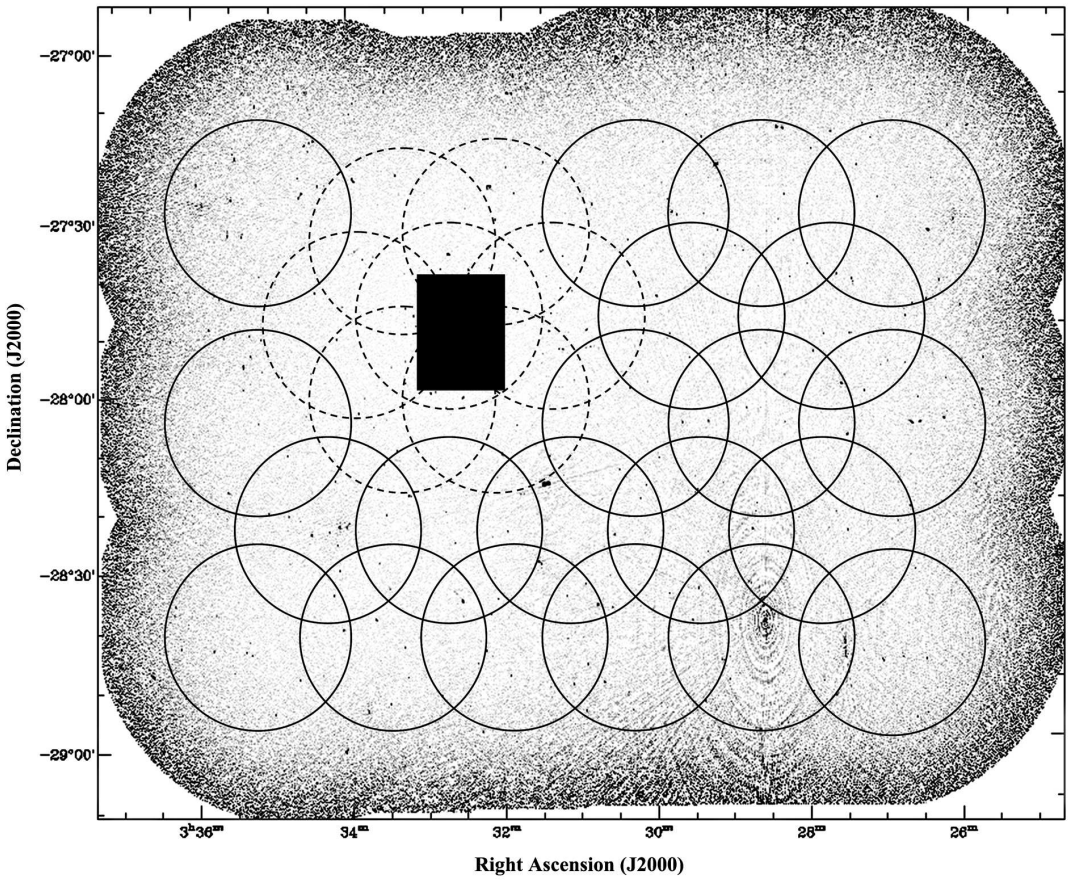

Figure 2.1: ATLAS 1.4 GHz radio image of CDFS from figure 1 of Norris et al. (2006). The circles show the FWHM of the primary beam. The solid circles show the new observations by Norris et al. (2006) while the dashed circles show the field observed previously by Koekemoer et al. (2003). The black solid rectangle shows the location of the GOODS field.

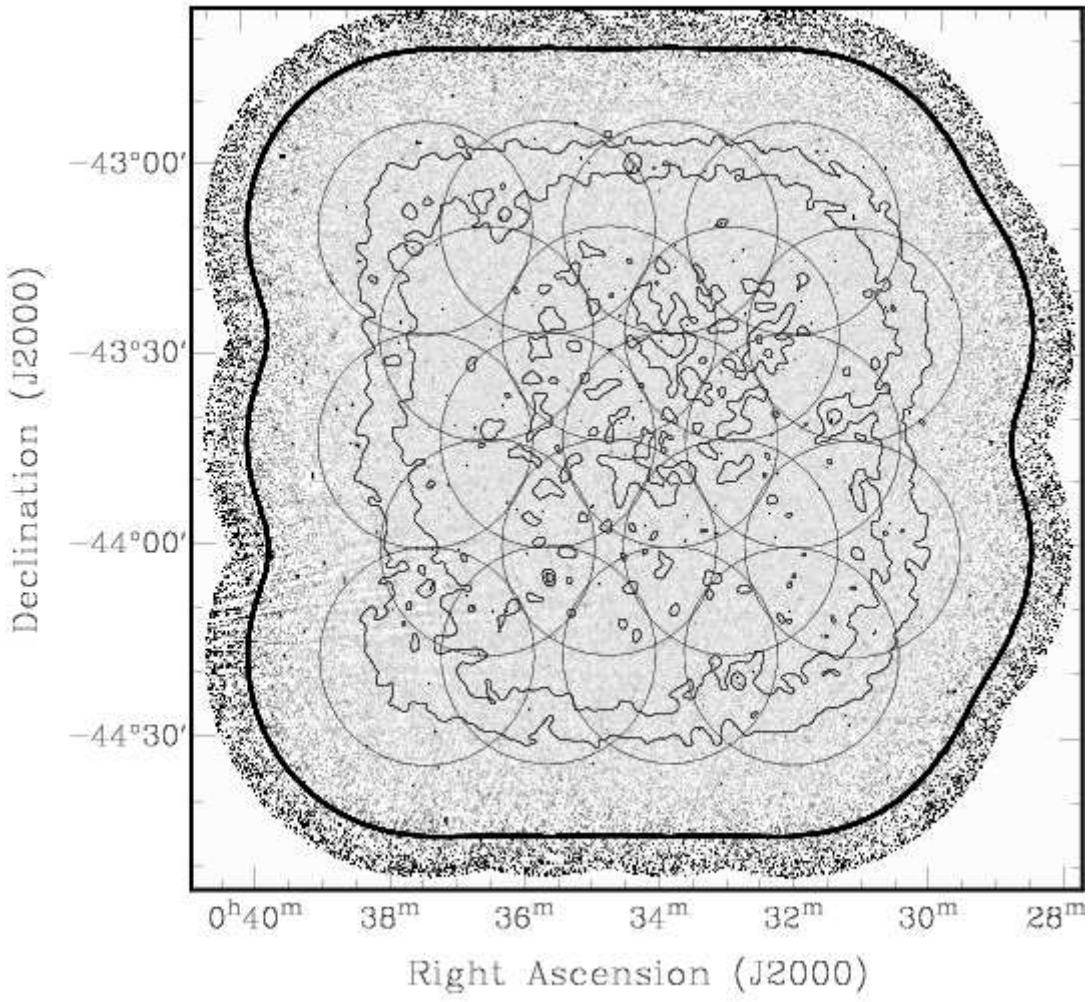

Figure 2.2: ATLAS 1.4 GHz radio image of ELAIS-S1 from figure 1 of Middelberg et al. (2008). The circles show the FWHM of the primary beam. The thin contours show the noise levels of 25 μJy, 35 μJy and 45 μJy and the thick contour marks the area Middelberg et al. (2008) used for analysis.

IFRS

Infrared Faint Radio Sources (IFRS) were first discovered by Norris et al. (2006) and have since spawned a great deal of interest. Although radio sources with no bright counterparts had been seen before (e.g. Richards et al. 1999), it was assumed that the hosts were obscured by dust. Consequently, it was expected that all radio sources detected by ATLAS would appear in the SWIRE catalogue (Norris et al. 2006).

It was an unexpected result that ~ 50 ATLAS sources did not have a counterpart at any *Spitzer* wavelength. Norris et al. (2006) termed these sources IFRS. IFRS were subsequently defined by Zinn et al. (2011) as sources that satisfied the following two criteria:

- the ratio of radio to mid-IR flux density ($S_{20\,cm}/S_{3.6\,\mu m}$) exceeds 500 and,
- the 3.6 μm flux density is less than 30 μJy.

The large radio to mid-IR flux density ratio ensures the IFRS is radio-loud and the faint infrared flux density limit ensures the IFRS is at $z > 1$.

The nature of the IFRS has been the subject of much debate. Norris et al. (2007) observed two ATLAS IFRS, using Very Long Baseline Interferometry (VLBI) with the Australian Long Baseline Array (LBA), and detected one. The VLBI detection implies a brightness temperature that can only be produced by non-thermal emission from an AGN. Middelberg et al. (2011) investigated the radio properties of IFRS and find their angular scales to be, in general, smaller than typical galaxies. Moreover, they tend to have steep spectral indices so Middelberg et al. (2011) conclude they are likely to be high-redshift AGN. Norris et al. (2011c) recently searched very deep 3.6 μm SERVS data for IFRS counterparts and made no firm detections. Stacking of the SERVS data at the IFRS positions yields a tentative detection in the image centre. Norris et al. (2011c) concludes that IFRS are likely to be radio-loud AGN at $z < 3$, or a new class of lower redshift ($1 < z < 3$) radio-loud AGN, whose hosts are severely obscured by dust.

Mid-Infrared Radio Correlation

Beswick et al. (2007) traced the mid-infrared radio correlation at 24 μm over seven orders of magnitude, down to sources with 24 μm flux densities of $\sim 80\,\mu$Jy. Boyle et al. (2007) stacked ATLAS radio data to probe the correlation at μJy levels and found that although the correlation held, it was inconsistent with previous

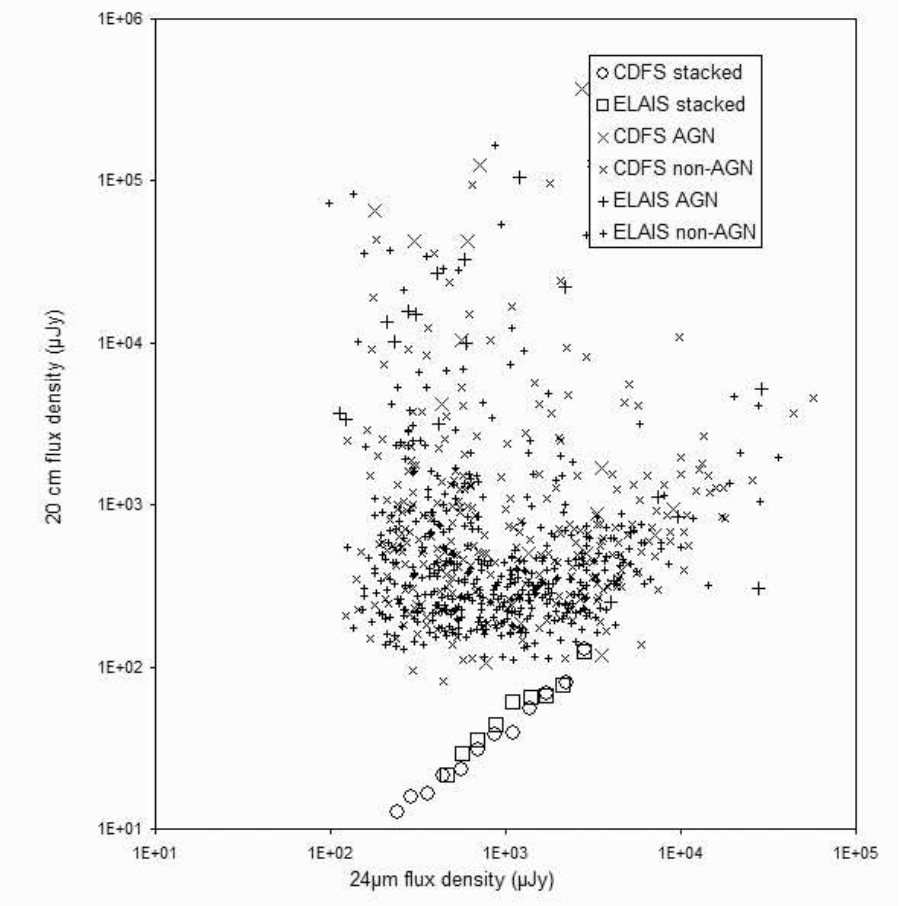

Figure 2.3: 24 μm infrared flux densities plotted against 1.4 GHz radio flux densities for ATLAS sources. The open symbols show the stacked data from Boyle et al. (2007). Image credit: Norris et al. (2007)

studies. The correlation from Boyle et al. (2007) for ATLAS data is shown in Figure 2.3, and also includes AGN, which may be distinguished by the fact that they do not lie on the correlation.

Boyle et al. (2007) discuss various explanations for their correlation, including the possibility of error, but their simulations appear to rule this out. Norris et al. (2007) suggest that the weak radio sources that are causing the correlation may represent a new population of objects. Consequently, Norris has selected a sample of 24 μm-excess sources in the ATLAS fields to study this population. The redshifts of these sources are presented in Appendix A.1.

2.2 Telescopes

When commencing this thesis, ATLAS radio observations were not yet complete and as a PhD student in the ATLAS team I was fortunate to participate in many hours of observing at the Australia Telescope Compact Array. At the time of writing, these data are close to being published in Banfield et al. (in preparation).

The initial aim of this thesis was to obtain spectroscopic redshifts for the ATLAS radio sources so that the formation and evolution of these sources could be investigated. In order to achieve this we spent a total of 24 nights over three years observing on the Anglo-Australian Telescope. Unfortunately, due to poor weather, the goal of measuring spectroscopic redshifts for all radio sources in ATLAS was not achieved, but sufficient data were obtained to measure the radio luminosity function for faint radio sources ($\sim 150\mu$Jy beam^{-1}) to moderate redshifts ($z \sim 0.8$). These data are presented in Chapter 3.

The following section provides a brief description of the two telescopes whose data this thesis relies on, including a brief description of the AAOmega observations that I was primarily responsbile for.

2.2.1 The Australia Telescope Compact Array

The Australia Telescope Compact Array (ATCA) is a radio telescope located 237 m above sea level at −30°18′47″ South and 149°33′01″ East. The ATCA is part of the Australia Telescope National Facility (ATNF), which is operated by CSIRO Astronomy and Space Science (CASS), a division of the Commonwealth Scientific and Industrial Research Organisation (CSIRO).

The ATCA is an array of six 22 metre antennas with a maximum baseline of 6 km. Five of the antennas can be moved along a three kilometre East-West railway track, with the sixth antenna located a further three kilometres away. There is also a 214 m North spur on the three kilometre track. The array may be used between frequencies of 1.1 GHz and 105 GHz.

The Compact Array Broadband Backend Wilson et al. (CABB 2011) was recently installed at the ATCA. The upgrade included a new correlator, increasing the maximum bandwidth from 128 MHz to 2 GHz in each of its two IF bands, and upgrades to the antenna feed and receiver systems. The CABB has improved the continuum sensitivity of the ATCA by at least a factor of four.

The radio data from the ATCA presented in this thesis are all pre-CABB, but I was actively involved in the commissioning of the CABB (Wilson et al. 2011) and

have been actively involved in projects that have utilised CABB's broad bandwidth (e.g. Emonts et al. 2011b,a).

2.2.2 The Anglo-Australian Telescope

The Anglo-Australian Telescope (AAT) is a 3.9 m optical telescope located 1165 m above sea level at −31°16′24″ South and 149°03′52″ East, near Coonabarabran in NSW. The AAT is operated by the Australian Astronomical Observatory (AAO), which was known as the Anglo-Australian Observatory until 2010. The AAT was commissioned in 1974 as a joint Australia and United Kingdom initiative, but Australia has funded it in its entirety since 2010, sparking the name change of the organisation. The AAT kept its name for posterity.

The AAT hosts a range of instruments, and AAOmega, the multifibre spectrograph (Sharp et al. 2006), was used for the ATLAS spectroscopy. The AAOmega spectrograph is a dual-beam system that can cover the spectral range between 3700Å and 8500Å using the 5700Å dichroic beam splitter, or 4700Å to 9500Å using the 6700Å dichroic.

AAOmega's two degree field (2dF) front-end has two sets of 392 fibres that may be distributed over a two degree field so as to obtain multiple spectra simultaneously. Positioning the fibres can take up to an hour so a tumbling mechanism allows one field to be observing while the alternate fibre set is being configured.

Although the ATLAS AAOmega observations and data reduction are summarised briefly in Chapter 3, some additional details are provided below. For the ATLAS observations, AAOmega was used in both the standard multi-object mode (Saunders et al. 2004; Sharp et al. 2006) and nod+shuffle mode (Glazebrook and Bland-Hawthorn 2001) with the low-resolution 580V and 385R Volume Phase Holographic gratings.

Science frames were generally observed for 1 – 2 hours with each exposure totalling 1200 – 1800 seconds. Multiple independent science observations are required for each science frame as exposures must be long enough to overcome read-out noise, but short enough such that cosmic rays do not dominate the CCD. Furthermore, a single observation could not exceed 3 hours of exposure as the rotation in the sky required a new field to be configured.

All science frame observations had associated quartz-halogen flat fields and combined CuAr+FeAr, Helium and Neon arc lamp frames. Additionally, zero-second "bias" frames and "dark frames" exposed for the same length of time as the science frames are taken.

AAOmega data were reduced using the 2dfDR package provided by the AAO. All data were preprocessed to remove bias and dark current structure. The observations of the "flat fields", uniformly illuminated by quartz-halogen lamps, were used to identify the fibres on the CCD and calibrate each individual fibre's relative response. The "arc frames", which observe well-known spectral lines, are used to determine the wavelength solution.

Although we are trying to observe extragalactic sources, the dominant signal received by the telescope is from the sky. The sky has both continuum emission and strong emission lines. In order to remove the sky spectrum from the science targets, there are ~20 dedicated sky fibres distributed over the 2dF plate. The number of sky fibres is required to decrease the noise in the sky spectrum. The sky fibres are averaged together to produce a less noisy sky spectrum that is scaled and subtracted from the science fibres.

Unfortunately, the averaged sky spectrum will have systematic errors, such as sky variations over the field, so the removal of the averaged sky spectrum makes the noise in the science fibre non-Poissonion. While the Poissonion noise decreases with the square root of the observing time, non-Poissonion noise from systematic errors do not (e.g. Sharp and Parkinson 2010). Consequently, faint sources cannot simply be observed for long integration times and other means of sky removal must be explored.

The sensitive Principle Component Analysis (PCA) method described in Sharp and Parkinson (2010) is ideal for observations of 10 – 100 hours. Unfortunately, this technique was still under development at the time of our observations and was not utilised.

Nod+shuffle (Glazebrook et al. 2004) allows for the accurate subtraction of the sky during spectroscopic observations. Nod+shuffle works on the basis that the unilluminated portions of a CCD may be used for storage. For example, after the telescope has observed the science target, this signal is "shuffled" into storage on the unilluminated portion of the CCD. Meanwhile, as the science target sits in storage, the sky is being observed *through the same fibre at the same pixels on the detector*. Consequently the observation of the sky has the same path and pixel response as the source enabling near-perfect sky subtraction. This method is less efficient than conventional modes of observing as two fibres must be dedicated to each science target, but as this method removes systematic errors, noise levels can be pushed closer to the Poisson limit leading to spectra being obtained for much fainter sources.

The resulting spectra were analysed using the RUNZ package with redshifts determined using either template cross-correlation or emission line fitting. Early-type spectra have strong continuum features and were more easily fitted using template cross-correlations to determine redshifts. Conversely, star-forming spectra have strong emission lines thus fitting to them was more easily achieved using emission line fitting. All spectra were visually inspected to ensure the validity of the redshift.

3

The Australia Telescope Large Area Survey: Spectroscopic Catalogue and Radio Luminosity Functions

This chapter is a reproduction of the first-author article *The Australia Telescope Large Area Survey: Spectroscopic Catalogue and Radio Luminosity Functions*, Mao M. Y., Sharp R., Norris R. P., Hopkins A. M., Seymour N., Lovell J. E. J., Middelberg E., Randall K. E., Sadler E. M., Saikia D. J., Shabala S. S., Zinn P., submitted to MNRAS on March 23, 2012. I was responsible for leading this work and was the primary person in charge of observing, reducing and analysing the optical data from the 2007, 2008 and 2010 AAT observations. The article was wholly written by me with the contributions of the coauthors as follows:

- Rob Sharp and Ray Norris supervised this work and assisted with the AAT observations. Rob also assisted with the data reduction, provided an independent set of eyes for the spectroscopic classifications and provided the IDL code that I modified to produce Figure 3.2.

- Andrew Hopkins, Nick Seymour and Elaine Sadler participated in many valuable discussions about the radio luminosity function. Elaine in particularly worked through the data in depth to ensure the generation of the radio luminosity function was correct.
- The remaining coauthors provided many valuable discussions towards the final manuscript.

The text is largely unchanged with only minor modifications for consistency.

Abstract

The Australia Telescope Large Area Survey (ATLAS) has surveyed seven square degrees of sky around the Chandra Deep Field South (CDFS) and the European Large Area ISO Survey - South 1 (ELAIS-S1) fields at 1.4 GHz to $\sim 30\,\mu$Jy beam^{-1} rms. Here we present 466 new spectroscopic redshifts for radio sources in ATLAS as part of our optical follow-up program. Of the 466 radio sources with new spectroscopic redshifts, 142 have star-forming optical spectra, 282 show evidence for AGN in their optical spectra, 10 have stellar spectra (which we attribute to chance alignments) and 32 have spectra revealing redshifts, but with insufficient features to classify. We compare our spectral classifications with two mid-infrared diagnostics and find them to be in broad agreement. We also construct the radio luminosity function for star-forming galaxies to z = 0.5 and for AGN to z = 0.8. The radio luminosity function for star-forming galaxies appears to be in good agreement with previous studies. The radio luminosity function for AGN is more puzzling and appears inconsistent with previous studies of the local AGN radio luminosity function. We explore the possibility of evolution, cosmic variance and classification techniques affecting the AGN radio luminosity function. ATLAS is a pathfinder for the forthcoming EMU survey and the data presented in this paper will be used to guide EMU's survey design and early science papers.

3.1 Introduction

Extragalactic radio sources comprise both star-forming (SF) galaxies and active galactic nuclei (AGN) (Condon 1992). In order to understand the history of the Universe we must unravel the cosmic evolution of both classes.

Radio galaxy hosts display a range of different optical spectra. SF galaxy spectra are made up of direct emission from starlight, and are quite easily identified at low redshifts. Some radio-loud AGN galaxies display strong high-excitation lines, either broad or narrow depending on obscuration and the orientation (Antonucci 1993), while others have weak or no emission features (e.g. Sadler et al. 2002). These spectral differences have been attributed to different accretion modes (Hardcastle et al. 2007; Croton et al. 2006). Sources without high-excitation lines are fuelled by the accretion of hot gas ('hot mode') while high-

excitation sources require fuelling by cold gas ('cold-mode'). The radiatively inefficient 'hot-mode' accretion is driven by the gravitational instability (Pope et al. 2012), and results in a geometrically thick, optically thin accretion disk within the hot broad-line region. On the other hand, the radiatively efficient "cold-mode" accretion results in a geometrically thin, optically thick accretion disk within the broad-line region, and a narrow-line region further out. 'Cold-mode' accretion may be triggered by a merger event (e.g. Shabala et al. 2011), which can also trigger star-formation within the galaxy. Consequently, sources undergoing 'cold-mode' accretion may appear as 'hybrid' objects, that is, objects whose radio emission results from both star-formation and an AGN component (e.g. PRONGS, Mao et al. 2010b). Norris et al. (2012) find that the extreme ULIRG, F00183-7111, is such an object.

Early radio surveys such as the 3C and 3CR Radio Surveys (Edge et al. 1959; Bennett 1962) had rms levels of a few Janskys and detected predominately powerful radio galaxies and quasars, allowing the cosmic history of these sources to be determined. Subsequent studies found that powerful radio galaxies and quasars evolve very strongly with redshift and the space density of these sources at $z \sim 2$ is orders of magnitude higher than in the local Universe (e.g. Dunlop and Peacock 1990).

More recent wide-field radio surveys such as NVSS (Condon et al. 1998), SUMSS (Mauch et al. 2003) and FIRST (Becker et al. 1995) have reached rms levels of a few mJy. At these flux densities the radio source population is dominated by radio galaxies and quasars powered by AGN (e.g. Sadler et al. 2002). The most powerful of these can be seen out to the edge of the visible Universe.

Source counts show a well-characterised upturn below 1 mJy beam^{-1}, which is above that predicted from the extrapolation of source counts for AGN with high-flux densities. Some studies attribute this to strong evolution of the SF galaxy luminosity function (e.g. Hopkins et al. 1998) while others find a significant contribution from lower-luminosity AGN (e.g. Huynh et al. 2007). Sadler et al. (2007) found that low-luminosity AGN undergo significant cosmic evolution out to z = 0.7, consistent with studies of the optical luminosity function for AGN (e.g. Croom et al. 2004).

The deepest radio surveys now reach rms levels below 10 μJy beam^{-1} (e.g. Owen and Morrison 2008), but cover very small areas on the sky. The distribution of AGN and SF galaxies at low flux densities is not well known, with some studies finding the proportion of AGN declining with decreasing flux density

and emission due to star-formation (SF) dominating (e.g. Mauch and Sadler 2007; Seymour et al. 2008), while other studies find the distribution is closer to a 50/50 split between SF galaxies and AGN down to $\sim$50 μJy beam^{-1} (e.g. Smolčić et al. 2008; Padovani et al. 2009). The lack of consensus of the distribution of AGN and SF at low flux densities is due to the small areas of sky surveyed at these sensitivities. Norris et al. (2011a) provide a brief comparison of the various studies and, in their figure 4, show that the fraction of SF galaxies at $<$100 μJy beam^{-1} could range from 30 - 80 per cent.

To date, understanding the evolution of the faint radio source population has been limited by the availability of sufficiently deep wide-area radio surveys. With the aim of imaging approximately seven square degrees of sky over two fields to 10 μJy beam^{-1} at 1.4 GHz, the Australia Telescope Large Area Survey (ATLAS, Norris et al. 2006; Middelberg et al. 2008) is the widest deep field radio survey yet attempted. ATLAS observes two separate fields so as to minimize cosmic variance (Moster et al. 2011): Chandra Deep Field South (CDFS) and European Large Area ISO Survey-South 1 (ELAIS-S1). The two fields were chosen to coincide with the *Spitzer* Wide-Area Infrared Extragalactic (SWIRE) Survey program (Lonsdale et al. 2003), so optical and mid-infrared identifications exist for most of the radio objects. CDFS also encompasses the Southern Great Observatories Origins Deep Survey (GOODS) field (Giavalisco et al. 2004).

The first data release (Data Release 1, or DR1) from ATLAS consists of the preliminary data published by Norris et al. (2006) and Middelberg et al. (2008) and reaches an rms sensitivity of $\sim$30 μJy beam^{-1}. The flux densities of DR1 are accurate to $\sim$10 per cent. The final ATLAS data release (DR3: Banfield et al., in preparation) will include additional data taken with the new CABB upgrade (Wilson et al. 2011) to the ATCA, and is expected to reach an rms sensitivity of $\sim$10 μJy beam^{-1}. For this paper we use radio data only from DR1.

Spectroscopic data provide accurate redshift information that can be used to determine absolute magnitudes, luminosities etc. This paper presents spectroscopic redshifts and spectral classifications of radio sources in the ATLAS fields obtained using the AAOmega multi-fibre spectrograph at the Anglo-Australian Telescope (AAT) of sources in the ATLAS fields. Section 2 describes the observations and data analysis while Section 3 provides spectral classifications and a description of the redshift catalogue. Section 4 discusses how the spectral classifications compare to mid-infrared diagnostics and presents the radio luminosity function for ELAIS. Section 5 summarises our conclusions.

This paper uses $H_0 = 70$ km s^{-1} Mpc^{-1}, $\Omega_M = 0.3$ and $\Omega_\Lambda = 0.7$ and the web-based calculator of Wright (2006) to estimate the physical parameters. Vega magnitudes are used throughout.

3.2 Observations and Data

3.2.1 Existing multi-wavelength data in ATLAS

Radio observations of ATLAS were carried out with the Australia Telescope Compact Array (ATCA, Project ID C1241). The ATCA was used in a variety of configurations to maximise uv coverage. ATLAS observations were performed in mosaic mode with 40 pointings. The radio data used in this paper are from DR1 (Norris et al. 2006; Middelberg et al. 2008). CDFS was observed for 173 hours in total, or 8.2 hours per pointing, and ELAIS was observed for 231 hours in total, or 10.5 hours per pointing. There are 2018 radio sources in ATLAS within a total area of 7.65 square degrees. Smaller subsets of the ATLAS-CDFS field have been observed using the VLA by Kellermann et al. (2008) and Miller et al. (2008) at 1.4 GHz. Cross-matching of the ATLAS radio sources to optical and infrared counterparts is discussed by Norris et al. (2006) and Middelberg et al. (2008).

Infrared observations of ATLAS were obtained by SWIRE (Lonsdale et al. 2003), the largest *Spitzer* legacy program. SWIRE covers seven different fields including CDFS and ELAIS, totalling 60 - 65 square degrees in area at all seven Spitzer bands. SWIRE observes at 3.6, 4.5, 5.8, 8 and 24 μm down to 5, 9, 43, 40 and 193 μJy beam^{-1} respectively. The SWIRE data used in this paper are all from the third SWIRE data release.

3.2.2 Anglo-Australian Telescope Observations and Data Reduction

Source Selection

The aim of the optical observations was to obtain spectra for all radio sources. A small fraction ($< 10\%$) have spectroscopic redshift information in the literature, predominately in CDFS. Consequently, these were assigned a low observation priority. Furthermore, radio sources with very faint or no optical counterparts were also assigned a low observation priority.

Table 3.1: Summary of AAT observations. N. obs gives the number of fibres placed on science sources. The seeing information is from the AAT observing log. All observations were performed in multi-object mode with the exception of 'CDFS A ns' and 'CDFS B ns', which were performed in nod+shuffle mode.

Observation	N. obs.	Exposure (s)	Obs. date	Dichroic	Seeing (arcseconds)
CDFS A bright	329	3 × 1200	20071202	5700Å	2.4
CDFS A bright	343	4 × 1200	20071204	5700Å	
CDFS B bright	329	4 × 1200	20071204	5700Å	
CDFS A med	343	4 × 1800	20071207	5700Å	1.9-2.5
CDFS B med	329	2 × 1200	20071205	5700Å	1.8-2.3
CDFS A ns	162	1 × 1500	20071206	5700Å	1.4
CDFS A ns	162	13 × 2400	20071206,07,08	5700Å	1.2-3
CDFS A ns	187	5 × 2400	20071208	5700Å	1.2 - 1.7
CDFS B ns	187	1 × 1500	20071205	5700Å	2.3
CDFS A 2010	329	6 × 2400	20101206	5700Å	
CDFS B 2010	329	2100+1500	20101207	5700Å	
ELAIS bright	343	7 × 1200	20071205	5700Å	1.8
ELAIS bright	343	4 × 1800	20081221,22	6700Å	1.6-1.7
ELAIS bright	329	4 × 1800	20081224,25,26	6700Å	1.6-2.4
ELAIS 2010	343	1270+1770	20101208	5700Å	1.4 - 1.6

The position of counterparts for optical spectroscopy were identified with the SWIRE mid-infrared positions to provide sub-arcsecond astrometry (Norris et al. 2006; Middelberg et al. 2008). Optical photometry at these positions was derived from SWIRE[1] (Lonsdale et al. 2003) to identify our sample (both 'bright' and 'med' in Table 3.1) consisting of sources with $16 < R < 22$, which were suitable for normal AAOmega observations. The optical photometric data in SWIRE is not uniform, with areas where no data are available. Within these areas we used photometric data from SuperCOSMOS (Hambly et al. 2001).

The 'bright' sample yielded the majority of the successfully determined redshifts presented in this paper. In addition, a 'faint' sample of sources with $R > 22$ was selected for nod+shuffle observing, but these were unable to be completed because of poor weather. Of the 1120 sources observed in total, 692 were in the 'bright' sample, which yielded high quality redshifts for 466 sources.

Observation

We obtained AAOmega observations of the ATLAS radio sources from December 1 to December 8, 2007 and December 20 to December 27, 2008, all of which were dark nights. AAOmega is the multi-object spectrograph on the Anglo-Australian

[1] http://swire.ipac.caltech.edu/swire/swire.html

Telescope (AAT). We also obtained some observations for ATLAS sources from December 1 to December 8, 2010 as part of a complementary project. The AAOmega spectrograph was used in multi-object mode (Saunders et al. 2004; Sharp et al. 2006) and nod+shuffle mode (Glazebrook and Bland-Hawthorn 2001). While the sensitive principle component analysis (PCA) based approach for deep observations with AAOmega (Sharp and Parkinson 2010) would likely have resulted in enhanced sensitivity, the technique was still under development at the time of our observations. We used the dual beam system with the 580V and 385R Volume Phase Holographic gratings. The 2007 and 2010 observations used the 5700Å dichroic beam splitter and covered the spectral range between 3700Å and 8500Å at central resolutions in each arm of R∼1300 per 3.4 pixel spectral resolution element. The 2008 observations used the 6700Å dichroic beam splitter and covered the spectral range between 4700Å and 9500Å, which allows detection of Hα to z $\sim$ 0.4.

Each of the three observing sessions over three years was compromised by poor weather, with only 16.9% of scheduled time able to be used, severely restricting the sensitivity of the observations. The seeing ranged from 1.2″ to 3.0″. The observations are summarised in Table 3.1.

The sensitivity limit with AAOmega for our estimated exposure times was $R \sim 22$. The surface density of ATLAS sources at this sensitivity limit is $\sim 100/\mathrm{deg}^2$, with this value decreasing markedly for brighter sensitivity limits. Optimising the placement of the fibres still resulted in 'spare fibres' that could not be placed on ATLAS radio sources. The remaining fibres were allocated to three ATLAS related projects: the detection of a cluster associated with a wide-angle-tail galaxy, a sample of luminous red galaxies and a large sample of 24 μm excess sources[2] in the ATLAS fields. The redshifts obtained for the cluster work have been published in Mao et al. (2010a) and the 24 μm data are presented in Appendix A.1 and will be discussed in further detail in Norris et al. (in preparation), but are not discussed further in the context of this work.

Data Reduction

The spectroscopic data were processed using the 2dfDR software provided by the AAO. Source redshifts were determined using the RUNZ package using template cross-correlation or emission line fitting with a redshift quality flag out of 5 assigned via visual inspection of the fit. Spectra with a quality flag of 2 or below

[2]Sources that have a high 24 μm to radio flux density ratio are defined as 24 μm excess sources.

were discarded.

621 ATLAS radio sources were observed in ELAIS, with spectra of quality > 2 obtained for 306 sources. 499 ATLAS radio sources were observed in CDFS, with spectra of quality > 2 obtained for 160 sources. A total of 1120 ATLAS radio sources were observed, with spectra obtained for 466 sources yielding reliable redshifts from the AAOmega observations.

Our observations achieve $\sim 70\%$ completeness at $R \sim 20$ (Figure 3.1). This corresponds to the ability to detect typical SF galaxies to $z \sim 0.4$ and typical early-type galaxies to $z \sim 0.5$.

3.3 Results

3.3.1 Spectral Classifications

In the course of measuring the redshift, each spectrum was inspected visually to determine whether the dominant physical process responsible for the radio emission was star-formation (SF) or an AGN. Sadler et al. (1999) reported that visual classifications can be used with confidence to analyse spectra from 2dF, the precursor to AAOmega.

SF galaxy spectra are typically dominated by strong, narrow emission lines including the Balmer series. We classified these spectra as 'SF'. AGN, on the other hand, can have pure absorption-line spectra ('E'), absorption-line spectra with some low-ionisation emission lines such as [OII] (3726 Å, 3729 Å) ('E+OII'), emission-line spectra whose line ratios are indicative of AGN activity ('AGNa') and broad-line spectra ('AGNb'). Figure 3.2 provides examples of each type of spectrum. Ten sources had stellar spectra and, upon visual inspection of the field, we attribute this to chance alignments and discard these data from further analysis in this work.

There are 142 SF, 282 AGN (110 E, 60 E+OII, 79 AGNe, 32 AGNb), 10 stars and 32 'unknown' spectra that we are unable to spectroscopically classify, despite sufficient features for a redshift to be determined. The spectra that are classified as 'unknown' are typically at $z > 0.4$, so Hα is redshifted out of the spectrum. Furthermore, a ratio of [OIII]/H$\beta \sim 1$ could either indicate SF or AGN, and without further information spectral classifications cannot be made.

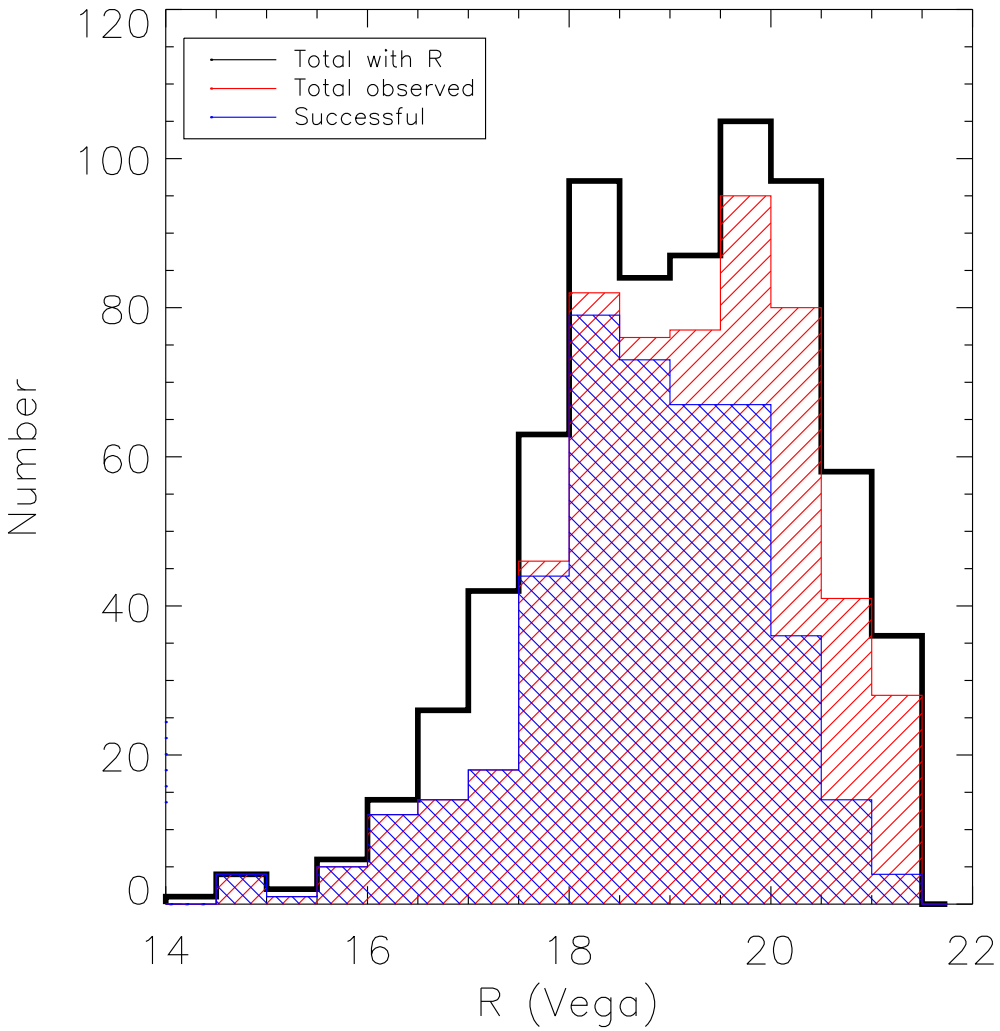

Figure 3.1: Histogram of *R*-band magnitudes for the target sources. The black histogram represents all ATLAS radio sources that have *R*-band magnitudes from SuperCOSMOS (Hambly et al. 2001), the red histogram represents the sources that were observed with AAOmega and the blue histogram represents all sources that had quality > 2 spectra.

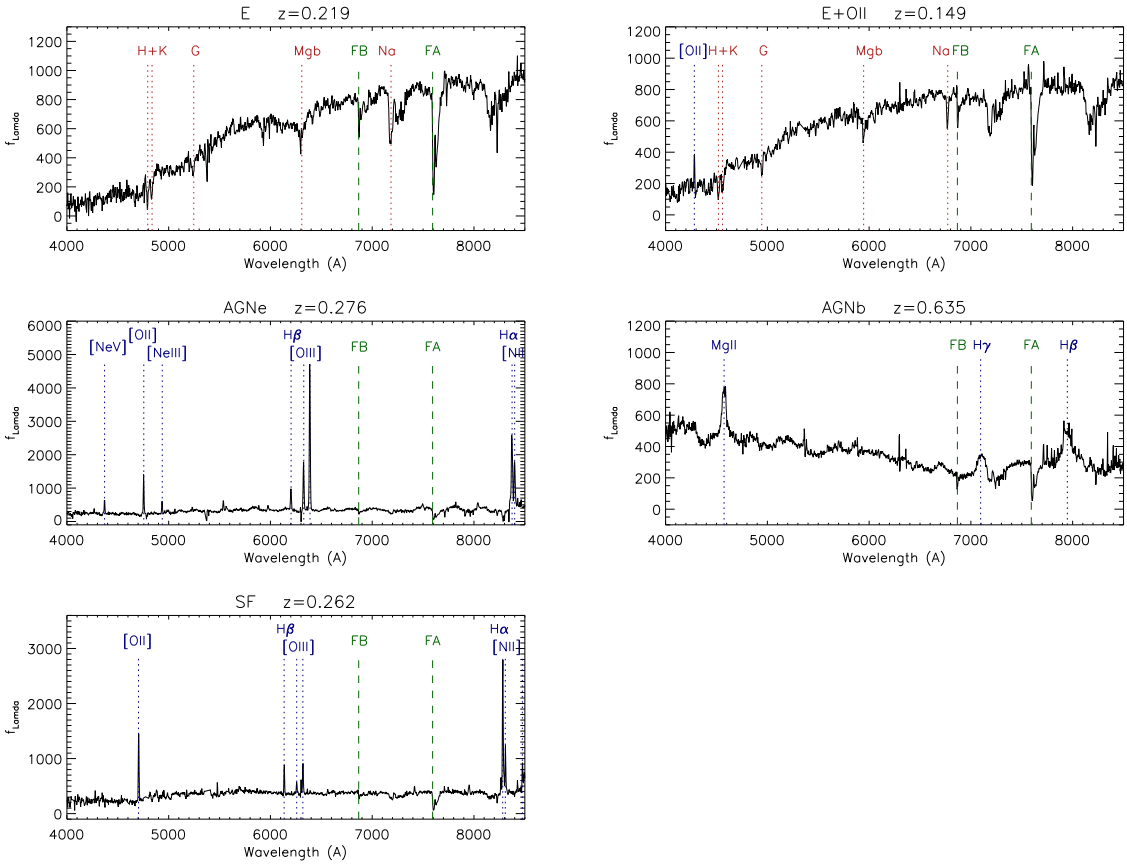

Figure 3.2: Examples of each spectral classification. From top left the spectra are 'E', 'E+OII', 'AGNe', 'AGNb' and 'SF'. The red dotted lines indicate prominent absorption features and the blue dotted lines indicate prominent emission features. The green dashed lines indicate the Fraunhofer A+B atmospheric absorption bands from O_2.

Table 3.2: First 10 lines of the catalogue of new spectroscopic redshifts and spectral classifications of the 466 radio-selected galaxies in ATLAS. Column 1 gives the 'SID' from Norris et al. (2006); Middelberg et al. (2008) and Columns 2 and 3 provide the position of the optical counterpart. The radio flux densities in Column 6 are from Norris et al. (2006); Middelberg et al. (2008) and are uncorrected for effects such as bandwidth smearing. Columns 5 and 6 give the SuperCOSMOS *R* and *B*-band magnitudes (Hambly et al. 2001). Columns 7 and 8 present the spectroscopic redshifts and spectral classifications determined in this paper and Columns 9 and 10 present the absolute *R*-band magnitude and 1.4 GHz radio luminosity.

SID	RA (J2000)	Dec (J2000)	S20 (mJy)	*R* (Vega)	*B* (Vega)	z	Spec. class.	M_R	log $L_{1.4GHz}$ (W Hz^{-1})
S007	03:26:15.42	-28:46:30.80	0.71	20.19	22.52	0.7108	E+OII	-23.68	24.15
S009	03:26:16.32	-28:00:14.72	1.66	20.46		0.5295	E+OII		24.22
S012	03:26:22.06	-27:43:24.53	27.81	19.12	19.37	1.3871	AGNb	-25.01	26.42
S014	03:26:26.90	-27:56:11.65	4.14	17.98	18.92	0.8106	AGNb	-25.46	25.05
S015	03:26:29.13	-28:06:50.80	0.31	16.66	17.21	0.0579	SF	-20.44	21.40
S021	03:26:30.65	-28:36:58.03	1.86	18.98	21.54	0.4731	E	-23.89	24.15
S031	03:26:39.12	-28:08: 1.57	42.29	16.89	18.43	0.2184	E	-23.55	24.75
S037	03:26:43.38	-28:13:28.06	0.50	17.93	19.79	0.2956	SF	-23.39	23.12
S038	03:26:43.34	-28:22:11.43	8.28	19.37	21.69	0.3220	AGNe	-22.32	24.42
S042	03:26:48.47	-27:49:38.06	5.00			2.9869	AGNb		26.43

3.3.2 Redshift and Spectral Classification Catalogue

The catalogue of redshifts and spectral classifications is available as supplementary material in the online version of this paper. Table 3.2 provides the first ten lines of the catalogue.

Figure 3.3 shows the redshift distribution of the 466 sources in ATLAS for which we obtained redshifts from AAOmega. The median redshift for the entire sample is 0.316 while the median redshift for CDFS is 0.332 and the median redshift for ELAIS is 0.315. The redshift peak in the CDFS redshift histogram at $0.6 < z < 0.7$ corresponds to a known cosmic sheet (e.g. Norris et al. 2006). There is also a redshift peak in the ELAIS redshift histogram at $0.2 < z < 0.4$. Mao et al. (2010a) discovered an overdensity in ELAIS at $z \sim 0.22$, associated with a large wide-angle tail galaxy (WAT). They also found an additional three WATs in ELAIS at $0.3 < z < 0.4$, each of which is likely to be associated with a cluster of galaxies.

The most distant radio source in our observed sample is SWIRE3 J032648.47-274938.0 at a redshift of $z = 2.99$, and has been spectroscopically confirmed as a broad-line quasar with a radio power of 2.8×10^{26} W Hz^{-1}.

Figure 3.4 shows the spectroscopic redshifts we have obtained plotted against

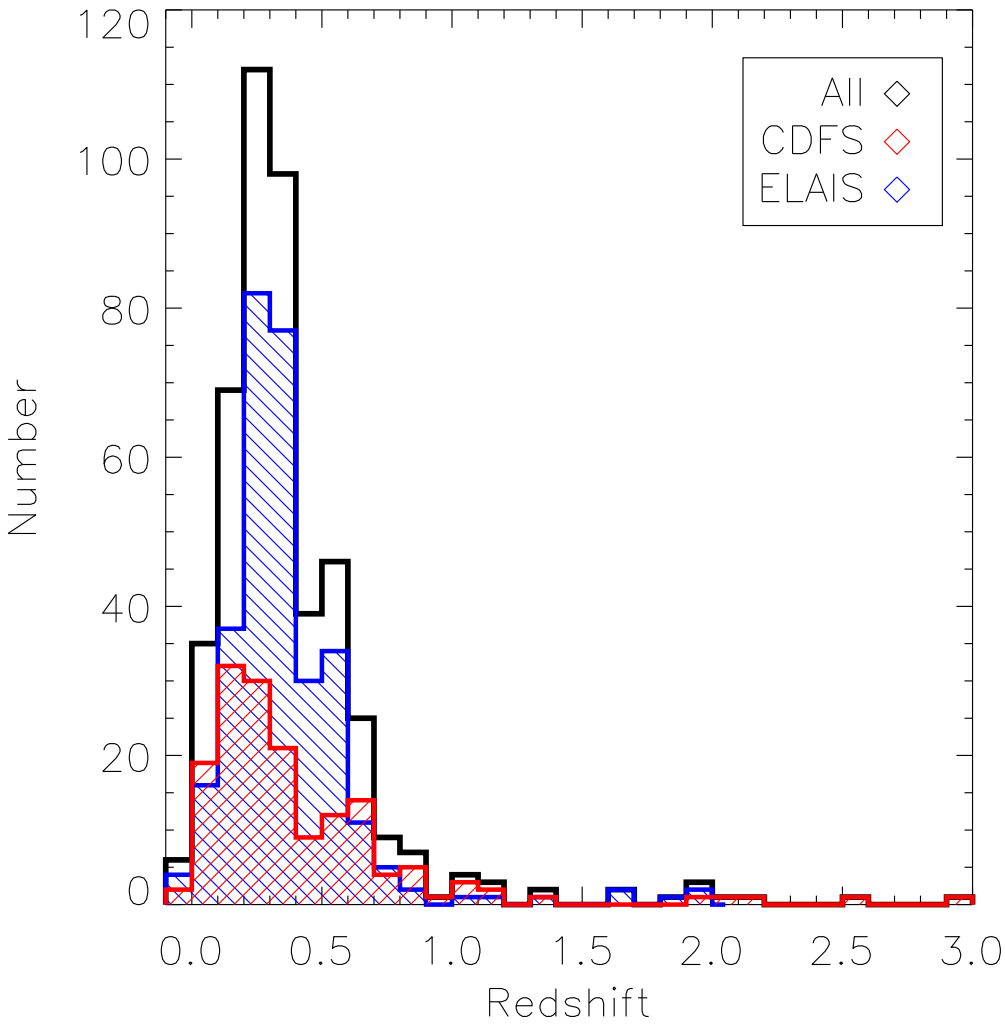

Figure 3.3: Histogram of spectroscopic redshifts in ATLAS. The red line shows data for CDFS and the blue line shows data for ELAIS. The black line is the total. The bins are 0.1 z wide.

photometric redshifts from Rowan-Robinson et al. (2008). There are 264 sources with both photometric redshifts and spectroscopic redshifts. We calculated the Pearson Product-Moment Correlation Coefficient for the entire sample to be $0.795^{+0.040}_{-0.049}$, with the errors being the 95% confidence interval. This implies a moderately strong positive relationship. However, when calculating this coefficient for only the early-type galaxies (spectral classification E or E+OII) we find this value to be $0.936^{+0.021}_{-0.032}$, which implies a very high degree of accuracy for the photometric redshifts for these sources. This result is perhaps unsurprising given the strong spectral break at ~4000Å rest-wavelength present in early-type spectra. The coefficient is $0.842^{+0.052}_{-0.075}$ for SF galaxies and $0.745^{+0.092}_{-0.134}$ for AGN. It is evident from Figure 3.4 that at higher redshifts (z>0.7), the correlation becomes weaker, consistent with Norris et al. (2006), who used a more limited spectroscopic redshift dataset.

We calculate the radio luminosity for each source with spectroscopic redshift information using

$$L_\nu = \frac{4\pi D_L^2 S_{\nu obs}}{(1+z)^{1+\alpha}} \tag{3.1}$$

where L_ν is the luminosity in W Hz^{-1} at the frequency ν, D_L is the luminosity distance in metres, $S_{\nu obs}$ is the observed flux density at the observing frequency, and α is the spectral index where spectral index is defined as $S \propto \nu^\alpha$. We assume α = -0.75, which is a typical mean value for the synchrotron emission observed from faint radio sources (Ibar et al. 2010).

Figure 3.5 presents the luminosity histogram for sources with redshift information. The median $L_{1.4GHz}$ for these sources is $\sim 10^{23.1}$ W Hz^{-1} with the SF source median $L_{1.4GHz} \sim 10^{22.6}$ W Hz^{-1} and the AGN median $L_{1.4GHz} \sim 10^{23.4}$ W Hz^{-1}. The large overlap between the radio luminosity ranges for SF and AGN sources makes it impossible to determine whether sources with the 'unknown' spectral classification are SF or AGN from this information alone.

3.4 Discussion

3.4.1 Mid-IR colours

We compare our spectral classifications with those determined from mid-infrared colour-colour diagrams similar to those of Lacy et al. (2004) using the SWIRE data

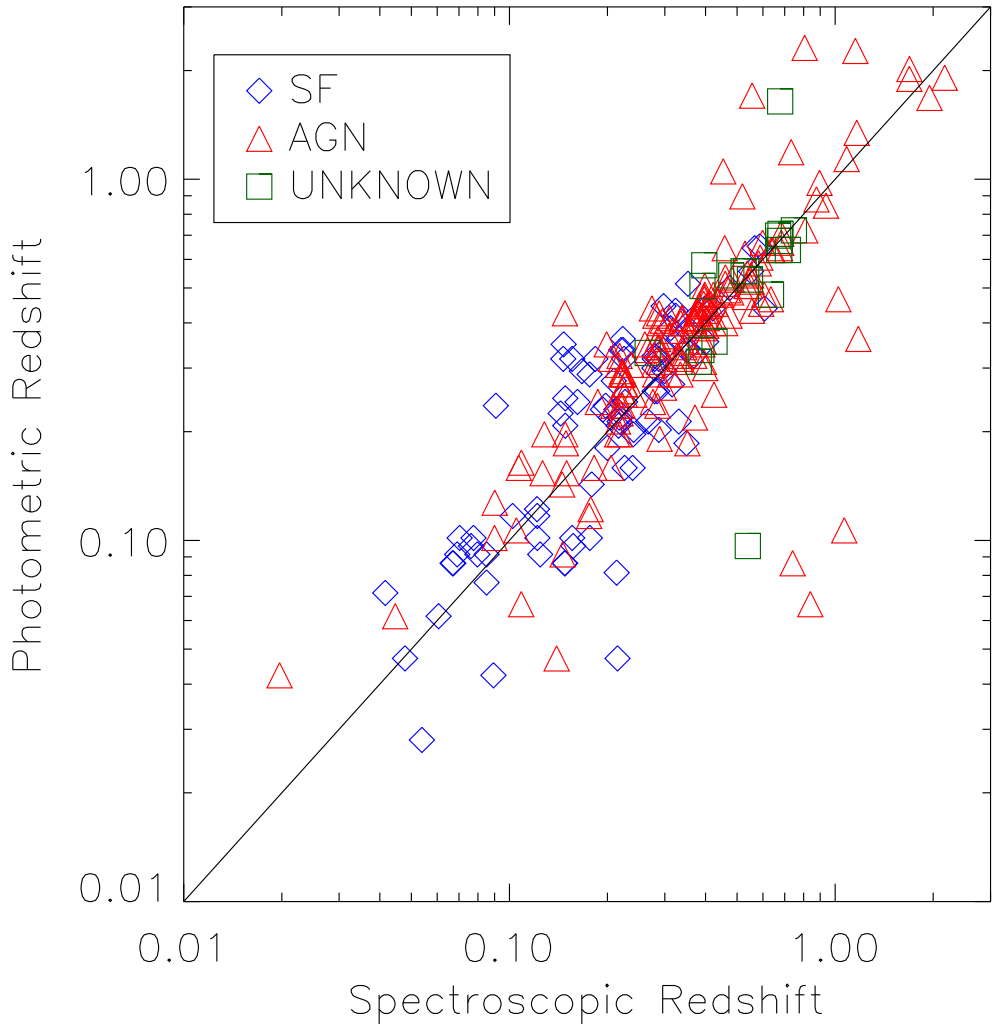

Figure 3.4: Spectroscopic redshifts plotted against photometric redshifts from Rowan-Robinson et al. (2008). Our spectral classifications are overplotted as different colours.

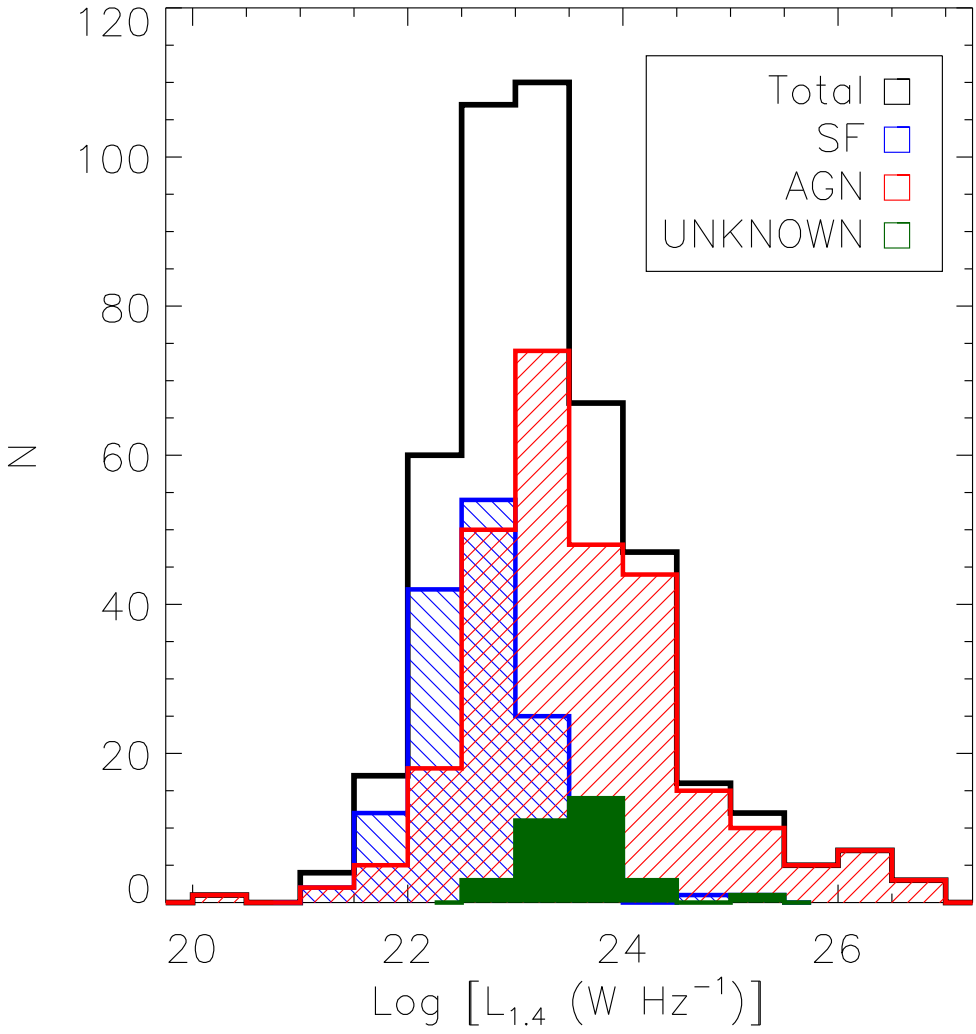

Figure 3.5: Radio luminosity histogram for our sample. Sources spectroscopically classified as SF are shown in blue, while those classified as AGN are shown in red. Those without spectral classifications are shown in green.

from *Spitzer*. Not all of the 466 sources with spectral classifications have infrared data at the SWIRE wavelengths and, as such, comparisons may only be made where data is available at all wavelengths.

Figure 3.6 shows the $[3.6\,\mu\mathrm{m}]-[4.5\,\mu\mathrm{m}]$ against $[3.6\,\mu\mathrm{m}]-[8\,\mu\mathrm{m}]$ plot, where $[1]-[2]=-2.5\log(S_1/S_2)$, that is, the SWIRE colours are given in AB magnitude units to allow direct comparison with Richards et al. (2006). The spectral classifications are plotted in different colours. The demarcation between AGN and SF galaxies is as expected (e.g Sajina et al. 2005), which provides an independent validation of our visual spectral classification method.

Richards et al. (2006) suggest that Type 1 quasars may be selected by taking $[3.6]-[4.5]>-0.1$. We apply this selection to our data and find 127 sources would be classified as Type 1 AGN (Figure 3.6). Of these 127 sources, we had spectroscopically classified 55 as SF, 67 as AGN (27 AGNb, 36 AGNe, 4 E or E+OII) and 5 were 'unknown'. While this method appears to select against E type sources more robustly than the Lacy et al. (2004) method below, the contamination by SF sources is considerable.

Lacy et al. (2004) imposed a MIR colour selection to select AGN in their sample of SDSS sources in the First Look Survey. Applying this selection criteria to the ATLAS data we classify 100 sources as AGN (Figure 3.7). Of the 100 AGN that satisfied the 'Lacy' AGN criteria, we had spectroscopically classified 18 as SF, 65 as AGN (26 AGNb, 27 AGNe, 12 E or E+OII) and 17 were 'unknown'. Our spectral classifications show that there is a significant region of overlap between SF and AGN sources on this MIR colour-colour plot. Indeed, the majority of the 'unknown' spectral classifications fall in this region of overlap. A more stringent 'diagonal boundary' on the AGN selection may be better for AGN selection, but this would also lose many AGN in the overlap region. We note that Lacy et al. (2007) shifted the vertical boundary of the 'Lacy' wedge slightly but this does not affect our result significantly.

3.4.2 Mid-infrared Radio Correlation

Norris et al. (2006) and Middelberg et al. (2008) both use the Mid-Infrared Radio Correlation (MRC) to discriminate AGN from SF galaxies with $q_{24}=S_{24\mu\mathrm{m}}/S_{1.4\mathrm{GHz}}\leq -0.16$ identified as AGN. We apply this discriminant and find 16 of the 466 sources satisfy this AGN criterion. The MRC using $24\,\mu$m data is plotted against redshift in Figure 3.8.

Only one source presents a conflict between the spectral classification and

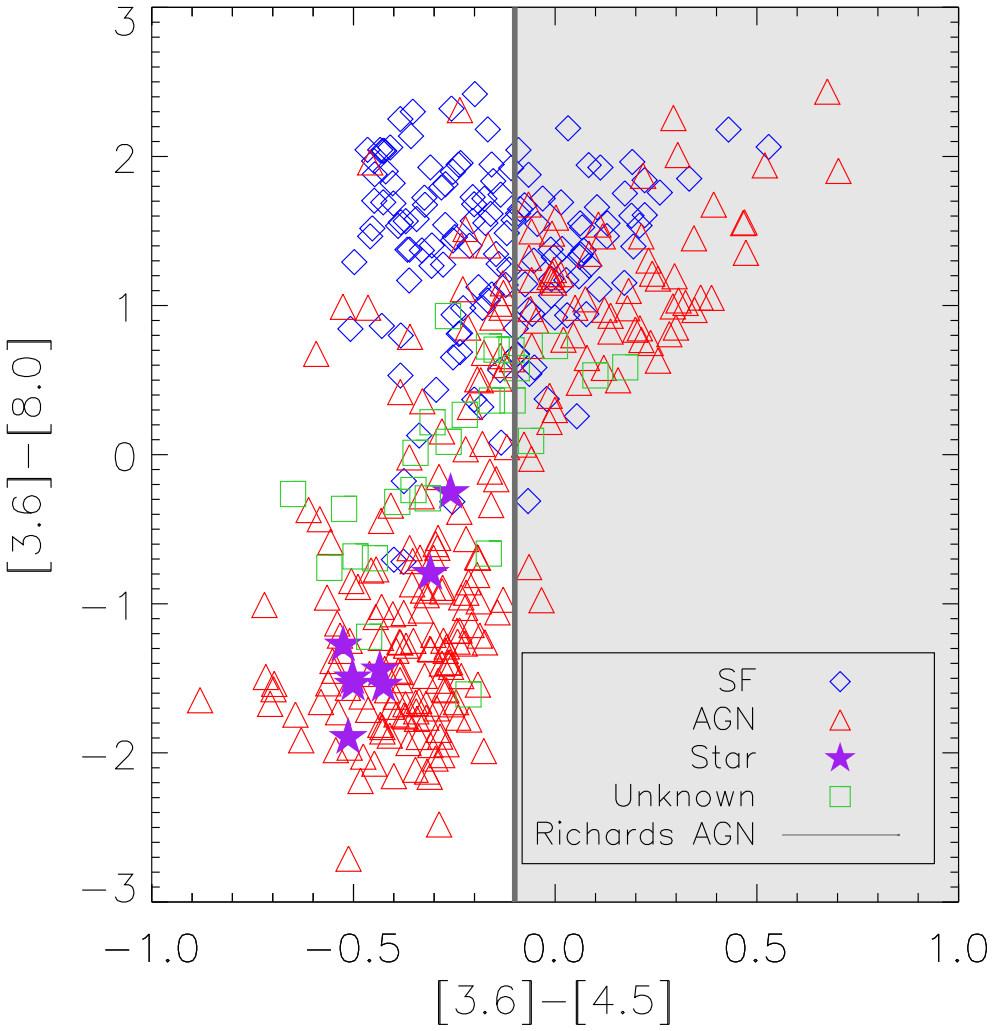

Figure 3.6: MIR [3.6 μm] – [4.5 μm] vs. [3.6 μm] – [8 μm] colour-colour plot. The data in blue show the sources classified spectroscopically as SF and those in red show the sources classified as AGN. Stars are shown in purple and the sources we were unable to classify spectroscopically are shown in green. The grey shaded region shows the location of the Richards et al. (2006) selection for Type 1 quasars.

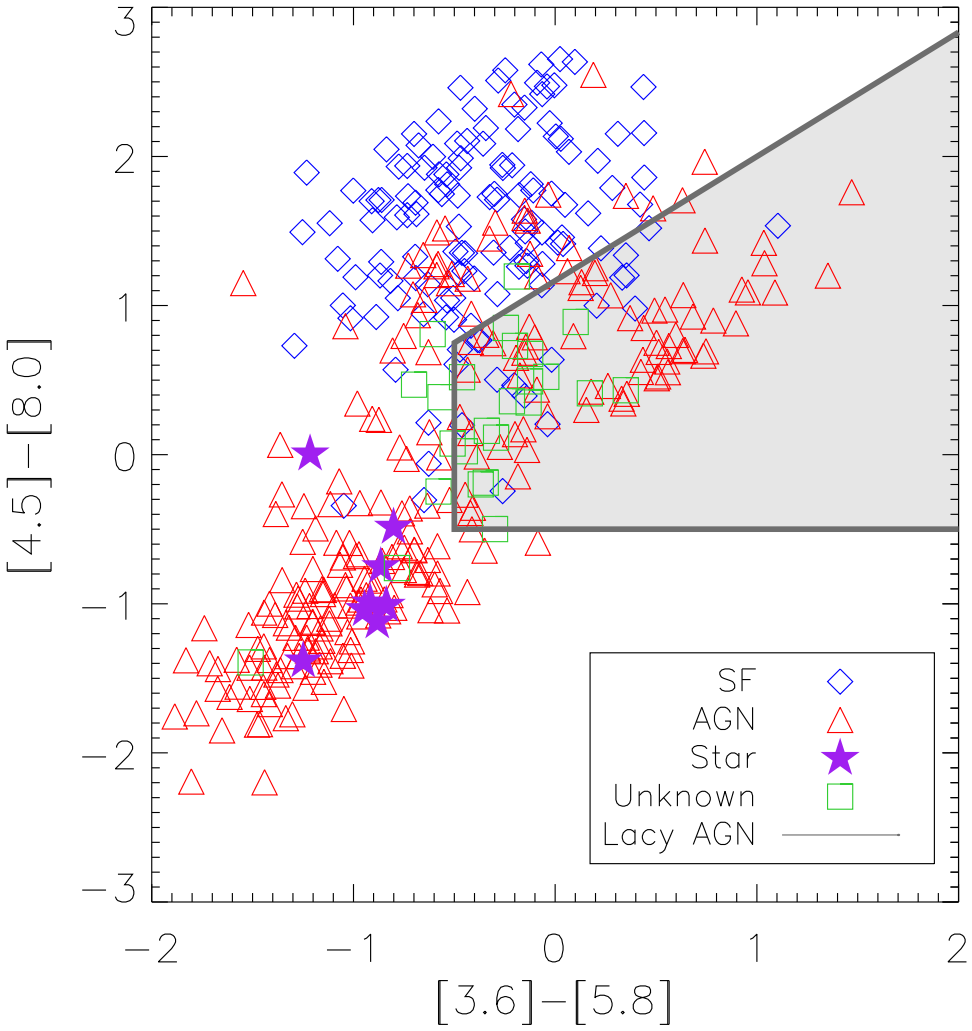

Figure 3.7: MIR [3.6 μm] – [5.8 μm] vs. [4.5 μm] – [8 μm] colour-colour plot. The data in blue show the sources classified spectroscopically as SF and those in red show the sources classified as AGN. Stars are shown in purple and the sources we were unable to classify spectroscopically are shown in green. The grey shaded region shows the location of the Lacy et al. (2004) selection for AGN.

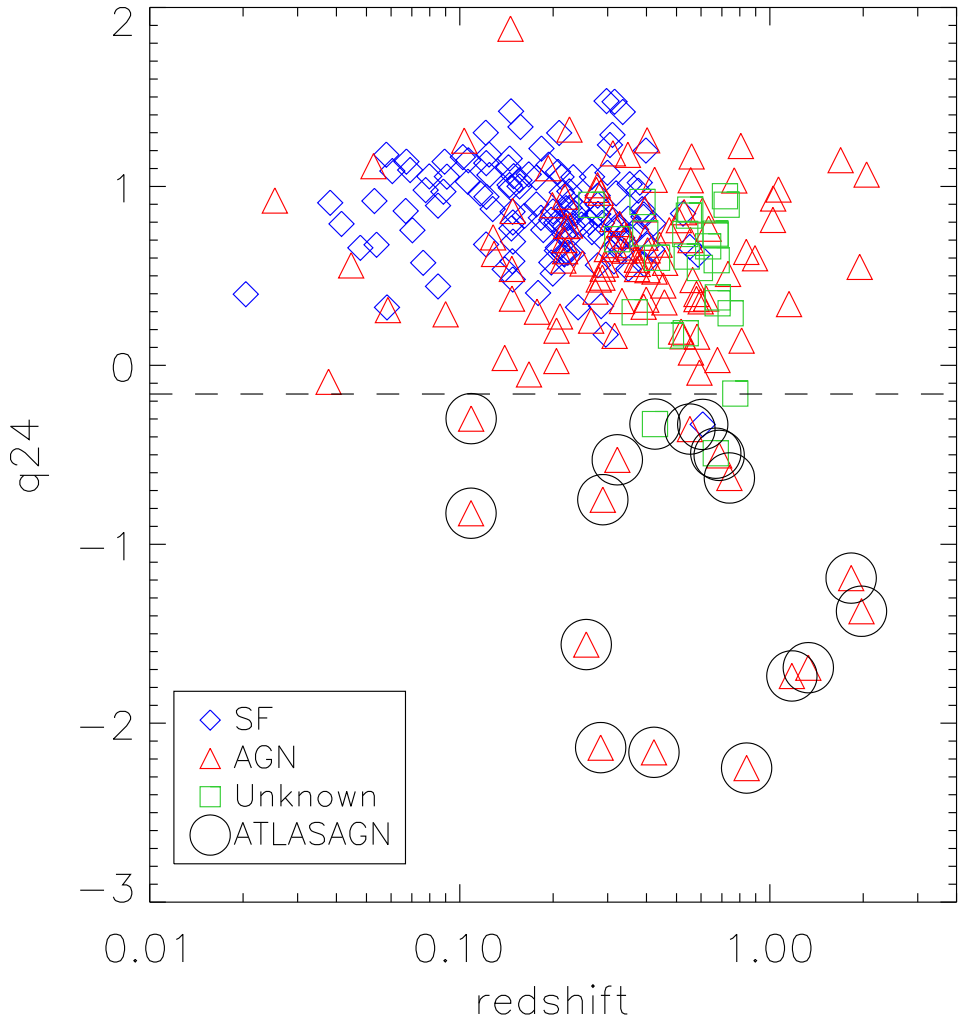

Figure 3.8: The mid-infrared radio ratio, q_{24}, against redshift. The data in blue show the sources that were classified spectroscopically as SF and those in red show the sources that were classified as AGN. The sources which we were unable to classify spectroscopically are shown in green. Sources with $q_{24} \leq -0.16$ are shown in black and the dotted line is at $q24 = -0.16$.

that based on q_{24}. The source, S385 in CDFS, is spectroscopically classified as a SF galaxy, and lies close to the selection boundary but, at $z = 0.6$, it is difficult to assign a spectral classification due to the dearth of strong optical features in the observed spectral range.

The IR colours and the MRC in this paper are primarily used to determine the validity of the spectral classifications that we presented in Section 3.3.1. We hereby conclude that our spectral classifications are broadly reliable and for the remainder of this paper we will use the spectral classifications only. The 32 sources that we were unable to classify spectroscopically as SF or AGN could not be unambiguously classified using the mid-infrared diagnostics.

We defer a more detailed exploration of classification limitations and ambiguities to a future paper that shall also utilise 843 MHz and 2.3 GHz ATLAS radio data from Randall et al. (2012) and Zinn et al. (in preparation). We also note the strength of classification techniques such as the *k*-Nearest Neighbour (*k*NN) classifier, which can operate on multi-dimensional datasets (e.g. Gieseke et al. 2011).

3.4.3 Computing the Radio Luminosity Function

The radio luminosity function (RLF) allows direct insight into the evolutionary history of galaxies. SF galaxies are known to positively evolve with redshift, that is, the radio luminosity and number density of SF galaxies is greater at higher redshifts (Hopkins et al. 1998; Afonso et al. 2005, Dwelly et al., in preparation). The evolution of powerful radio AGN is well understood with powerful radio AGN also evolving positively with redshift. The evolution of low-luminosity radio AGN is less well understood with some studies finding no evidence for any evolution of the RLF for low-luminosity radio AGN (e.g. Clewley and Jarvis 2004) and others finding that low-luminosity AGN do evolve with redshift, albeit more slowly than their high-luminosity counterparts (e.g Smolčić et al. 2009; McAlpine and Jarvis 2011). Best and Heckman (2012) suggest that the luminosity dependence of the evolution of the AGN RLF may be attributed to the varying fractions of 'hot' and 'cold' mode sources with redshift.

In order to calculate luminosity functions, the sample must have known redshifts as well as both an optical magnitude limit and a radio flux density limit (Schmidt 1968, 1977). Moreover, the sample volume must be large enough to mitigate the effects of cosmic variance (Moster et al. 2011). It is imperative that any incompleteness in the dataset is well understood.

RLF Survey Area

The ATLAS radio data cover ~ 7.5 square degrees on the sky, 2.96 square degrees in CDFS and 4.69 square degrees in ELAIS. AAOmega observations of ATLAS comprised two overlapping pointings in CDFS and a single pointing in ELAIS. The total area covered by AAOmega in CDFS is 2.83 square degrees and the total area covered by AAOmega in ELAIS is π square degrees[3]. The discrepancies in size and coverage are due to CDFS's shape and the AAOmega observations actually extended beyond the boundary of the radio observations, whereas in ELAIS the AAOmega pointing was within the radio observations. For the construction of the RLF, the survey area must be limited to where there is data at both radio and optical bands.

Due to the presence of a strong (> 1 Jy) source near the centre of the CDFS field (Norris et al. 2006) the CDFS radio image contains a number of artefacts. More advanced data reduction techniques have been applied to DR2 and DR3 and the CDFS radio image from these data releases is less affected by artefacts and has a more uniform rms. Due to the varying rms of the DR1 CDFS radio image, the remainder of this Section will deal only with ELAIS[4]. The RLF for CDFS will be deferred to the release of DR2 and DR3.

The AAT observations for ELAIS cover only a single pointing so we limit the total area with which we can construct the RLF to π square degrees, the field-of-view (FOV) of AAOmega.

The Radio Data

ATLAS DR1 is nominally quoted as having an rms of 30 μJy beam^{-1}, but the sensitivity of the radio images is not uniform, typically being less sensitive closer to the edges. Figures 3.9 and 3.10 shows the varying rms in ELAIS at each radio source position. These values were calculated by producing an rms map and calculating the mean rms in the 75 × 75 pixels (~15 × 15 synthesised beams) surrounding the source position. To mitigate the effect of outlier pixels the brightest and faintest pixel in the rms grid were discarded when calculating the mean rms.

In order to construct the radio luminosity function we must calculate the maximum volume to which a source of a given radio luminosity may be detected (V_{MAX}). If the radio image had uniform sensitivity,

[3] AAOmega has a radius of 1 degree and hence an area of π square degrees.

[4] Although we could have taken the subset of the CDFS radio image that was uniform, this area has fewer than 30 radio sources with optical counterparts, so we construct the RLF for ELAIS only.

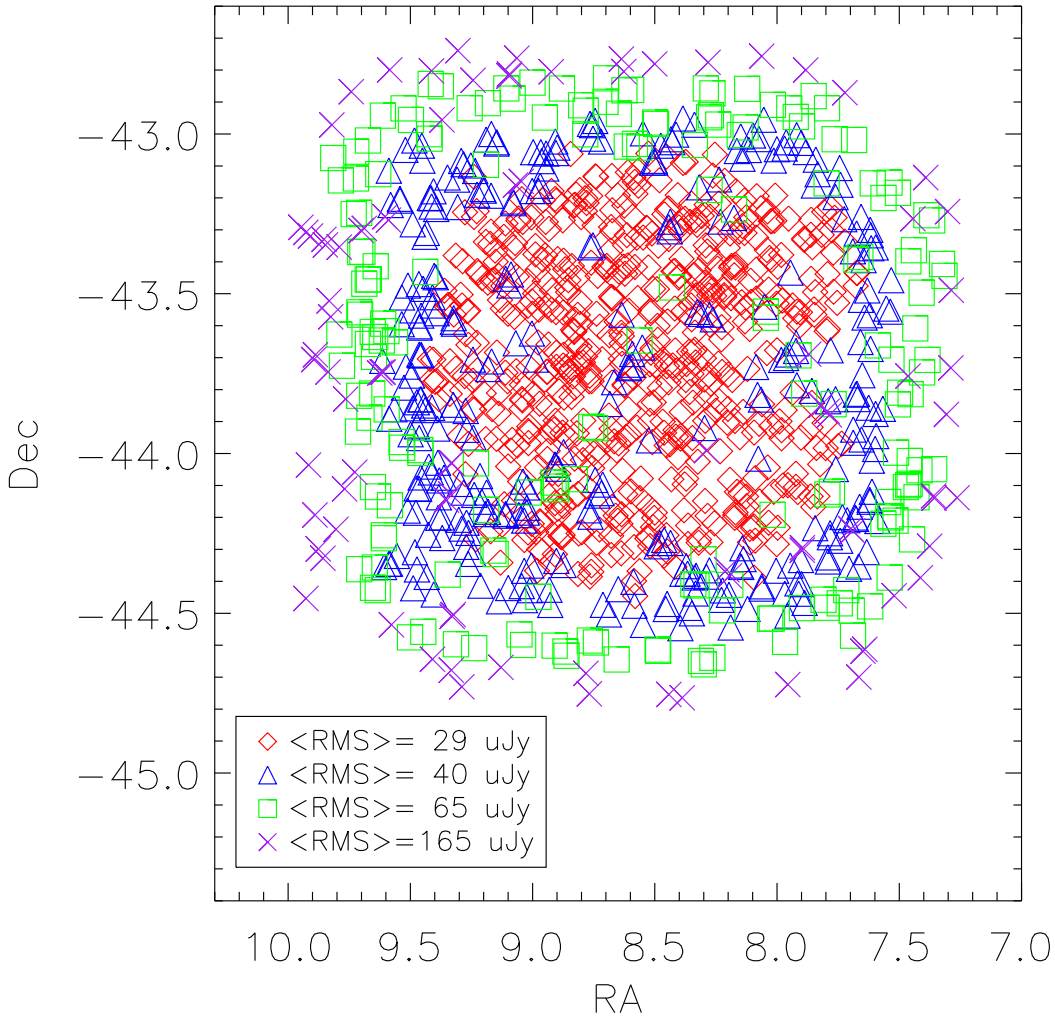

Figure 3.9: ELAIS's rms characteristics, with four different rms bins chosen, and colour-coded.

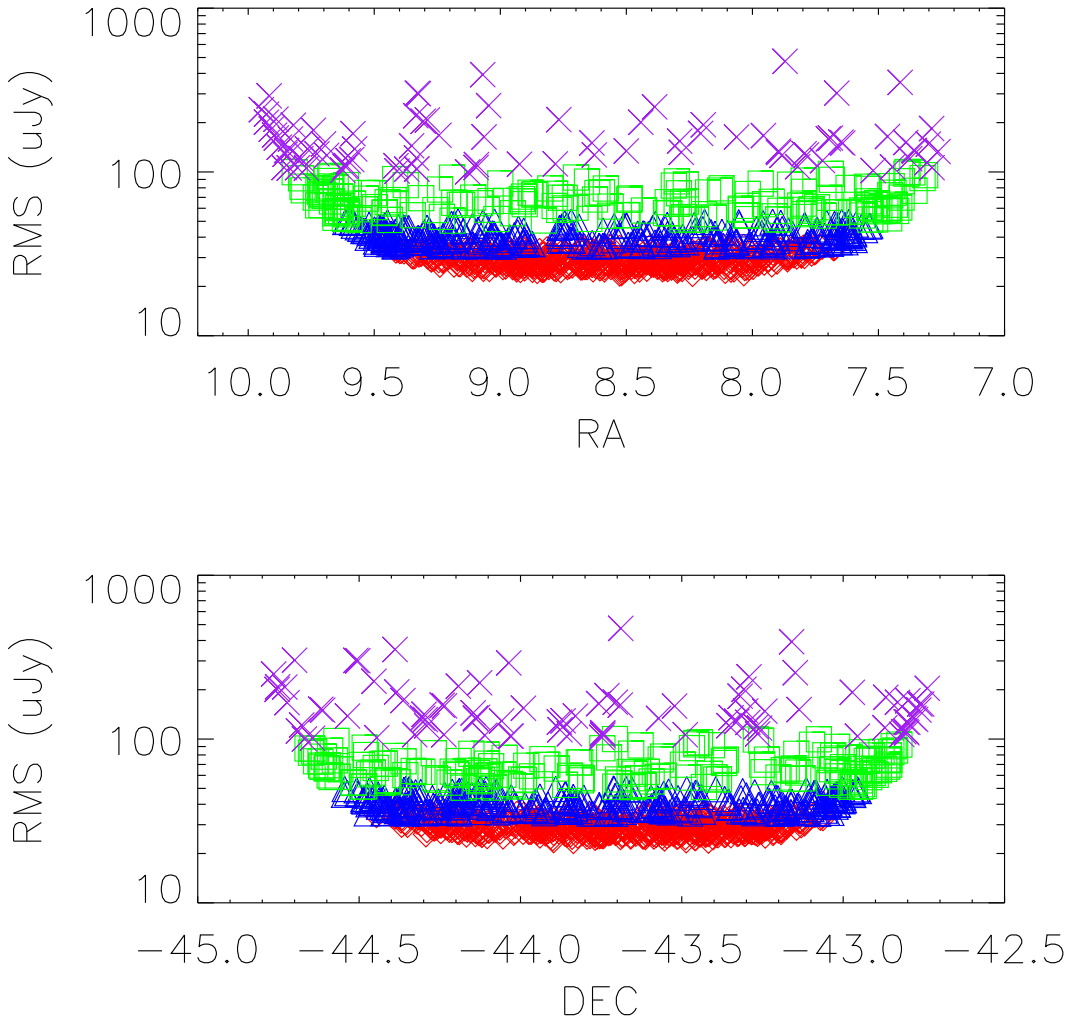

Figure 3.10: RMS against both RA and Dec for ELAIS with the same symbol scheme as above.

$$V_{MAX} = \frac{4}{3}\pi\Omega D^3_{MMAX} \quad (3.2)$$

where Ω is the solid angle (in steradians) subtended by the image, and D_{MMAX} is the maximum comoving distance in Mpc for a source of a given radio luminosity (Hogg 1999).

In order to account for the non-uniform sensitivity however, we must treat the radio image as a number of nested subimages, each with its own limiting flux density. Consequently, each subimage may be approximated by a uniform radio image, and sources that fall below 5× rms (Figure 3.9) are discarded. For a sample with regions that have different sensitivies, the maximum volume available to each source may be calculated using the method described in section IIc of Avni and Bahcall (1980).

Using the Miriad task IMHIST we are able to calculate the total area of the radio image above each chosen flux density limit. Consequently, for each source we are able to calculate the total volume available to the source, as well as the actual volume enclosed by that source using the method of Avni and Bahcall (1980). The calculations for $V_{enclosed}$ and $V_{available}$ are shown in Appendix A.2.

The Optical Data

We use the SuperCOSMOS (Hambly et al. 2001) optical magnitude data, which is limited at $B_j \sim 23$ and $R \sim 22$. Sources fainter than these limits are discarded. Although deeper photometry exist within parts of the ATLAS fields (e.g., Lonsdale et al. 2003), SuperCOSMOS is the only survey to date that covers our region of interest uniformly. Moreover, the faintest sources observed successfully in our spectroscopic observations using the AAT have $R \sim 22$. Optical k-corrections were applied using the method from De Propris et al. (2004). Because both R and B band magnitudes are necessary to calculate the k-correction when calculating absolute magnitudes, we must determine magnitude limits for our spectroscopic observations for both photometric bands.

Figure 3.11 shows the completeness functions for both bands. We choose R_{lim}=20 and B_{lim}=22.5. There is still some incompleteness (~30 per cent) at these magnitude limits, but we choose these limits to maximise the number of sources that we can use to calculate the luminosity function. There is an additional incompleteness that we must account for (top panels of Figure 3.11) due to the

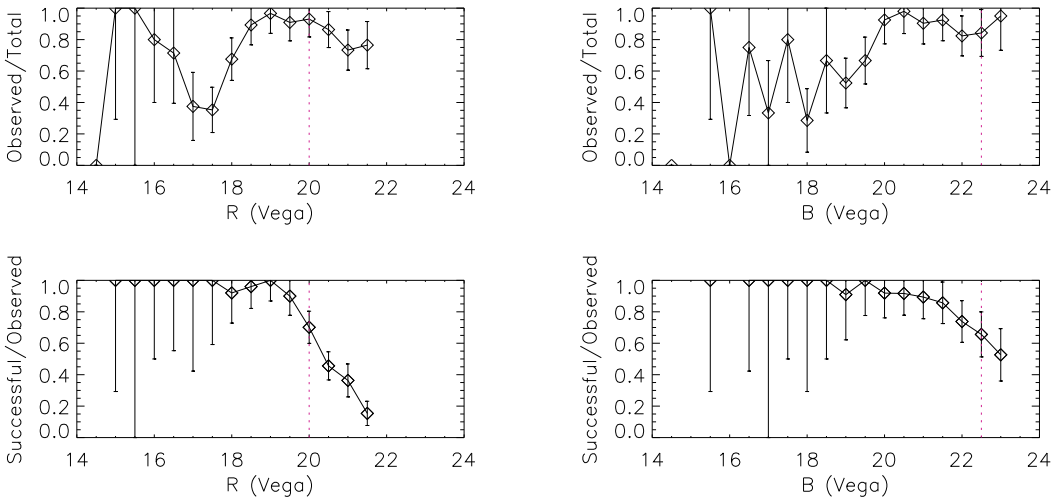

Figure 3.11: The top panels shows the fraction of sources observed against optical magnitude (left: R-band, right: B-band) within the FOV and the bottom panel shows the fraction of sources whose observations yielded quality spectra. The pink dotted lines indicate the magnitude limits. The error bars are Poisson. The error bars at bright magnitudes are large due to the small numbers in each bin.

fraction of sources that were not observed with the AAT. This is, in part, due to the poor observing conditions. In order to observe a dense field of sources completely it is often necessary to observe a number of fibre configurations and the poor observing conditions limited our ability to observe multiple configurations. We also selected against bright sources ($R < 18$) because the magnitude range for any single observation is limited to ∼2 magnitudes to avoid the problem of scattered light. To account for these completeness issues, we take the product of these two corrections (C_i) and weight each source of a given magnitude by this correction when calculating the RLF (below). We can now calculate the maximum volume out to which the optical source could be detected. As two optical bands are necessary for k-correcting this dataset, we calculate V_{MAX} at both bands and take the smaller of the two to be the limiting value. The maximum volume to which the optical source can be detected may be calulated using Equation 3.2.

V/V_{MAX} test

All sources fainter than the radio flux density and optical magnitude limits for our dataset have now been discarded. We remove any sources with stellar spectra as these are believed to be chance alignments, leaving a total of 226 sources in

ELAIS out of the original 306 with which to calculate the radio luminosity function. Perhaps unsurprisingly, 71 per cent (17/24) of the 'unknown' spectral-type sources were discarded due to their faint optical magnitudes. We do not account for the 'unknown' spectra for the remainder of this section. Although they will undoubtedly affect either or both the SF or the AGN RLF, there are only seven of these sources in our sample and their inclusion would not significantly change any of our results.

We can now check the completeness of our dataset using the V/V_{MAX} test of Schmidt (1968, 1977). We calculated both the available and enclosed volumes for each radio source, as well as both the volume and maximum volume out to which the optical source might be detected. We compare the maximum volume out to which the optical source may be detected (Equation 3.2) with the maximum volume available to each radio source (Equation A.2) and take the smaller of the two as the limiting value, as in Equation 3.3.

$$V_{MAX} = \min[V_{(MAX,OPT)}, V_{(available,RAD)}] \tag{3.3}$$

where $V_{MAX,OPT}$ is the maximum volume to which the optical source may be detected, and $V_{MAX,OPT}$ is the maximum volume available to the radio source.

Of the 226 radio sources in ELAIS with which we are able to construct the RLF, 146 (65 per cent) are detection-limited by the radio flux density limits. The detection of sources with radio luminosities greater than 10^{24} W Hz^{-1} is almost entirely governed by the optical magnitude limits. There is no discernable difference in the detection limit between SF and AGN. We calculate $\langle V/V_{MAX} \rangle$ to be 0.563 ± 0.011, which is consistent with positive evolution as $\langle V/V_{MAX} \rangle > 0.5$.

The radio luminosity function for our sources was calculated using

$$\Phi = \sum_{i=0}^{n} \frac{1}{V_{MAX,i}} \pm \sqrt{\sum_{i=0}^{n} \frac{1}{(V_{MAX,i})^2}} \tag{3.4}$$

where Φ is the density of sources in Mpc^{-3}dex^{-1}, n is the number of sources, and V_{MAX} is the maximum volume out to which we can see the source.

To correct for incompleteness, we apply the corrections from Figure 3.11. The optical band that limits V_{MAX} is used to determine which completeness correction is used.

$$\Phi = \sum_{i=0}^{n} \frac{1}{C_i \times V_{MAX,i}} \pm \sum_{i=0}^{n} \frac{1}{\sqrt{(\Delta V_{MAX,i}^2 + \Delta C_i^2)}} \tag{3.5}$$

where C_i is from the completeness functions (Figure 3.11). Where the number of sources is small ($n < 40$), the standard $\sqrt{n}$ approximation to Poisson errors are inaccurate, so for $n < 40$ we have evaluated the 1-sigma Poisson errors using Gehrels (1986).

3.4.4 The RLF for ELAIS

Figure 3.12 and Table 3.3 show the resulting RLF over our entire redshift range. We overplot data from Mauch and Sadler (2007) who calculated the local radio luminosity functions for both SF galaxies and radio-loud AGN. The data from Mauch and Sadler (2007) span a redshift range of $0.003 < z < 0.3$ with a median redshift of 0.043. The SF galaxy RLF for ATLAS-ELAIS appears to be higher than the SF galaxy RLF of Mauch and Sadler (2007), especially for more luminous sources. This may be attributed to our more sensitive radio observations, which results in a higher median redshift for our sample. The median redshift for our complete sample is $z \sim 0.316$ compared to Mauch and Sadler (2007) whose median sample redshift is $z \sim 0.043$. The SF galaxy RLF is known to positively evolve with redshift, so our higher SF RLF is likely due to cosmic evolution of the SF RLF. The AGN RLF also appears to be higher than the AGN RLF of Mauch and Sadler (2007) by a factor of ~3. This may be due to evolution, cosmic variance, differences between how we classify sources, particularly composite sources, or a combination of these factors. Detailed discussion of the SF galaxy and AGN luminosity functions are presented below in Sections 3.4.5 and 3.4.6.

The dashed line in Figure 3.13 shows the flux density limit for the study from Mauch and Sadler (2007). The dotted line in Figure 3.13 shows the flux density limit for the COSMOS survey (Scoville et al. 2007). Smolčić et al. (2009) calculated the RLF for low-power AGN in the COSMOS sample using predominately photometric redshifts and found mild evolution to z~1.3.

3.4.5 RLF for SF galaxies

The RLF for SF galaxies has been proposed to evolve positively with redshift (e.g. Rowan-Robinson et al. 1993; Hopkins et al. 1998). We compare our RLF for SF galaxies with that of previous work by Afonso et al. (2005) and Mauch

Table 3.3: Radio luminosity function at 1.4 GHz for all radio sources, SF galaxies and AGN in ELAIS.

		Total		SF		AGN
$\log_{10}L_{1.4}$ (W Hz^{-1})	N	$\log_{10}\Phi$ (Mpc^{-3} dex^{-1})	N	$\log_{10}\Phi$ (Mpc^{-3} dex^{-1})	N	$\log_{10}\Phi$ (Mpc^{-3} dex^{-1})
20.5	1	$-2.19^{+0.52}_{-0.76}$	0		1	$-2.19^{+0.52}_{-0.76}$
21.0	0		0		0	
21.5	3	$-2.68^{+0.30}_{-0.35}$	1	$-3.38^{+0.52}_{-0.76}$	2	$-2.77^{+0.37}_{-0.47}$
22.0	10	$-2.86^{+0.16}_{-0.17}$	5	$-3.08^{+0.23}_{-0.26}$	5	$-3.26^{+0.23}_{-0.26}$
22.5	25	$-3.33^{+0.10}_{-0.10}$	16	$-3.61^{+0.12}_{-0.12}$	9	$-3.66^{+0.16}_{-0.18}$
23.0	67	$-3.42^{+0.06}_{-0.07}$	32	$-3.73^{+0.08}_{-0.08}$	33	$-3.74^{+0.08}_{-0.08}$
23.5	66	$-3.89^{+0.06}_{-0.07}$	17	$-4.55^{+0.12}_{-0.12}$	48	$-4.02^{+0.07}_{-0.08}$
24.0	28	$-4.51^{+0.09}_{-0.09}$	3	$-5.60^{+0.30}_{-0.34}$	22	$-4.58^{+0.10}_{-0.10}$
24.5	17	$-4.78^{+0.12}_{-0.12}$	0		16	$-4.82^{+0.12}_{-0.12}$
25.0	6	$-5.18^{+0.20}_{-0.22}$	0		6	$-5.18^{+0.20}_{-0.22}$
25.5	2	$-5.82^{+0.37}_{-0.46}$	0		2	$-5.82^{+0.37}_{-0.46}$
26.0	0		0		0	
26.5	0		0		0	
27.0	1	$-7.72^{+0.52}_{-0.77}$	0		1	$-7.72^{+0.52}_{-0.77}$
Total	226		74		145	
$<V/V_{MAX}>$		0.564± 0.011		0.594± 0.020		0.532± 0.013

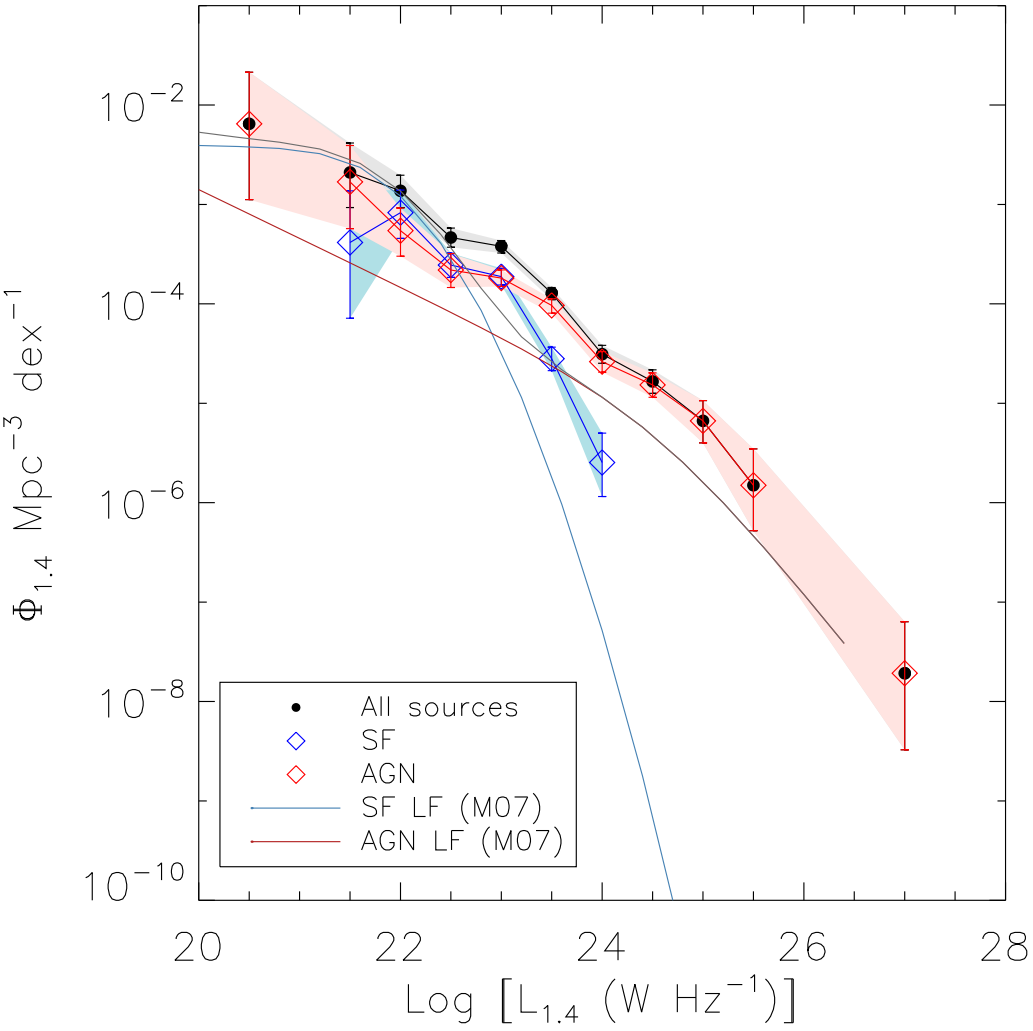

Figure 3.12: The blue diamonds are the RLF for SF sources, the red diamonds are for the AGN RLF and black is the total. The solid pale blue and pink lines are the parametric fits to the local RLF from Mauch and Sadler (2007). Errors are Poisson.

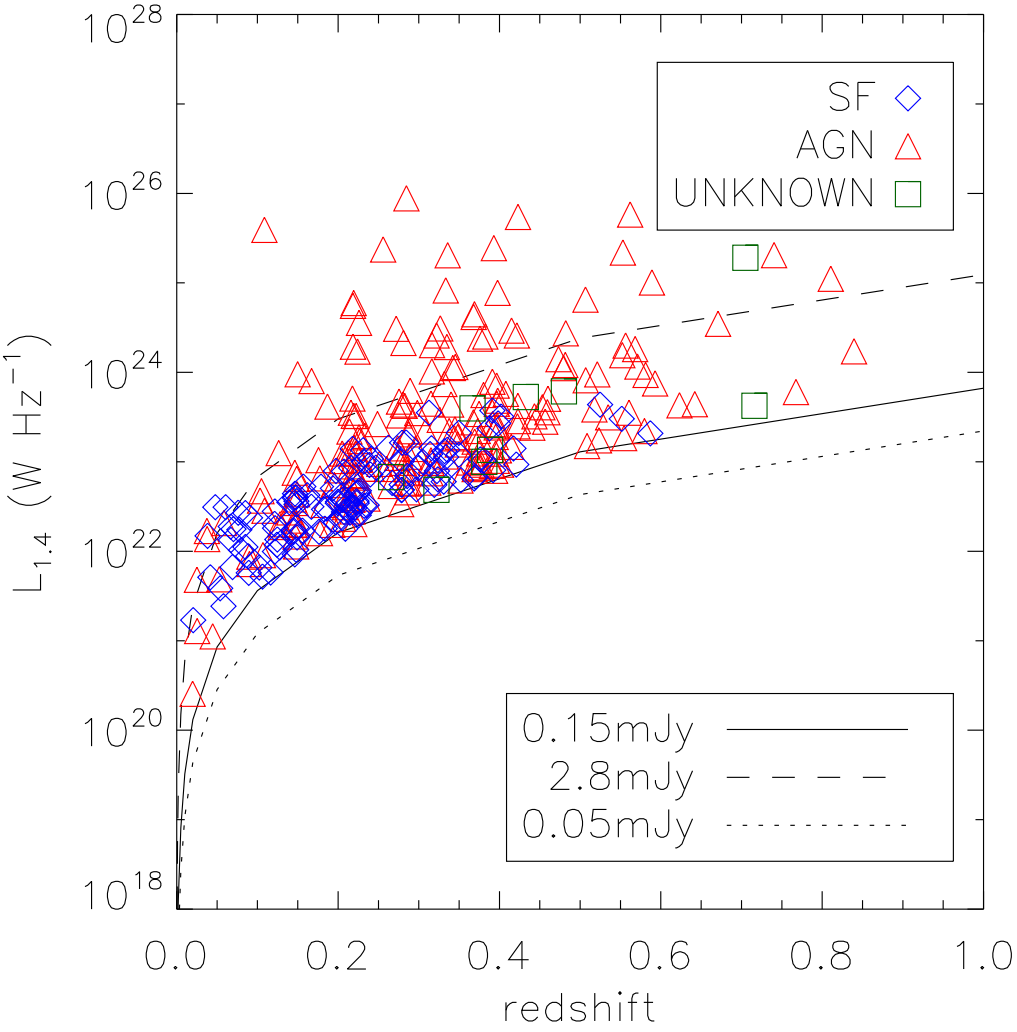

Figure 3.13: Radio luminosity plotted against redshift for our sources. The lines show different flux density limits. The solid line corresponds to a flux density limit of 150 μJy beam^{-1}, which is ~5 × rms for our data. The dashed line corresponds to the flux density limit for Mauch and Sadler (2007) and the dotted line corresponds to the flux density limit for COSMOS (Smolčić et al. 2009).

Table 3.4: Radio luminosity function at 1.4 GHz for SF galaxies and AGN in ELAIS at two different redshift bins.

	SF 0<z≤0.2		SF 0.2<z≤0.5		AGN 0<z≤0.2		AGN 0.2<z≤0.4		AGN 0.4<z≤0.8	
$\log_{10}L_{1.4}$ (W Hz^{-1})	N	$\log_{10}\Phi$ (Mpc^{-3} dex^{-1})	N	$\log_{10}\Phi$ (Mpc^{-3} dex^{-1})	N	$\log_{10}\Phi$ (Mpc^{-3} dex^{-1})	N	$\log_{10}\Phi$ (Mpc^{-3} dex^{-1})	N	$\log_{10}\Phi$ (Mpc^{-3} dex^{-1})
20.5	0		0		1	$-2.19^{+0.52}_{-0.76}$	0		0	
21.0	0		0		0		0		0	
21.5	1	$-3.38^{+0.52}_{-0.76}$	0		2	$-2.77^{+0.37}_{-0.47}$	0		0	
22.0	5	$-3.08^{+0.23}_{-0.26}$	0		5	$-3.26^{+0.23}_{-0.26}$	0		0	
22.5	8	$-3.78^{+0.17}_{-0.19}$	8	$-3.25^{+0.17}_{-0.19}$	6	$-3.73^{+0.20}_{-0.23}$	3	$-3.62^{+0.30}_{-0.34}$	0	
23.0	8	$-3.89^{+0.17}_{-0.19}$	24	$-3.63^{+0.10}_{-0.10}$	5	$-3.90^{+0.23}_{-0.26}$	27	$-3.64^{+0.09}_{-0.09}$	1	$-5.03^{+0.52}_{-0.76}$
23.5	0		16	$-4.49^{+0.12}_{-0.12}$	2	$-4.35^{+0.37}_{-0.49}$	35	$-3.97^{+0.08}_{-0.08}$	11	$-4.43^{+0.15}_{-0.15}$
24.0	0		3	$-5.46^{+0.30}_{-0.34}$	1	$-4.49^{+0.52}_{-0.83}$	11	$-4.53^{+0.15}_{-0.15}$	10	$-4.95^{+0.15}_{-0.16}$
24.5	0		0		0		7	$-4.71^{+0.19}_{-0.20}$	7	$-4.98^{+0.19}_{-0.20}$
25.0	0		0		0		5	$-4.87^{+0.22}_{-0.25}$	1	$-6.10^{+0.52}_{-0.77}$
25.5	0		0		0		1	$-5.69^{+0.52}_{-0.77}$	1	$-5.83^{+0.52}_{-0.77}$
Total	22		51		22		89		31	
$<V/V_{MAX}>$		0.632± 0.039		0.480± 0.019		0.526± 0.032		0.548± 0.017		0.578± 0.030

and Sadler (2007) (Figure 3.14 and Table 3.4). Although the total SF galaxy RLF for our dataset is higher than the SF galaxy RLF of Mauch and Sadler (2007) – especially for more luminous sources – this is attributed to cosmic evolution. When the SF galaxy RLF is separated into two redshift bins[5] it is apparent that the low redshift bin is in good agreement with Mauch and Sadler (2007). Afonso et al. (2005) found their data were consistent with pure luminosity evolution in the form $L_{1.4GHz} \propto (1+z)^Q$, with $Q = 2.7 \pm 0.6$ (Hopkins 2004). Our dataset has very similar optical and radio limits to Afonso et al. (2005), and we find our SF RLF to agree within the uncertainties with theirs at both redshift bins.

3.4.6 RLF For AGN

To determine the cosmic evolution of the RLF for AGN, we bin the data in redshift and compute the RLFs for each redshift bin. Figure 3.15 and Table 3.4 show the RLFs for the three redshift bins. We compare our AGN RLF with Mauch and Sadler (2007) and find that our data is systematically inconsistent with the AGN RLF from Mauch and Sadler (2007), being a factor of ∼3 higher.

Padovani et al. (2011) calculated the RLF for AGNs using the VLA-CDFS sample (Kellermann et al. 2008) and also find their RLF to be a factor of 3 – 4 higher than Mauch and Sadler (2007). We compare our data with theirs over the same redshift range and find them to be in good agreement (Figure 3.16).

[5]In order to construct the RLF for different redshift slices it is necessary to impose a maximum and minimum z. Consequently, $V_{MAX} = \min(V_{ZMAX}, V_{MAX}) - V_{ZMIN}$.

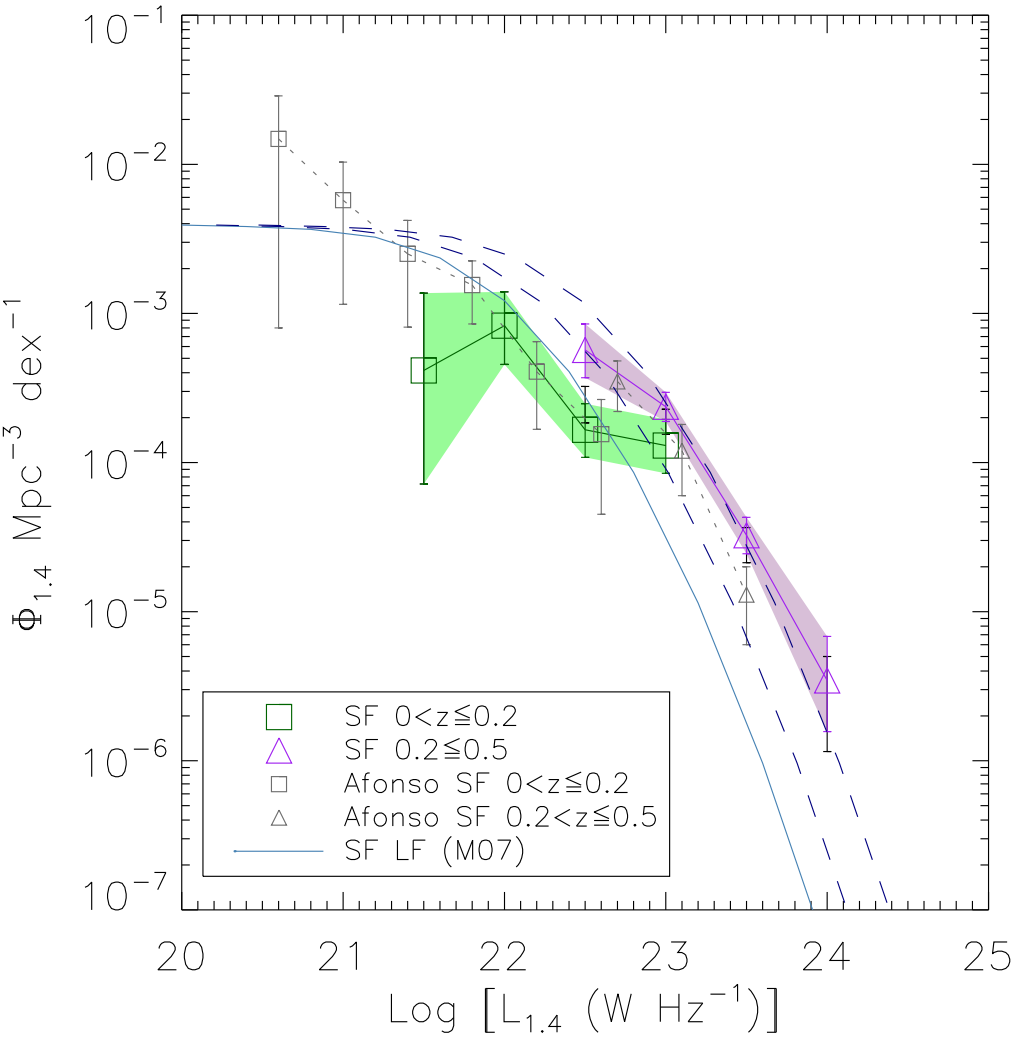

Figure 3.14: Radio luminosity function for SF galaxies in ATLAS. We have split our data into two redshift bins so as to allow for direct comparison against Afonso et al. (2005). The grey data points are from Afonso et al. (2005). Errors are Poisson. The parametric fit to the SF RLF from Mauch and Sadler (2007) is also shown, both in its original form and after applying luminosity evolution in the form $L_{1.4GHz} \propto (1+z)^Q$, with $Q = 2.7 \pm 0.6$ (Hopkins 2004) and z = 0.2 and z = 0.5.

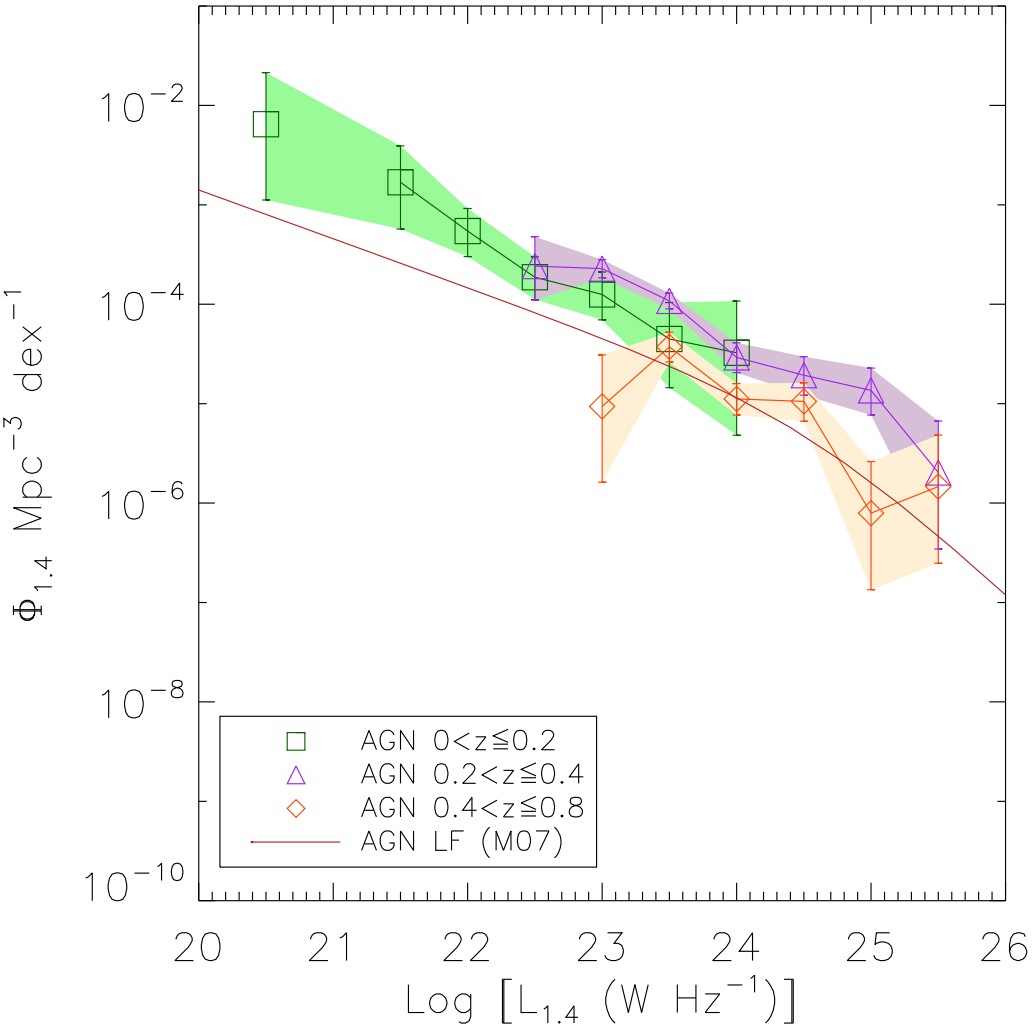

Figure 3.15: Radio luminosity function for AGN in ATLAS-ELAIS. We have split our data into three redshift bins. The pink line is the local AGN RLF from Mauch and Sadler (2007). Errors are Poisson.

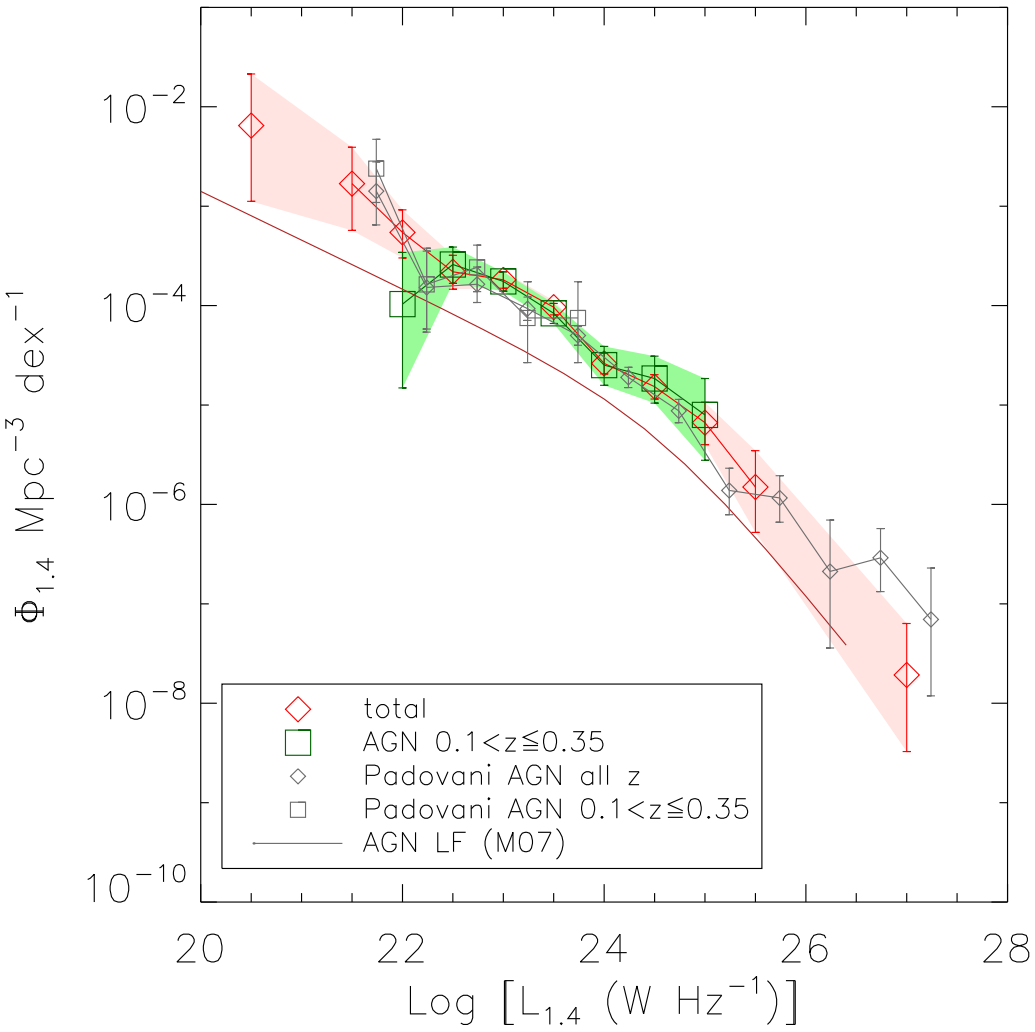

Figure 3.16: Radio luminosity function for AGN in ATLAS-ELAIS with data from Padovani et al. (2011) overplotted. Both the total AGN RLF and the RLF for the redshift range $0.1 < z \leq 0.35$ are plotted to allow direct comparison with Padovani et al. (2011). The pink line is the local AGN RLF from Mauch and Sadler (2007). Errors are Poisson.

Why is our AGN RLF 'high'?

The AGN RLF for ELAIS is puzzling as it appears inconsistent with the local AGN RLF of Mauch and Sadler (2007). For example, the median redshift for the eight lowest luminosity AGN (the left-most three green data points in Figure 3.15) is $z \sim 0.05$, which is comparable to the median redshift of $z \sim 0.07$ from Mauch and Sadler (2007). We specifically investigate whether these eight sources may have been mis-classified in some way. Four of the eight have clear evidence for AGN acitivity in their optical spectra (e.g. broad lines, high NII/Hα ratios etc) and the other four have early-type spectra. The one source that also had sufficient mid-infrared data is likely to be AGN as it has mid-infrared colours consistent with other early-type galaxies.

The AAOmega spectra are obtained through fibres 2 arcsec in diameter, which corresponds to a projected diameter of 6.4 kpc at z=0.2. Consequently, in the cases where we detect an early-type spectrum, it is possible that we are only seeing the bulge of a star-forming galaxy (see e.g. Mauch and Sadler 2007). This is supported by the fact that the total RLF in Figure 3.12 agrees very well with Mauch and Sadler (2007) at $L_{1.4\,GHz} < 10^{22.5}$ W Hz^{-1}, but the SF RLF is lower and the AGN RLF is higher.

The next redshift slice, $0.2 < z \leq 0.4$ is equally puzzling as it too is a factor of ~ 3 higher than the local AGN RLF. Some of this may be attributed to evolution, although the large error bars preclude us from drawing any strong conclusions. We note the further possibility that these sources are hybrid in nature, and it is possible for a source to have both a star-forming disk and a nuclear AGN. While an investigation into this would be useful, it is beyond the scope of this paper.

Another factor contributing to the higher number density of AGN may be the presence of clusters or other large-scale structures, which can have the effect of inflating the AGN RLF in ELAIS due to the small volumes probed (e.g. Padovani et al. 2011). For example, Mao et al. (2010a) detected a large overdensity at $z \sim 0.2$ associated with a wide-angle tailed galaxy. The removal of galaxies in this overdensity lowers the overall AGN RLF, although not by a significant amount ($\delta\Phi < 15\%$). However, there are three additional WATs in ELAIS (Mao et al. 2010a) at $0.3 < z < 0.4$, each of which is likely to be associated with a cluster. The sampling of a larger volume would mitigate the effects of cosmic variance.

Sadler et al. (2007) calculated the RLF for AGNs at $0.4 < z \leq 0.7$ using radio data from FIRST and optical data from 2SLAQ. We compare our data with theirs over the same redshift range and find them to be in good agreement (Figure 3.17).

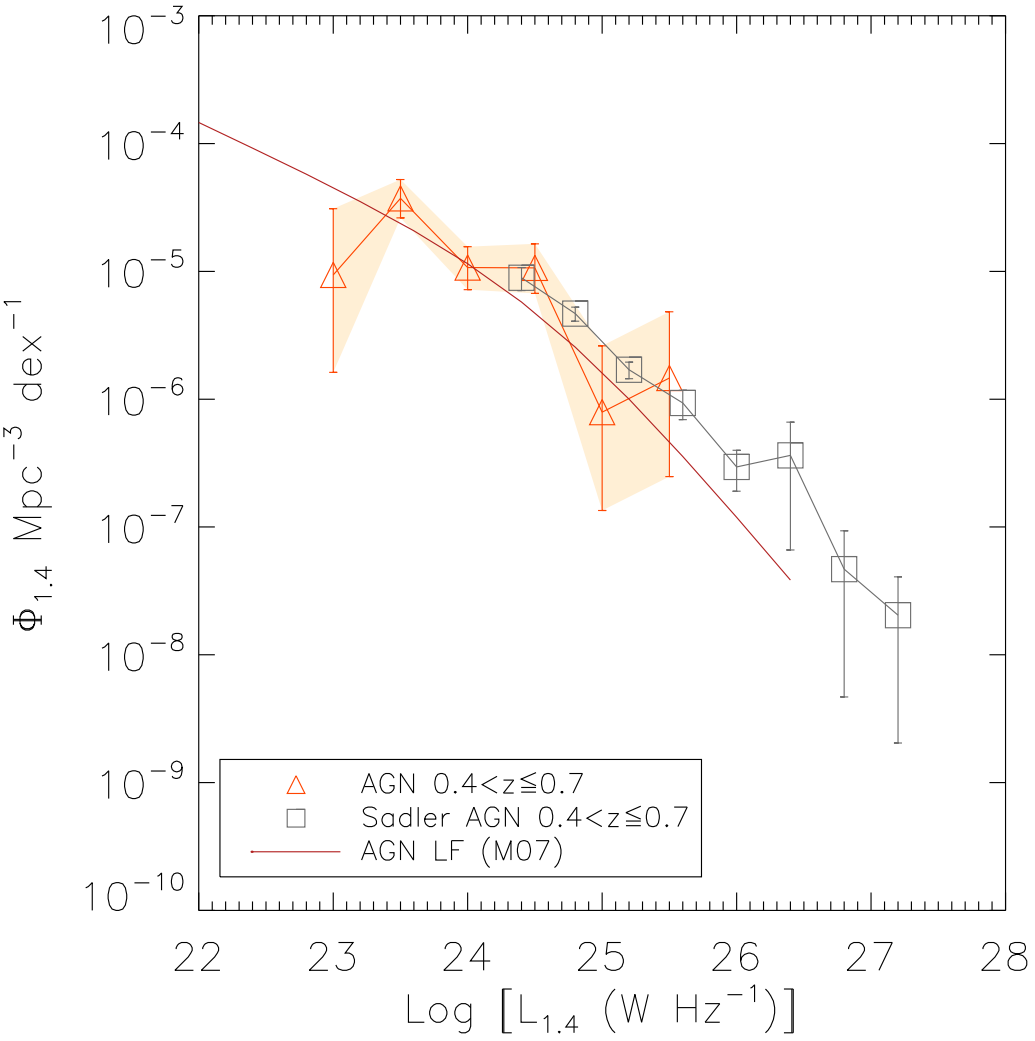

Figure 3.17: Radio luminosity function for AGN in ATLAS-ELAIS with data from Sadler et al. (2007) overplotted. The RLF for the redshift range $0.4 < z \leq 0.7$ is plotted to allow direct comparison with Sadler et al. (2007). The pink line is the local AGN RLF from Mauch and Sadler (2007). Errors are Poisson.

At this redshift range we should be probing a volume large enough to sample the Universe fairly and hence be free of the effects of cosmic variance.

We are not able to determine definitively why the AGN RLF for ELAIS appears to be 'high'. We have explored the possibility of evolution, cosmic variance and the possibility of spectra being unrepresentative of the source. The AGN RLF may be suffering the effects of any one of these factors, or possibly a combination. DR3 will provide this study with more data so that we may determine why our AGN RLF is high.

3.5 Summary and Conclusions

We have presented 466 new spectroscopic redshifts for radio sources in ELAIS and CDFS as part of ATLAS, using AAOmega on the AAT. We have classified the sources as AGN or SF based on their spectra and compared these spectral classifications with mid-IR diagnostics and found them to be in good agreement. Of the 466 sources, 282 are AGN, 142 are SF, 32 are either SF or AGN (none of the diagnostics used in this paper were able to determine if they were SF or AGN) and 10 are chance alignments with stars.

We have constructed the RLF for ELAIS for both SF galaxies and AGN. We find positive evolution, consistent with previous studies, to z = 0.5 for the SF RLF. We find our AGN RLF to be consistent with previous work by Padovani et al. (2011), and a factor of ∼3 higher than the work by Mauch and Sadler (2007).

We cannot make any definitive statements as to why the SF RLF for ELAIS is consistent with previous studies whereas the AGN RLF for ELAIS appears inconsistent. We attribute the inconsistencies to the possibility of evolution, cosmic variance, obtaining spectra of only the bulge of a SF galaxy leading to an overestimate of early-type galaxies, or possibly an amalgamation of all these factors. We shall perform these analyses on DR3 where the extra data will allow us to draw more definitive conclusions.

ATLAS is the pathfinder for the forthcoming EMU Survey (Norris et al. 2011a), planned for the new ASKAP telescope (Johnston et al. 2008), which will survey the entire visible sky to an rms depth of $10\,\mu\mathrm{Jy\,beam^{-1}}$. Because the ATLAS and EMU surveys are well-matched in sensitivity and resolution, the results obtained in this and other papers on the ATLAS survey will be used to guide the survey design and early science papers for EMU. In particular, the spectroscopy on ATLAS sources will provide a valuable training set to guide the algorithms

(e.g. for statistical redshifts) used to determine the redshift distribution of the anticipated 70 million EMU sources.

Acknowledgements

We thank Jamie Stevens, John Dickey, Jay Blanchard, Alastair Edge, Tom Mauch and the ATLAS team for many fruitful discussions. We thank Paolo Padovani for providing data for us to compare our RLFs. MYM acknowledges the support of an Australian Postgraduate Award as well as Postgraduate Scholarships from AAO and ATNF. NS is a recipient of an Australian Research Council Future Fellowship. We thank the staff at AAO and ATCA for making these observations possible. The ATCA is part of the Australia Telescope, which is funded by the Commonwealth of Australia for operation as a National Facility managed by CSIRO. This research has also made use of NASA's Astrophysics Data System.

Radio galaxies are often linear
But in some cases they are not
We call these bent-looking sources
Wide-angle tailed galaxies or WATs

WATs are found in high-density regions
In cluster mergers, an unrelaxed place
Thus they are often used as probes
For high density regions in space

We searched for WATs in ATLAS
And found six in our sample of lots
Evidence is found for overdensities
In four of the detected WATs

I'll leave you with one last thought
WATs can probe an overdense place
With the advent of EMU with ASKAP
We'll probe ten-to-the-five clusters in space

My 30-second "Sparkler" talk, presented at the 2010 Astronomical Society of Australia's Annual General Meeting in Hobart

4

Wide-Angle Tail Galaxies in ATLAS

This chapter is a reproduction of the first-author peer-reviewed journal article *Wide-angle tail galaxies in ATLAS*, Mao M. Y., Sharp R., Saikia D. J., Norris R. P., Johnston-Hollitt M., Middelberg E., Lovell J. E. J., 2010, MNRAS, 406, 2578. I was responsible for leading this work and the article was wholly written by me with the contributions of the coauthors as follows:

- Rob Sharp supervised this work, helped with the target selection for the observations, performed the AAT service observations on October18,2008, reduced the resulting data and produced Figure 4.3.
- Dhruba Saikia participated in many valuable discussions about the individual sources and noted the potential importance of the asymmetric FRI source in the vicinity of S1189.
- Ray Norris supervised this work and helped develop the model discussed in Section 4.5.
- Melanie Johnston-Hollitt participated in many valuable discussions about clusters of galaxies in general.

- Enno Middelberg made the initial discovery of the relic in ELAIS and spurred the generation of this work.
- Jim Lovell supervised this work and partipated in many useful discussions for the overall paper.

The text is largely unchanged with only minor modifications for consistency.

Abstract

We present radio images of a sample of six Wide-Angle Tail (WAT) radio sources identified in the ATLAS 1.4 GHz radio survey, and new spectroscopic redshifts for four of these sources. These WATs are in the redshift range of 0.1469–0.3762, and we find evidence of galaxy overdensities in the vicinity of four of the WATs from either spectroscopic or photometric redshifts. We also present follow-up spectroscopic observations of the area surrounding the largest WAT, S1189, which is at a redshift of ∼0.22. The spectroscopic observations, taken using the AAOmega spectrograph on the AAT, show an overdensity of galaxies at this redshift. The galaxies are spread over an unusually large area of ∼12 Mpc with a velocity spread of ∼4500 km s^{-1}. This large-scale structure includes a highly asymmetric FRI radio galaxy and also appears to host a radio relic. It may represent an unrelaxed system with different sub-structures interacting or merging with one another. We discuss the implications of these observations for future large-scale radio surveys.

4.1 Introduction

Wide-Angle Tail (WAT) galaxies are radio galaxies whose radio jets appear to bend in a common direction. They are generally detected in dynamical, non-relaxed clusters of galaxies (e.g. Burns 1990) and may be used as probes or tracers for clusters (Blanton et al. 2000, 2001). Clusters of galaxies are the largest gravitationally bound structures in the Universe and are powerful testbeds of cosmological models (e.g. Borgani et al. 2004; Sahlén et al. 2009; Kravtsov et al. 2009). Clusters also host diffuse radio emission in the form of radio haloes and relics (Giovannini and Feretti 2000; Feretti 2005; Ferrari et al. 2008; Giovannini et al. 2009).

The bent nature of WATs has commonly been attributed to strong intra-cluster winds caused by dynamical interactions such as cluster-cluster mergers (Burns 1998). WATs are preferentially found in enhanced X-ray regions (Pinkney et al. 2000) and are usually associated with dominant cluster galaxies (Owen and Rudnick 1976). Mao et al. (2009a) found the tailed radio galaxies, including WATs, to be located in the densest regions of clusters in the local Universe, consistent with earlier studies (e.g. Burns 1990; Blanton et al. 2000, 2001). Thus WATs represent valuable tracers of high density regions in the intracluster medium (ICM),

and this approach has been used in a number of recent studies (e.g. Blanton et al. 2000, 2003; Smolčić et al. 2007; Giacintucci and Venturi 2009; Kantharia et al. 2009; Oklopčić et al. 2010).

Here we present the radio properties of six WATs that we have identified in ATLAS, the Australia Telescope Large Area Survey, carried out with the Australia Telescope Compact Array (ATCA) at 1.4 GHz (Norris et al. 2006; Middelberg et al. 2008). ATLAS [1] will image seven square degrees of sky over two fields to an rms sensitivity of 10 μJy beam^{-1}. The ATLAS fields have been observed with a number of different ATCA configurations, and the typical resolution of the observations is ∼10 arcsec. The two ATLAS fields, Chandra Deep Field South (CDFS) and European Large Area ISO Survey-South 1 (ELAIS-S1), were chosen to coincide with the *Spitzer* Wide-Area InfraRed Extragalactic (SWIRE) survey program (Lonsdale et al. 2003) so that corresponding optical and infrared photometric data are available.

In addition to the radio properties we present new spectroscopic redshifts for four of the WATs and follow-up spectroscopic observations of galaxies in the vicinity of the largest WAT in order to probe its surrounding structure. This WAT was first identified as radio source S1189 by Middelberg et al. (2008), and is associated with the SWIRE source SWIRE4_J003427.54-430222.5 (Lonsdale et al. 2003).

In this paper we present a summary of the data in Section 2, while the WATs in ATLAS are presented in Section 3. Section 4 presents the results of spectroscopic observations of S1189 and its surrounding region, and discusses the large-scale structure in its vicinity. In Section 5 we discuss cosmological inverse-Compton quenching and the implications for deep wide radio surveys and ATLAS. This paper uses $H_0 = 71$ km s^{-1} Mpc^{-1}, $\Omega_M = 0.27$ and $\Omega_\Lambda = 0.73$ and the web-based calculator of Wright (2006) to estimate the physical parameters. Vega magnitudes are used throughout.

4.2 Data

4.2.1 Radio Data

ATLAS radio observations are currently partially complete with an rms noise of ∼20 - 30 μJy beam^{-1} at 1.4 GHz. The data used in this paper are taken from the

[1] http://www.atnf.csiro.au/research/deep/index.html

first ATLAS catalogues (Norris et al. 2006; Middelberg et al. 2008) which contain 2004 radio sources. We expect ∼16000 radio sources at the completion of the survey.

4.2.2 Spectroscopy

As part of ATLAS, we are undertaking a program of redshift determination and source classification of all ATLAS radio sources with AAOmega (Sharp et al. 2006) on the Anglo-Australian Telescope (AAT). We are currently partway through our ATLAS spectroscopy campaign. A summary of these observations are presented by Mao et al. (2009b) while the detailed results will be presented by Mao et al. (in preparation). 169 ATLAS sources already have spectroscopic redshifts from the literature. We have obtained 395 new spectroscopic redshifts using AAOmega giving a total so far of 564 spectroscopic redshifts: 261 in CDFS and 303 in ELAIS-S1. All of the WATs presented in this paper have spectroscopic data from either our AAT observations or 2dFGRS (Colless et al. 2001).

4.2.3 Follow-up Spectroscopy of the region around S1189

There appears to be a cluster of galaxies within ∼2 arcmin of S1189 in the optical and infrared images (see Fig. 4.1). We obtained AAOmega observations for sources within a degree of S1189 in service mode during the night of 2008 October 18. The AAOmega spectrograph was used in multi-object mode (Saunders et al. 2004; Sharp et al. 2006) and centred on the WAT. We used the dual beam system with the 580V and 385R Volume Phase Holographic (VPH) gratings centred at λ4800 and λ7150 covering the spectral range between 3700Å and 8500Å at central resolutions in each arm of R∼1300 per 3.4 pixel spectral resolution element. The 5700Å dichroic beam splitter was used. Observing conditions were good with clear skies and an average seeing of ∼1.6 arcsec. Two fibre configurations were observed with 3×1200 sec integrations and associated quartz-halogen flat fields and combined CuAr+FeAr, Helium and Neon arc lamp frames.

Targets were identified from the SWIRE catalogues (Lonsdale et al. 2003). The target magnitude range was limited to $19 < R < 20.5$. The bright limit was chosen to select against foreground galaxies based on the expected low number of galaxies brighter than L* in the potential cluster. The faint limit was chosen due to the bright-of-moon service observations. The magnitude range yielded ∼7000 sources within a one degree radius (the field of view of the 2dF/AAOmega fibre

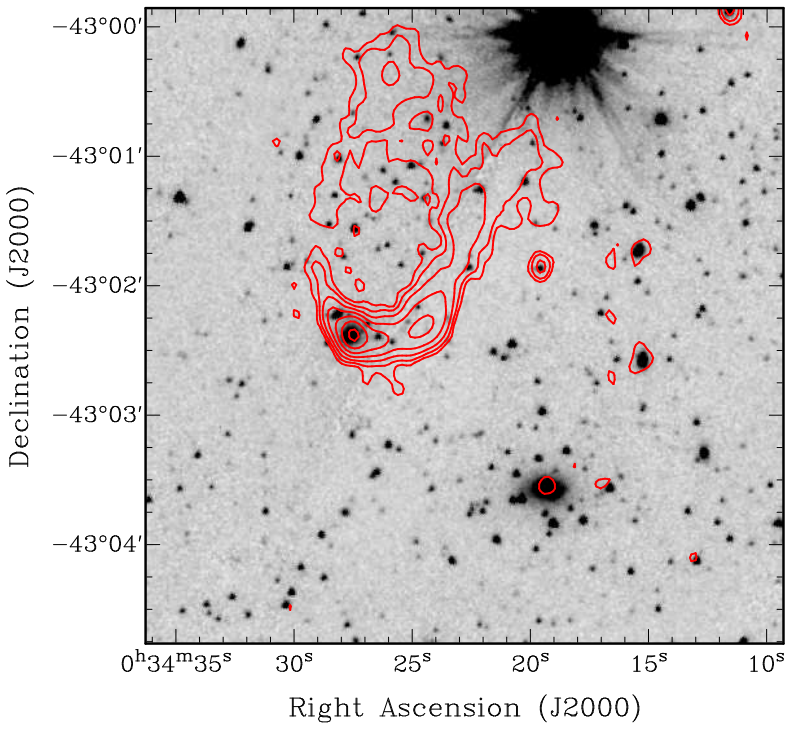

Figure 4.1: SWIRE 3.6-μm image of the WAT, S1189, and the putative cD galaxy located south-west of the WAT. The 1.4 GHz radio contours which are overlaid start from 100 μJy beam^{-1} (3 $\times$ rms) and increase by factors of 2.

Table 4.1: Priority assignment for the target observations. AAOmega is configured based on source location and user-defined priority assignment with 9 being the highest priority and 1 being the lowest. Columns 1 and 2 list the priority assignment and the number of sources in each priority bin. Column 3 presents the number of sources for which we were able to obtain redshifts, while Column 4 gives the radii of the priority bin from S1189. Column 5 describes how many sources were selected randomly using Fisher-Yates shuffles. Priority 1 sources were not included in the target list.

Priority	No. sources	Redshifts	Radii	Comment
9	1	1		putative cD
8	12	0	$< 2'$	
7	60	7	$2'$ to $5'$	
6	100	8	$5'$ to $10'$	100/187 randomly selected
5	200	15	$10'$ to $15'$	200/328 randomly selected
4	200	28	$1'5$ to $30'$	200/1956 randomly selected
3	200	19	$30'$ to 1 deg	200/4426 randomly selected
2	46	8		sources with previously determined z_{spec}
1	6197	0	$> 5'$	sources not randomly selected

positioner (Lewis et al. 2002)) centered on S1189[2]. Targets were prioritized based on radial separation from the WAT S1189 with the exception of the putative cD galaxy which was assigned the highest priority to ensure that its redshift was obtained. Targets farther than 5 arcmin were randomly sampled using Fisher-Yates shuffles, to decrease the input catalogue to a practical working sample for the CONFIGURE software and the Simulated Annealing fibre allocation algorithm (Miszalski et al. 2006), as given in Table 4.1. Regrettably no star-galaxy separation was performed resulting in the inclusion of stars in the input catalogue. Although ~400 AAOmega science fibres are available, fibre allocation requires target separations in excess of 30 arcsec due to physical limitations. Consequently two independent fibre configurations were observed to secure as many high priority sources as possible.

Data reduction followed the standard pattern for AAOmega spectroscopy using the `2dfdr` software package. The red and blue arms were reduced independently and then spliced together so as to produce a continuous spectrum. The redshift was then determined from the spectra using `runz`.

[2]The SWIRE input catalogue of Lonsdale et al. (2003) excludes a number of small regions at the outer edge of the field.

4.3 WATs in ATLAS

We have identified six WATs in ATLAS by visually examining the greyscale ATLAS images (Norris et al. 2006; Middelberg et al. 2008). Fig. 4.2 shows the ATLAS greyscale radio images of the WATs in the left column, while images of the WATs superposed on the Digitized Sky Survey (DSS) red and 3.6-μm Infrared Array Camera (IRAC) images are shown in the middle and right columns respectively. The WATs range in redshift from 0.1469 to 0.3762, and their properties are summarized in Table 4.2. The radio luminosities at 1.4 GHz range from $\sim$2–6$\times10^{24}$ W Hz^{-1} which places them in the FRI (Fanaroff and Riley 1974) category. For comparison the median luminosities of radio sources associated with cD galaxies in rich and poor clusters studied by Giacintucci et al. (2007) are 0.7×10^{24} and 0.2×10^{24} W Hz^{-1} at 1.4 GHz. We have estimated the absolute R-band magnitudes of our ATLAS sources and find that these lie close to the transition region in the absolute red-magnitude–1.4 GHz radio luminosity plot of Owen and Ledlow (1994). The optical spectra of the five sources for which we have determined redshifts, of which four (S132, S483, S1189 and S1192) are new, are presented in Fig. 4.3. The redshift of the sixth WAT galaxy, S409, was determined by Colless et al. (2001).

We have probed for overdensities of galaxies in the vicinity of the WATs. In addition to our observations of S1189 mentioned earlier, we have examined the 2dFGRS (Colless et al. 2001) spectroscopic survey, as well as the photometric redshifts of galaxies in the *SWIRE* field by Rowan-Robinson et al. (2008). The 2dFGRS shows an overdensity of galaxies associated with S409, which is the nearest WAT in our sample, while the photometric redshifts indicate overdensities of galaxies associated with S483 and S1192.

We have examined archival *ROSAT* All-Sky Survey (RASS) data for X-ray detections, and found no RASS detections towards these WATs. This implies an upper limit to the X-ray luminosity of potential host clusters of $\sim$2–11$\times10^{37}$ W s^{-1} which spans the upper values typical for clusters of galaxies with known X-ray emission (Böhringer et al. 2001). This indicates upper limits to the masses of $\sim$2–6$\times$ 10^{14}M$_\odot$ (Pratt et al. 2009).

4.3.1 S132

The largest angular size of the source from end to end along the axis of the source is 0.96 arcmin, corresponding to a physical size of $\sim$309 kpc. The peak of emis-

Table 4.2: Sample of WATs in ATLAS. Columns 1 and 2 give the ATLAS and SWIRE names, Column 3 gives the redshift. Column 4 lists the observed R-band magnitude from SWIRE, except for S132 where we have listed the value from super-COSMOS since a value from SWIRE is not available, while Column 5 lists the absolute R-band magnitude. Columns 6 and 7 list the flux density and luminosity respectively at 1.4 GHz. Columns 8 and 9 list the angular and physical size. All the WAT redshifts were obtained from our AAT observations with the exception of S409 whose redshift was determined by Colless et al. (2001).

ATLAS	SWIRE Counterpart	z	R_{obs} (mag)	R_{abs} (mag)	$Flux_{1.4}$ (mJy)	$Power_{1.4}$ (10^{24}W/Hz)	$Size_{ang}$ (arcmin)	$Size_{phys}$ (kpc)
ELAIS-1								
S132	SWIRE4_J003236.18-442101.1	0.3762	18.1	−23.41	5.35	2.58	1.0	309
S483	SWIRE4_J003311.21-435512.3	0.3164	18.28	−22.79	6.72	2.16	1.5	413
S1189	SWIRE4_J003427.54-430222.5	0.2193	17.12	−23.04	45.03	6.25	5.0	1053
S1192	SWIRE4_J003320.68-430203.6	0.3690	18.92	−22.54	10.46	4.82	0.9	274
CDFS								
S031	SWIRE3_J032639.11-280801.5	0.2183	16.63	−23.52	42.29	5.81	2.7	567
S409	SWIRE3_J033210.74-272635.5	0.1469	16.35	−22.84	42.35	2.41	2.6	396

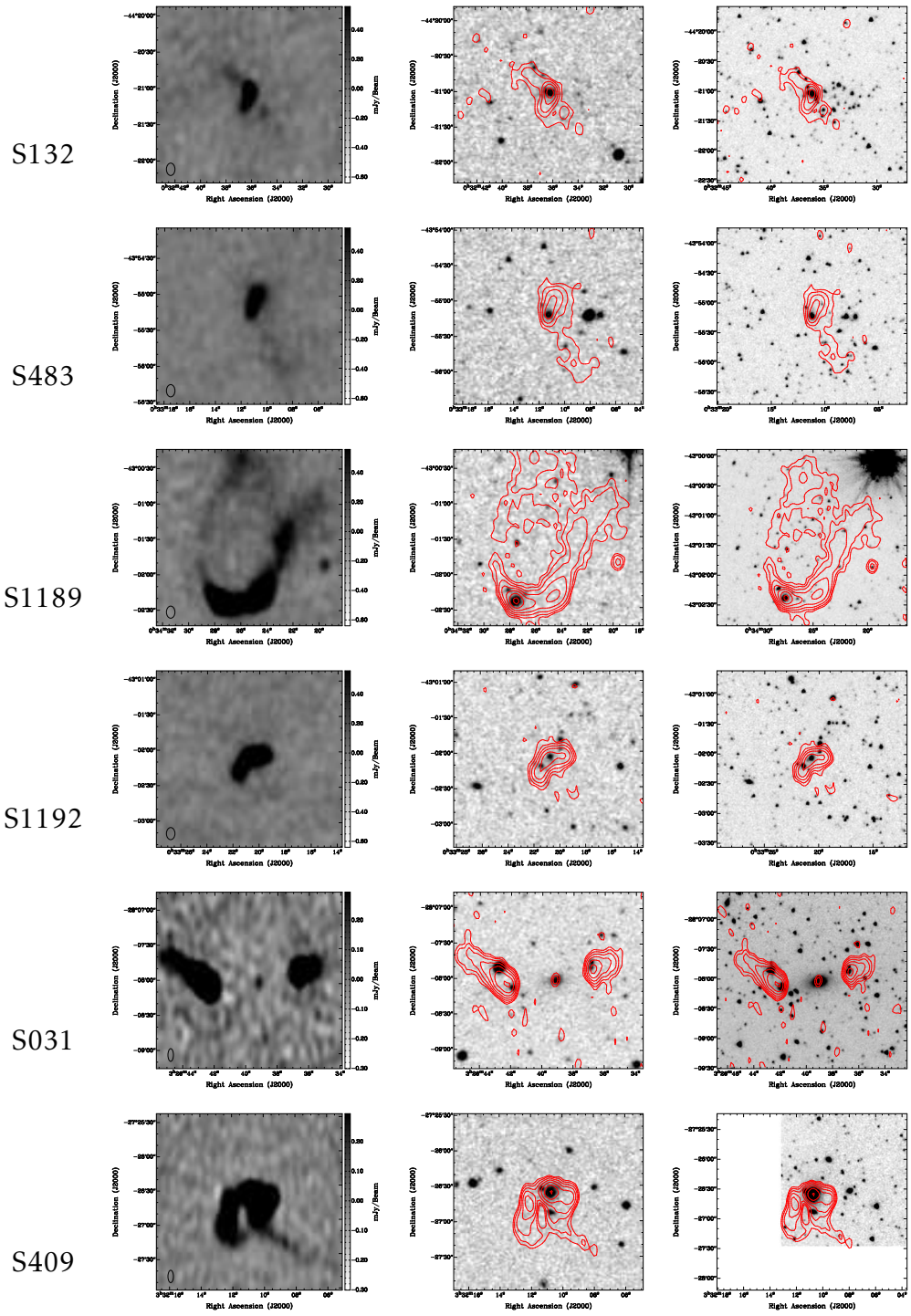

Figure 4.2: The six WATs in ATLAS. From top to bottom the WATs are S132, S483, S1189 and S1192 in ELAIS-S1, and S031 and S409 in CDFS. The left column shows the 1.4 GHz radio continuum emission of the WATs in greyscale.The middle column shows the radio contours overlaid on DSS red images. The right column shows the radio contours overlaid on 3.6-μm IRAC images. The radio contours start from 100 μJy beam $^{-1}$(3 $\times$ rms) and increase by factors of 2. S409 is located at the edge of the 3.6-μm image.

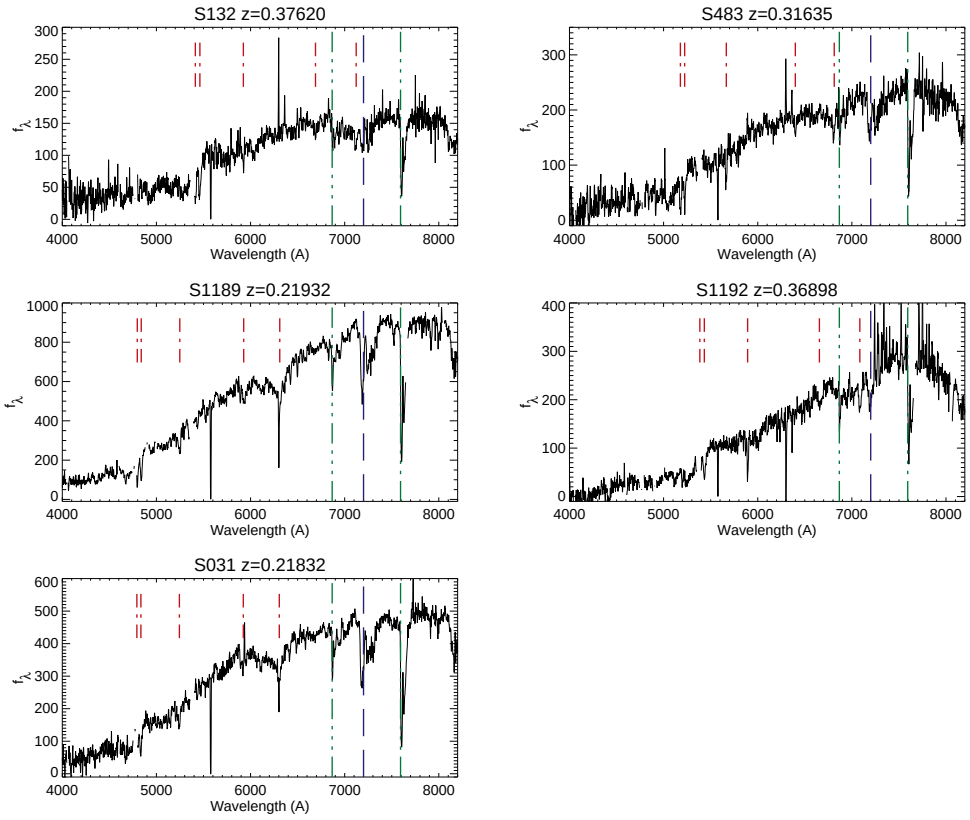

Figure 4.3: Spectra of the host galaxies of the five WATs for which we have measured redshifts using the AAOmega spectrograph on the AAT. The spectra are typical of early-type galaxies that host luminous radio sources. The red dot-dashed lines indicate the prominent stellar absorption features typical of an early-type galaxy spectrum (Ca H+K, G-band, H-beta and Mg-b) from which the redshift has been derived via template cross correlation. The green dash-dot-dot-dot lines indicate the Fraunhofer A+B atmospheric absorption bands from O_2 and the blue long dashed lines indicate the atmospheric water absorption band, neither of which have been corrected due to the absence of appropriate telluric standards in the redshift survey data.

sion to the southwest of the host galaxy has been determined to be an unrelated source, S131 (Middelberg et al. 2008). There are several galaxies to the west of the southern tail which are seen more clearly in the 3.6-μm image, but at present no redshift information is available for these galaxies. The tails appear to bend away from this overdensity of galaxies.

4.3.2 S483

This WAT, which has an overall linear size of 413 kpc, is highly asymmetric in the brightness of the two tails, with the peak brightness in the northern tail being higher by a factor of ∼5. It would be useful to image the source, especially the southern tail, with higher surface brightness sensitivity to confirm the present classification. The photometric redshifts of the galaxies (Rowan-Robinson et al. 2008) within a radius of 2 arcmin, which corresponds to ∼550 kpc at z=0.3164, show a concentration of galaxies at about the redshift of S483 (Fig. 4.4).

4.3.3 S1189

S1189 is the largest WAT in our sample with an overall linear size of ∼1053 kpc. Its opening angle, defined by the lines connecting the regions of highest surface brightness to the optical galaxy is ∼70°, which is slightly smaller than for the high-redshift WAT reported by Blanton et al. (2001) which has an opening angle of ∼80°. Clearly these opening angles would depend on the resolution of the observations and projection effects. Rudnick and Owen (1977) distinguish between narrow-, intermediate- and wide-angle tails by requiring that the opening angle be less than ∼20° for narrow-angle tailed sources and greater than ∼90° for WATs, based largely on tailed sources at smaller redshifts than our sources. Although it would be relevant to examine the effects of resolution and surface brightness sensitivity as one finds more tailed sources at moderate and high redshifts, the opening angle of S1189 is close to that of a WAT. Although WATs do tend to be associated with the dominant galaxy, it could be associated with a bright galaxy close to the brightest galaxy in a cluster or group (see Rudnick and Owen 1977; Blanton et al. 2001). The associated galaxy of S1189 is the next brightest galaxy, only 0.75 mag fainter than the cD galaxy. Rudnick and Owen (1977) also suggested that WATs tend to have larger sizes than the narrow-angle tailed sources. With a total size of over a Mpc, it would be more consistent with the sizes of WATs. Considering all the aspects, we presently classify it as a WAT. We discuss

the results of our AAOmega observations and the environment of this source in Section 4.4.

4.3.4 S1192

S1192 is similar to S132 in both shape and extent, but the two tails in S1192 are more symmetric in brightness. Both the DSS red and 3.6-μm images show a number of galaxies forming a filamentary-like structure along with the host galaxy of the WAT. The photometric redshifts (Rowan-Robinson et al. 2008) within a radius of 2 arcmin, which corresponds to ~500 kpc at z=0.3690, show a concentration of galaxies at about the redshift of S1192 (Fig. 4.5). This overdensity is largely due to the galaxies in the filamentary-like structure.

4.3.5 S031

Although S031 exhibits distinct gaps of emission between the radio core and the two tails of emission, the identification process described by Norris et al. (2006) unambiguously classifies these three components as a triple radio source. The peaks of emission in the tails are towards the radio core as expected in FRI radio sources. We do not have redshift information at present to determine which of the galaxies seen in Fig. 4.2 may be a part of the group or cluster associated with S031. The gaps of emission between the central source and the lobes are reminiscent of the large radio galaxy in Abell 2372 (Owen and Ledlow 1997; Giacintucci et al. 2007), which has been suggested by Giacintucci et al. (2007) to be due to recurrent radio activity (see Saikia & Jamrozy 2009 for a review). Although such a possibility cannot be ruled out, more detailed spectral and structural information are required to clarify whether this is indeed the case.

4.3.6 S409

S409 is the closest of the WATs in ATLAS with a redshift of 0.1469 (Colless et al. 2001) and a size of 396 kpc. It has an interesting radio structure with the western lobe exhibiting two sharp bends and forming a long narrow tail of emission. A deep X-ray image would be useful to understand how the gas distribution may have shaped the unusual radio structure. The 2dFGRS data (Colless et al. 2001) within a radius of ~1 Mpc show a clear excess of galaxies in the same redshift bin as S409 (Fig. 4.6). Within a radius of 500 kpc (3.5 arcmin at z = 0.1469) we find 3 galaxies at about the redshift of S409.

4.4 Large-Scale Structure Around S1189

There are a total of 309 galaxies with spectroscopic redshifts within a radius of one degree of S1189, including 94 galaxies whose redshifts we have measured from our service mode observations with the AAOmega spectrograph. The other redshifts are obtained from spectroscopic observations of ATLAS sources (Section 4.2.2). The redshifts of these 94 new galaxies are listed in Appendix A.

4.4.1 Redshift distribution

The redshifts of the 309 galaxies within a radius of one degree (~12.6 Mpc at z ~ 0.22) from the WAT source extend to ~1.95. The distribution for the subset of 299 galaxies with z≤0.8 is shown in Fig. 4.7. The data are binned in intervals of $\Delta z = 0.005$ which corresponds to 1500 km s^{-1}. There is a clear excess of galaxies at the redshift of the WAT source, with a distinct peak at the redshift bin $0.22 \leq z < 0.225$. 20 galaxies lie in the peak-redshift bin, and a further 22 galaxies lie in the two neighbouring bins resulting in 42 galaxies over three redshift bins, the concentration being significant at ~7σ. Properties of the galaxies in the peak histogram bin and the two adjacent bins, which includes the putative cD galaxy at a redshift of 0.2204, are listed in Table 4.3. The total spread in velocity of the 42 galaxies is ~4500 km s^{-1}, and the velocity dispersion is ~870 km s^{-1}. This is similar to the spread for typical rich clusters in the local Universe undergoing mergers such as A3667 and A3376 which both show **radio** relic emission and have a velocity spread of ~4200 km s^{-1} (Johnston-Hollitt et al. 2008; Owers et al. 2009). The redshift distribution of the 42 galaxies is shown in greater detail as an inset in Fig. 4.7. The distribution is not a smooth Gaussian and shows sub-structure, consistent with dynamic, merging systems.

4.4.2 Spatial Distribution

In Fig. 4.8 we plot the positions of the 42 galaxies listed in Table 4.3, with the galaxies in the three redshift bins ($0.215 \leq z < 0.22$; $0.22 \leq z < 0.225$; $0.225 \leq z < 0.23$) indicated by circles of varying size. Despite considerable overlap, there is a suggestion of a velocity gradient with the galaxies in the lowest redshift bin (largest circles) extending towards the south-west and those in the highest redshift bin (smallest circles) extending towards the south-east. Although galaxy redshifts were measured within a radius of ~12 Mpc from the WAT, ~60 per cent

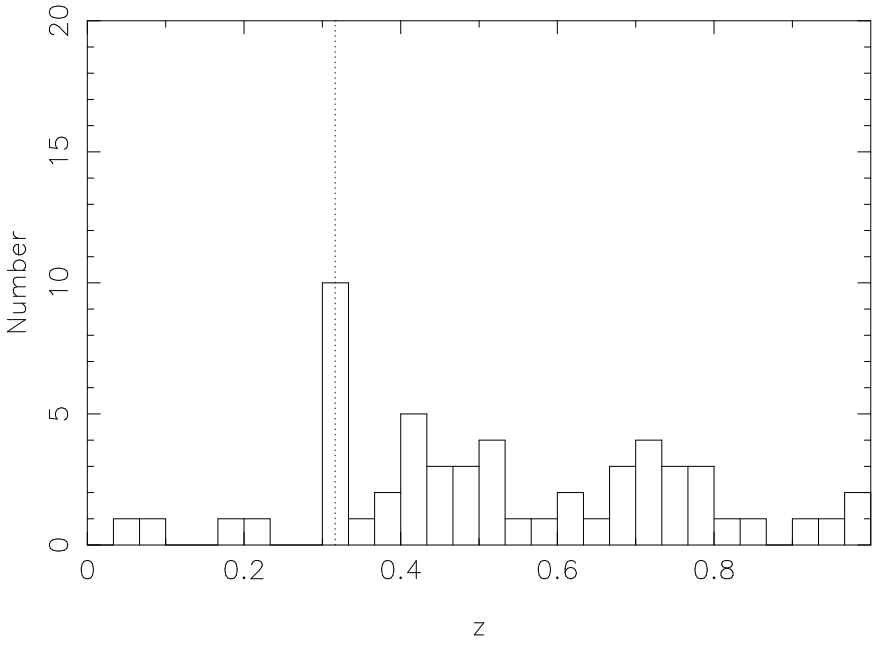

Figure 4.4: Photometric redshift distribution of galaxies within 2 arcmin of S483 (~550 kpc at z = 0.3164). The data is binned in intervals of $\Delta z = 0.03$. The vertical dotted line indicates the redshift of the host galaxy.

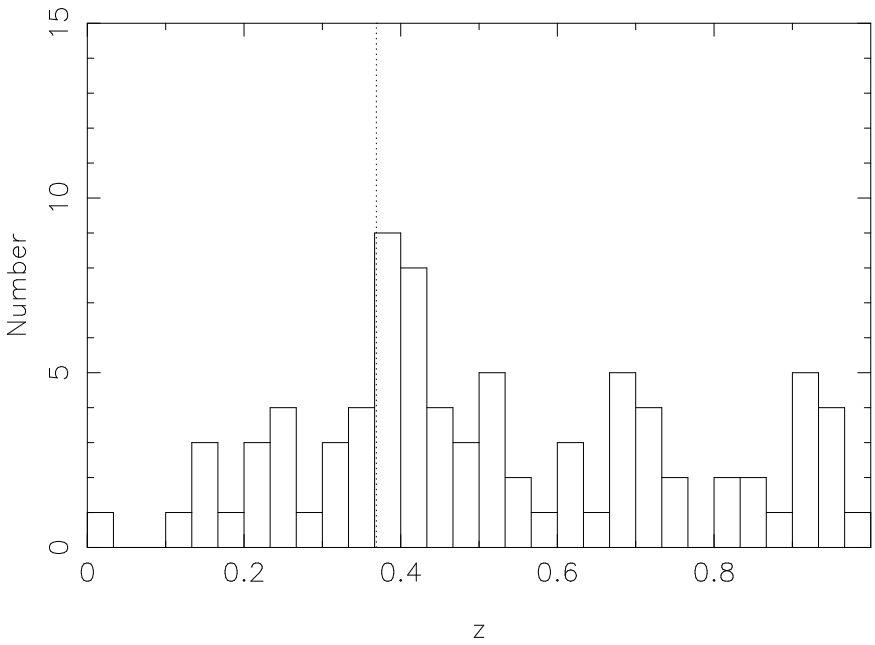

Figure 4.5: Photometric redshift distribution within 2 arcmin of S1192 (~500 kpc at z = 0.3690). The data is binned in intervals of $\Delta z = 0.03$. The vertical dotted line indicates the redshift of the host galaxy.

Table 4.3: Optical and infrared properties of the putative cluster members. Column 1 gives the SWIRE identification. Column 2 lists the R-band magnitude from SWIRE while Column 3 lists the redshifts. Column 4 lists the radio flux density at 1.4 GHz while Column 5 provides comments.

SWIRE ID	R mag	z	Radio flux (mJy)	comment
SWIRE3_J003236.91-432040.8	19.44	0.2169		
SWIRE4_J003411.57-425952.0	18.92	0.2171	0.53	
SWIRE4_J003107.43-434037.5		0.2176	0.24	
SWIRE4_J003559.43-430324.8	18.74	0.2180	0.21	
SWIRE4_J003109.85-435010.9		0.2181	3.93	
SWIRE4_J003512.31-425437.5		0.2181	14.79	
SWIRE3_J003203.05-434121.6	18.07	0.2184		
SWIRE3_J003500.92-430309.5	20.06	0.2187		
SWIRE3_J003355.92-424153.9		0.2190		
SWIRE4_J003123.87-430940.5		0.2191	0.34	
SWIRE4_J003427.54-430222.5	17.12	0.2193	45.03	WAT
SWIRE3_J003422.08-430623.7	19.53	0.2201		
SWIRE4_J003432.80-424555.1		0.2202	1.08	
SWIRE4_J003748.72-430211.9	18.65	0.2203	0.23	
SWIRE4_J003525.13-432941.4	18.93	0.2204	0.15	
SWIRE3_J003419.26-430334.0	16.37	0.2204		cD galaxy
SWIRE4_J003713.54-431342.8	17.53	0.2214	2.39	
SWIRE3_J003339.84-430908.8	18.07	0.2215		
SWIRE3_J003711.92-430711.4	18.32	0.2215		
SWIRE3_J003415.87-430840.9	18.97	0.2220		
SWIRE4_J003714.11-430833.3	17.59	0.2221	0.53	
SWIRE3_J003526.70-430418.7	18.45	0.2222		
SWIRE3_J003503.98-425710.2		0.2222		
SWIRE4_J003645.81-432016.0	17.73	0.2222	0.49	
SWIRE3_J003443.66-424544.6		0.2225		
SWIRE4_J003344.79-431627.8	17.87	0.2228	0.91	
SWIRE3_J003707.12-430302.7	19.18	0.2229		
SWIRE4_J003242.01-432630.6	18.78	0.2230	0.32	
SWIRE4_J003326.18-434051.0	18.76	0.2232	0.27	
SWIRE3_J003229.91-425457.7		0.2233		
SWIRE3_J003242.01-432630.5	18.78	0.2233		
SWIRE4_J003721.05-434240.0	17.40	0.2251	1.33	
SWIRE4_J003306.30-431029.8	17.71	0.2252	12.33	double radio
SWIRE4_J003609.95-435002.2	19.84	0.2252	0.32	
SWIRE3_J003322.00-430419.5	20.12	0.2253		
SWIRE4_J003604.09-435802.3		0.2255	0.18	
SWIRE4_J003340.23-432542.2	18.24	0.2258	0.34	
SWIRE4_J003640.42-430000.1	17.32	0.2263	0.75	
SWIRE4_J003734.09-433339.3	17.92	0.2263	1.20	
SWIRE3_J003659.30-431824.1	18.20	0.2263		
SWIRE4_J003502.52-432410.9	18.02	0.2265	0.19	
SWIRE3_J003300.09-432819.9	18.26	0.2267		

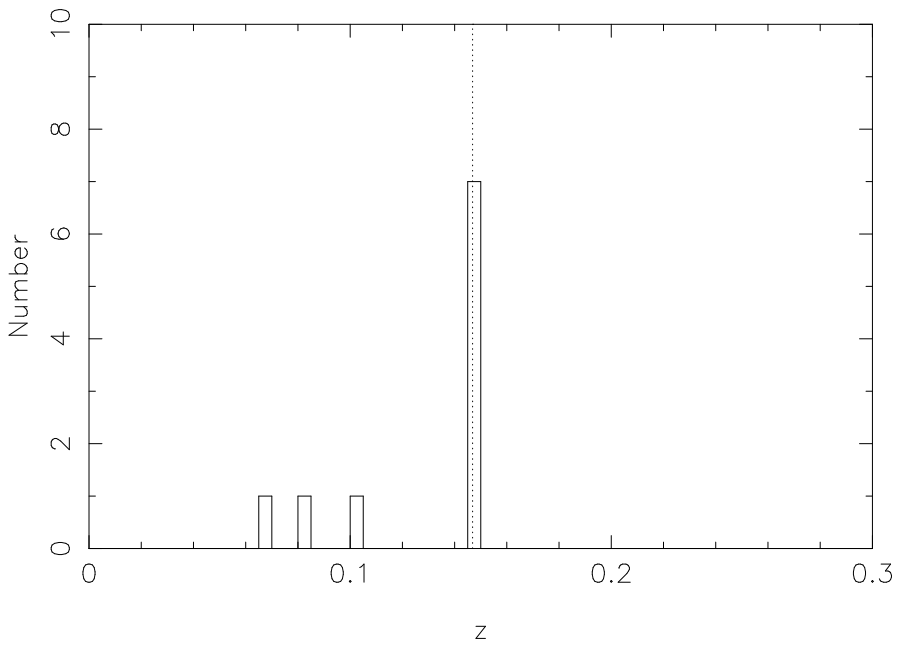

Figure 4.6: 2dFGRS spectroscopic redshifts (Colless et al. 2001) of sources within 7 arcmin of S409 (∼1 Mpc at z = 0.1469). The data is binned in intervals of $\Delta z = 0.005$. The vertical dotted line indicates the redshift of the host galaxy.

of the galaxies listed in Table 4.3 are within 6 Mpc of the WAT (30 arcmin). We also note that the larger number of sources in the southern part of Fig. 4.8 is due to the uneven coverage of the one-degree-radius field surrounding S1189.

4.4.3 cD Galaxy

The bright galaxy, SWIRE3_J003419.26-430334.0, located southwest of the WAT source, has a redshift of 0.2204, implying a velocity difference between the two galaxies of ∼320 km s^{-1}. Their projected separation is ∼2 arcmin, corresponding to ∼420 kpc at a redshift of 0.22. SWIRE3_J003419.26-430334.0 is the brightest galaxy in the cluster and has a diffuse envelope, therefore we classify it as a possible cD galaxy. There is a marginal detection of associated radio emission with a flux density of ∼140 μJy at 1.4 GHz which corresponds to a radio luminosity of 1.96×10^{22} W Hz^{-1}. Centrally dominant cD galaxies are usually giant ellipticals residing in the centres of clusters of galaxies. These are much larger and brighter than other galaxies in the cluster and are often surrounded by a diffuse envelope (Matthews et al. 1964). Their large size is usually attributed to mergers and galaxy cannibalism (e.g. De Lucia and Blaizot 2007).

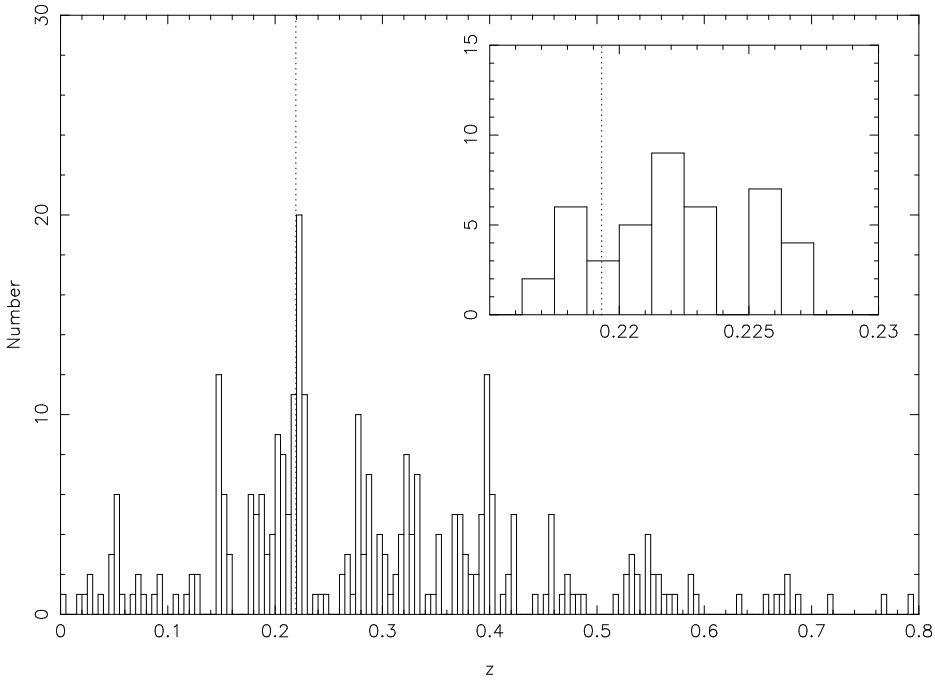

Figure 4.7: Histogram of redshifts of 299 galaxies located within a one degree radius centred on the WAT, S1189, and with redshifts less than or equal to 0.8. The redshift bin size is 0.005 which corresponds to 1500 km s^{-1}. The inset shows the redshift distribution of the galaxies at the peak and two adjacent bins ($0.215 \leq z < 0.23$). The redshift bin size is 0.00125 which corresponds to 375 km s^{-1}. The vertical dotted lines in both histograms are at z=0.2193, the redshift of the WAT source.

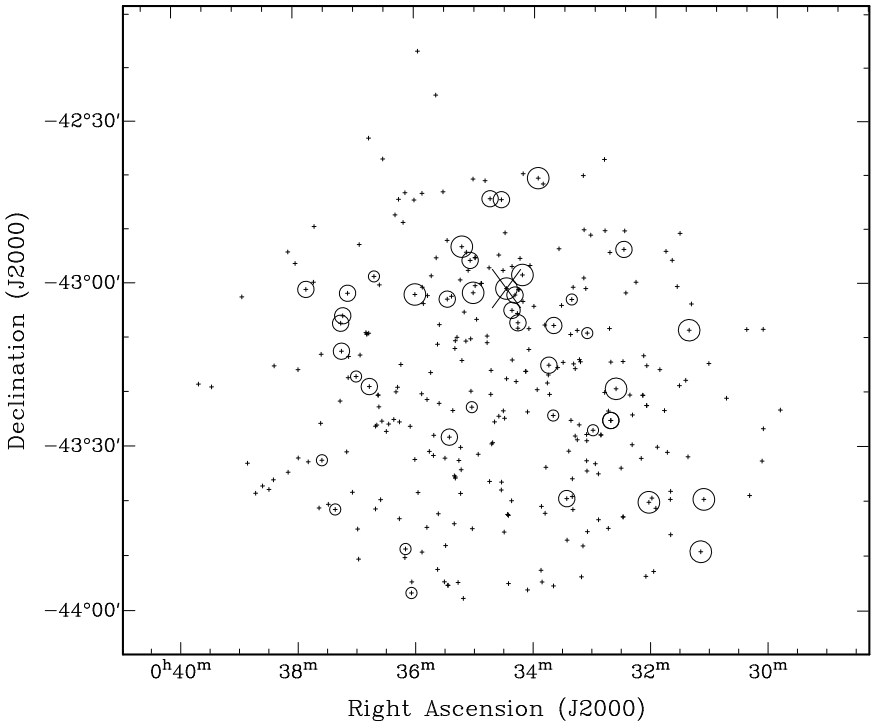

Figure 4.8: Spatial distribution of all galaxies in the field surrounding S1189 that have spectroscopic redshifts. The circled sources are at $0.215 \leq z < 0.23$. The largest circles show the sources that are at $0.215 \leq z < 0.22$. The medium circles show the sources that are at $0.22 \leq z < 0.225$ and the smallest circles show the sources that are at $0.225 \leq z < 0.23$. The location of the WAT is indicated by the large "X".

4.4.4 Extended radio sources in the vicinity of the WAT

In addition to double-lobed radio sources, radio haloes, relics and core haloes or mini haloes may also be associated with clusters of galaxies. Core-haloes are usually less than ~500 kpc in extent and associated with the dominant galaxy in cooling core clusters. Haloes and relics are not associated with any particular galaxy, and are often larger in size. Radio haloes are usually projected towards the cluster centre, while relics are seen towards the periphery (e.g. Giovannini and Feretti 2004). There are ~30 radio haloes in nearby (z<0.4) clusters of galaxies (e.g. Giovannini et al. 2009), and there are ~30 clusters of galaxies with at least one radio relic (Giovannini and Feretti 2004). While models for haloes range from re-acceleration of particles by turbulence to production of relativistic electrons by hadronic collisons, relics are believed to arise due to cluster mergers and/or matter accretion (Sarazin 1999; Ryu et al. 2003; Pfrommer et al. 2006; Giacintucci et al. 2008; Johnston-Hollitt et al. 2008; Brown and Rudnick 2009).

Recent work suggests that halos are found in massive, unrelaxed clusters, with the radio and X-ray luminosity being strongly correlated, consistent with the re-acceleration scenario (Brunetti et al. 2007; Venturi et al. 2008; Cassano 2009). However, the present studies have been based on X-ray selected clusters of galaxies, and possible biases arising from it should be borne in mind. For example, the limited sensitivity of the radio observations would make it easier to detect halos in only the more X-ray luminous clusters of galaxies.

Radio relics on the other hand are believed to arise due to mergers accompanied by shocks and/or matter accretion (e.g. Bagchi et al. 2006, and references therein). These shocks are capable of accelerating particles to high energies, giving rise to the observed synchrotron radio emission. Harris et al. (1980) and Tribble (1993) were amongst the early ones to suggest and explore the possibility of acceleration of particles due to shock fronts on a large scale caused by mergers. These ideas were expanded upon by Ensslin et al. (1998), Roettiger et al. (1999) Enßlin and Gopal-Krishna (2001) and Ricker and Sarazin (2001), producing more sophisticated models.

The ATLAS radio image at 1.4 GHz (Fig. 4.9) shows two more extended sources within ~20 arcmin of the WAT source, one of which (S1081) appears to be a radio relic (Middelberg et al. 2008), while the other (S1110) is an FRI radio galaxy. Superpositions of the radio image of the relic on an optical DSS red image as well as an infrared 3.6–μm image are shown in Fig. 4.10. While no optical object is visible within the radio contours, there is an infrared ob-

ject towards the central region of the source. This object has been classified as an Sbc galaxy (optical template type 5) using a total of 6 photometric bands by Rowan-Robinson et al. (2008). Its photometric redshift has been estimated to be 1.18. Given the properties of the object, it is likely to be unrelated. The radio properties of the WAT and these two sources are summarised in Table 4.4. At a redshift of 0.22, the relic would have a physical size of ∼274 kpc and a luminosity of $\mathbf{3.3}\times10^{23}$ W Hz^{-1}, which would make it similar to the relics found in the periphery of clusters of galaxies in the local Universe (Ferrari et al. 2008). The relic is at a projected distance of ∼2 Mpc from the cD galaxy. Typically relics have been observed at distances of about a Mpc from the cluster centre, although some systems are known to have relics up to distances of ∼4 Mpc (e.g. Giovannini and Feretti 2004). Some of the known examples of relics which lie at distances beyond ∼2 Mpc from the nearest cluster core, such as B0917+75 (Harris et al. 1993; Johnston-Hollitt 2003), are typically associated with structure larger than a single cluster. In the case of B0917+75 it is the Rood 27 cluster group. This is similar to our situation. It is also relevant to note that the minor axis of the relic does not point towards either the WAT source or the cD galaxy, suggesting sub-structure in this large-scale structure. Simulations of shock generation during hierarchical mass assembly suggest relics can be produced over 8 Mpc from the cluster centre (Miniati et al. 2000; Pfrommer et al. 2006, 2008; Hoeft et al. 2008; Vazza et al. 2009). These aspects along with its radio structure and lack of an obvious optical identification make it very likely to be a radio relic. One could enquire whether this object might be a dying radio galaxy. The non-detection of an early-type galaxy associated with it suggests that this is unlikely to be the case. There are very few relics known beyond a redshift of ∼0.2 (e.g. Giovannini and Feretti 2004), which makes this finding a significant one.

The other interesting source in the field is the FRI radio source S1110. The radio emission from S1110 is symmetric within ∼80 kpc from the host galaxy, SWIRE4_J003306.30-431029.8, reminiscent of the large-scale jets in FRI radio sources. However, the extended lobes are highly asymmetric, the peak brightness in the outer extremities differing by a factor of ∼4. This may be due to density asymmetries on opposite sides of the source.

Table 4.4: Radio properties of S1189 and extended radio sources in its vicinity. The size of the WAT (S1189) was measured from the outer edge of one lobe to the core and out to the outer edge of the other lobe. The relic is assumed to be at a redshift of 0.22.

	ATLAS ID	RA (J2000)	Dec (J2000)	Redshift	$S_{1.4}$ (mJy)	$Power_{1.4}$ (10^{24} W Hz^{-1})	$size_{ang}$ (arcmin)	$size_{phy}$ (kpc)
WAT	S1189	00 34 27.6	-43 02 22.5	0.2193	45.03	6.25	5.0	1053
Double radio	S1110	00 33 06.3	-43 10 29.8	0.2252	12.33	1.82	2.6	559
Relic	S1081	00 34 11.7	-43 12 39.4	(0.22)	2.35	(0.33)	1.25	(274)

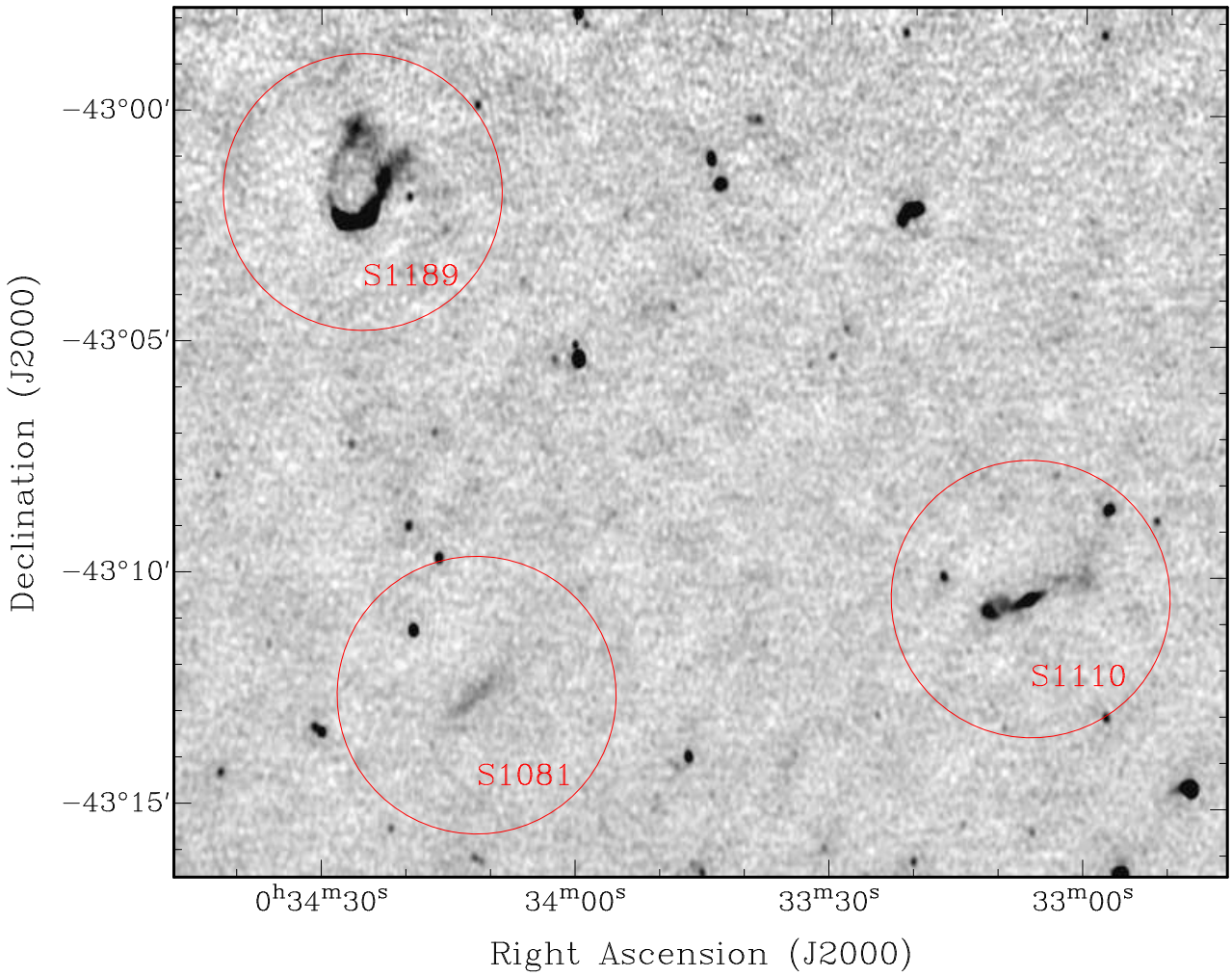

Figure 4.9: 1.4 GHz radio image showing the WAT (S1189), the double-lobed radio galaxy (S1110) and the radio relic (S1081). The WAT S1192 , at z = 0.3690, is also seen in the image.

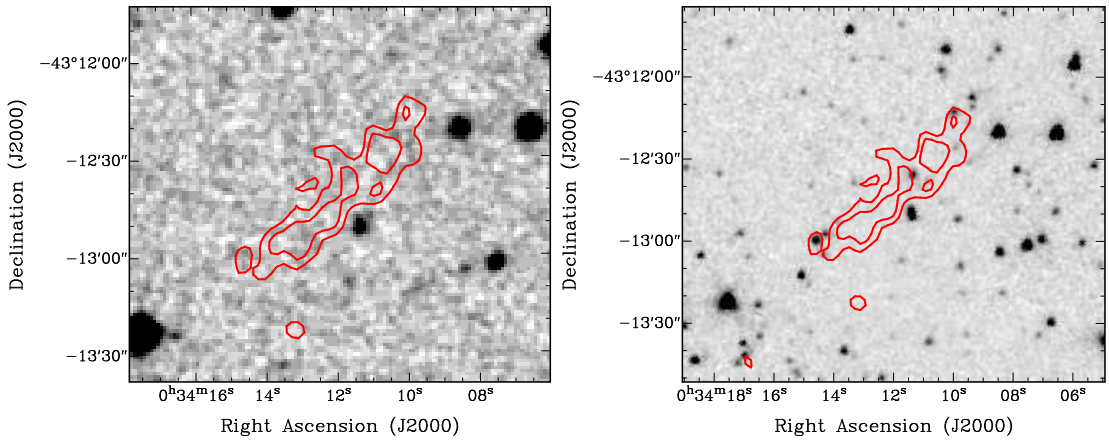

Figure 4.10: 1.4 GHz radio contours of the relic (S1081) overlaid on the DSS red optical image (left panel) and the 3.6 μm IRAC image (right panel) The contours start at 100 μJy beam^{-1} and increase by factors of $\sqrt{2}$.

4.5 Implications for Deep Wide Radio Surveys and ATLAS

In this paper we have reported the detection of six WATs from a sample of 2004 radio sources. Extrapolating this to future deep wide surveys, we might expect to detect about 200,000 WATs from the catalogue of 70 million radio sources that will be generated by the ASKAP-EMU (Australia SKA Pathfinder - Evolutionary Map of the Universe) project (Norris 2009). Since each of these WATs is likely to be associated with a cluster, such surveys will be powerful tools for detecting clusters and exploring their properties, particularly since the radio luminosity of WATs makes them detectable and capable of being studied up to high redshifts.

Such surveys are therefore likely to contribute significantly to areas such as the formation and evolution of clusters, the formation of massive ellipticals, and the relationship between giant ellipticals and supermassive black holes, or SMBHs (e.g. Blanton et al. 2003; Chiaberge et al. 2009). Furthermore, while optical and X-ray surveys tend to select the optically-rich or most X-ray-luminous clusters of galaxies at moderate and high redshifts, sensitive radio observations could help identify clusters with a wide range of optical and X-ray properties.

However, WATs are characterized by diffuse lobes of emission extending to hundreds of kpc, and two effects potentially make such structures difficult to observe at high redshift.

First, the radiating electrons of a synchrotron source lose energy by inverse-

Compton (iC) scattering of the cosmic microwave background radiation (CMBR), whose energy density increases as $(1+z)^4$. This effect is supported by evidence that the X-ray emission from the lobes of large radio galaxies is due to iC scattering of the radiating electrons with the CMBR, which has been used to make an independent estimate of the magnetic field strength of the radio lobes (e.g. Croston et al. 2004, 2005; Konar et al. 2009). Furthermore, Konar et al. (2004) have found that the bridge emission in giant radio sources is less prominent at higher redshifts, which they interpret as being caused by iC scattering with the CMBR.

Loss of electron energy by iC scattering from the CMBR overtakes synchrotron cooling at a redshift $z \sim 0.556\sqrt{B}-1$ where B is the synchrotron magnetic flux density in μGauss (Schwartz et al. 2006). So, for a constant B, one might expect synchrotron emission to fall sharply above that redshift.

However, if a low-luminosity radio source is modelled as two cones of expanding plasma on either side of the central SMBH, then the magnetic field would be expected to fall as the square of the distance r from the SMBH, resulting in a transition radius r_{crit} at which the dominant electron cooling mechanism switches from synchrotron to iC, where $r_{crit} \propto (1+z)^{-1}$. Thus, rather than synchrotron emission falling sharply above some redshift, the size of the synchrotron-emitting region shrinks linearly with redshift.

We conclude that, while iC cooling reduces the apparent size of the emitting region, it does not impose a fundamental redshift limit above which WATs will be invisible.

Second, high-redshift galaxies are subject to cosmological surface brightness dimming, (e.g. Lanzetta et al. 2002, and references therein) which causes the observed surface brightness per unit frequency interval of a resolved source to decrease as $(1+z)^3$. Thus, nearby radio galaxies are detectable to much lower intrinsic surface brightness thresholds than high-redshift sources.

While both these effects are going to present challenges to the identification of WATs at high redshifts, they accentuate the normal challenges of resolution and sensitivity, rather than presenting fundamental limits of observability. In their search for FRI radio sources in the redshift range $1<z<2$ using the Faint Images of the Radio Sky at Twenty-Centimeters (FIRST) radio survey, Chiaberge et al. (2009) find that most of the sources are compact. Blanton et al. (2003) have identified a WAT galaxy at z=0.96, while Saikia et al. (1993) and Saikia et al. (1987) explored the possibility that B1222+216 (4C21.35) and B2 1419+315 might be WAT quasars at redshifts of 0.435 and 1.547 respectively.

To explore and understand these aspects will require more detailed modelling and significantly deeper large-scale radio surveys, which is the primary goal of ASKAP-EMU.

4.6 Conclusions

We have identified a sample of six Wide-Angle Tail (WAT) radio sources. We present new spectroscopic redshifts for four of these sources, and find that these WATs lie in the redshift range 0.1469–0.3762. We have examined the fields using both spectroscopic and photometric redshifts of galaxies in the vicinity of the WATs and find evidence of an overdensity of galaxies in four of these WATs.

From a more detailed study of the field around S1189 we find an overdensity of galaxies which is spread over ∼12 Mpc and has a velocity spread of ∼4500 km s^{-1}, and a velocity dispersion of ∼870 km s^{-1}. This large-scale structure hosts a putative cD galaxy with, at best, weak radio emission, a radio relic which has a size of ∼274 kpc, and an asymmetric FRI radio galaxy with an extent of ∼559 kpc. The peak brightness at the extremities of the outer lobes of the FRI source differ by a factor of ∼4, possibly due to differences in the environment on opposite sides. The minor axis of the relic is not directed towards either the host galaxy of the WAT or the putative cD galaxy. This large-scale structure may represent an unrelaxed system with different sub-structures interacting or merging with one another. Therefore, deep X-ray observations of the field would be very valuable to further understand this interesting large-scale structure.

WATs are known to occur in clusters of galaxies, and could in principle be useful tracers of clusters at moderate and high redshifts. IC cooling of electrons by interaction with CMBR increases rapidly with z. However, this does not imply a sharp drop in the number of WATs at high z. Deep and wide-field surveys, such as the Evolutionary Map of the Universe (EMU) (Norris 2009), should provide additional information and insights on the range of structures at moderate and high redshifts. We expect these to be invaluable probes of large-scale structure.

Acknowledgements

We thank Emil Lenc and Jamie Stevens for their help, the ATLAS team and Mark Birkinshaw for many fruitful discussions, and an anonymous referee whose comments helped improve the manuscript. MYM acknowledges the support of an

Australian Postgraduate Award as well as Postgraduate Scholarships from AAO and ATNF. We thank the staff at AAO and ATCA for making these observations possible. The ATCA is part of the Australia Telescope, which is funded by the Commonwealth of Australia for operation as a National Facility managed by CSIRO. This research has also made use of NASA's Astrophysics Data System.

5

No Evidence for Evolution in the Far-Infrared-Radio Correlation out to $z \sim 2$ in the ECDFS

This chapter is a reproduction of the first-author peer-reviewed journal article *No Evidence for Evolution in the Far-Infrared-Radio Correlation out to $z \sim 2$ in the ECDFS*, Mao M. Y., Huynh M. T., Norris R. P., Dickinson M., Frayer D., Helou G., Monkiewicz J. A., 2011, ApJ, 731, 79. This work was performed in part during a six-month period as an IPAC Graduate Research Fellowship at Caltech. The majority of this work was performed after the Fellowship's completion and as such I have included it in this thesis. Although the project was conceived by Dr Minh Huynh, I was responsible for leading this work and the article was wholly written by me with the contributions of the coauthors as follows:

- Minh Huynh supervised this work at IPAC Caltech, provided me with example IDL code for many tasks. Minh performed the stacking analysis and produced Figure 5.11.
- Ray Norris supervised this work upon my return to Australia.

- Mark Dickinson is PI of FIDEL and participated in valuable discussions about the FIDEL data.
- Dave Frayer participated in many valuable discussions about the evolution of the FRC, and provided us with the AGN and SF templates in Figure 5.8.
- George Helou partipated in many valuable discussions about the evolution of the FRC.
- Jacqueline Monkiewicz was involved in the data reduction process of the FIDEL data that we use.

The text is largely unchanged with only minor modifications for consistency.

Abstract

We investigate the 70 μm Far-Infrared Radio Correlation (FRC) of star-forming galaxies in the Extended Chandra Deep Field South (ECDFS) out to $z > 2$. We use 70 μm data from the Far-Infrared Deep Extragalactic Legacy Survey (FIDEL), which comprises the most sensitive (~0.8 mJy rms) and extensive far-infrared deep field observations using MIPS on the Spitzer Space Telescope, and 1.4 GHz radio data (~8 μJy beam^{-1} rms) from the VLA. In order to quantify the evolution of the FRC we use both survival analysis and stacking techniques which we find give similar results. We also calculate the FRC using total infrared luminosity and rest-frame radio luminosity, q_{TIR}, and find that q_{TIR} is constant (within 0.22) over the redshift range 0 - 2. We see no evidence for evolution in the FRC at 70 μm, which is surprising given the many factors that are expected to change this ratio at high redshifts.

5.1 Introduction

The correlation between the far-infrared (FIR) and radio emission for star-forming galaxies in the local Universe was first observed by van der Kruit (1971, 1973) and is the tightest and most universal correlation known among global parameters of galaxies (Helou and Bicay 1993). The correlation is linear, spans five orders of magnitude of bolometric luminosity and has been shown to hold for a wide range of Hubble types (de Jong et al. 1985; Helou et al. 1985; Condon 1992; Yun et al. 2001).

The FIR-radio correlation (FRC) has been attributed to the presence of young, high-mass ($M > 8M_{\odot}$) stars. The FIR emission arises from the absorption by dust of the UV emission and subsequent reradiation of the energy at IR wavelengths. The radio emission is dominated by non-thermal synchrotron emission from cosmic ray electrons which are accelerated by supernovae shocks. There is also a thermal component which arises from free-free emission from ionized hydrogen in HII regions, but this contributes only ~10% of the radio emission at lower frequencies (<5 GHz, Condon 1992), and becomes more significant at higher frequencies.

The "calorimeter theory" (Voelk 1989) suggests that the FRC holds because galaxies are both electron calorimeters and UV calorimeters so the total radio and IR outputs remain proportional independent of variations within the galaxy.

This theory however, requires that galaxies are optically thick to UV light from the young high-mass stars, and thus does not hold for optically-thin galaxies. Helou and Bicay (1993) proposed the non-calorimetric "optically thin" scenario involving a correlation between disk scale height and the escape scale length for cosmic ray electrons, while Bell (2003) concludes that the linearity of the FRC is a conspiracy as the star-formation rate is underestimated for low-luminosity galaxies at both radio and infrared frequencies. However, these models typically leave out proton losses and non-synchrotron cooling (Lacki et al. 2010). Ultimately, the physical origin of the FRC is still not clear.

The far-reaching nature of the FRC has made it a valuable diagnostic. Some examples of its application include: using the FRC to identify radio-loud AGN (Donley et al. 2005; Norris et al. 2006); using the FRC to define the radio luminosity/SFR relation (Bell 2003); and, at higher redshifts, using the FRC to estimate distances to submillimetre galaxies without optical counterparts (e.g., Carilli and Yun 1999). Consequently it is of great importance to determine whether the FRC holds at high redshifts.

The FRC may fail at high redshifts for a number of reasons. Electrons are expected to lose energy by inverse Compton interactions with the cosmic microwave background, whose energy density scales as $(1+z)^4$, implying a lower level of radio emission at higher redshifts. Moreover, synchrotron emission is proportional to the magnetic field strength squared, so evolution of magnetic field strength should affect the FRC at higher redshifts (e.g., Murphy 2009). Changes in the spectral energy distributions (SEDs) may also be expected due to evolution in dust properties and metallicity (e.g., Amblard et al. 2010; Hwang et al. 2010; Chapman et al. 2010). Nonetheless, current studies show no firm evidence for evolution in the FRC (e.g., Garrett 2002; Appleton et al. 2004; Seymour et al. 2009; Bourne et al. 2011; Ivison et al. 2010a,b; Sargent et al. 2010a,b; Huynh et al. 2010).

Herschel was launched in May 2009 and can probe the FIR to submillimetre regime from 55 μm to 671 μm, deeper than ever before (Pilbratt et al. 2010). Most recently, Jarvis et al. (2010) and Ivison et al. (2010b) used data from Herschel and found no evidence for evolution in the FRC out to $z = 0.5$ and $z = 2$ respectively.

This paper studies the dependence of the FRC on redshift using deep 70 μm data from the Spitzer Space Telescope and 1.4 GHz data from the Very Large Array (VLA). This work differs from previous studies as we are using FIDEL (Far-Infrared Deep Extragalactic Legacy Survey) 70 μm data, which is the deepest

70 μm data taken to date. FIDEL reaches a point source rms sensitivity of 0.8 mJy at 70 μm, making it far more sensitive than previous studies of the FIR at 70 μm such as Sargent et al. (2010b) whose data reached a point source rms sensitivity of 1.7 mJy.

We focus on the 70 μm data as this band probes closer to the dust emission peak (~100 μm) than, for example, 24 μm. Furthermore, for $z < 3$, the 70 μm band is not affected by emission from polycyclic aromatic hydrocarbons (PAHs; 7 - 12 μm). While Bourne et al. (2011) also study the FRC using FIDEL data, their work was entirely based on stacking analysis. This work is the first to use such deep 70 μm data to study the evolution of the FRC based on individual sources.

The data are described in Section 2, Section 3 describes the data analysis while Section 4 presents our results and analysis. This paper uses $H_0 = 71$ km s^{-1} Mpc^{-1}, $\Omega_M = 0.27$ and $\Omega_\Lambda = 0.73$.

5.2 Data

5.2.1 FIDEL

FIDEL, the Far-Infrared Deep Extragalactic Legacy Survey, is a legacy science program (PI: Dickinson) which comprises the most sensitive and extensive FIR deep field observations using the Multiband Imaging Photometer for SIRTF (MIPS) on the Spitzer Space Telescope. Characteristics of the FIDEL data are described in detail in Magnelli et al. (2009) and other papers. FIDEL observed three fields: ECDFS, EGS and GOODS-North. Observations were taken at 3 bands: 24 μm, 70 μm and 160 μm, focusing specifically on the 70 μm data. This paper concentrates only on the 30′ × 30′ ECDFS field centred on 03 32 00, -27 48 00 (J2000). The observations were designed to achieve roughly uniform sensitivity at 70 μm across most of the ECDFS, although the FIDEL data include a somewhat deeper central region with data from a GO program (PI: Frayer). The mean 70 μm exposure time over the ECDFS is approximately 6600s, yielding an RMS point source sensitivity of approximately 0.8 mJy. The 24 μm exposure time varies considerably more over the field, from 5000 to 35000 seconds over most of the ECDFS, with an average exposure time of approximately 16000 seconds. The RMS point source sensitivity at 24 μm thus also varies, but is typically in the range 8 to 14 μJy over most of the field. FIDEL data were processed using the Mosaicking and Point-source Extraction (MOPEX, Makovoz and Marleau 2005) package to form

the mosaicked images. The final 70 μm mosaic has a pixel scale of 4.0″/pixel and a point response function (PRF) with an 18″ *FWHM*. The final 24 μm mosaic has a pixel scale of 1.2″/pixel and a PRF with a 5.9″ *FWHM*.

5.2.2 Ancillary data

Radio data

The ECDFS has been observed at 1.4 GHz by both the VLA and the ATCA (Norris et al. 2006; Kellermann et al. 2008; Miller et al. 2008). Here we use the Miller et al. (2008) radio data due to its high angular resolution and sensitivity over our field. The radio data encompass a 34′ × 34′ region, centred on 03 32 28.0, -27 48 30.0 (J2000). The data have a typical rms sensitivity of 8 μJy per 2.8″ × 1.6″ beam. The catalogue contains 464 sources above a 7 sigma cutoff.

Redshift data

We obtained both spectroscopic and photometric redshift data from COMBO-17 (Wolf et al. 2004), MUSYC (Gawiser et al. 2006; Cardamone et al. 2010), GOODS (Balestra et al. 2010) and ATLAS (Mao et al. 2009b).

COMBO-17 has photometric data in 17 passbands from 350 nm to 930 nm for 63501 objects in the ECDFS. The photometric redshifts are most reliable for sources with R $\leq$ 24 (Wolf et al. 2004).

MUSYC (Multiwavelength Survey by Yale-Chile) has photometric data in the ECDFS. Cardamone et al. (2010) combined photometric data from the literature with new deep 18-medium-band photometry into a public catalogue of ∼80000 galaxies in ECDFS, from which they computed the photometric redshifts. The photometric redshifts are most reliable for sources with R $\leq$ 25.5. Cardamone et al. (2010) also compile a spectroscopic redshift catalogue of 2551 galaxies from the literature (e.g., Balestra et al. 2010; Vanzella et al. 2008; Le Fèvre et al. 2004).

Balestra et al. (2010) observed the GOODS-South field (within the ECDFS) using VIMOS to obtain spectroscopic redshifts. Their campaign used two different grisms to cover different redshift ranges and used 20 VIMOS masks. They combined their resulting redshifts with those available in the literature to produce a catalogue containing 7332 spectroscopic redshifts. Quality flags were provided for all the redshifts and we took only those redshifts that had quality flags of "secure" and "likely" yielding a catalogue of 5528 spectroscopic redshifts. Although

Cardamone et al. (2010) includes Balestra et al. (2010) data in their compilation of spectroscopic redshifts, they only include a subset of the data.

Mao et al. (2009b) are undertaking a program of redshift determination and source classification of all ATLAS (Australia Telescope Large Area Survey) radio sources with AAOmega (Sharp et al. 2006) on the Anglo-Australian Telescope (AAT). Using redshifts from both the literature and their own campaign they have a total of 261 spectroscopic redshifts in ECDFS and its surrounding region.

X-ray data

We use the 2 Ms Chandra Deep Field South X-ray catalogues from Luo et al. (2008) to identify AGN in our 70 μm catalogue (Section 5.4.1). This is one of the most sensitive X-ray surveys ever performed and detects 462 sources in 436 arcmin^2. While the X-ray data cover a smaller region than the FIDEL data, we use these data to eliminate some AGN from our sample (Section 5.4.1).

5.3 Data Analysis

5.3.1 FIDEL

70 μm

The 70 μm catalogue was produced with the Astronomical Point Source Extraction (APEX) module within the MOPEX package. APEX subtracts the local background by calculating the median in a region, which we set to 34 × 34 pixels, surrounding each pixel, and removing the 100 brightest pixels. Peak values with a S/N greater than three were fitted using the PRF. The 3-sigma catalogue extracted using APEX contained 515 sources.

24 μm

A similar source detection and extraction process to the 70 μm data were used for the 24 μm data. However a four sigma cutoff was used to reduce the number of spurious sources. Visual inspection was required to remove spurious sources due to artefacts surrounding bright objects. The final catalogue of 24 μm sources in the ∼30′ × 30′ region of interest contained 5319 sources.

Final catalogue

To test the completeness of the 70 μm catalogue, we performed Monte-Carlo simulations. A simulated source was injected at a random location in the 70 μm image, and source extraction was performed using the same technique as for the production of the catalogue. The input flux density of the simulated source varied over the range of flux densities in the "real" image. This process was repeated 10000 times and we tracked the simulated source recovery rate, which enables us to estimate the overall completeness over the entire image. Figure 5.1 presents the completeness as a function of flux density. Our catalogue is almost 100% complete at 9 mJy, and 50% complete at ~2.5 mJy. This high level of completeness at 2.5 mJy (~3 sigma) is probably due to the 70 μm image not being completely uniform. The 10 × 10 arcminute region in the centre has an RMS point source sensitivity of ~0.6 mJy, so 2.5 mJy is a >4 sigma limit for ~11% of the image area. The completeness plot does not reach 100% due to the random positioning of the simulated source. If, by chance, the simulated source is injected upon a real source, the simulated source is not recovered as an individual source, and instead, the "real" source is recovered with a larger flux density.

The 70 μm catalogue of 515 sources obtained using APEX may contain confused sources, as well as spurious sources. We determined which sources required deblending by comparing it with the 24 μm catalogue which has better resolution. First, we matched the 70 μm catalogue to the 24 μm catalogue using a matching radius of 9″ (the half-width at half maximum of the PRF at 70 μm). We then calculated the ratio of the flux density of the brightest 24 μm source to the total flux density of all 24 μm sources within the 9″ matching radius (see Figure 5.2). Those sources for which the ratio is one would not require deblending. Using arguments similar to those of Pope et al. (2006), we assume that if a source is bright at 24 μm, it will also be bright at 70 μm. Consequently, if the ratio was greater than 0.8 (that is, if the brightest 24 μm source contributed >80% of the total flux density in the matching radius), the 70 μm emission was determined to be from the brightest 24 μm source. If the ratio is less than 0.8, we considered the 70 μm source as a candidate for deblending. Using these criteria we determined that 164 sources were deblend candidates. In principle, it is possible that for sources with a ratio of greater than 0.8, we are overestimating the 70 μm flux density by up to 20%. An overestimation of the 70 μm flux density may result in a higher FRC, but this effect is much less than $\Delta q_{70} = 0.1$.

The sources were deblended using double, triple or even quadruple Gaussian

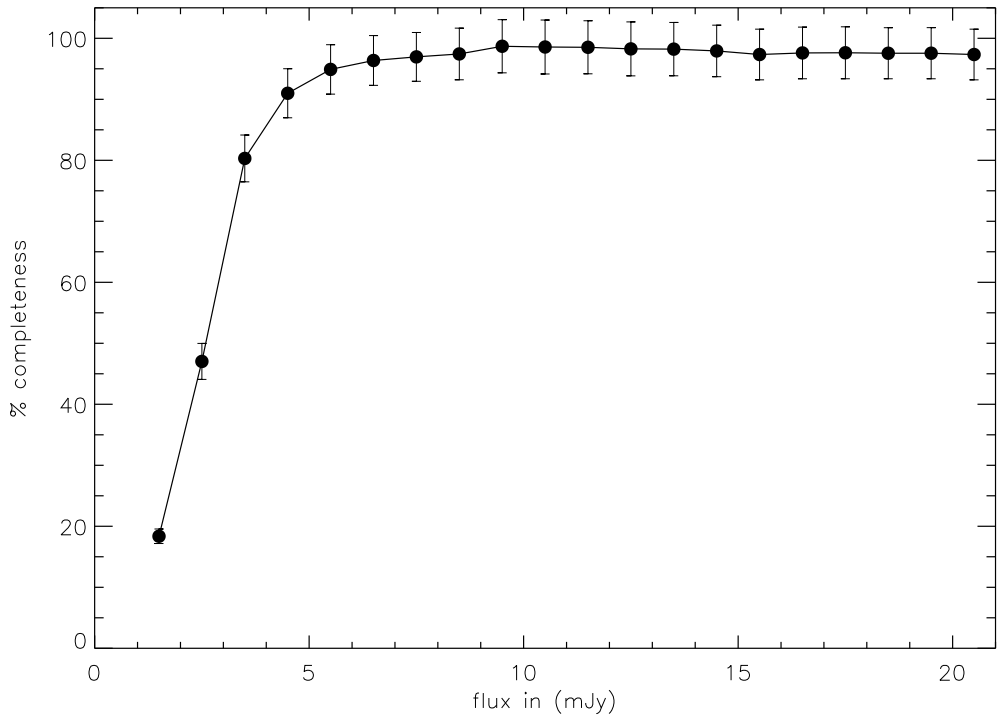

Figure 5.1: The percentage completeness plotted against flux density. Our catalogue is almost 100% complete at 9 mJy, and 50% complete at ~2.5 mJy.

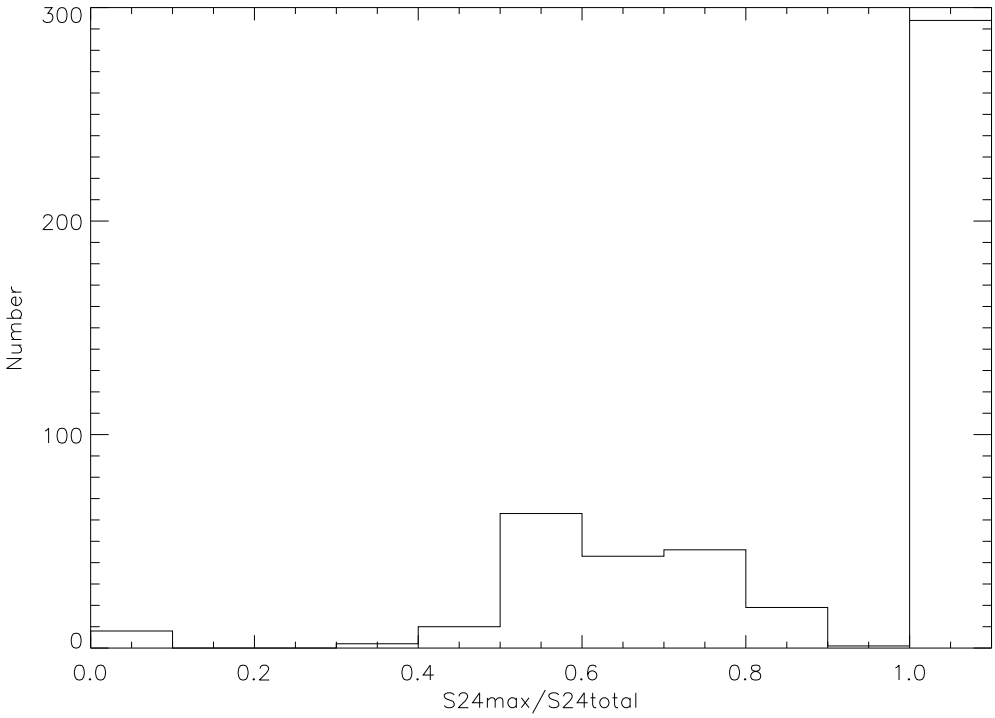

Figure 5.2: Histogram of the ratio of the maximum 24 μm flux density over the total 24 μm flux density within a 9″ radius. Sources with a ratio less than 0.8 were deemed deblend candidates.

fits, constraining the centres of the Gaussians to the 24 μm positions. We visually inspected all the deblend candidates and a small number of these clearly did not require deblending as the secondary 24 μm source was right on the edge of the 9 arcsecond radius with which we computed the deblend criteria, and were subsequently discarded as deblend candidates. In total, 143 sources were deblended resulting in a total catalogue of 658 putative sources. In the course of the visual inspection, we identified 41 spurious sources. 30 of these were sources that were faint (<4 σ) in the 70 μm catalogue, and did not have 24 μm counterparts, and 11 were clearly part of the Airy ring of an adjacent, bright source. This resulted in a final catalogue containing 617 70 μm sources.

Assuming Gaussian statistics, noise spikes are expected to produce approximately 34 spurious sources above our 3-sigma cutoff in the 70 μm data, and approximately 7 spurious sources above our 4-sigma cutoff in the 24 μm data. The probability of any spurious 70 μm source lying within a 9 arcsec radius of any spurious 24 μm source is approximately 2%, and so we conclude that none of the 617 sources is likely to be spurious.

We note that after deblending the 70 μm catalogue we increased the number of faint sources, which changes the completeness levels. While we have improved our completeness at the fainter flux density levels, this change cannot easily be quantified.

This catalogue of 617 70 μm sources was matched to the 24 μm catalogue using a matching radius of 4''. Following Huynh et al. (2008), the matching radius was determined by plotting the number of candidate matches against position offset (Figure 5.3). The matches from chance alone are determined from the source densities of the catalogues. Although Figure 5.3 suggests that a greater number of matches would be obtained using a matching radius of 8'', we choose the more conservative 4'' as our matching radius to minimise spurious matches.

Given the relative sensitivities of the 70 μm and 24 μm data it is expected that most, if not all the 70 μm sources will have a 24 μm counterpart. A small number (10) of strong 70 μm sources did not have 24 μm counterparts in the catalogues, while the 24 μm image showed faint detections. We therefore performed aperture photometry on these faint sources and successfully extracted eight. The final catalogue has only two 70 μm sources without 24 μm counterparts but neither of these have extreme S70/S24 ratios.

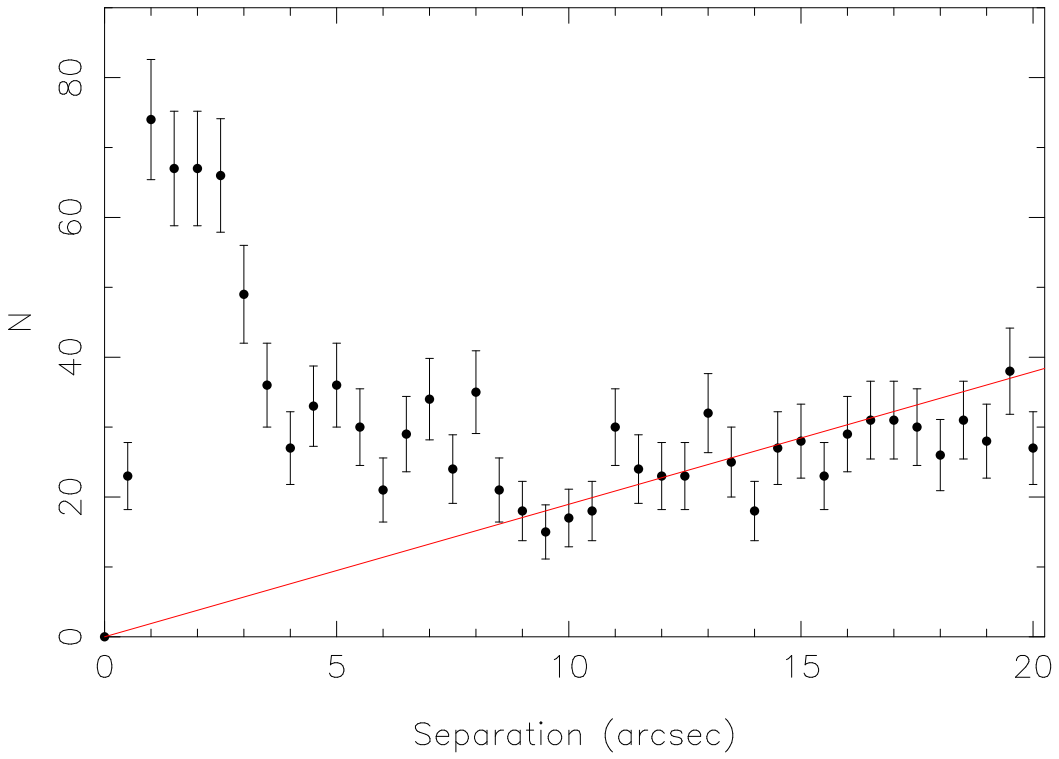

Figure 5.3: Number of candidate 24 μm counterparts of 70 μm sources as a function of position offset. The line shows the number of matches from chance alone.

5.3.2 Radio, Optical and X-ray Counterparts

Radio Counterparts

The 70 μm catalogue was matched to the radio catalogue of Miller et al. (2008), hereafter M08, using a matching radius of 5″. The matching radius was determined in a similar manner to that described in the previous section. Where available, the 24 μm position was used because the higher resolution at 24 μm allows for better positional accuracy. This resulted in 171 radio sources matched to the 70 μm catalogue.

The M08 radio catalogue has a 7 sigma cutoff. In order to increase the number of radio counterparts, and given that we have the additional information of the 70 μm sources, we extracted radio sources at the known 70 μm source positions that had radio detections greater than 3 sigma. This was done by performing Gaussian fits twice, first with a fixed size (2.8″ x 1.6″ - the beam of M08 data), and then without a fixed size. The relationship between peak and integrated flux densities was determined by:

$$\frac{S_{int}}{S_{peak}} = \frac{\theta_{maj}\theta_{min}}{b_{maj}b_{min}}, \tag{5.1}$$

where S_{int} is the total integrated flux density, S_{peak} is the peak flux density, θ_{maj} is the semi-major axis of the free Gaussian, θ_{min} is the semi-minor axis of the free Gaussian, b_{maj} is the semi-major axis of the fixed Gaussian, and b_{min} is the semi-minor axis of the fixed Gaussian.

If S_{int}/S_{peak} was less than 1.2, the source was determined to be unresolved and the peak flux density for the fixed Gaussian was determined to be the final flux density. If the ratio was greater than 1.2, the source was determined to be extended, and the integrated flux density was taken to be the final radio flux density. This resulted in 353 70 μm sources with radio counterparts.

In summary, our final 70 μm catalogue contains 617 sources, 615 of which have a 24 μm counterpart. 353 of these have a radio detection greater than 3 sigma from Miller et al. (2008). Figure 5.4 shows the histogram of the 70 μm flux densities. We also overplot the population of sources with and without radio counterparts. Sources with no radio counterparts have a median 70 μm flux density of 3.3 mJy while sources with radio counterparts have a median 70 μm flux density of 5.2 mJy.

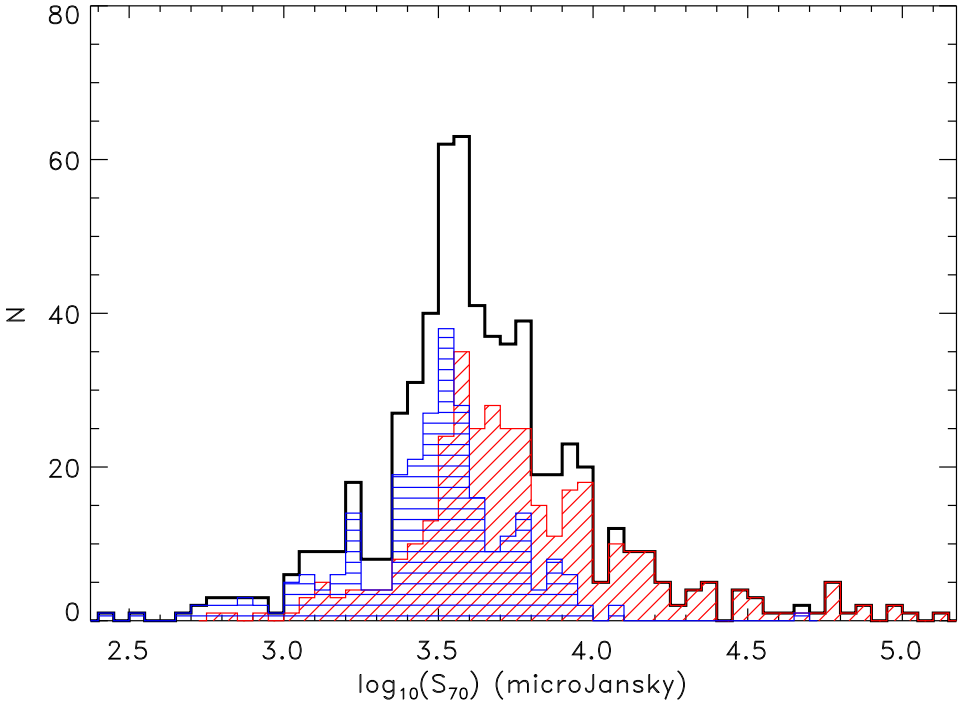

Figure 5.4: Histogram of 70 μm flux densities. The black line is the histogram for all 617 sources, while the red diagonally shaded histogram shows the 353 sources that have a radio detection and the blue horizontally shaded histogram shows the 264 sources that do not have a radio detection.

Table 5.1: Table of redshift catalogues. Column 1 names the catalogue while Column 2 gives the matching radius which was used to match the redshift data to the 70 μm data. Columns 3 and 4 give the catalogue size and whether the redshift data is photometric or spectroscopic and Columns 5 and 6 give the total number of sources that are matched to the 70 μm data as well as the number that are in the final catalogue. Column 7 gives the reference for the catalogue. There are 562 sources with redshifts, of which 206 are spectroscopic.

Catalogue	Radius (arcsec)	Spec/Phot	Size	$N_{matched}$	N_{final}	Reference
COMBO-17	2	phot	62337	555	122	Wolf et al. (2004)
MUSYC	1.5	phot	59693	410	234	Cardamone et al. (2010)
MUSYC	1.5	spec	2551	114	26	Cardamone et al. (2010)
GOODS	2	spec	7332 (5528)	160	148	Balestra et al. (2010)
ATLAS	5	spec	254	32	32	Mao et al. (2009b)

Redshift Data and Infrared Luminosities

The final 70 μm catalogue was matched to the various redshift catalogues using the matching radii shown in Table 5.1. Due to the better resolution of the radio data we used radio positions where available, followed by 24 μm positions where available to match to the redshift catalogues.

Where possible we matched spectroscopic redshifts to the sources. Where more than one spectroscopic redshift was available, we chose to prioritise ATLAS spectroscopic redshifts over GOODS spectroscopic data as we have access to the ATLAS spectra. The difference in redshift, Δz, was <0.0015 for the 12 sources in common.

Where no spectroscopic data were available we used photometric redshifts. Where both COMBO-17 and MUSYC photometric redshifts were available we chose to prioritize MUSYC data over COMBO-17 because MUSYC's photometric redshifts are derived from 32 bands as opposed to COMBO-17, which uses 17. Furthermore, MUSYC has photometric data extending into the near-infrared (JHK), which improves the accuracy of the photometric redshift.

In summary, 562 of the 617 (91%) 70 μm sources have redshift information, 206 (33%) of which are spectroscopic (Figure 5.5).

The total infrared luminosity (8 – 1000 μm) of the sources in our sample was estimated by fitting the 24 μm and 70 μm flux density to the SED templates of Chary and Elbaz (2001), hereafter CE01, while letting the templates scale in luminosity. The CE01 templates show observed 24 μm/70 μm flux density ratios which are more representative of $z \sim 1$ galaxies than Dale and Helou (2002) or Lagache et al. (2003) templates. Magnelli et al. (2009) found that 70 μm data

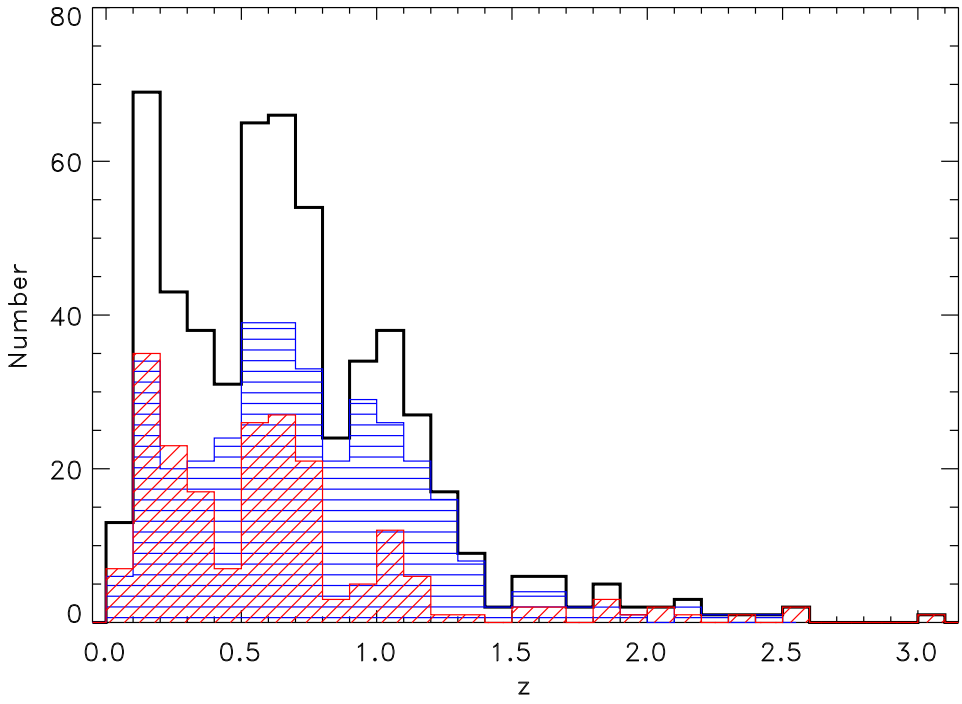

Figure 5.5: Histogram of all 562 sources that have redshift information. The black line is the histogram for all sources that have redshift information while the red diagonally shaded histogram shows sources with spectroscopic redshifts and the blue horizontally shaded histogram shows sources with photometric redshifts.

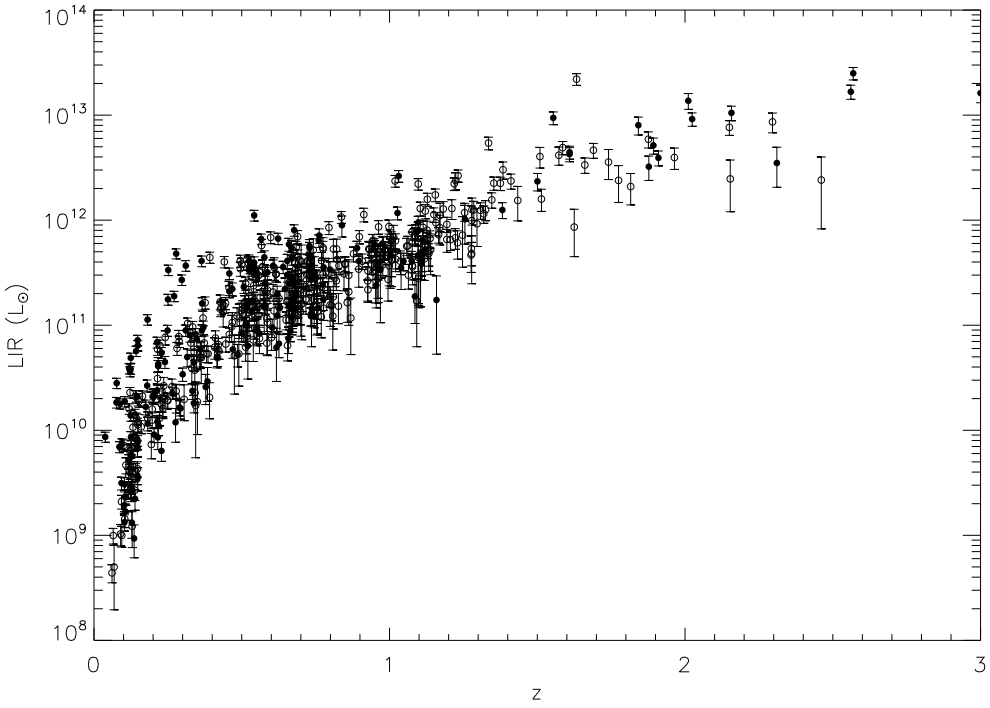

Figure 5.6: The total IR luminosity (8 – 1000 μm) as a function of redshift for all IR sources with redshift information (562/617). Sources with spectroscopic redshifts are shown with filled circles while sources with photometric redshifts are shown with open circles.

seems to provide an estimate of L_{IR} that is nearly independent of the SED library used, but this is partly because 70 μm is close to the peak emission, and therefore carries the largest fraction of FIR power.

We integrate the best fit template over 8 – 1000 μm to derive the total IR luminosity (L_{IR}) (Figure 5.6). We find luminous IR galaxies (LIRGs, $10^{11} L_{\odot} < L_{IR} < 10^{12} L_{\odot}$) are detected out to $z \sim 1.25$, while ultraluminous IR galaxies (ULIRGs, $L_{IR} > 10^{12} L_{\odot}$) are detected out to $z = 3$.

X-ray Counterparts

Using the 2Ms Chandra data (Luo et al. 2008), we find 55 of the 70 μm sources are within 2 arcseconds of an X-ray source. We use this data to calculate the hardness ratio so as to discriminate against AGN (Section 5.4.1).

5.4 Results and Analysis

We define q_{IR} as

$$q_{IR} = \log_{10}(\frac{S_{IR}}{S_{radio}}), \tag{5.2}$$

where S_{IR} is the observed infrared flux density at the specified IR wavelength (e.g. 70 μm), and S_{radio} is the observed flux density at 1.4 GHz.

5.4.1 AGN identification

We wish to study the FRC of predominantly star-forming galaxies and so we removed galaxies from our sample if they satisfied any of the following four criteria which indicate AGN.

1. The source has a radio morphology that displays the classic double-lobed AGN morphlogy. Figure 5.7 shows the three sources that were identified and subsequently removed from our sample.

2. The source has log(S70/S24) < 0.5, because AGNs are expected to have low S70/S24 ratios (Frayer et al. 2006). 22 sources were identified as AGN in this way. Figure 5.8 shows the log of the ratio of 70 μm flux density over 24 μm flux density, plotted against redshift.

3. The source has a hardness ratio > 0.2 based on the 2Ms Chandra data (Luo et al. 2008), where hardness ratio is defined as:

$$HR = \frac{S_{hard} - S_{soft}}{S_{hard} + S_{soft}}, \tag{5.3}$$

   where HR is the hardness ratio, S_{hard} is the flux density of the 2 - 8 keV band, S_{soft} is the flux density of the 0.5 - 2.0 keV band (Rosati et al. 2002). 14 sources were identified as AGN in this way.

4. The source has a soft X-ray (0.5-2 keV) to R-band flux density ratio of greater than one, as used by Luo et al. (2008) to classify AGN. 14 sources were identified as AGN in this way.

Low q_{70} and q_{24} values may also be used to discriminate against AGN (e.g. Middelberg et al. 2008). However, doing so could potentially bias our results

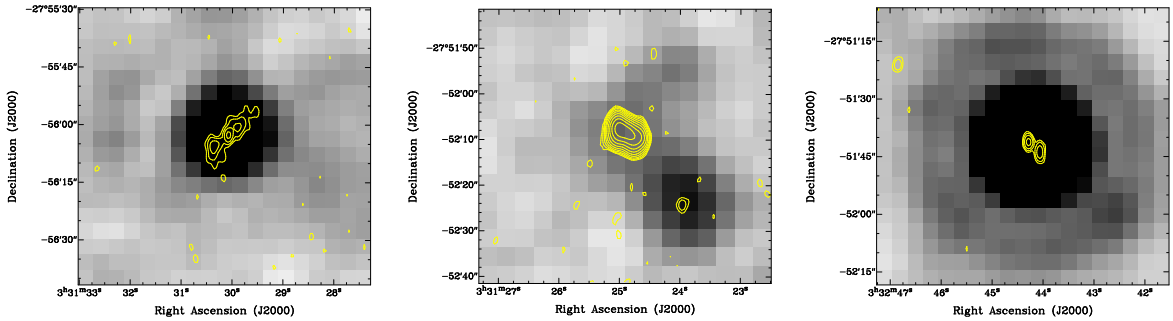

Figure 5.7: Sources which we classified as AGN based on radio morphology. The greyscale image is the 70 μm image and contours are the 1.4 GHz image starting at 24 μJy (~3 times the rms) and increasing by factors of 2.

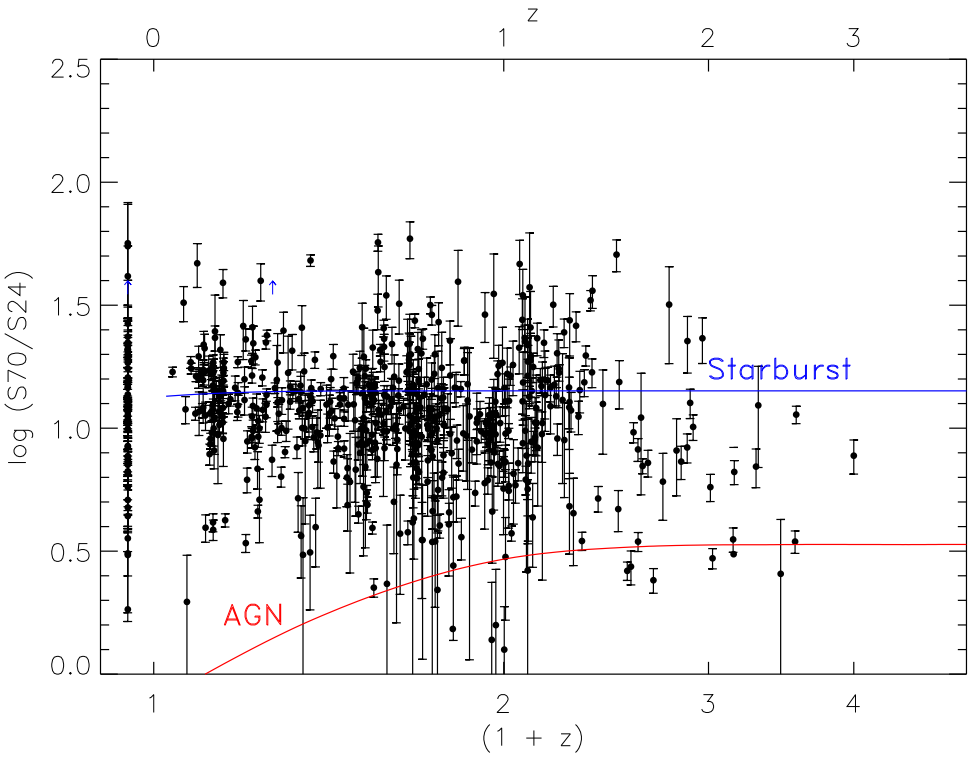

Figure 5.8: The ratio of 70 μm flux density over 24 μm flux density plotted against redshift. Sources with no redshift information are shown at an artificial redshift of -0.05. The blue line represents a simple modified blackbody SED model for starbursts with a dust temperature of 30K with a mid-infrared slope of α = 2.4, while the red line represents a model for AGNs with a dust temperature of 90K with a mid-infrared slope of 1.1 (Frayer et al. 2006). Error bars are derived by combining in quadrature the standard errors in radio and IR flux densities.

against low values of q. Applying these criteria removed only a further five AGN from our sample and we found made a negligible difference to our results, so we do not use these criteria here.

In total, 44 (~7%) sources were classified as AGN and subsequently removed from further analysis, leaving us with a final catalogue of 573 70 μm sources. Most of the sources were identified as AGN based on only one of the above four diagnostics, highlighting the need for multiple AGN diagnostics. There were only six sources that were identified as AGN by both the X-ray diagnostics. 41/44 of the sources identified as AGN had redshift information. The median redshift of the AGNs is 0.969, slightly higher than the median redshift of the entire sample (0.655). The median L_{IR} of the AGNs is 5.10×10^{11} $L_{\odot}$, also higher than the median L_{IR} of the entire sample (2.07×10^{11} $L_{\odot}$). The AGN tend to be at higher redshifts and higher L_{IR} due to Malmquist bias.

5.4.2 q_{70}

To explore how the FRC, as probed by the observed 70 μm band, changes with redshift, we plot q_{70} against redshift in Figure 5.9. Our data are plotted in black and lower limits of q_{70} from the radio non-detections are plotted as blue arrows. The lower limits are calculated by choosing the upper limit to the radio flux density for the radio non-detections to be 3 × rms. Data from the Spitzer Extragalactic First Look Survey (xFLS, Appleton et al. 2004) are plotted as red open circles. It is immediately evident that our data contain many more high redshift ($z > 1$) sources than the xFLS data. Appleton et al. (2004) found a q_{70} value of 2.15 ± 0.16 for their sample. The data points that are at low q_{70} values are likely to be AGN.

We also overplot the expected q_{70} ratio as a function of redshift from IR SED templates of Dale and Helou (2002) (DH02) and Chary and Elbaz (2001) (CE01). The CE01 SED templates are obtained from low-redshift galaxies with appropriate luminosities. We use four CE01 templates which range in L_{IR} from 10^9 (normal galaxy) to 10^{13} $L_{\odot}$ (ULIRGs). The DH02 SED templates are derived from combining theoretical SEDs from dust emission of individual regions within a galaxy. We use four DH02 templates with α= 1, 1.5, 2 and 2.5, where α represents the relative contributions of the different dust emission SEDs. The overplotted q_{70} tracks are derived using the IR SED templates, while the radio flux density is derived from the infrared flux density assuming both thermal and non-thermal components and a constant value of q.

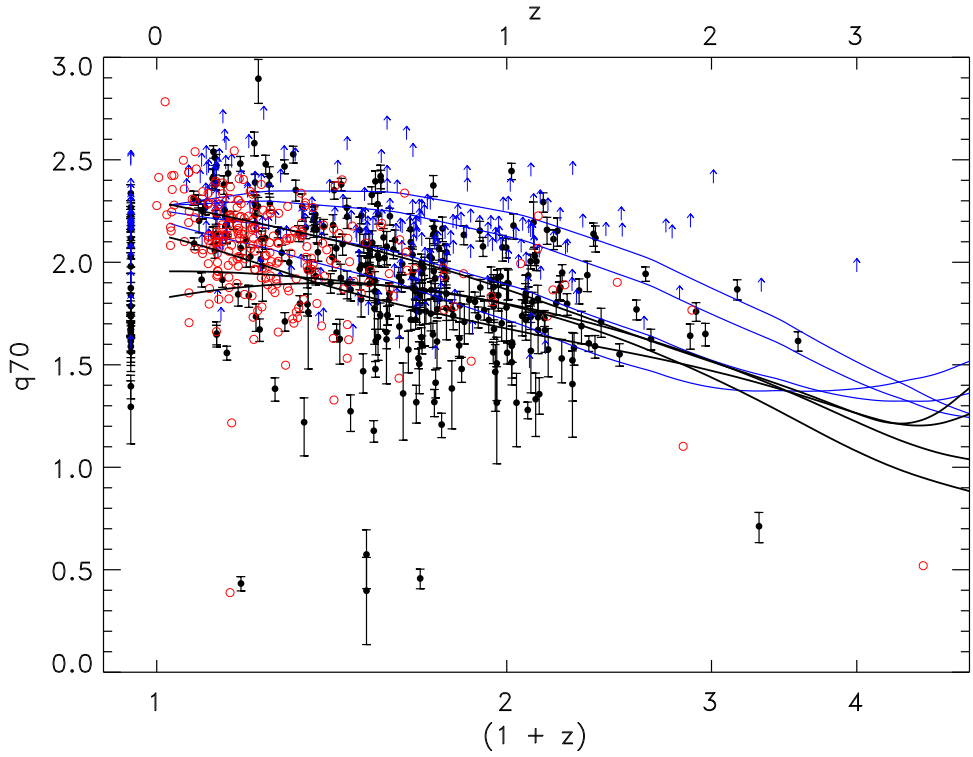

Figure 5.9: The 70 μm FIR-radio correlation plotted against redshift. The black points are sources that have both 70 μm and 1.4 GHz detections while the blue arrows show the lower limit of q_{70} for sources with no radio detection. The red open circles are data from xFLS (Appleton et al. 2004). The black lines are expected q_{70} tracks derived from SED templates for galaxies with total infrared luminosities of 10^9 (normal galaxies), 10^{11}, 10^{12} and $10^{13} L_{\odot}$ (ULIRGs) going from bottom to top, from Chary and Elbaz (2001) and the blue lines are q_{70} tracks derived from SED templates from Dale and Helou (2002). Sources with no redshift information are shown at an artificial redshift of -0.05. Error bars are derived by combining in quadrature the standard errors in radio and IR fluxes.

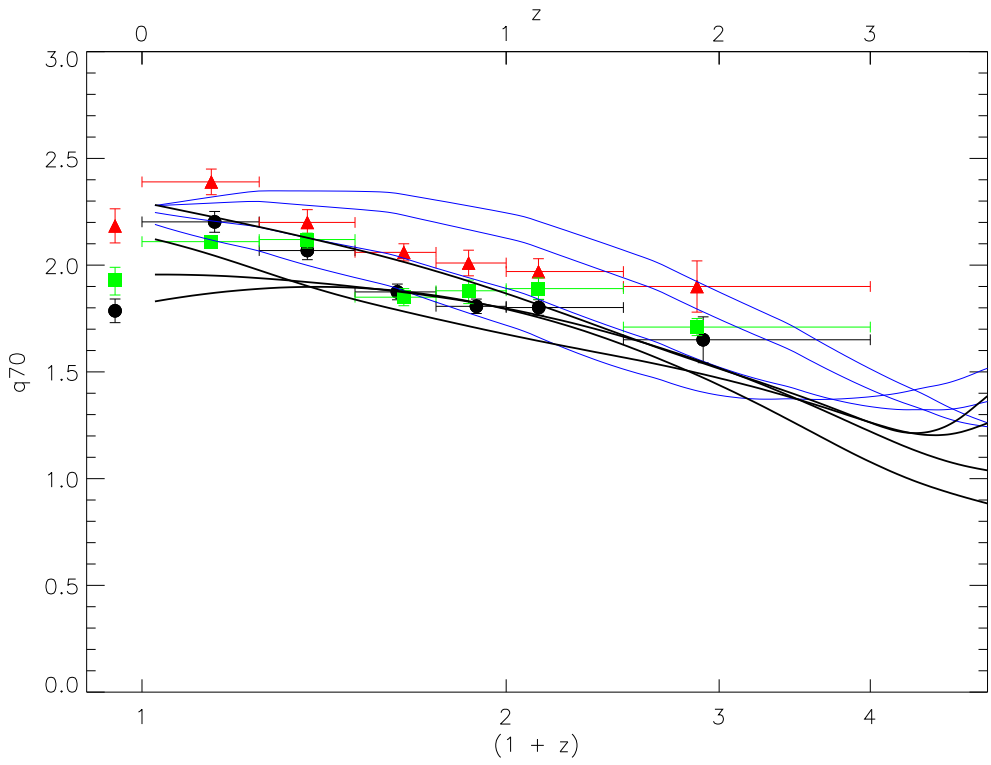

Figure 5.10: Median q values for different redshift bins. The black circles show the median q_{70} values for sources with both 70 μm and 1.4 GHz detections, the red triangles show the median q_{70} value for all sources taking into account the lower limits using survival analysis and the green squares show the median q_{70} value after stacking. The tracks derived from the SED templates are the same as in Figure 5.9. Vertical error bars denote standard errors and horizontal error bars indicate the range of the redshift bin.

In order to quantify the evolution of q_{70}, we binned all data with both 70 μm and radio detections in redshift and determined the median q_{70} in each redshift bin. The results are shown in Table 5.2 as well as in the black points of Figure 5.10. We calculate a median q_{70} of 2.16 ± 0.03 out to $z = 0.5$, which is in agreement with Appleton et al. (2004), as well as other previous studies (e.g., Seymour et al. 2009). Sources with no redshift information have a mean q_{70} ratio similar to $z \sim 1$ sources.

Figure 5.10 shows no evidence for evolution in the FIR-radio correlation because the data points are consistent with the overplotted q_{70} tracks. At $z > 1.25$ we are detecting only ULIRGs (see Figure 5.6), and this is reflected in the higher median q_{70} values, which are better traced by the q_{70} track derived from the ULIRG SED template.

Table 5.2: Median q_{70} for different redshift bins for only sources with both 70um and radio detections, and are not classed as AGN. There are a total of 323 sources.

z	median z	$N_{sources}$	median q_{70}
$0 \leq z < 0.25$	0.148	53	2.20 ± 0.05
$0.25 \leq z < 0.50$	0.370	46	2.07 ± 0.04
$0.50 \leq z < 0.75$	0.626	93	1.87 ± 0.04
$0.75 \leq z < 1.00$	0.890	43	1.81 ± 0.03
$1.00 \leq z < 1.50$	1.13	52	1.80 ± 0.04
$z \geq 1.50$	1.91	10	1.65 ± 0.11
no redshift		26	1.79 ± 0.06

5.4.3 Survival Analysis

Our 70 μm selected sample has sources with both 70 μm and 1.4 GHz detections, as well as sources that do not have 1.4 GHz detections. To study the full IR sample, we have to include radio non-detections. As we know the rms of the 1.4 GHz data we can estimate an upper limit to the radio flux density, which translates to a lower limit for q_{70}. We choose the upper limit to the radio flux density for the radio non-detections to be 3 $\times$ rms. One method of including limits from non-detections is using a branch of statistics called survival analysis. Survival analysis is an extensive field of statistics and was first applied to astronomy by Feigelson and Nelson (1985). We perform survival analysis on our data using the ASURV (Astronomical SURVival analysis) package developed by Lavalley et al. (1992).

We took the 50^{th} percentile of the Kaplan-Meier estimator to obtain a median q_{70} value for each redshift bin. The results are shown in Table 5.3, as well as in Figure 5.10. The two highest redshift bins appear to have higher median q_{70} values, but this is because at $z > 1.25$ we are detecting only ULIRGs, and hence these two points lie along the most actively star-forming, or ULIRG track.

Our q_{70} values appear to agree, within the errors, to the q_{70} tracks derived from the empirical SED templates from the local Universe. This is evidence for little, if any evolution in q_{70}, which implies that galaxies at high redshifts ($z \sim 2.5$) share many of the same properties as galaxies in the local Universe.

Table 5.3: Median q_{70} for different redshift bins, calculated using survival analysis, for all 70um sources that are not classed as AGN. Survival analysis was performed for radio flux density limits of 3 × rms. The range of values given for the q_{70} values derived from model SED templates of DH02 are for $\alpha = 2.5$ (first value) and $\alpha = 1$. The range of values given for the model q_{70} values derived from SED templates of CE01 are for normal galaxies and ULIRGs. There are a total of 573 sources.

z	median z	$N_{sources}$	median q_{70} (3σ)	q_{70} (DH02)	q_{70} (CE01)
$0 \leq z < 0.25$	0.141	107	2.39 ± 0.06	2.11 - 2.32	1.87 - 2.22
$0.25 \leq z < 0.50$	0.370	80	2.20 ± 0.06	2.00 - 2.35	1.90 - 2.13
$0.50 \leq z < 0.75$	0.646	154	2.06 ± 0.04	1.88 - 2.33	1.88 - 2.01
$0.75 \leq z < 1.00$	0.862	75	2.01 ± 0.06	1.77 - 2.28	1.83 - 1.92
$1.00 \leq z < 1.50$	1.13	85	1.97 ± 0.06	1.66 - 2.20	1.75 - 1.81
$z \geq 1.50$	1.88	20	1.90 ± 0.12	1.41 - 1.92	1.48 - 1.55
no redshift		52	2.18 ± 0.08		

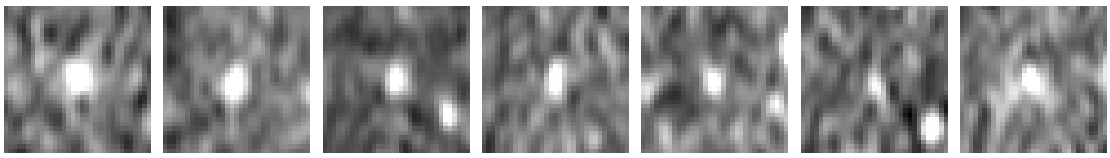

Figure 5.11: Postage stamps of the radio stacks of the IR sources, for the redshift bins as shown. The stacks are 16 × 16 arcsec in size. There is a significant radio detection at the centre of the stack in all of the redshift bins. The measured flux densities are reported in Table 5.4.

5.4.4 Stacking

To extend the results we performed a stacking analysis of the IR sources by stacking the radio sources in bins of redshift. We started by stacking the M08 radio data at the positions of all sources not detected in the radio image, using a noise-weighted mean, for which the noise was determined from the radio image in the vicinity of the IR source. The stacked radio flux density was then obtained from a Gaussian fit to the signal at the centre of the radio stack, leaving all Gaussian parameters unconstrained. The resulting stacks are shown in Figure 5.11, and each has a significant detection.

To derive an average q_{70} for all IR sources in the various redshift bins (green

Table 5.4: Summary of radio stacking results of IR sources. N_{det} is the number of IR sources in each bin which are detected in the radio image. N_{stack} is the number of IR sources not detected in the radio image and therefore the number stacked in this analysis, resulting in the stacked $S_{1.4GHz}$ listed in column 5. Average q_{70} is the FIR-radio flux density ratio for all IR sources in the redshift bin, obtained by combining the detections with the stacked results.

z	median z	N_{det}	N_{stack}	stacked $S_{1.4GHz}$ (μJy)	average q_{70}
$0 \leq z < 0.25$	0.141	53	54	27.7 ± 2.8	$2.11^{+0.02}_{-0.03}$
$0.25 \leq z < 0.50$	0.370	46	34	25.4 ± 1.9	$2.12^{+0.03}_{-0.04}$
$0.50 \leq z < 0.75$	0.646	93	61	19.7 ± 1.5	$1.85^{+0.04}_{-0.04}$
$0.75 \leq z < 1.00$	0.862	43	32	18.9 ± 1.6	$1.88^{+0.05}_{-0.06}$
$1.00 \leq z < 1.50$	1.13	52	33	13.6 ± 0.9	$1.89^{+0.05}_{-0.05}$
$z \geq 1.50$	1.88	10	10	19.5 ± 2.5	$1.71^{+0.04}_{-0.04}$
no redshift		26	26	46.8 ± 9.4	$1.93^{+0.06}_{-0.07}$

points in Figure 5.10), we calculated a mean by adding the flux densities of the detected sources to the stacked flux density. Each was added with a weight =1/n (where n is the total number of measurements, including both stacked and detected images) and the stacked flux density was weighted by m/n where m is the number of stacked images. The results are summarised in Table 5.4. The higher redshift bins have higher q values when compared to the survival analysis results because stacking analysis imposes lower limits on the radio flux densities. As before, the FIR-radio flux density ratios appear to follow the ratios expected for local SEDs and hence we find little evolution in the FIR-radio correlation as a function of time.

5.4.5 q_{TIR}

We computed the ratio of total infrared luminosity over rest frame radio luminosity to compare our results from Sections 5.4.2 to 5.4.4. Furthermore, this allows us to make direct comparisons with other studies that compute the FRC in this way.

We computed q_{TIR} for all 521 sources that had redshift information (and were not identified as AGN) using:

$$q_{TIR} = \log(\frac{L_{IR}}{3.75 \times 10^{12}\mathrm{W}}) - \log(\frac{L_{1.4GHz}}{\mathrm{WHz}^{-1}}), \tag{5.4}$$

Table 5.5: Median q_{TIR} for different redshift bins for only sources with both 70 μm and radio detections, and are not classed as AGN. There are a total of 297 sources.

z	median z	$N_{sources}$	median q_{TIR}
$0 \leq z < 0.25$	0.148	53	2.54 ± 0.05
$0.25 \leq z < 0.50$	0.370	46	2.52 ± 0.04
$0.50 \leq z < 0.75$	0.626	93	2.41 ± 0.03
$0.75 \leq z < 1.00$	0.890	43	2.35 ± 0.04
$1.00 \leq z < 1.50$	1.13	52	2.33 ± 0.03
$z \geq 1.50$	1.91	10	2.52 ± 0.11

Table 5.6: Median q_{TIR} for different redshift bins, calculated using survival analysis, for all 70 μm sources that are not classed as AGN. Survival analysis was performed using $L_{1.4GHz}$ calculated from radio flux density limits of 3 $\times$ rms. There are a total of 521 sources.

z	median z	$N_{sources}$	median q_{TIR} (3σ)
$0 \leq z < 0.25$	0.141	107	2.74 ± 0.06
$0.25 \leq z < 0.50$	0.370	80	2.70 ± 0.06
$0.50 \leq z < 0.75$	0.646	154	2.60 ± 0.04
$0.75 \leq z < 1.00$	0.862	75	2.53 ± 0.06
$1.00 \leq z < 1.50$	1.13	85	2.55 ± 0.06
$z \geq 1.50$	1.88	20	2.75 ± 0.12

where L_{IR} is the total infrared luminosity (Section 5.3.2), and $L_{1.4GHz}$ is the rest-frame 1.4 GHz luminosity. In order to account for k-correction in the radio, we set the spectral index, α, to 0.8[1], following the work of Ibar et al. (2010) and Sargent et al. (2010b).

Figure 5.12 shows the distribution of q_{TIR} as a function of redshift. For sources without a radio detection we set an upper limit to the radio flux density of 3 × rms. Similar to Figure 5.9, sources without a radio detection (ie. lower limits) tend to have higher q_{TIR} when compared to sources with a radio detection. In order to take into account the effect of the radio non-detections, we bin our data in redshift and perform survival analysis. Figure 5.13 shows the median q_{TIR} for only the detected sources (black circles), and for all sources by using survival analysis (red triangles). We have included results from previous studies in Figure 5.13. The blue star at $z = 0$ is at $q_{TIR} = 2.64$, the mean q_{TIR} found by Bell (2003). The open upside-down triangles are q_{TIR} derived from stacking analyses by Bourne et al. (2011) and the open squares are the "uncorrected" q_{TIR} for star-forming galaxies, from Sargent et al. (2010b) (See Section 5.4.5 for a discussion on the Kellermann Correction).

Our q_{TIR} values are all within ~0.22 of each other. Our values agree, within the errors, with the work of Sargent et al. (2010b), and also agree with the work of Bourne et al. (2011), with the exception of the redshift bins 0.75 < z <1 and z > 1.5, where our values differ by <2σ compared to the values given by Bourne et al. (2011) for similar redshift ranges. Sargent et al. (2010b) use 3 × rms to determine the upper limit of the radio flux density for their dataset. Unlike the work by Bourne et al. (2011) and Sargent et al. (2010b), our q_{TIR} values do not consistently increase or decrease over the redshift range studied, although we do see marginally significant evidence for a decreasing q_{TIR} over the redshift range 0 to 1.5, followed by an increase from 1.5 to 3. However, Figure 5.13 shows that the data points that use survival analysis (which are more reliable than those that do not) are statistically consistent with a horizontal line at about $q_{TIR} = 2.62$, and so we conclude that these apparent variations of q_{TIR} with redshift may not be statistically significant.

Bourne et al. (2011) find their q_{TIR} values are systematically higher than the median q_{TIR} found by Bell (2003) of 2.64 ± 0.02, except at $z > 1$ where it appears to decline. They suggest the apparent decline may be attributed to the assumptions they make about spectral indices. Sargent et al. (2010b) find that their q_{TIR}

[1] $S_\nu \propto \nu^{-\alpha}$, where S_ν is the flux density at frequency ν.

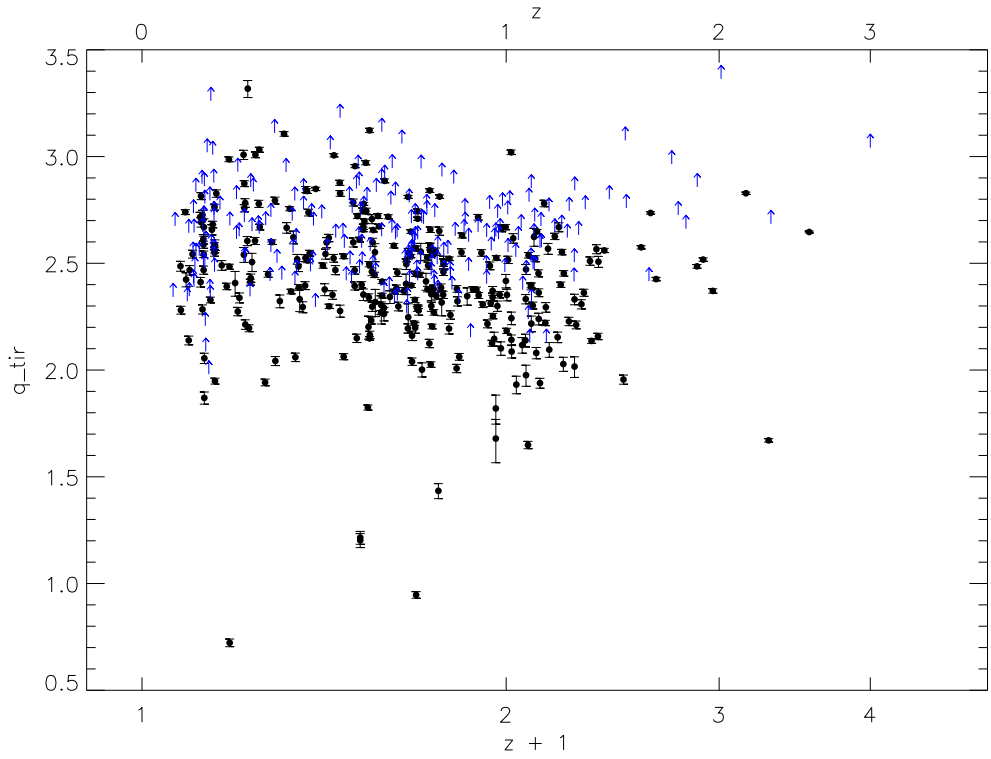

Figure 5.12: The total infrared luminosity FIR-radio correlation plotted against redshift. The same symbol and colour scheme is used as for Figure 5.9.

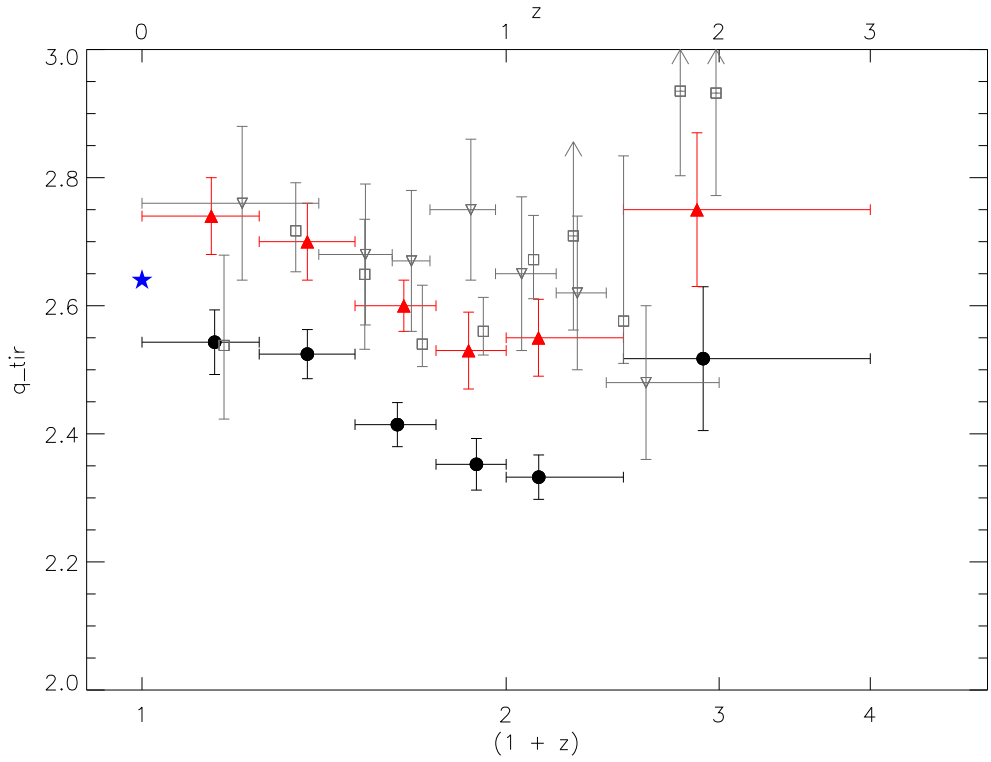

Figure 5.13: Median q_{TIR} values for different redshift bins. The black filled circles show the median q_{TIR} values for sources with both 70 μm and 1.4 GHz detections and the red triangles show the median q_{TIR} value for all sources taking into account the lower limits using survival analysis. The grey upside-down open triangles show the median q_{TIR} values derived by Bourne et al. (2011) and the grey open squares show the median q_{TIR} values derived by Sargent et al. (2010b) for star-forming galaxies. None of the data shown include the Kellermann correction (Section 5.4.5). Vertical error bars are standard errors for both our dataset and Bourne's data, but the vertical error bars for Sargent's data are upper and lower 95% confidence levels. The blue star at (1+z) = 1 represents the median q_{TIR}= 2.64 ± 0.02 from Bell (2003).

values are constant with redshift when they apply a correction (see Section 5.4.5), otherwise ∼0.3 dex of evolution is found. While Bourne et al. (2011) also uses FIDEL data in the ECDFS, their sample is IRAC selected whereas our sample is 70 μm selected. Sargent et al. (2010b) use a 24 μm selected sample to study the q_{TIR} in the COSMOS field.

There are a number of factors that may contribute to uncertainties in q_{TIR}. The predominant source of uncertainty is in the estimation of L_{IR} as we are fitting the 24 μm and 70 μm fluxes to SED templates. The uncertainty from the choice of model SEDs can add 0.2 to 0.3 dex (Magnelli et al. 2009; Le Floc'h et al. 2005). Uncertainties also arise from the rest-frame radio luminosity where we are assuming $\alpha = 0.8$.

Jarvis et al. (2010) suggest that the slight upturn in q_{IR} seen at low redshifts ($z < 0.5$) in high redshift studies of the FRC (e.g. Bourne et al. 2011) may be attributed to the resolving of extended structure, which means radio flux density would be missed and hence increase the FRC. Our radio data has a $2.8'' \times 1.6''$ beam, so if the Jarvis hypothesis is correct, we would expect to see this effect at low redshifts.

Although we see a slight upturn in q_{TIR} from $z = 1$ to $z = 0$, this increase has a roughly constant gradient, implying that resolution effects are important as high as $z = 1$. However, at $z = 1$ a typical star-forming galaxy of diameter 10 kpc is unresolved by our beam. Thus, the increasing q_{TIR} towards low redshifts is probably not due to this effect.

The Kellermann Correction

Kellermann (1964) showed that flux density ratios (such as q) or spectral indices of a flux density-limited sample are biased by a factor which depends sensitively on the scatter in the flux density ratio and on the source intensity distribution, and in particular on the power law index β of the differential source counts (i.e., $dN/dS \propto S^{-\beta}$). Other formulations of the same effect are given by Condon (1984), Francis (1993) and Lauer et al. (2007), and were first noted as being relevant to the evolution of q by Sargent et al. (2010a).

Sargent et al. (2010b) assume a Euclidean (β=2.5) source intensity distribution at $z < 1.4$ and a sub-Euclidean ($\beta \sim 1.5$) at $1.4 < z < 2$ to derive a correction of 0.22 in their value of q at $z > 1.4$. However we note that (a) the expression assumes a common value of β for both the radio and infrared source counts, and (b) the value of β is very uncertain at low flux densities. For example, the median radio

flux density for our detected sources at $z < 1.4$ is ~ 72 μJy, at which the radio source count power law index lies in the range $\sim$ 1.5 - 2.5 (e.g., Huynh et al. 2005), leading to a correction factor between 0.22 (the adopted value of Sargent, which gives no evolution of q with z) and 0.51 (which implies that q decreases with z with marginal significance).

Because of this uncertainty in the value of the Kellermann correction for faint sources such as those studied here and for consistency with other authors (e.g., Appleton et al. 2004; Seymour et al. 2009; Bourne et al. 2011), we do not apply it to our data but note that it is responsible for a further uncertainty in the slope of q as a function of redshift. The range of possible Kellermann corrections (which depend strongly on the assumed value of β) to the variation of q over our redshift range is roughly centred on zero, with a total spread of about $\pm$ 0.3.

5.5 Summary and Conclusions

We have studied the FRC out to $z > 2$ of ULIRGs in ECDFS. Our results for q_{70} showed that they could be broadly described by q_{70} tracks derived from the SED templates of Chary and Elbaz (2001) and Dale and Helou (2002). To quantify the evolution of q_{70} we binned our data in redshift and determined the median q_{70} using both survival analysis and a stacking analysis. Both survival analysis and the stacking analysis gave similar results. We see no clear evidence for evolution in the FRC at 70 μm.

We also calculate the FRC using L_{IR} and $L_{1.4GHz}$ and find that evolution in q_{TIR} is constrained within 0.22. Our calculated q_{TIR} appears slightly lower than previous studies but this may merely be due to uncertainties involved in calculating q_{TIR}. We also acknowledge the importance of the Kellermann correction but due to uncertainties in the value we do not apply it to our data.

A lack of evolution in the FRC is surprising because it implies that the myriad of effects on which the FRC rely must either also not evolve, or must evolve in such a way so as to preserve the FRC. Effects such as inverse Compton cooling of the electrons (Murphy 2009), evolution of the magnetic field strength, and evolution in the SEDs due to dust and metallicity changes should all affect the FRC.

We therefore conclude that either all these factors are insignificant at $z \sim 2$ or there is a complex interplay between these factors conspiring in the preservation of the FRC at high redshifts.

Early science results from *Herschel* have already hinted that the FRC shows no evidence for evolution to $z = 2$ (Jarvis et al. 2010; Ivison et al. 2010b). More results on the FRC from Herschel are expected over the next few years as observations are completed and the data analysed. *Herschel* will measure the far-infrared properties of normal galaxies to $z \sim 1$ and ULIRGs out to $z \sim 4$. Consequently, we will be able to study the FRC out to higher redshifts and hence gain a better understanding of the evolution of star-forming galaxies, especially in the high redshift Universe.

Acknowledgements

We wish to thank our anonymous referee whose insightful comments helped improve this paper. We wish to thank Neal Miller for providing the radio data. MYM was supported by the IPAC Visiting Graduate Research Fellowship Program for this work.

6

Summary and Conclusions

The discovery of galaxies beyond our own has led to a gamut of studies in extragalactic astronomy, with the formation and evolution of galaxies remaining one of the hottest topics in modern astronomy.

With the aim of imaging seven square degrees of sky to 10 μJy beam^{-1}, ATLAS is one of the widest deep radio surveys attempted to date. ATLAS pushes the limit of conventional telescopes in order to study how galaxies have formed and evolved since the Big Bang.

This thesis has presented work based on the optical spectroscopy of ATLAS radio sources.

- Chapters 1 and 2 set the scene for this thesis and summarised ATLAS including its science goals and current status.
- Chapter 3 presented the optical data that we obtained throughout the duration of my thesis, including redshifts and classifications based on the spectra. The cosmic evolution of radio sources was studied in detail and we have constructed the radio luminosity function for both star-forming galaxies and AGN.
- Chapter 4 presented six wide-angle tail galaxies in ATLAS. This work be-

gan as a side-project after our first year of optical observations was almost completely washed out. Armed with the knowledge that WATs tend to be associated with dynamical clusters of galaxies, we obtained service time[1] on the AAT using AAOmega to probe the environment surrounding the largest WAT in our sample.

- Chapter 5 presented an investigation into the far-infrared radio correlation and, despite the myriad of elements upon which the FRC is dependent, we found no evidence for its evolution to redshifts of ∼2.

6.1 ATLAS Spectroscopic Catalogue and RLFs

The ATLAS Spectroscopic Catalogue presents 466 new spectroscopic redshifts obtained using AAOmega on the AAT for radio sources in ATLAS. The catalogue includes spectroscopic classifications of the sources as either star-forming or AGN-driven. The spectroscopic classifications were performed by visual inspection and a sample of these were independently verified by at least one other collaborator. These spectroscopic classifications were compared to mid-infrared SF/AGN diagnostics and found to be in good agreement.

60% (282) of sources were classified as AGN, 30% (142) were found to be star-forming galaxies and we were not able to unambiguously classify 32 spectra. 10 radio sources appeared to have stellar spectra but these were found to be chance-alignments.

The RLF was constructed for ELAIS for both SF galaxies and AGN. We were unable to do this for CDFS due to the presence of artefacts in the DR1 radio image. The SF galaxy RLF is found to evolve to $z \sim 0.5$, with a higher number density of SF galaxies at higher redshifts. This is consistent with previous studies. The AGN RLF was less clear cut, and although consistent with work by Padovani et al. (2011), it appears inconsistent with work by others, such as Mauch and Sadler (2007).

We have demonstrated that by using ATLAS radio data with optical spectroscopy follow-up data from AAOmega, we were able to distinguish between AGN and star-forming galaxies, and construct the RLF for ELAIS. ATLAS DR3 has solved the artefact issue in CDFS so our future work will include constructing the RLF for CDFS thereby overcoming the cosmic variance problem we may

[1] The weather for the service observations was very good.

be facing having only constructed the RLF for ELAIS. Furthermore, as our optical observations suffered from poor weather conditions we were unable to achieve our target magnitude limit. Obtaining deeper optical spectroscopy, especially for DR3, will also occur in the near future.

This work has important value as it will provide the training set to guide algorithms that will be used to determine the redshift distribution for EMU and other next-generation radio surveys.

6.2 WATs in ATLAS

Wide-angle tail radio sources are associated with clusters of galaxies and are usually found near the centres of clusters that are undergoing mergers. We identified a sample of six WATs in ATLAS and all four that had sufficient data in their immediate vicinity showed evidence for residing in overdense environments.

The largest WAT in our sample is S1189 in ELAIS, which has a redshift of ~ 0.22. We obtained service time on AAOmega to investigate the environment of S1189 and found an overdensity of galaxies that is spread over $\sim 12\,\mathrm{Mpc}$. The overdensity has a velocity dispersion of $\sim 870\,\mathrm{km\ s^{-1}}$, consistent with rich clusters undergoing mergers in the local Universe. We conclude that the overdensity probably represents an unrelaxed system that may be undergoing a cluster-cluster merger. The true nature of the system could be probed using deep X-ray observations.

We also investigated the likelihood of using WATs to probe clusters at high redshifts and found that while inverse Compton cooling will reduce the apparent size of the emitting region, WATs should still be detectable at high redshifts if they exist. We estimate that up to 2×10^5 WATs may be detected in EMU. Given that each WAT is likely to be associated with a cluster, EMU will be invaluable for the detection of clusters.

6.3 The Far-Infrared Radio Correlation

The far-infrared correlation was discovered over 40 years ago and holds for a wide range of Hubble types over five orders of magnitude of bolometric luminosity. We studied the FRC of ULIRGs in ECDFS to $z > 2$ in order to determine if the FRC evolved with redshift.

Using both stacking analysis and survival analysis we find no clear evidence

for evolution in the FRC at 70 μm. This is surprising because the FRC relies on a number of effects including inverse Compton cooling of electrons and magnetic field strength. We concluded that these effects must either be insignificant over the redshift range we are looking at, or there is some complex interplay resulting in the apparent conspiracy to preserve the FRC.

Herschel will measure the far-infrared properties of ULIRGs to z $\sim$ 4 allowing the FRC to be probed to higher redshifts.

6.4 Legacy of ATLAS and future work

The work presented in this thesis is already being utilised by the EMU team to design the EMU Survey see Norris et al. (2011a) for more details). While EMU science could be greatly enhanced by redshift data, EMU expects to detect ~70 million radio sources, and obtaining spectroscopic redshifts for all of these would be impossible. Consequently, the EMU team (Salvato et al. in preparation) are investigating the possibility of using statistical redshifts. To optimise the accuracy of statistical redshifts, well-studied spectroscopic surveys are imperative. The ATLAS spectrocopic catalogue presented in this thesis is already being used by the EMU team as a training set to guide the statistical redshift algorithms. Furthermore, as demonstrated by this thesis, spectrosopic redshifts are imperative for many different studies.

With the release of ATLAS DR3 (Banfield et al. in preparation), many more radio sources will be detected in ATLAS. Proposals aiming to obtain spectrosopic redshifts for these sources have already been submitted. I intend to use the current data on hand, and DR3 data in the future, to produce a more in-depth investigation into discriminating between star-forming galaxies and AGN, making use of the deep ancillary data available (e.g. infrared from SWIRE and SERVS, X-ray data from Chandra). I shall also focus specifically on determining the relative contributions of star-formation and AGN in composite sources, of which we suspect there to be many. It is only with the advent of sensitive radio observations, such as ATLAS, that such studies have been made possible.

Although ATLAS radio observations have been completed and the project is drawing to a close, the legacy of ATLAS will remain strong. ATLAS is already acting as a pathfinder to EMU, which will use the ASKAP, heralding a new era of radio survey astronomy with the next-generation of radio telescopes.

He wasn't the first person to tread this path, but his steps had been a little firmer, his pace a little longer, than those who had passed this way before.

Ray Norris - Graven Images

Bibliography

J. Afonso, A. Georgakakis, C. Almeida, A. M. Hopkins, L. E. Cram, B. Mobasher, and M. Sullivan. The Phoenix Deep Survey: Spectroscopic Catalog. *ApJ*, 624: 135–154, May 2005.

A. Amblard, A. Cooray, P. Serra, P. Temi, E. Barton, M. Negrello, R. Auld, M. Baes, I. K. Baldry, S. Bamford, A. Blain, J. Bock, D. Bonfield, D. Burgarella, S. Buttiglione, E. Cameron, A. Cava, D. Clements, S. Croom, A. Dariush, G. de Zotti, S. Driver, J. Dunlop, L. Dunne, S. Dye, S. Eales, D. Frayer, J. Fritz, J. P. Gardner, J. Gonzalez-Nuevo, D. Herranz, D. Hill, A. Hopkins, D. H. Hughes, E. Ibar, R. J. Ivison, M. Jarvis, D. H. Jones, L. Kelvin, G. Lagache, L. Leeuw, J. Liske, M. Lopez-Caniego, J. Loveday, S. Maddox, M. Michałowski, P. Norberg, H. Parkinson, J. A. Peacock, C. Pearson, E. Pascale, M. Pohlen, C. Popescu, M. Prescott, A. Robotham, E. Rigby, G. Rodighiero, S. Samui, A. Sansom, D. Scott, S. Serjeant, R. Sharp, B. Sibthorpe, D. J. B. Smith, M. A. Thompson, R. Tuffs, I. Valtchanov, E. van Kampen, P. van der Werf, A. Verma, J. Vieira, and C. Vlahakis. Herschel-ATLAS: Dust temperature and redshift distribution of SPIRE and PACS detected sources using submillimetre colours. *A&A*, 518:L9, July 2010.

R. Antonucci. Unified models for active galactic nuclei and quasars. *ARA&A*, 31: 473–521, 1993.

P. N. Appleton, D. T. Fadda, F. R. Marleau, D. T. Frayer, G. Helou, J. J. Condon, P. I. Choi, L. Yan, M. Lacy, G. Wilson, L. Armus, S. C. Chapman, F. Fang, I. Heinrichson, M. Im, B. T. Jannuzi, L. J. Storrie-Lombardi, D. Shupe, B. T. Soifer, G. Squires, and H. I. Teplitz. The Far- and Mid-Infrared/Radio Correlations in the Spitzer Extragalactic First Look Survey. *ApJS*, 154:147–150, September 2004.

C. Auriemma, G. C. Perola, R. D. Ekers, R. Fanti, C. Lari, W. J. Jaffe, and M. H. Ulrich. A Determination of the Local Radio Luminosity Function of Elliptical Galaxies. *A&A*, 57:41, May 1977.

Y. Avni and J. N. Bahcall. On the simultaneous analysis of several complete samples - The V/Vmax and Ve/Va variables, with applications to quasars. *ApJ*, 235: 694–716, February 1980.

W. Baade and R. Minkowski. On the Identification of Radio Sources. *ApJ*, 119: 215, January 1954.

J. N. Bahcall, S. Kirhakos, D. H. Saxe, and D. P. Schneider. Hubble Space Telescope Images of a Sample of 20 Nearby Luminous Quasars. *ApJ*, 479:642, April 1997.

I. Balestra, V. Mainieri, P. Popesso, M. Dickinson, M. Nonino, P. Rosati, H. Teimoorinia, E. Vanzella, S. Cristiani, C. Cesarsky, R. A. E. Fosbury, H. Kuntschner, and A. Rettura. The Great Observatories Origins Deep Survey. VLT/VIMOS spectroscopy in the GOODS-south field: Part II. *A&A*, 512: A12, March 2010.

R. H. Becker, R. L. White, and D. J. Helfand. The FIRST Survey: Faint Images of the Radio Sky at Twenty Centimeters. *ApJ*, 450:559, September 1995.

S. V. W. Beckwith, M. Stiavelli, A. M. Koekemoer, J. A. R. Caldwell, H. C. Ferguson, R. Hook, R. A. Lucas, L. E. Bergeron, M. Corbin, S. Jogee, N. Panagia, M. Robberto, P. Royle, R. S. Somerville, and M. Sosey. The Hubble Ultra Deep Field. *AJ*, 132:1729–1755, November 2006.

E. F. Bell. Estimating Star Formation Rates from Infrared and Radio Luminosities: The Origin of the Radio-Infrared Correlation. *ApJ*, 586:794–813, April 2003.

A. S. Bennett. The revised 3C catalogue of radio sources. *MmRAS*, 68:163, 1962.

S. Berta, S. Rubele, A. Franceschini, E. V. Held, L. Rizzi, C. J. Lonsdale, T. H. Jarrett, G. Rodighiero, S. J. Oliver, J. E. Dias, H. J. Buttery, F. Fiore, F. La Franca, S. Puccetti, F. Fang, D. Shupe, J. Surace, and C. Gruppioni. The ESO-Spitzer Imaging extragalactic Survey (ESIS). I. WFIB, V, R deep observations of ELAIS-S1 and comparison to Spitzer and GALEX data. *A&A*, 451:881–900, June 2006.

P. N. Best and T. M. Heckman. On the fundamental dichotomy in the local radio-AGN population: accretion, evolution and host galaxy properties. *MNRAS*, 421:1569–1582, April 2012.

P. N. Best, G. Kauffmann, T. M. Heckman, J. Brinchmann, S. Charlot, Ž. Ivezić, and S. D. M. White. The host galaxies of radio-loud active galactic nuclei: mass dependences, gas cooling and active galactic nuclei feedback. *MNRAS*, 362: 25–40, September 2005.

R. J. Beswick, T. W. B. Muxlow, H. Thrall, and A. M. S. Richards. Sub-arcsecond, microJansky Radio Properties of Spitzer Identified Mid-infrared Sources in the HDF-N/GOODS-N Field. In J. Afonso, H. C. Ferguson, B. Mobasher, & R. Norris, editor, *Deepest Astronomical Surveys*, volume 380 of *Astronomical Society of the Pacific Conference Series*, page 265, December 2007.

C. Blake, T. Davis, G. B. Poole, D. Parkinson, S. Brough, M. Colless, C. Contreras, W. Couch, S. Croom, M. J. Drinkwater, K. Forster, D. Gilbank, M. Gladders, K. Glazebrook, B. Jelliffe, R. J. Jurek, I.-H. Li, B. Madore, D. C. Martin, K. Pimbblet, M. Pracy, R. Sharp, E. Wisnioski, D. Woods, T. K. Wyder, and H. K. C. Yee. The WiggleZ Dark Energy Survey: testing the cosmological model with baryon acoustic oscillations at z= 0.6. *MNRAS*, 415:2892–2909, August 2011.

E. L. Blanton, M. D. Gregg, D. J. Helfand, R. H. Becker, and R. L. White. FIRST Bent-Double Radio Sources: Tracers of High-Redshift Clusters. *ApJ*, 531:118–136, March 2000.

E. L. Blanton, M. D. Gregg, D. J. Helfand, R. H. Becker, and K. M. Leighly. The Environments of a Complete Moderate-Redshift Sample of FIRST Bent-Double Radio Sources. *AJ*, 121:2915–2927, June 2001.

E. L. Blanton, M. D. Gregg, D. J. Helfand, R. H. Becker, and R. L. White. Discovery of a High-Redshift (z=0.96) Cluster of Galaxies Using a FIRST Survey Wide-Angle-Tailed Radio Source. *AJ*, 125:1635–1641, April 2003.

G. R. Blumenthal, S. M. Faber, J. R. Primack, and M. J. Rees. Formation of galaxies and large-scale structure with cold dark matter. *Nature*, 311:517–525, October 1984.

H. Böhringer, P. Schuecker, L. Guzzo, C. A. Collins, W. Voges, S. Schindler, D. M. Neumann, R. G. Cruddace, S. De Grandi, G. Chincarini, A. C. Edge, H. T.

MacGillivray, and P. Shaver. The ROSAT-ESO flux limited X-ray (REFLEX) galaxy cluster survey. I. The construction of the cluster sample. *A&A*, 369: 826–850, April 2001.

J. G. Bolton and G. J. Stanley. Variable Source of Radio Frequency Radiation in the Constellation of Cygnus. *Nature*, 161:312–313, February 1948.

S. Borgani, G. Murante, V. Springel, A. Diaferio, K. Dolag, L. Moscardini, G. Tormen, L. Tornatore, and P. Tozzi. X-ray properties of galaxy clusters and groups from a cosmological hydrodynamical simulation. *MNRAS*, 348:1078–1096, March 2004.

N. Bourne, L. Dunne, R. J. Ivison, S. J. Maddox, M. Dickinson, and D. T. Frayer. Evolution of the far-infrared-radio correlation and infrared spectral energy distributions of massive galaxies over z= 0-2. *MNRAS*, 410:1155–1173, January 2011.

I. S. Bowen. The Origin of the Nebulium Spectrum. *Nature*, 120:473, October 1927.

B. J. Boyle, T. J. Cornwell, E. Middelberg, R. P. Norris, P. N. Appleton, and I. Smail. Extending the infrared radio correlation. *MNRAS*, 376:1182–1188, April 2007.

J. W. Broderick and R. P. Fender. Is there really a dichotomy in active galactic nucleus jet power? *MNRAS*, 417:184–197, October 2011.

S. Brown and L. Rudnick. Diffuse Cluster-Like Radio Emission in Poor Environments. *AJ*, 137:3158–3171, February 2009.

G. Brunetti, T. Venturi, D. Dallacasa, R. Cassano, K. Dolag, S. Giacintucci, and G. Setti. Cosmic Rays and Radio Halos in Galaxy Clusters: New Constraints from Radio Observations. *ApJ*, 670:L5–L8, November 2007.

J. O. Burns. The radio properties of cD galaxies in Abell clusters. I - an X-ray selected sample. *AJ*, 99:14–30, January 1990.

J. O. Burns. Stormy Weather in Galaxy Clusters. *Science*, 280:400, April 1998.

C. N. Cardamone, P. G. van Dokkum, C. M. Urry, Y. Taniguchi, E. Gawiser, G. Brammer, E. Taylor, M. Damen, E. Treister, B. E. Cobb, N. Bond, K. Schawinski, P. Lira, T. Murayama, T. Saito, and K. Sumikawa. The Multiwavelength Sur-

vey by Yale-Chile (MUSYC): Deep Medium-band Optical Imaging and High-quality 32-band Photometric Redshifts in the ECDF-S. *ApJS*, 189:270–285, August 2010.

C. L. Carilli and M. S. Yun. The Radio-to-Submillimeter Spectral Index as a Redshift Indicator. *ApJ*, 513:L13–L16, March 1999.

R. Cassano. Large-scale Diffuse Radio Emission from Clusters of Galaxies and the Importance of Low Frequency Radio Observations. In D. J. Saikia, D. A. Green, Y. Gupta, & T. Venturi, editor, *The Low-Frequency Radio Universe*, volume 407 of *Astronomical Society of the Pacific Conference Series*, page 223, September 2009.

S. C. Chapman, R. J. Ivison, I. G. Roseboom, R. Auld, J. Bock, D. Brisbin, D. Burgarella, P. Chanial, D. L. Clements, A. Cooray, S. Eales, A. Franceschini, E. Giovannoli, J. Glenn, M. Griffin, A. M. J. Mortier, S. J. Oliver, A. Omont, M. J. Page, A. Papageorgiou, C. P. Pearson, I. Pérez-Fournon, M. Pohlen, J. I. Rawlings, G. Raymond, G. Rodighiero, M. Rowan-Robinson, D. Scott, N. Seymour, A. J. Smith, M. Symeonidis, K. E. Tugwell, M. Vaccari, J. D. Vieira, L. Vigroux, L. Wang, and G. Wright. Herschel-SPIRE, far-infrared properties of millimetre-bright and -faint radio galaxies. *MNRAS*, 409:L13–L18, November 2010.

R. Chary and D. Elbaz. Interpreting the Cosmic Infrared Background: Constraints on the Evolution of the Dust-enshrouded Star Formation Rate. *ApJ*, 556:562–581, August 2001.

M. Chiaberge, G. Tremblay, A. Capetti, F. D. Macchetto, P. Tozzi, and W. B. Sparks. Low-Power Radio Galaxies in the Distant Universe: A Search for FR I at $1 < z < 2$ in the Cosmos Field. *ApJ*, 696:1103–1115, May 2009.

Hong-Yee Chiu. Gravitational collapse. *Physics Today*, 17(5):21–34, 1964. URL `http://link.aip.org/link/?PTO/17/21/1`.

M. Cirasuolo, A. Celotti, M. Magliocchetti, and L. Danese. Is there a dichotomy in the radio loudness distribution of quasars? *MNRAS*, 346:447–455, December 2003.

L. Clewley and M. J. Jarvis. The cosmic evolution of low-luminosity radio sources from the Sloan Digital Sky Survey Data Release 1. *MNRAS*, 352:909–914, August 2004.

M. Colless, G. Dalton, S. Maddox, W. Sutherland, P. Norberg, S. Cole, J. Bland-Hawthorn, T. Bridges, R. Cannon, C. Collins, W. Couch, N. Cross, K. Deeley, R. De Propris, S. P. Driver, G. Efstathiou, R. S. Ellis, C. S. Frenk, K. Glazebrook, C. Jackson, O. Lahav, I. Lewis, S. Lumsden, D. Madgwick, J. A. Peacock, B. A. Peterson, I. Price, M. Seaborne, and K. Taylor. The 2dF Galaxy Redshift Survey: spectra and redshifts. *MNRAS*, 328:1039–1063, December 2001.

J. J. Condon. Cosmological evolution of radio sources. *ApJ*, 287:461–474, December 1984.

J. J. Condon. Radio emission from normal galaxies. *ARA&A*, 30:575–611, 1992.

J. J. Condon, W. D. Cotton, E. W. Greisen, Q. F. Yin, R. A. Perley, G. B. Taylor, and J. J. Broderick. The NRAO VLA Sky Survey. *AJ*, 115:1693–1716, May 1998.

N. Copernicus. *D revolutionibus orbium coelestium*. 1543.

S. M. Croom, R. J. Smith, B. J. Boyle, T. Shanks, L. Miller, P. J. Outram, and N. S. Loaring. The 2dF QSO Redshift Survey - XII. The spectroscopic catalogue and luminosity function. *MNRAS*, 349:1397–1418, April 2004.

J. H. Croston, M. Birkinshaw, M. J. Hardcastle, and D. M. Worrall. X-ray emission from the nuclei, lobes and hot-gas environments of two FR II radio galaxies. *MNRAS*, 353:879–889, September 2004.

J. H. Croston, M. J. Hardcastle, D. E. Harris, E. Belsole, M. Birkinshaw, and D. M. Worrall. An X-Ray Study of Magnetic Field Strengths and Particle Content in the Lobes of FR II Radio Sources. *ApJ*, 626:733–747, June 2005.

D. J. Croton, V. Springel, S. D. M. White, G. De Lucia, C. S. Frenk, L. Gao, A. Jenkins, G. Kauffmann, J. F. Navarro, and N. Yoshida. The many lives of active galactic nuclei: cooling flows, black holes and the luminosities and colours of galaxies. *MNRAS*, 365:11–28, January 2006.

D. A. Dale and G. Helou. The Infrared Spectral Energy Distribution of Normal Star-forming Galaxies: Calibration at Far-Infrared and Submillimeter Wavelengths. *ApJ*, 576:159–168, September 2002.

T. de Jong, U. Klein, R. Wielebinski, and E. Wunderlich. Radio continuum and far-infrared emission from spiral galaxies - A close correlation. *A&A*, 147:L6–L9, June 1985.

G. De Lucia and J. Blaizot. The hierarchical formation of the brightest cluster galaxies. *MNRAS*, 375:2–14, February 2007.

R. De Propris, M. Colless, J. A. Peacock, W. J. Couch, S. P. Driver, M. L. Balogh, I. K. Baldry, C. M. Baugh, J. Bland-Hawthorn, T. Bridges, R. Cannon, S. Cole, C. Collins, N. Cross, G. Dalton, G. Efstathiou, R. S. Ellis, C. S. Frenk, K. Glazebrook, E. Hawkins, C. Jackson, O. Lahav, I. Lewis, S. Lumsden, S. Maddox, D. Madgwick, P. Norberg, W. Percival, B. A. Peterson, W. Sutherland, and K. Taylor. The 2dF Galaxy Redshift Survey: the blue galaxy fraction and implications for the Butcher-Oemler effect. *MNRAS*, 351:125–132, June 2004.

M. Dickinson, M. Giavalisco, and GOODS Team. The Great Observatories Origins Deep Survey. In R. Bender & A. Renzini, editor, *The Mass of Galaxies at Low and High Redshift*, page 324, 2003.

J. L. Donley, G. H. Rieke, J. R. Rigby, and P. G. Pérez-González. Unveiling a Population of AGNs Not Detected in X-Rays. *ApJ*, 634:169–182, November 2005.

J. S. Dunlop and J. A. Peacock. The Redshift Cut-Off in the Luminosity Function of Radio Galaxies and Quasars. *MNRAS*, 247:19, November 1990.

J. S. Dunlop, R. J. McLure, M. J. Kukula, S. A. Baum, C. P. O'Dea, and D. H. Hughes. Quasars, their host galaxies and their central black holes. *MNRAS*, 340:1095–1135, April 2003.

D. O. Edge, J. R. Shakeshaft, W. B. McAdam, J. E. Baldwin, and S. Archer. A survey of radio sources at a frequency of 159 Mc/s. *MmRAS*, 68:37–60, 1959.

J. A. Ekers. The Parkes catalogue of radio sources, declination zone +20 to -90 . *Australian Journal of Physics Astrophysical Supplement*, 7:3–75, 1969.

B. H. C. Emonts, I. Feain, M. Y. Mao, R. P. Norris, G. Miley, R. D. Ekers, M. Villar-Martín, H. J. A. Röttgering, E. M. Sadler, G. Rees, R. Morganti, D. J. Saikia, T. A. Oosterloo, J. B. Stevens, and C. N. Tadhunter. Molecular CO(1-0) Gas in the z ˜ 2 Radio Galaxy MRC 0152-209. *ApJ*, 734:L25, June 2011a.

B. H. C. Emonts, R. P. Norris, I. Feain, G. Miley, E. M. Sadler, M. Villar-Martín, M. Y. Mao, T. A. Oosterloo, R. D. Ekers, J. B. Stevens, M. H. Wieringa, K. E. K. Coppin, and C. N. Tadhunter. CO observations of high-z radio galaxies MRC

2104-242 and MRC 0943-242: spectral-line performance of the Compact Array Broadband Backend. *MNRAS*, 415:655–664, July 2011b.

T. A. Enßlin and Gopal-Krishna. Reviving fossil radio plasma in clusters of galaxies by adiabatic compression in environmental shock waves. *A&A*, 366:26–34, January 2001.

T. A. Ensslin, P. L. Biermann, U. Klein, and S. Kohle. Cluster radio relics as a tracer of shock waves of the large-scale structure formation. *A&A*, 332:395–409, April 1998.

B. L. Fanaroff and J. M. Riley. The morphology of extragalactic radio sources of high and low luminosity. *MNRAS*, 167:31P–36P, May 1974.

E. D. Feigelson and P. I. Nelson. Statistical methods for astronomical data with upper limits. I - Univariate distributions. *ApJ*, 293:192–206, June 1985.

L. Feretti. Non-thermal emission from the intracluster medium. *Advances in Space Research*, 36:729–737, 2005.

L. Ferrarese and D. Merritt. A Fundamental Relation between Supermassive Black Holes and Their Host Galaxies. *ApJ*, 539:L9–L12, August 2000.

C. Ferrari, F. Govoni, S. Schindler, A. M. Bykov, and Y. Rephaeli. Observations of Extended Radio Emission in Clusters. *Space Sci. Rev.*, 134:93–118, February 2008.

P. J. Francis. The continuum slopes and evolution of active galactic nuclei. *ApJ*, 407:519–524, April 1993.

P. J. Francis, P. C. Hewett, C. B. Foltz, F. H. Chaffee, R. J. Weymann, and S. L. Morris. A high signal-to-noise ratio composite quasar spectrum. *ApJ*, 373: 465–470, June 1991.

D. T. Frayer, D. Fadda, L. Yan, F. R. Marleau, P. I. Choi, G. Helou, B. T. Soifer, P. N. Appleton, L. Armus, R. Beck, H. Dole, C. W. Engelbracht, F. Fang, K. D. Gordon, I. Heinrichsen, D. Henderson, T. Hesselroth, M. Im, D. M. Kelly, M. Lacy, S. Laine, W. B. Latter, W. Mahoney, D. Makovoz, F. J. Masci, J. E. Morrison, M. Moshir, A. Noriega-Crespo, D. L. Padgett, M. Pesenson, D. L. Shupe, G. K. Squires, L. J. Storrie-Lombardi, J. A. Surace, H. I. Teplitz, and G. Wilson. Spitzer 70 and 160 μm Observations of the Extragalactic First Look Survey. *AJ*, 131:250–260, January 2006.

M. A. Garrett. The FIR/Radio correlation of high redshift galaxies in the region of the HDF-N. *A&A*, 384:L19–L22, March 2002.

E. Gawiser, P. G. van Dokkum, D. Herrera, J. Maza, F. J. Castander, L. Infante, P. Lira, R. Quadri, R. Toner, E. Treister, C. M. Urry, M. Altmann, R. Assef, D. Christlein, P. S. Coppi, M. F. Durán, M. Franx, G. Galaz, L. Huerta, C. Liu, S. López, R. Méndez, D. C. Moore, M. Rubio, M. T. Ruiz, S. Toft, and S. K. Yi. The Multiwavelength Survey by Yale-Chile (MUSYC): Survey Design and Deep Public UBVRIz' Images and Catalogs of the Extended Hubble Deep Field-South. *ApJS*, 162:1–19, January 2006.

K. Gebhardt, R. Bender, G. Bower, A. Dressler, S. M. Faber, A. V. Filippenko, R. Green, C. Grillmair, L. C. Ho, J. Kormendy, T. R. Lauer, J. Magorrian, J. Pinkney, D. Richstone, and S. Tremaine. A Relationship between Nuclear Black Hole Mass and Galaxy Velocity Dispersion. *ApJ*, 539:L13–L16, August 2000.

N. Gehrels. Confidence limits for small numbers of events in astrophysical data. *ApJ*, 303:336–346, April 1986.

A. M. Ghez, S. Salim, N. N. Weinberg, J. R. Lu, T. Do, J. K. Dunn, K. Matthews, M. R. Morris, S. Yelda, E. E. Becklin, T. Kremenek, M. Milosavljevic, and J. Naiman. Measuring Distance and Properties of the Milky Way's Central Supermassive Black Hole with Stellar Orbits. *ApJ*, 689:1044–1062, December 2008. doi: 10.1086/592738.

R. Giacconi, A. Zirm, J. Wang, P. Rosati, M. Nonino, P. Tozzi, R. Gilli, V. Mainieri, G. Hasinger, L. Kewley, J. Bergeron, S. Borgani, R. Gilmozzi, N. Grogin, A. Koekemoer, E. Schreier, W. Zheng, and C. Norman. Chandra Deep Field South: The 1 Ms Catalog. *ApJS*, 139:369–410, April 2002.

S. Giacintucci and T. Venturi. Tailed radio galaxies as tracers of galaxy clusters. Serendipitous discoveries with the GMRT. *A&A*, 505:55–61, October 2009.

S. Giacintucci, T. Venturi, M. Murgia, D. Dallacasa, R. Athreya, S. Bardelli, P. Mazzotta, and D. J. Saikia. Radio morphology and spectral analysis of cD galaxies in rich and poor galaxy clusters. *A&A*, 476:99–119, December 2007.

S. Giacintucci, T. Venturi, G. Macario, D. Dallacasa, G. Brunetti, M. Markevitch, R. Cassano, S. Bardelli, and R. Athreya. Shock acceleration as origin of the radio relic in A 521? *A&A*, 486:347–358, August 2008.

M. Giavalisco, H. C. Ferguson, A. M. Koekemoer, M. Dickinson, D. M. Alexander, F. E. Bauer, J. Bergeron, C. Biagetti, W. N. Brandt, S. Casertano, C. Cesarsky, E. Chatzichristou, C. Conselice, S. Cristiani, L. Da Costa, T. Dahlen, D. de Mello, P. Eisenhardt, T. Erben, S. M. Fall, C. Fassnacht, R. Fosbury, A. Fruchter, J. P. Gardner, N. Grogin, R. N. Hook, A. E. Hornschemeier, R. Idzi, S. Jogee, C. Kretchmer, V. Laidler, K. S. Lee, M. Livio, R. Lucas, P. Madau, B. Mobasher, L. A. Moustakas, M. Nonino, P. Padovani, C. Papovich, Y. Park, S. Ravindranath, A. Renzini, M. Richardson, A. Riess, P. Rosati, M. Schirmer, E. Schreier, R. S. Somerville, H. Spinrad, D. Stern, M. Stiavelli, L. Strolger, C. M. Urry, B. Vandame, R. Williams, and C. Wolf. The Great Observatories Origins Deep Survey: Initial Results from Optical and Near-Infrared Imaging. *ApJ*, 600:L93–L98, January 2004.

F. Gieseke, K. L. Polsterer, A. Thom, P.-C. Zinn, D. Bomanns, R.-J. Dettmar, O. Kramer, and J. Vahrenhold. Detecting Quasars in Large-Scale Astronomical Surveys. *ArXiv e-prints*, August 2011.

S. Gillessen, F. Eisenhauer, S. Trippe, T. Alexander, R. Genzel, F. Martins, and T. Ott. Monitoring Stellar Orbits Around the Massive Black Hole in the Galactic Center. *ApJ*, 692:1075–1109, February 2009. doi: 10.1088/0004-637X/692/2/1075.

G. Giovannini and L. Feretti. Halo and relic sources in clusters of galaxies. *New A*, 5:335–347, September 2000.

G. Giovannini and L. Feretti. Radio Relics in Clusters of Galaxies. *Journal of Korean Astronomical Society*, 37:323–328, December 2004.

G. Giovannini, A. Bonafede, L. Feretti, F. Govoni, M. Murgia, F. Ferrari, and G. Monti. Radio halos in nearby ($z < 0.4$) clusters of galaxies. *A&A*, 507:1257–1270, December 2009.

K. Glazebrook and J. Bland-Hawthorn. Microslit Nod-Shuffle Spectroscopy: A Technique for Achieving Very High Densities of Spectra. *PASP*, 113:197–214, February 2001.

K. Glazebrook, R. G. Abraham, P. J. McCarthy, S. Savaglio, H.-W. Chen, D. Crampton, R. Murowinski, I. Jørgensen, K. Roth, I. Hook, R. O. Marzke, and R. G. Carlberg. A high abundance of massive galaxies 3-6 billion years after the Big Bang. *Nature*, 430:181–184, July 2004.

C. Gruppioni, P. Ciliegi, M. Rowan-Robinson, L. Cram, A. Hopkins, C. Cesarsky, L. Danese, A. Franceschini, R. Genzel, A. Lawrence, D. Lemke, R. G. McMahon, G. Miley, S. Oliver, J.-L. Puget, and B. Rocca-Volmerange. A 1.4-GHz survey of the southern European Large-Area ISO Survey region. *MNRAS*, 305:297–308, April 1999.

K. Gültekin, D. O. Richstone, K. Gebhardt, T. R. Lauer, S. Tremaine, M. C. Aller, R. Bender, A. Dressler, S. M. Faber, A. V. Filippenko, R. Green, L. C. Ho, J. Kormendy, J. Magorrian, J. Pinkney, and C. Siopis. The M-σ and M-L Relations in Galactic Bulges, and Determinations of Their Intrinsic Scatter. *ApJ*, 698: 198–221, June 2009.

N. C. Hambly, H. T. MacGillivray, M. A. Read, S. B. Tritton, E. B. Thomson, B. D. Kelly, D. H. Morgan, R. E. Smith, S. P. Driver, J. Williamson, Q. A. Parker, M. R. S. Hawkins, P. M. Williams, and A. Lawrence. The SuperCOSMOS Sky Survey - I. Introduction and description. *MNRAS*, 326:1279–1294, October 2001.

M. J. Hardcastle, D. A. Evans, and J. H. Croston. Hot and cold gas accretion and feedback in radio-loud active galaxies. *MNRAS*, 376:1849–1856, April 2007.

D. E. Harris, V. K. Kapahi, and R. D. Ekers. Westerbork synthesis observations of 8 clusters of galaxies which contain tailed radio galaxies. *A&AS*, 39:215–233, February 1980.

T. M. Heckman. An optical and radio survey of the nuclei of bright galaxies - Activity in normal galactic nuclei. *A&A*, 87:152–164, July 1980.

G. Helou and M. D. Bicay. A physical model of the infrared-to-radio correlation in galaxies. *ApJ*, 415:93–100, September 1993.

G. Helou, B. T. Soifer, and M. Rowan-Robinson. Thermal infrared and nonthermal radio - Remarkable correlation in disks of galaxies. *ApJ*, 298:L7–L11, November 1985.

W. Herschel. Catalogue of One Thousand New Nebulae and Clusters of Stars. *Royal Society of London Philosophical Transactions Series I*, 76:457–499, 1786.

L. C. Ho, A. V. Filippenko, and W. L. W. Sargent. A Search for "Dwarf" Seyfert Nuclei. V. Demographics of Nuclear Activity in Nearby Galaxies. *ApJ*, 487:568, October 1997.

M. Hoeft, M. Brüggen, G. Yepes, S. Gottlöber, and A. Schwope. Diffuse radio emission from clusters in the MareNostrum Universe simulation. *MNRAS*, 391: 1511–1526, December 2008.

D. W. Hogg. Distance measures in cosmology. *ArXiv Astrophysics e-prints*, May 1999.

A. M. Hopkins. On the Evolution of Star-forming Galaxies. *ApJ*, 615:209–221, November 2004.

A. M. Hopkins, B. Mobasher, L. Cram, and M. Rowan-Robinson. The PHOENIX Deep Survey: 1.4-GHz source counts. *MNRAS*, 296:839–846, June 1998.

F. Hoyle. A New Model for the Expanding Universe. *MNRAS*, 108:372, 1948.

E. Hubble. No. 324. Extra-galactic nebulae. *Contributions from the Mount Wilson Observatory / Carnegie Institution of Washington*, 324:1–49, 1926.

E. P. Hubble. NGC 6822, a remote stellar system. *ApJ*, 62:409–433, December 1925.

M. T. Huynh, C. A. Jackson, R. P. Norris, and I. Prandoni. Radio Observations of the Hubble Deep Field-South Region. II. The 1.4 GHz Catalog and Source Counts. *AJ*, 130:1373–1388, October 2005.

M. T. Huynh, C. A. Jackson, and R. P. Norris. Radio Observations of the Hubble Deep Field-South Region. III. The 2.5, 5.2, and 8.7 GHz Catalogs and Radio Source Properties. *AJ*, 133:1331–1344, April 2007.

M. T. Huynh, C. A. Jackson, R. P. Norris, and A. Fernandez-Soto. Radio Observations of the Hubble Deep Field-South Region. Iv. Optical Properties of the Faint Radio Population. *AJ*, 135:2470–2495, June 2008.

M. T. Huynh, E. Gawiser, D. Marchesini, G. Brammer, and L. Guaita. MIPS 24 μm Observations of the Hubble Deep Field South: Probing the IR-Radio Correlation of Galaxies at z>1. *ApJ*, 723:1110–1118, November 2010.

H. S. Hwang, D. Elbaz, G. Magdis, E. Daddi, M. Symeonidis, B. Altieri, A. Amblard, P. Andreani, V. Arumugam, R. Auld, H. Aussel, T. Babbedge, S. Berta, A. Blain, J. Bock, A. Bongiovanni, A. Boselli, V. Buat, D. Burgarella, N. Castro-Rodríguez, A. Cava, J. Cepa, P. Chanial, E. Chapin, R.-R. Chary, A. Cimatti,

D. L. Clements, A. Conley, L. Conversi, A. Cooray, H. Dannerbauer, M. Dickinson, H. Dominguez, C. D. Dowell, J. S. Dunlop, E. Dwek, S. Eales, D. Farrah, N. F. Schreiber, M. Fox, A. Franceschini, W. Gear, R. Genzel, J. Glenn, M. Griffin, C. Gruppioni, M. Halpern, E. Hatziminaoglou, E. Ibar, K. Isaak, R. J. Ivison, W.-S. Jeong, G. Lagache, D. Le Borgne, E. Le Floc'h, H. M. Lee, J. C. Lee, M. G. Lee, L. Levenson, N. Lu, D. Lutz, S. Madden, B. Maffei, B. Magnelli, G. Mainetti, R. Maiolino, L. Marchetti, A. M. J. Mortier, H. T. Nguyen, R. Nordon, B. O'Halloran, K. Okumura, S. J. Oliver, A. Omont, M. J. Page, P. Panuzzo, A. Papageorgiou, C. P. Pearson, I. Pérez-Fournon, A. M. P. García, A. Poglitsch, M. Pohlen, P. Popesso, F. Pozzi, J. I. Rawlings, D. Rigopoulou, L. Riguccini, D. Rizzo, G. Rodighiero, I. G. Roseboom, M. Rowan-Robinson, A. Saintonge, M. S. Portal, P. Santini, M. Sauvage, B. Schulz, D. Scott, N. Seymour, L. Shao, D. L. Shupe, A. J. Smith, J. A. Stevens, E. Sturm, L. Tacconi, M. Trichas, K. E. Tugwell, M. Vaccari, I. Valtchanov, J. D. Vieira, L. Vigroux, L. Wang, R. Ward, G. Wright, C. K. Xu, and M. Zemcov. Evolution of dust temperature of galaxies through cosmic time as seen by Herschel. *MNRAS*, 409:75–82, November 2010.

E. Ibar, R. J. Ivison, P. N. Best, K. Coppin, A. Pope, I. Smail, and J. S. Dunlop. Deep multi-frequency radio imaging in the Lockman Hole - II. The spectral index of submillimetre galaxies. *MNRAS*, 401:L53–L57, January 2010.

Ž. Ivezić, K. Menou, G. R. Knapp, M. A. Strauss, R. H. Lupton, D. E. Vanden Berk, G. T. Richards, C. Tremonti, M. A. Weinstein, S. Anderson, N. A. Bahcall, R. H. Becker, M. Bernardi, M. Blanton, D. Eisenstein, X. Fan, D. Finkbeiner, K. Finlator, J. Frieman, J. E. Gunn, P. B. Hall, R. S. J. Kim, A. Kinkhabwala, V. K. Narayanan, C. M. Rockosi, D. Schlegel, D. P. Schneider, I. Strateva, M. SubbaRao, A. R. Thakar, W. Voges, R. L. White, B. Yanny, J. Brinkmann, M. Doi, M. Fukugita, G. S. Hennessy, J. A. Munn, R. C. Nichol, and D. G. York. Optical and Radio Properties of Extragalactic Sources Observed by the FIRST Survey and the Sloan Digital Sky Survey. *AJ*, 124:2364–2400, November 2002.

R. J. Ivison, D. M. Alexander, A. D. Biggs, W. N. Brandt, E. L. Chapin, K. E. K. Coppin, M. J. Devlin, M. Dickinson, J. Dunlop, S. Dye, S. A. Eales, D. T. Frayer, M. Halpern, D. H. Hughes, E. Ibar, A. Kovács, G. Marsden, L. Moncelsi, C. B. Netterfield, E. Pascale, G. Patanchon, D. A. Rafferty, M. Rex, E. Schinnerer, D. Scott, C. Semisch, I. Smail, A. M. Swinbank, M. D. P. Truch, G. S. Tucker, M. P. Viero, F. Walter, A. Weiß, D. V. Wiebe, and Y. Q. Xue. BLAST: the far-

infrared/radio correlation in distant galaxies. *MNRAS*, 402:245–258, February 2010a.

R. J. Ivison, B. Magnelli, E. Ibar, P. Andreani, D. Elbaz, B. Altieri, A. Amblard, V. Arumugam, R. Auld, H. Aussel, T. Babbedge, S. Berta, A. Blain, J. Bock, A. Bongiovanni, A. Boselli, V. Buat, D. Burgarella, N. Castro-Rodríguez, A. Cava, J. Cepa, P. Chanial, A. Cimatti, M. Cirasuolo, D. L. Clements, A. Conley, L. Conversi, A. Cooray, E. Daddi, H. Dominguez, C. D. Dowell, E. Dwek, S. Eales, D. Farrah, N. Förster Schreiber, M. Fox, A. Franceschini, W. Gear, R. Genzel, J. Glenn, M. Griffin, C. Gruppioni, M. Halpern, E. Hatziminaoglou, K. Isaak, G. Lagache, L. Levenson, N. Lu, D. Lutz, S. Madden, B. Maffei, G. Magdis, G. Mainetti, R. Maiolino, L. Marchetti, G. E. Morrison, A. M. J. Mortier, H. T. Nguyen, R. Nordon, B. O'Halloran, S. J. Oliver, A. Omont, F. N. Owen, M. J. Page, P. Panuzzo, A. Papageorgiou, C. P. Pearson, I. Pérez-Fournon, A. M. Pérez García, A. Poglitsch, M. Pohlen, P. Popesso, F. Pozzi, J. I. Rawlings, G. Raymond, D. Rigopoulou, L. Riguccini, D. Rizzo, G. Rodighiero, I. G. Roseboom, M. Rowan-Robinson, A. Saintonge, M. Sanchez Portal, P. Santini, B. Schulz, D. Scott, N. Seymour, L. Shao, D. L. Shupe, A. J. Smith, J. A. Stevens, E. Sturm, M. Symeonidis, L. Tacconi, M. Trichas, K. E. Tugwell, M. Vaccari, I. Valtchanov, J. Vieira, L. Vigroux, L. Wang, R. Ward, G. Wright, C. K. Xu, and M. Zemcov. The far-infrared/radio correlation as probed by Herschel. *A&A*, 518:L31, July 2010b.

K. G. Jansky. Radio Waves from Outside the Solar System. *Nature*, 132:66, July 1933.

K. G. Jansky. A Note on the Source of Interstellar Interference. *Proc. IRE*, 23: 1158–1163, October 1935.

N. Jarosik, C. L. Bennett, J. Dunkley, B. Gold, M. R. Greason, M. Halpern, R. S. Hill, G. Hinshaw, A. Kogut, E. Komatsu, D. Larson, M. Limon, S. S. Meyer, M. R. Nolta, N. Odegard, L. Page, K. M. Smith, D. N. Spergel, G. S. Tucker, J. L. Weiland, E. Wollack, and E. L. Wright. Seven-year Wilkinson Microwave Anisotropy Probe (WMAP) Observations: Sky Maps, Systematic Errors, and Basic Results. *ApJS*, 192:14, February 2011.

M. J. Jarvis, D. J. B. Smith, D. G. Bonfield, M. J. Hardcastle, J. T. Falder, J. A. Stevens, R. J. Ivison, R. Auld, M. Baes, I. K. Baldry, S. P. Bamford, N. Bourne, S. Buttiglione, A. Cava, A. Cooray, A. Dariush, G. de Zotti, J. S. Dunlop,

L. Dunne, S. Dye, S. Eales, J. Fritz, D. T. Hill, R. Hopwood, D. H. Hughes, E. Ibar, D. H. Jones, L. Kelvin, A. Lawrence, L. Leeuw, J. Loveday, S. J. Maddox, M. J. Michałowski, M. Negrello, P. Norberg, M. Pohlen, M. Prescott, E. E. Rigby, A. Robotham, G. Rodighiero, D. Scott, R. Sharp, P. Temi, M. A. Thompson, P. van der Werf, E. van Kampen, C. Vlahakis, and G. White. Herschel-ATLAS: the far-infrared-radio correlation at z < 0.5. *MNRAS*, 409:92–101, November 2010.

S. Johnston, R. Taylor, M. Bailes, N. Bartel, C. Baugh, M. Bietenholz, C. Blake, R. Braun, J. Brown, S. Chatterjee, J. Darling, A. Deller, R. Dodson, P. Edwards, R. Ekers, S. Ellingsen, I. Feain, B. Gaensler, M. Haverkorn, G. Hobbs, A. Hopkins, C. Jackson, C. James, G. Joncas, V. Kaspi, V. Kilborn, B. Koribalski, R. Kothes, T. Landecker, A. Lenc, J. Lovell, J.-P. Macquart, R. Manchester, D. Matthews, N. McClure-Griffiths, R. Norris, U.-L. Pen, C. Phillips, C. Power, R. Protheroe, E. Sadler, B. Schmidt, I. Stairs, L. Staveley-Smith, J. Stil, S. Tingay, A. Tzioumis, M. Walker, J. Wall, and M. Wolleben. Science with ASKAP. The Australian square-kilometre-array pathfinder. *Experimental Astronomy*, 22:151–273, December 2008.

M. Johnston-Hollitt, R. W. Hunstead, and E. Corbett. The optical morphology of A3667 re-examined. *A&A*, 479:1–8, February 2008.

N. G. Kantharia, M. Das, and Gopal-Drishna. GMRT Detection of a New Wide-Angle Tail (WAT) Radio Source Associated with the Galaxy PGC 1519010. *Journal of Astrophysics and Astronomy*, 30:37–52, March 2009.

K. I. Kellermann. The Spectra of Non-Thermal Radio Sources. *ApJ*, 140:969, October 1964.

K. I. Kellermann, R. Sramek, M. Schmidt, D. B. Shaffer, and R. Green. VLA observations of objects in the Palomar Bright Quasar Survey. *AJ*, 98:1195–1207, October 1989.

K. I. Kellermann, R. A. Sramek, M. Schmidt, R. F. Green, and D. B. Shaffer. The radio structure of radio loud and radio quiet quasars in the Palomar Bright Quasar Survey. *AJ*, 108:1163–1177, October 1994.

K. I. Kellermann, E. B. Fomalont, V. Mainieri, P. Padovani, P. Rosati, P. Shaver, P. Tozzi, and N. Miller. The VLA Survey of the Chandra Deep Field-South. I. Overview and the Radio Data. *ApJS*, 179:71–94, November 2008.

L. M. Ker, P. N. Best, E. E. Rigby, H. J. A. Röttgering, and M. A. Gendre. New insights on the z–α correlation from complete radio samples. *MNRAS*, 420: 2644–2661, March 2012.

E. Y. Khachikian and D. W. Weedman. An atlas of Seyfert galaxies. *ApJ*, 192: 581–589, September 1974.

A. E. Kimball, K. I. Kellermann, J. J. Condon, Ž. Ivezić, and R. A. Perley. The Two-component Radio Luminosity Function of Quasi-stellar Objects: Star Formation and Active Galactic Nucleus. *ApJ*, 739:L29, September 2011.

A. M. Koekemoer, B. Mobasher, and R. P. Norris. The ultra-deep 20 cm Australia telescope survey of the Chandra Deep Field South. *New A Rev.*, 47:391–396, September 2003.

C. Konar, D. J. Saikia, C. H. Ishwara-Chandra, and V. K. Kulkarni. Radio observations of a few giant sources. *MNRAS*, 355:845–854, December 2004.

C. Konar, M. J. Hardcastle, J. H. Croston, and D. J. Saikia. The dynamics of the giant radio galaxy 3C457. *MNRAS*, 400:480–491, November 2009.

J. D. Kraus. *Radio astronomy*. 1966.

A. Kravtsov, A. Gonzalez, A. Vikhlinin, D. Marrone, A. Zabludoff, D. Nagai, M. Markevitch, B. Benson, S. Golwala, S. Meyers, M. Gladders, D. Rudd, A. Evrard, C. Conroy, and S. Allen. Towards the 2020 vision of the baryon content of galaxy groups and clusters. In *astro2010: The Astronomy and Astrophysics Decadal Survey*, volume 2010 of *Astronomy*, page 164, 2009.

B. C. Lacki, T. A. Thompson, and E. Quataert. The Physics of the Far-infrared-Radio Correlation. I. Calorimetry, Conspiracy, and Implications. *ApJ*, 717:1–28, July 2010.

M. Lacy and SERVS Team. The Spitzer Extragalactic Representative Volume Survey. In *American Astronomical Society Meeting Abstracts #214*, volume 214 of *American Astronomical Society Meeting Abstracts*, page #202.04, May 2009.

M. Lacy, L. J. Storrie-Lombardi, A. Sajina, P. N. Appleton, L. Armus, S. C. Chapman, P. I. Choi, D. Fadda, F. Fang, D. T. Frayer, I. Heinrichsen, G. Helou, M. Im, F. R. Marleau, F. Masci, D. L. Shupe, B. T. Soifer, J. Surace, H. I. Teplitz, G. Wilson, and L. Yan. Obscured and Unobscured Active Galactic Nuclei in

the Spitzer Space Telescope First Look Survey. *ApJS*, 154:166–169, September 2004.

M. Lacy, A. O. Petric, A. Sajina, G. Canalizo, L. J. Storrie-Lombardi, L. Armus, D. Fadda, and F. R. Marleau. Optical Spectroscopy and X-Ray Detections of a Sample of Quasars and Active Galactic Nuclei Selected in the Mid-Infrared from Two Spitzer Space Telescope Wide-Area Surveys. *AJ*, 133:186–205, January 2007.

G. Lagache, H. Dole, and J.-L. Puget. Modelling infrared galaxy evolution using a phenomenological approach. *MNRAS*, 338:555–571, January 2003.

K. M. Lanzetta, N. Yahata, S. Pascarelle, H.-W. Chen, and A. Fernández-Soto. The Star Formation Rate Intensity Distribution Function: Implications for the Cosmic Star Formation Rate History of the Universe. *ApJ*, 570:492–501, May 2002.

T. R. Lauer, S. Tremaine, D. Richstone, and S. M. Faber. Selection Bias in Observing the Cosmological Evolution of the M-σ and M-L Relationships. *ApJ*, 670: 249–260, November 2007.

M. Lavalley, T. Isobe, and E. Feigelson. ASURV: Astronomy Survival Analysis Package. In D. M. Worrall, C. Biemesderfer, & J. Barnes, editor, *Astronomical Data Analysis Software and Systems I*, volume 25 of *Astronomical Society of the Pacific Conference Series*, page 245, 1992.

O. Le Fèvre, G. Vettolani, S. Paltani, L. Tresse, G. Zamorani, V. Le Brun, C. Moreau, D. Bottini, D. Maccagni, J. P. Picat, R. Scaramella, M. Scodeggio, A. Zanichelli, C. Adami, S. Arnouts, S. Bardelli, M. Bolzonella, A. Cappi, S. Charlot, T. Contini, S. Foucaud, P. Franzetti, B. Garilli, I. Gavignaud, L. Guzzo, O. Ilbert, A. Iovino, H. J. McCracken, D. Mancini, B. Marano, C. Marinoni, G. Mathez, A. Mazure, B. Meneux, R. Merighi, R. Pellò, A. Pollo, L. Pozzetti, M. Radovich, E. Zucca, M. Arnaboldi, M. Bondi, A. Bongiorno, G. Busarello, P. Ciliegi, L. Gregorini, Y. Mellier, P. Merluzzi, V. Ripepi, and D. Rizzo. The VIMOS VLT Deep Survey. Public release of 1599 redshifts to $I_{AB}\leq 24$ across the Chandra Deep Field South. *A&A*, 428:1043–1049, December 2004.

E. Le Floc'h, C. Papovich, H. Dole, E. F. Bell, G. Lagache, G. H. Rieke, E. Egami, P. G. Pérez-González, A. Alonso-Herrero, M. J. Rieke, M. Blaylock, C. W.

Engelbracht, K. D. Gordon, D. C. Hines, K. A. Misselt, J. E. Morrison, and J. Mould. Infrared Luminosity Functions from the Chandra Deep Field-South: The Spitzer View on the History of Dusty Star Formation at 0 <~ z <~ 1. *ApJ*, 632:169–190, October 2005.

H. S. Leavitt. 1777 variables in the Magellanic Clouds. *Annals of Harvard College Observatory*, 60:87–108, 1908.

G. Lemaître. Un Univers homogène de masse constante et de rayon croissant rendant compte de la vitesse radiale des nébuleuses extra-galactiques. *Annales de la Societe Scietifique de Bruxelles*, 47:49–59, 1927.

Y. Letawe, G. Letawe, and P. Magain. Study of a homogeneous QSO sample: relations between the QSO and its host galaxy. *MNRAS*, 403:2088–2104, April 2010.

I. J. Lewis, R. D. Cannon, K. Taylor, K. Glazebrook, J. A. Bailey, I. K. Baldry, J. R. Barton, T. J. Bridges, G. B. Dalton, T. J. Farrell, P. M. Gray, A. Lankshear, C. McCowage, I. R. Parry, R. M. Sharples, K. Shortridge, G. A. Smith, J. Stevenson, J. O. Straede, L. G. Waller, J. D. Whittard, J. K. Wilcox, and K. C. Willis. The Anglo-Australian Observatory 2dF facility. *MNRAS*, 333:279–299, June 2002.

C. J. Lonsdale, H. E. Smith, M. Rowan-Robinson, J. Surace, D. Shupe, C. Xu, S. Oliver, D. Padgett, F. Fang, T. Conrow, A. Franceschini, N. Gautier, M. Griffin, P. Hacking, F. Masci, G. Morrison, J. O'Linger, F. Owen, I. Pérez-Fournon, M. Pierre, R. Puetter, G. Stacey, S. Castro, M. d. C. Polletta, D. Farrah, T. Jarrett, D. Frayer, B. Siana, T. Babbedge, S. Dye, M. Fox, E. Gonzalez-Solares, M. Salaman, S. Berta, J. J. Condon, H. Dole, and S. Serjeant. SWIRE: The SIRTF Wide-Area Infrared Extragalactic Survey. *PASP*, 115:897–927, August 2003.

B. Luo, F. E. Bauer, W. N. Brandt, D. M. Alexander, B. D. Lehmer, D. P. Schneider, M. Brusa, A. Comastri, A. C. Fabian, A. Finoguenov, R. Gilli, G. Hasinger, A. E. Hornschemeier, A. Koekemoer, V. Mainieri, M. Paolillo, P. Rosati, O. Shemmer, J. D. Silverman, I. Smail, A. T. Steffen, and C. Vignali. The Chandra Deep Field-South Survey: 2 Ms Source Catalogs. *ApJS*, 179:19–36, November 2008.

B. Magnelli, D. Elbaz, R. R. Chary, M. Dickinson, D. Le Borgne, D. T. Frayer, and C. N. A. Willmer. The 0.4 < z < 1.3 star formation history of the Universe as viewed in the far-infrared. *A&A*, 496:57–75, March 2009.

J. Magorrian, S. Tremaine, D. Richstone, R. Bender, G. Bower, A. Dressler, S. M. Faber, K. Gebhardt, R. Green, C. Grillmair, J. Kormendy, and T. Lauer. The Demography of Massive Dark Objects in Galaxy Centers. *AJ*, 115:2285–2305, June 1998.

D. Makovoz and F. R. Marleau. Point-Source Extraction with MOPEX. *PASP*, 117: 1113–1128, October 2005.

M. Y. Mao, M. Johnston-Hollitt, J. B. Stevens, and S. J. Wotherspoon. Head-tail Galaxies: beacons of high-density regions in clusters. *MNRAS*, 392:1070–1079, January 2009a.

M. Y. Mao, R. P. Norris, R. Sharp, and J. E. J. Lovell. Cosmic Evolution of Radio Sources in ATLAS. In W. Wang, Z. Yang, Z. Luo, & Z. Chen, editor, *The Starburst-AGN Connection*, volume 408 of *Astronomical Society of the Pacific Conference Series*, page 380, October 2009b.

M. Y. Mao, R. Sharp, D. J. Saikia, R. P. Norris, M. Johnston-Hollitt, E. Middelberg, and J. E. J. Lovell. Wide-angle tail galaxies in ATLAS. *MNRAS*, 406:2578–2590, August 2010a.

M. Y. Mao, R. P. Norris, R. Sharp, and J. E. J. Lovell. PRONGS: Powerful Radio Objects Nested in Galaxies with Star Formation. In *IAU Symposium*, volume 267 of *IAU Symposium*, pages 119–119, May 2010b.

T. A. Matthews, W. W. Morgan, and M. Schmidt. A Discussion of Galaxies Indentified with Radio Sources. *ApJ*, 140:35, July 1964.

T. Mauch and E. M. Sadler. Radio sources in the 6dFGS: local luminosity functions at 1.4GHz for star-forming galaxies and radio-loud AGN. *MNRAS*, 375: 931–950, March 2007.

T. Mauch, T. Murphy, H. J. Buttery, J. Curran, R. W. Hunstead, B. Piestrzynski, J. G. Robertson, and E. M. Sadler. SUMSS: a wide-field radio imaging survey of the southern sky - II. The source catalogue. *MNRAS*, 342:1117–1130, July 2003.

K. McAlpine and M. J. Jarvis. The evolution of radio sources in the UKIDSS-DXS-XMM-LSS field. *MNRAS*, 413:1054–1060, May 2011.

E. Middelberg, R. P. Norris, T. J. Cornwell, M. A. Voronkov, B. D. Siana, B. J. Boyle, P. Ciliegi, C. A. Jackson, M. T. Huynh, S. Berta, S. Rubele, C. J. Lonsdale, R. J. Ivison, and I. Smail. Deep Australia Telescope Large Area Survey Radio Observations of the European Large Area ISO Survey S1/Spitzer Wide-Area Infrared Extragalactic Field. *AJ*, 135:1276–1290, April 2008.

E. Middelberg, R. P. Norris, C. A. Hales, N. Seymour, M. Johnston-Hollitt, M. T. Huynh, E. Lenc, and M. Y. Mao. The radio properties of infrared-faint radio sources. *A&A*, 526:A8, February 2011.

G. K. Miley, G. C. Perola, P. C. van der Kruit, and H. van der Laan. Active Galaxies with Radio Trails in Clusters. *Nature*, 237:269–272, June 1972.

N. A. Miller, E. B. Fomalont, K. I. Kellermann, V. Mainieri, C. Norman, P. Padovani, P. Rosati, and P. Tozzi. The VLA 1.4 GHz Survey of the Extended Chandra Deep Field-South: First Data Release. *ApJS*, 179:114–123, November 2008.

F. Miniati, D. Ryu, H. Kang, T. W. Jones, R. Cen, and J. P. Ostriker. Properties of Cosmic Shock Waves in Large-Scale Structure Formation. *ApJ*, 542:608–621, October 2000.

B. Miszalski, K. Shortridge, W. Saunders, Q. A. Parker, and S. M. Croom. Multi-object spectroscopy field configuration by simulated annealing. *MNRAS*, 371: 1537–1549, October 2006.

M. Miyoshi, J. Moran, J. Herrnstein, L. Greenhill, N. Nakai, P. Diamond, and M. Inoue. Evidence for a black hole from high rotation velocities in a sub-parsec region of NGC4258. *Nature*, 373:127–129, January 1995.

B. Moore, S. Ghigna, F. Governato, G. Lake, T. Quinn, J. Stadel, and P. Tozzi. Dark Matter Substructure within Galactic Halos. *ApJ*, 524:L19–L22, October 1999.

B. P. Moster, R. S. Somerville, J. A. Newman, and H.-W. Rix. A Cosmic Variance Cookbook. *ApJ*, 731:113, April 2011.

E. J. Murphy. The Far-Infrared-Radio Correlation at High Redshifts: Physical Considerations and Prospects for the Square Kilometer Array. *ApJ*, 706:482–496, November 2009.

R. P. Norris. Overcoming the challenges of wide deep continuum surveys. In *Panoramic Radio Astronomy: Wide-field 1-2 GHz Research on Galaxy Evolution*, 2009.

R. P. Norris, J. Afonso, P. N. Appleton, B. J. Boyle, P. Ciliegi, S. M. Croom, M. T. Huynh, C. A. Jackson, A. M. Koekemoer, C. J. Lonsdale, E. Middelberg, B. Mobasher, S. J. Oliver, M. Polletta, B. D. Siana, I. Smail, and M. A. Voronkov. Deep ATLAS Radio Observations of the Chandra Deep Field-South/Spitzer Wide-Area Infrared Extragalactic Field. *AJ*, 132:2409–2423, December 2006.

R. P. Norris, S. Tingay, C. Phillips, E. Middelberg, A. Deller, and P. N. Appleton. Very long baseline interferometry detection of an Infrared-Faint Radio Source. *MNRAS*, 378:1434–1438, July 2007.

R. P. Norris, A. M. Hopkins, J. Afonso, S. Brown, J. J. Condon, L. Dunne, I. Feain, R. Hollow, M. Jarvis, M. Johnston-Hollitt, E. Lenc, E. Middelberg, P. Padovani, I. Prandoni, L. Rudnick, N. Seymour, G. Umana, H. Andernach, D. M. Alexander, P. N. Appleton, D. Bacon, J. Banfield, W. Becker, M. J. I. Brown, P. Ciliegi, C. Jackson, S. Eales, A. C. Edge, B. M. Gaensler, G. Giovannini, C. A. Hales, P. Hancock, M. T. Huynh, E. Ibar, R. J. Ivison, R. Kennicutt, A. E. Kimball, A. M. Koekemoer, B. S. Koribalski, Á. R. López-Sánchez, M. Y. Mao, T. Murphy, H. Messias, K. A. Pimbblet, A. Raccanelli, K. E. Randall, T. H. Reiprich, I. G. Roseboom, H. Röttgering, D. J. Saikia, R. G. Sharp, O. B. Slee, I. Smail, M. A. Thompson, J. S. Urquhart, J. V. Wall, and G.-B. Zhao. EMU: Evolutionary Map of the Universe. *PASA*, 28:215–248, August 2011a.

R. P. Norris, J. Afonso, A. Cava, D. Farrah, M. T. Huynh, R. J. Ivison, M. Jarvis, M. Lacy, M. Mao, C. Maraston, J.-C. Mauduit, E. Middelberg, S. Oliver, N. Seymour, and J. Surace. Deep Spitzer Observations of Infrared-faint Radio Sources: High-redshift Radio-loud Active Galactic Nuclei? *ApJ*, 736:55, July 2011c.

R. P. Norris, E. Lenc, A. L. Roy, and H. Spoon. The radio core of the ultraluminous infrared galaxy F00183-7111: watching the birth of a quasar. *MNRAS*, page 2673, March 2012.

A. Oklopčić, V. Smolčić, S. Giodini, G. Zamorani, L. Bîrzan, E. Schinnerer, C. L. Carilli, A. Finoguenov, S. Lilly, A. Koekemoer, and N. Z. Scoville. Identifying Dynamically Young Galaxy Groups Via Wide-angle Tail Galaxies: A Case Study in the COSMOS Field at z = 0.53. *ApJ*, 713:484–490, April 2010.

D. E. Osterbrock. Observational Model of the Ionized Gas in Seyfert and Radio-Galaxy Nuclei. *Proceedings of the National Academy of Science*, 75:540–544, February 1978.

D. E. Osterbrock. Seyfert galaxies with weak broad H alpha emission lines. *ApJ*, 249:462–470, October 1981.

F. N. Owen and M. J. Ledlow. The FRI/II Break and the Bivariate Luminosity Function in Abell Clusters of Galaxies. In G. V. Bicknell, M. A. Dopita, & P. J. Quinn, editor, *The Physics of Active Galaxies*, volume 54 of *Astronomical Society of the Pacific Conference Series*, page 319, 1994.

F. N. Owen and M. J. Ledlow. A 20 Centimeter VLA Survey of Abell Clusters of Galaxies. VII. Detailed Radio Images. *ApJS*, 108:41, January 1997.

F. N. Owen and G. E. Morrison. The Deep Swire Field. I. 20 cm Continuum Radio Observations: A Crowded Sky. *AJ*, 136:1889–1900, November 2008.

F. N. Owen and L. Rudnick. Radio sources with wide-angle tails in Abell clusters of galaxies. *ApJ*, 205:L1–L4, April 1976.

M. S. Owers, W. J. Couch, and P. E. J. Nulsen. Substructure in the Cold Front Cluster Abell 3667. *ApJ*, 693:901–913, March 2009.

P. Padovani, V. Mainieri, P. Tozzi, K. I. Kellermann, E. B. Fomalont, N. Miller, P. Rosati, and P. Shaver. The Very Large Array Survey of the Chandra Deep Field South. IV. Source Population. *ApJ*, 694:235–246, March 2009.

P. Padovani, N. Miller, K. I. Kellermann, V. Mainieri, P. Rosati, and P. Tozzi. The VLA Survey of Chandra Deep Field South. V. Evolution and Luminosity Functions of Sub-millijansky Radio Sources and the Issue of Radio Emission in Radio-quiet Active Galactic Nuclei. *ApJ*, 740:20, October 2011.

S. Perlmutter, G. Aldering, G. Goldhaber, R. A. Knop, P. Nugent, P. G. Castro, S. Deustua, S. Fabbro, A. Goobar, D. E. Groom, I. M. Hook, A. G. Kim, M. Y. Kim, J. C. Lee, N. J. Nunes, R. Pain, C. R. Pennypacker, R. Quimby, C. Lidman, R. S. Ellis, M. Irwin, R. G. McMahon, P. Ruiz-Lapuente, N. Walton, B. Schaefer, B. J. Boyle, A. V. Filippenko, T. Matheson, A. S. Fruchter, N. Panagia, H. J. M. Newberg, W. J. Couch, and Supernova Cosmology Project. Measurements of Omega and Lambda from 42 High-Redshift Supernovae. *ApJ*, 517:565–586, June 1999.

B. M. Peterson. *An Introduction to Active Galactic Nuclei*. February 1997.

C. Pfrommer, V. Springel, T. A. Enßlin, and M. Jubelgas. Detecting shock waves in cosmological smoothed particle hydrodynamics simulations. *MNRAS*, 367: 113–131, March 2006.

C. Pfrommer, T. A. Enßlin, and V. Springel. Simulating cosmic rays in clusters of galaxies - II. A unified scheme for radio haloes and relics with predictions of the γ-ray emission. *MNRAS*, 385:1211–1241, April 2008.

G. L. Pilbratt, J. R. Riedinger, T. Passvogel, G. Crone, D. Doyle, U. Gageur, A. M. Heras, C. Jewell, L. Metcalfe, S. Ott, and M. Schmidt. Herschel Space Observatory. An ESA facility for far-infrared and submillimetre astronomy. *A&A*, 518: L1, July 2010.

J. Pinkney, J. O. Burns, M. J. Ledlow, P. L. Gómez, and J. M. Hill. Substructure in Clusters Containing Wide-Angle-Tailed Radio Galaxies. I. New Redshifts. *AJ*, 120:2269–2277, November 2000.

A. Pope, D. Scott, M. Dickinson, R.-R. Chary, G. Morrison, C. Borys, A. Sajina, D. M. Alexander, E. Daddi, D. Frayer, E. MacDonald, and D. Stern. The Hubble Deep Field-North SCUBA Super-map - IV. Characterizing submillimetre galaxies using deep Spitzer imaging. *MNRAS*, 370:1185–1207, August 2006.

E. C. D. Pope, J. T. Mendel, and S. S. Shabala. Investigating the properties of active galactic nucleus feedback in hot atmospheres triggered by cooling-induced gravitational collapse. *MNRAS*, 419:50–56, January 2012.

G. W. Pratt, J. H. Croston, M. Arnaud, and H. Böhringer. Galaxy cluster X-ray luminosity scaling relations from a representative local sample (REXCESS). *A&A*, 498:361–378, May 2009.

Ptolemy. *Almagest*. 150BC.

K. E. Randall, A. M. Hopkins, R. P. Norris, P.-C. Zinn, E. Middelberg, M. Y. Mao, and R. G. Sharp. Spectral index properties of milliJansky radio sources. *MNRAS*, 421:1644–1660, April 2012.

G. Reber. Cosmic Static. *ApJ*, 100:279, November 1944.

E. A. Richards, E. B. Fomalont, K. I. Kellermann, R. A. Windhorst, R. B. Partridge, L. L. Cowie, and A. J. Barger. Optically Faint Microjansky Radio Sources. *ApJ*, 526:L73–L76, December 1999.

G. T. Richards, M. Lacy, L. J. Storrie-Lombardi, P. B. Hall, S. C. Gallagher, D. C. Hines, X. Fan, C. Papovich, D. E. Vanden Berk, G. B. Trammell, D. P. Schneider, M. Vestergaard, D. G. York, S. Jester, S. F. Anderson, T. Budavári, and A. S. Szalay. Spectral Energy Distributions and Multiwavelength Selection of Type 1 Quasars. *ApJS*, 166:470–497, October 2006.

D. Richstone, E. A. Ajhar, R. Bender, G. Bower, A. Dressler, S. M. Faber, A. V. Filippenko, K. Gebhardt, R. Green, L. C. Ho, J. Kormendy, T. R. Lauer, J. Magorrian, and S. Tremaine. Supermassive black holes and the evolution of galaxies. *Nature*, 395:A14, October 1998.

P. M. Ricker and C. L. Sarazin. Off-Axis Cluster Mergers: Effects of a Strongly Peaked Dark Matter Profile. *ApJ*, 561:621–644, November 2001.

K. Roettiger, J. O. Burns, and J. M. Stone. A Cluster Merger and the Origin of the Extended Radio Emission in Abell 3667. *ApJ*, 518:603–612, June 1999.

P. Rosati, P. Tozzi, R. Giacconi, R. Gilli, G. Hasinger, L. Kewley, V. Mainieri, M. Nonino, C. Norman, G. Szokoly, J. X. Wang, A. Zirm, J. Bergeron, S. Borgani, R. Gilmozzi, N. Grogin, A. Koekemoer, E. Schreier, and W. Zheng. The Chandra Deep Field-South: The 1 Million Second Exposure. *ApJ*, 566:667–674, February 2002.

H. Röttgering, J. Afonso, P. Barthel, F. Batejat, P. Best, A. Bonafede, M. Brüggen, G. Brunetti, K. Chyży, J. Conway, F. D. Gasperin, C. Ferrari, M. Haverkorn, G. Heald, M. Hoeft, N. Jackson, M. Jarvis, L. Ker, M. Lehnert, G. Macario, J. McKean, G. Miley, R. Morganti, T. Oosterloo, E. Orrù, R. Pizzo, D. Rafferty, A. Shulevski, C. Tasse, I. V. Bemmel, B. van der Tol, R. van Weeren, M. Verheijen, G. White, and M. Wise. LOFAR and APERTIF Surveys of the Radio Sky: Probing Shocks and Magnetic Fields in Galaxy Clusters. *Journal of Astrophysics and Astronomy*, 32:557–566, December 2011.

M. Rowan-Robinson, C. R. Benn, A. Lawrence, R. G. McMahon, and T. J. Broadhurst. The evolution of faint radio sources. *MNRAS*, 263:123–130, July 1993.

M. Rowan-Robinson, S. Oliver, A. Efstathiou, C. Gruppioni, S. Serjeant, C. J. Cesarsky, L. Danese, A. Franceschini, R. Genzel, A. Lawrence, D. Lemke, R. McMahon, G. Miley, I. Perez-Fournon, J. L. Puget, B. Rocca-Volmerange, P. Ciliegi, P. Heraudeau, C. Surace, F. La Franca, and ElAIS Consortium. The European large area ISO survey: ELAIS. In P. Cox & M. Kessler, editor, *The Universe as Seen by ISO*, volume 427 of *ESA Special Publication*, page 1011, March 1999.

M. Rowan-Robinson, T. Babbedge, S. Oliver, M. Trichas, S. Berta, C. Lonsdale, G. Smith, D. Shupe, J. Surace, S. Arnouts, O. Ilbert, O. Le Févre, A. Afonso-Luis, I. Perez-Fournon, E. Hatziminaoglou, M. Polletta, D. Farrah, and M. Vaccari. Photometric redshifts in the SWIRE Survey. *MNRAS*, 386:697–714, May 2008.

L. Rudnick and F. N. Owen. Interferometer observations of radio sources in clusters of galaxies. IV. *AJ*, 82:1–20, January 1977.

M. Ryle and A. Hewish. The Cambridge radio telescope. *Mem. R. Astron. Soc.*, 67: 97–105, 1955.

D. Ryu, H. Kang, E. Hallman, and T. W. Jones. Cosmological Shock Waves and Their Role in the Large-Scale Structure of the Universe. *ApJ*, 593:599–610, August 2003.

E. M. Sadler, V. J. McIntyre, C. A. Jackson, and R. D. Cannon. Radio sources in the 2dF Galaxy Redshift Survey. I. Radio source populations. *PASA*, 16:247–56, December 1999.

E. M. Sadler, C. A. Jackson, R. D. Cannon, V. J. McIntyre, T. Murphy, J. Bland-Hawthorn, T. Bridges, S. Cole, M. Colless, C. Collins, W. Couch, G. Dalton, R. De Propris, S. P. Driver, G. Efstathiou, R. S. Ellis, C. S. Frenk, K. Glazebrook, O. Lahav, I. Lewis, S. Lumsden, S. Maddox, D. Madgwick, P. Norberg, J. A. Peacock, B. A. Peterson, W. Sutherland, and K. Taylor. Radio sources in the 2dF Galaxy Redshift Survey - II. Local radio luminosity functions for AGN and star-forming galaxies at 1.4 GHz. *MNRAS*, 329:227–245, January 2002.

E. M. Sadler, R. D. Cannon, T. Mauch, P. J. Hancock, D. A. Wake, N. Ross, S. M. Croom, M. J. Drinkwater, A. C. Edge, D. Eisenstein, A. M. Hopkins, H. M. Johnston, R. Nichol, K. A. Pimbblet, R. de Propris, I. G. Roseboom, D. P. Schneider, and T. Shanks. Radio galaxies in the 2SLAQ Luminous Red Galaxy Survey -

I. The evolution of low-power radio galaxies to z ˜ 0.7. *MNRAS*, 381:211–227, October 2007.

M. Sahlén, P. T. P. Viana, A. R. Liddle, A. K. Romer, M. Davidson, M. Hosmer, E. Lloyd-Davies, K. Sabirli, C. A. Collins, P. E. Freeman, M. Hilton, B. Hoyle, S. T. Kay, R. G. Mann, N. Mehrtens, C. J. Miller, R. C. Nichol, S. A. Stanford, and M. J. West. The XMM Cluster Survey: forecasting cosmological and cluster scaling-relation parameter constraints. *MNRAS*, 397:577–607, August 2009.

D. J. Saikia, L. Staveley-Smith, D. Wills, T. J. Cornwell, C. J. Salter, W. Junor, and P. Shastri. A wide-angle radio-tail quasar - B2 1419+315. *MNRAS*, 229: 495–503, December 1987.

D. J. Saikia, P. J. Wiita, and T. W. B. Muxlow. 1222+216 - A wide-angle-tailed quasar? *AJ*, 105:1658–1665, May 1993.

A. Sajina, M. Lacy, and D. Scott. Simulating the Spitzer Mid-Infrared Color-Color Diagrams. *ApJ*, 621:256–268, March 2005.

M. Salvato, G. Hasinger, O. Ilbert, G. Zamorani, M. Brusa, N. Z. Scoville, A. Rau, P. Capak, S. Arnouts, H. Aussel, M. Bolzonella, A. Buongiorno, N. Cappelluti, K. Caputi, F. Civano, R. Cook, M. Elvis, R. Gilli, K. Jahnke, J. S. Kartaltepe, C. D. Impey, F. Lamareille, E. Le Floc'h, S. Lilly, V. Mainieri, P. McCarthy, H. McCracken, M. Mignoli, B. Mobasher, T. Murayama, S. Sasaki, D. B. Sanders, D. Schiminovich, Y. Shioya, P. Shopbell, J. Silverman, V. Smolčić, J. Surace, Y. Taniguchi, D. Thompson, J. R. Trump, M. Urry, and M. Zamojski. Photometric Redshift and Classification for the XMM-COSMOS Sources. *ApJ*, 690: 1250–1263, January 2009.

C. L. Sarazin. The Energy Spectrum of Primary Cosmic-Ray Electrons in Clusters of Galaxies and Inverse Compton Emission. *ApJ*, 520:529–547, August 1999.

M. T. Sargent, E. Schinnerer, E. Murphy, H. Aussel, E. Le Floc'h, D. T. Frayer, A. Martínez-Sansigre, P. Oesch, M. Salvato, V. Smolčić, G. Zamorani, M. Brusa, N. Cappelluti, C. L. Carilli, C. M. Carollo, O. Ilbert, J. Kartaltepe, A. M. Koekemoer, S. J. Lilly, D. B. Sanders, and N. Z. Scoville. The VLA-COSMOS Perspective on the Infrared-Radio Relation. I. New Constraints on Selection Biases and the Non-Evolution of the Infrared/Radio Properties of Star-Forming and Active Galactic Nucleus Galaxies at Intermediate and High Redshift. *ApJS*, 186: 341–377, February 2010a.

M. T. Sargent, E. Schinnerer, E. Murphy, C. L. Carilli, G. Helou, H. Aussel, E. Le Floc'h, D. T. Frayer, O. Ilbert, P. Oesch, M. Salvato, V. Smolčić, J. Kartaltepe, and D. B. Sanders. No Evolution in the IR-Radio Relation for IR-luminous Galaxies at z < 2 in the COSMOS Field. *ApJ*, 714:L190–L195, May 2010b.

W. Saunders, T. Bridges, P. Gillingham, R. Haynes, G. A. Smith, J. D. Whittard, V. Churilov, A. Lankshear, S. Croom, D. Jones, and C. Boshuizen. AAOmega: a scientific and optical overview. In A. F. M. Moorwood & M. Iye, editor, *Society of Photo-Optical Instrumentation Engineers (SPIE) Conference Series*, volume 5492 of *Society of Photo-Optical Instrumentation Engineers (SPIE) Conference Series*, pages 389–400, September 2004.

B. P. Schmidt, N. B. Suntzeff, M. M. Phillips, R. A. Schommer, A. Clocchiatti, R. P. Kirshner, P. Garnavich, P. Challis, B. Leibundgut, J. Spyromilio, A. G. Riess, A. V. Filippenko, M. Hamuy, R. C. Smith, C. Hogan, C. Stubbs, A. Diercks, D. Reiss, R. Gilliland, J. Tonry, J. Maza, A. Dressler, J. Walsh, and R. Ciardullo. The High-Z Supernova Search: Measuring Cosmic Deceleration and Global Curvature of the Universe Using Type IA Supernovae. *ApJ*, 507:46–63, November 1998.

M. Schmidt. Space Distribution and Luminosity Functions of Quasi-Stellar Radio Sources. *ApJ*, 151:393, February 1968.

M. Schmidt. Cosmological interpretation of redshift data on quasars through the V/V max test. In D. L. Jauncey, editor, *Radio Astronomy and Cosmology*, volume 74 of *IAU Symposium*, pages 259–265, 1977.

R. Schödel, T. Ott, R. Genzel, R. Hofmann, M. Lehnert, A. Eckart, N. Mouawad, T. Alexander, M. J. Reid, R. Lenzen, M. Hartung, F. Lacombe, D. Rouan, E. Gendron, G. Rousset, A.-M. Lagrange, W. Brandner, N. Ageorges, C. Lidman, A. F. M. Moorwood, J. Spyromilio, N. Hubin, and K. M. Menten. A star in a 15.2-year orbit around the supermassive black hole at the centre of the Milky Way. *Nature*, 419:694–696, October 2002.

D. A. Schwartz, H. L. Marshall, J. E. J. Lovell, D. W. Murphy, G. V. Bicknell, M. Birkinshaw, J. Gelbord, M. Georganopoulos, L. Godfrey, D. L. Jauncey, E. S. Perlman, and D. M. Worrall. Chandra Observations of Magnetic Fields and Relativistic Beaming in Four Quasar Jets. *ApJ*, 640:592–602, April 2006.

N. Scoville, H. Aussel, M. Brusa, P. Capak, C. M. Carollo, M. Elvis, M. Giavalisco, L. Guzzo, G. Hasinger, C. Impey, J.-P. Kneib, O. LeFevre, S. J. Lilly, B. Mobasher, A. Renzini, R. M. Rich, D. B. Sanders, E. Schinnerer, D. Schminovich, P. Shopbell, Y. Taniguchi, and N. D. Tyson. The Cosmic Evolution Survey (COSMOS): Overview. *ApJS*, 172:1–8, September 2007.

C. K. Seyfert. Nuclear Emission in Spiral Nebulae. *ApJ*, 97:28, January 1943.

N. Seymour, T. Dwelly, D. Moss, I. McHardy, A. Zoghbi, G. Rieke, M. Page, A. Hopkins, and N. Loaring. The star formation history of the Universe as revealed by deep radio observations. *MNRAS*, 386:1695–1708, May 2008.

N. Seymour, M. Huynh, T. Dwelly, M. Symeonidis, A. Hopkins, I. M. McHardy, M. J. Page, and G. Rieke. Investigating the far-IR/radio correlation of star-forming Galaxies to z = 3. *MNRAS*, 398:1573–1581, September 2009.

S. S. Shabala, Y.-S. Ting, S. Kaviraj, C. Lintott, R. M. Crockett, J. Silk, M. Sarzi, K. Schawinski, S. P. Bamford, and E. Edmondson. Galaxy Zoo: Dust lane early-type galaxies are tracers of recent, gas-rich minor mergers. *ArXiv e-prints*, July 2011.

R. Sharp and H. Parkinson. Sky subtraction at the Poisson limit with fibre-optic multiobject spectroscopy. *MNRAS*, 408:2495–2510, November 2010.

R. Sharp, W. Saunders, G. Smith, V. Churilov, D. Correll, J. Dawson, T. Farrel, G. Frost, R. Haynes, R. Heald, A. Lankshear, D. Mayfield, L. Waller, and D. Whittard. Performance of AAOmega: the AAT multi-purpose fiber-fed spectrograph. In *Society of Photo-Optical Instrumentation Engineers (SPIE) Conference Series*, volume 6269 of *Society of Photo-Optical Instrumentation Engineers (SPIE) Conference Series*, July 2006.

V. Smolčić, E. Schinnerer, A. Finoguenov, I. Sakelliou, C. L. Carilli, C. S. Botzler, M. Brusa, N. Scoville, M. Ajiki, P. Capak, L. Guzzo, G. Hasinger, C. Impey, K. Jahnke, J. S. Kartaltepe, H. J. McCracken, B. Mobasher, T. Murayama, S. S. Sasaki, Y. Shioya, Y. Taniguchi, and J. R. Trump. A Wide-Angle Tail Radio Galaxy in the COSMOS Field: Evidence for Cluster Formation. *ApJS*, 172:295–313, September 2007.

V. Smolčić, E. Schinnerer, M. Scodeggio, P. Franzetti, H. Aussel, M. Bondi, M. Brusa, C. L. Carilli, P. Capak, S. Charlot, P. Ciliegi, O. Ilbert, Ž. Ivezić,

K. Jahnke, H. J. McCracken, M. Obrić, M. Salvato, D. B. Sanders, N. Scoville, J. R. Trump, C. Tremonti, L. Tasca, C. J. Walcher, and G. Zamorani. A New Method to Separate Star-forming from AGN Galaxies at Intermediate Redshift: The Submillijansky Radio Population in the VLA-COSMOS Survey. *ApJS*, 177: 14–38, July 2008.

V. Smolčić, G. Zamorani, E. Schinnerer, S. Bardelli, M. Bondi, L. Bîrzan, C. L. Carilli, P. Ciliegi, M. Elvis, C. D. Impey, A. M. Koekemoer, A. Merloni, T. Paglione, M. Salvato, M. Scodeggio, N. Scoville, and J. R. Trump. Cosmic Evolution of Radio Selected Active Galactic Nuclei in the Cosmos Field. *ApJ*, 696:24–39, May 2009.

D. N. Spergel, L. Verde, H. V. Peiris, E. Komatsu, M. R. Nolta, C. L. Bennett, M. Halpern, G. Hinshaw, N. Jarosik, A. Kogut, M. Limon, S. S. Meyer, L. Page, G. S. Tucker, J. L. Weiland, E. Wollack, and E. L. Wright. First-Year Wilkinson Microwave Anisotropy Probe (WMAP) Observations: Determination of Cosmological Parameters. *ApJS*, 148:175–194, September 2003.

V. Springel, S. D. M. White, A. Jenkins, C. S. Frenk, N. Yoshida, L. Gao, J. Navarro, R. Thacker, D. Croton, J. Helly, J. A. Peacock, S. Cole, P. Thomas, H. Couchman, A. Evrard, J. Colberg, and F. Pearce. Simulations of the formation, evolution and clustering of galaxies and quasars. *Nature*, 435:629–636, June 2005.

M. Tegmark, A. J. S. Hamilton, and Y. Xu. The power spectrum of galaxies in the 2dF 100k redshift survey. *MNRAS*, 335:887–908, October 2002.

P. C. Tribble. Radio haloes, cluster mergers, and cooling flows. *MNRAS*, 263: 31–36, July 1993.

C. M. Urry and P. Padovani. Unified Schemes for Radio-Loud Active Galactic Nuclei. *PASP*, 107:803, September 1995.

P. C. van der Kruit. Observations of core sources in Seyfert and normal galaxies with the Westerbork synthesis radio telescope at 1415 MHz. *A&A*, 15:110–122, November 1971.

P. C. van der Kruit. High-resolution Radio Continuum Observations of Bright Spiral Galaxies at 1415 MHz: A General Discussion. *A&A*, 29:263, December 1973.

E. Vanzella, S. Cristiani, M. Dickinson, M. Giavalisco, H. Kuntschner, J. Haase, M. Nonino, P. Rosati, C. Cesarsky, H. C. Ferguson, R. A. E. Fosbury, A. Grazian, L. A. Moustakas, A. Rettura, P. Popesso, A. Renzini, D. Stern, and GOODS Team. The great observatories origins deep survey. VLT/FORS2 spectroscopy in the GOODS-South field: Part III. *A&A*, 478:83–92, January 2008.

F. Vazza, G. Brunetti, and C. Gheller. Shock waves in Eulerian cosmological simulations: main properties and acceleration of cosmic rays. *MNRAS*, 395:1333–1354, May 2009.

T. C. A. Venkatesan, D. J. Batuski, R. J. Hanisch, and J. O. Burns. Why do head-tail sources exist in poor clusters of galaxies? *ApJ*, 436:67–78, November 1994.

T. Venturi, S. Giacintucci, D. Dallacasa, R. Cassano, G. Brunetti, S. Bardelli, and G. Setti. GMRT radio halo survey in galaxy clusters at z = 0.2-0.4. II. The eBCS clusters and analysis of the complete sample. *A&A*, 484:327–340, June 2008.

H. J. Voelk. The correlation between radio and far-infrared emission for disk galaxies - A calorimeter theory. *A&A*, 218:67–70, July 1989.

R. L. White, R. H. Becker, M. D. Gregg, S. A. Laurent-Muehleisen, M. S. Brotherton, C. D. Impey, C. E. Petry, C. B. Foltz, F. H. Chaffee, G. T. Richards, W. R. Oegerle, D. J. Helfand, R. G. McMahon, and J. E. Cabanela. The FIRST Bright Quasar Survey. II. 60 Nights and 1200 Spectra Later. *ApJS*, 126:133–207, February 2000.

W. E. Wilson, R. H. Ferris, P. Axtens, A. Brown, E. Davis, G. Hampson, M. Leach, P. Roberts, S. Saunders, B. S. Koribalski, J. L. Caswell, E. Lenc, J. Stevens, M. A. Voronkov, M. H. Wieringa, K. Brooks, P. G. Edwards, R. D. Ekers, B. Emonts, L. Hindson, S. Johnston, S. T. Maddison, E. K. Mahony, S. S. Malu, M. Massardi, M. Y. Mao, D. McConnell, R. P. Norris, D. Schnitzeler, R. Subrahmanyan, J. S. Urquhart, M. A. Thompson, and R. M. Wark. The Australia Telescope Compact Array Broad-band Backend: description and first results. *MNRAS*, 416:832–856, September 2011.

C. Wolf, K. Meisenheimer, M. Kleinheinrich, A. Borch, S. Dye, M. Gray, L. Wisotzki, E. F. Bell, H.-W. Rix, A. Cimatti, G. Hasinger, and G. Szokoly. A catalogue of the Chandra Deep Field South with multi-colour classification and photometric redshifts from COMBO-17. *A&A*, 421:913–936, July 2004.

L. Woltjer. Emission Nuclei in Galaxies. *ApJ*, 130:38, July 1959.

E. L. Wright. A Cosmology Calculator for the World Wide Web. *PASP*, 118:1711–1715, December 2006.

Y. Q. Xue, B. Luo, W. N. Brandt, F. E. Bauer, B. D. Lehmer, P. S. Broos, D. P. Schneider, D. M. Alexander, M. Brusa, A. Comastri, A. C. Fabian, R. Gilli, G. Hasinger, A. E. Hornschemeier, A. Koekemoer, T. Liu, V. Mainieri, M. Paolillo, D. A. Rafferty, P. Rosati, O. Shemmer, J. D. Silverman, I. Smail, P. Tozzi, and C. Vignali. The Chandra Deep Field-South Survey: 4 Ms Source Catalogs. *ApJS*, 195:10, July 2011.

M. S. Yun and C. L. Carilli. Radio-to-Far-Infrared Spectral Energy Distribution and Photometric Redshifts for Dusty Starburst Galaxies. *ApJ*, 568:88–98, March 2002.

M. S. Yun, N. A. Reddy, and J. J. Condon. Radio Properties of Infrared-selected Galaxies in the IRAS 2 Jy Sample. *ApJ*, 554:803–822, June 2001.

W. Zheng, M. Postman, A. Zitrin, J. Moustakas, X. Shu, S. Jouvel, O. Host, A. Molino, L. Bradley, D. Coe, L. A. Moustakas, M. Carrasco, H. Ford, N. Benıtez, T. R. Lauer, S. Seitz, R. Bouwens, A. Koekemoer, E. Medezinski, M. Bartelmann, T. Broadhurst, M. Donahue, C. Grillo, L. Infante, S. Jha, D. D. Kelson, O. Lahav, D. Lemze, P. Melchior, M. Meneghetti, J. Merten, M. Nonino, S. Ogaz, P. Rosati, K. Umetsu, and A. van der Wel. A highly magnified candidate for a young galaxy seen when the Universe was 500 Myrs old. *ArXiv e-prints*, April 2012.

P.-C. Zinn, E. Middelberg, and E. Ibar. Infrared-faint radio sources: a cosmological view. AGN number counts, the cosmic X-ray background and SMBH formation. *A&A*, 531:A14, July 2011.

A

Appendix for Chapter 3

A.1 Redshifts for 24 μm excess sources

Redshifts for 697 of 1080 non-ATLAS sources were obtained. 472 of these are 24 μm excess sources and form the basis of further investigation into the radio-FIR correlation (Norris et al., in preparation). Their redshifts were determined in the process of determining ATLAS redshifts and are presented here for the first time in Table A.1.

A.2 $\mathbf{V}_{enclosed}/\mathbf{V}_{available}$

The ELAIS radio image is ~4.7 square degrees, of which π square degrees were observed with the AAT. In Figure 3.9 we presented the rms at each radio source position. Figure A.1 presents the same data with the AAOmega field-of-view overlaid.

We can treat this non-uniform radio image as four overlapping radio images each with a different rms. Table A.2 presents these areas, designated images A - D with A being the deepest and D being the shallowest image. The following equations and analyses are based on the equations provided in Avni and Bahcall

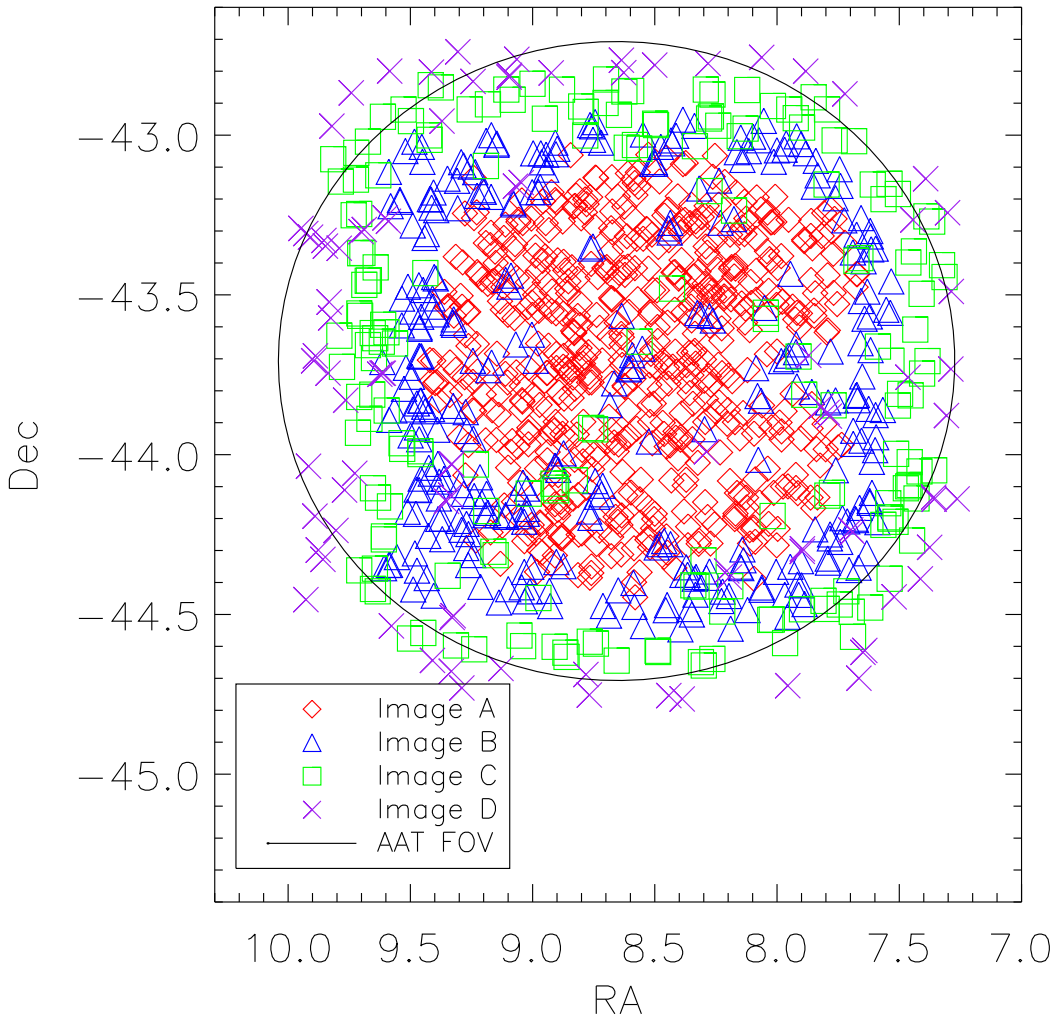

Figure A.1: RA-Dec plot of ELAIS's rms characteristics, with four different rms bins chosen, and colour-coded. To keep the plot simple, only parts of the image that aren't also part of a deeper image are plotted. That is, Image D covers the entire radio image, and Image C's datapoints can be thought of as being overlaid on Image D. The field-of-view of AAOmega is overlaid.

Table A.1: First 10 lines of the catalogue of new spectrosopic redshifts for 24 μm excess sources in ATLAS.

SID	RA (J2000)	Dec (J2000)	z
SWIRE3 J033350.32-280807.2	3:33:50.32	-28:08:07.30	0.2885
SWIRE3 J033300.84-280957.3	3:33:00.84	-28:09:57.30	0.2147
SWIRE3 J033246.75-280846.9	3:32:46.76	-28:08:47.00	3.1880
SWIRE3 J033223.92-281126.8	3:32:23.92	-28:11:26.80	0.1961
SWIRE3 J033221.93-281005.8	3:32:21.94	-28:10:05.90	0.1811
SWIRE3 J033347.81-281622.0	3:33:47.82	-28:16:22.00	0.1029
SWIRE3 J033159.87-280953.0	3:31:59.87	-28:09:53.00	0.2363
SWIRE3 J033154.67-281035.9	3:31:54.67	-28:10:36.00	0.2148
SWIRE3 J033417.62-281712.8	3:34:17.62	-28:17:12.90	0.3400
SWIRE3 J033237.30-280847.2	3:32:37.30	-28:08:47.30	0.7683

Table A.2: The rms limits for the four overlapping radio images ELAIS is broken down into.

Image	RMS limit (μJy beam^{-1})	Area (deg^2)
A	30	0.95
B	40	1.75
C	65	2.56
D	100	3.14

(1980).

Although whether the source is detected is both a function of the source's position in the field, and its luminosity, the actual volume available to the source is dependent only upon its luminosity. That is to say, the source may be distributed anywhere within the total volume. This is because the volume available to the source is bound by the flux density limits presented in Table A.2.

For a source of a given luminosity, the volume available (in Mpc^3) to a source in our sample is

$$
\begin{aligned}
V_{\text{available}} &= \frac{1}{4\pi}\frac{4}{3}\pi(\Omega_{(D-C)}D^3_{MMAX,D} \\
&\quad +\Omega_{(C-B)}D^3_{MMAX,C} \\
&\quad +\Omega_{(B-A)}D^3_{MMAX,B} \\
&\quad +\Omega_A D^3_{MMAX,A}) \qquad \text{(A.1)} \\
&= \frac{1}{3}(\Omega_{(D-C)}D^3_{MMAX,D} \\
&\quad +\Omega_{(C-B)}D^3_{MMAX,C} \\
&\quad +\Omega_{(B-A)}D^3_{MMAX,B} \\
&\quad +\Omega_A D^3_{MMAX,A}) \qquad \text{(A.2)}
\end{aligned}
$$

where Ω_X is the solid angle (in steradians) subtended by the image X, and $D_{MMAX,X}$ is the maximum comoving distance in Mpc for image X. In this way, each source is accounted for only once. This corresponds to Equation 9 of Avni and Bahcall (1980).

The actual volume enclosed by the source, corresponding to Equation 10 of Avni and Bahcall (1980), is dependent on the source's redshift (and hence $D_{M,source}$). For a source whose redshift is less than the maximum redshift the shallowest image (D) can detect, the enclosed volume is simply

$$V_{\text{enclosed}} = \frac{1}{3}(\Omega_D D^3_{M,source}) \qquad \text{(A.3)}$$

where $D_{M,source}$ is the comoving distance in Mpc for the source.

However, for a source whose redshift is less than or equal to the maximum redshift the deepest image (A) can detect, the enclosed volume is

$$
\begin{aligned}
V_{\text{enclosed}} &= \frac{1}{3}(\Omega_{(D-C)}D^3_{MMAX,D} \\
&\quad +\Omega_{(C-B)}D^3_{MMAX,C} \\
&\quad +\Omega_{(B-A)}D^3_{MMAX,B} \\
&\quad +\Omega_A D^3_{M,source}) \qquad \text{(A.4)}
\end{aligned}
$$

This is shown schematically in Figure A.2. These are for the two extremes but the same procedure is followed for sources with redshifts between $z_{MAX,C}$ and

$z_{MAX,D}$ as well as for sources with redshifts between $z_{MAX,B}$ and $z_{MAX,C}$.

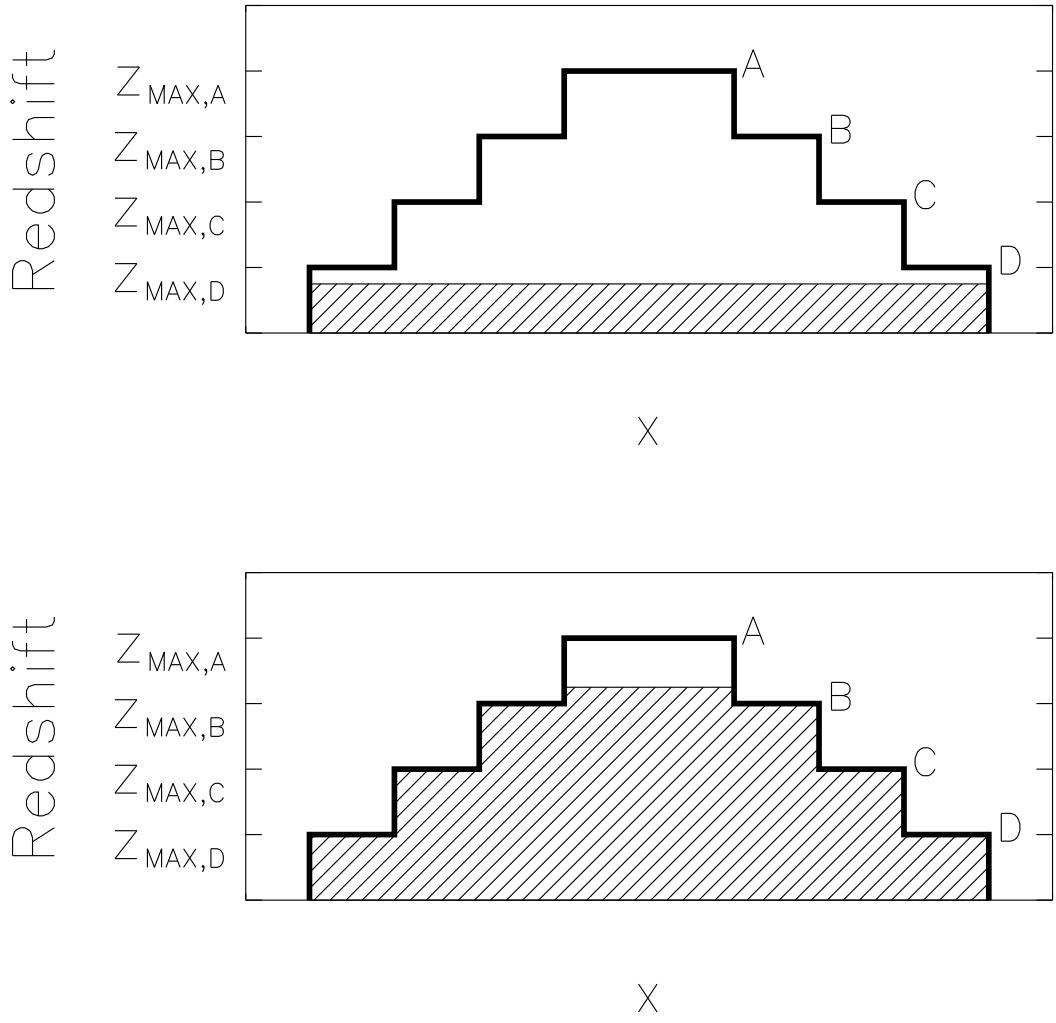

Figure A.2: A simple model depicting $V_{available}$ (solid black line) and $V_{enclosed}$ (shaded region) for a source whose redshift is less than the maximum redshift detectable in the shallowest image (upper panel) and for a source whose redshift is less than the maximum redshift detectable in the deepest image (lower panel). The x-axis is an idealised cross-section of the area and the y-axis is the redshift.

B

Appendix for Chapter 4

B.1 New Redshifts

Table B.1: New redshifts of galaxies near S1189.

SWIRE ID	z	SWIRE ID	z
SWIRE3_J003134.02-425148.8	0.21061	SWIRE3_J003443.66-424544.6	0.22247
SWIRE3_J003147.97-432431.8	0.44433	SWIRE3_J003445.06-425832.2	0.42247
SWIRE3_J003152.98-431701.7	0.24509	SWIRE3_J003446.92-431108.0	0.32148
SWIRE3_J003203.05-434121.6	0.21837	SWIRE3_J003446.92-431221.4	0.02507
SWIRE3_J003205.98-432339.9	0.39604	SWIRE3_J003448.84-424223.5	0.38740
SWIRE3_J003209.95-432147.1	0.20451	SWIRE3_J003452.68-430124.9	0.18383
SWIRE3_J003223.48-432147.1	0.27936	SWIRE3_J003455.92-433249.9	0.18833
SWIRE3_J003229.13-434406.2	0.35209	SWIRE3_J003458.93-430150.5	0.31710
SWIRE3_J003229.91-425457.7	0.22330	SWIRE3_J003458.95-425637.6	0.32933
SWIRE3_J003236.91-432040.8	0.21686	SWIRE3_J003459.03-425642.3	0.33043
SWIRE3_J003242.01-432630.5	0.22334	SWIRE3_J003500.92-430309.5	0.21871
SWIRE3_J003243.83-430936.9	0.20711	SWIRE3_J003501.04-424205.0	0.41316
SWIRE3_J003243.91-425533.9	0.14944	SWIRE3_J003503.98-425710.2	0.22218
SWIRE3_J003248.95-425132.5	0.21149	SWIRE3_J003506.23-425900.7	0.12141
SWIRE3_J003249.79-423818.9	0.30177	SWIRE3_J003509.89-430642.4	0.20673
SWIRE3_J003251.92-432910.4	0.28767	SWIRE3_J003513.81-430046.2	0.32167
SWIRE3_J003300.09-432819.9	0.22674	SWIRE3_J003519.09-431158.8	0.17832
SWIRE3_J003308.14-430217.3	0.18372	SWIRE3_J003526.70-430418.7	0.22216
SWIRE3_J003309.95-430020.2	0.37209	SWIRE3_J003526.75-435641.2	0.32339
SWIRE3_J003310.94-424121.5	1.24725	SWIRE3_J003527.25-425327.0	0.04506
SWIRE3_J003312.88-431547.4	0.27951	SWIRE3_J003530.92-424426.3	0.53011
SWIRE3_J003313.91-432722.2	0.33233	SWIRE3_J003535.18-430900.6	0.32241
SWIRE3_J003317.94-432925.6	0.19152	SWIRE3_J003537.70-422625.0	0.03611
SWIRE3_J003322.00-430419.5	0.22525	SWIRE3_J003538.08-425640.0	0.26549
SWIRE3_J003322.79-431047.0	0.07282	SWIRE3_J003542.74-425959.5	0.05296
SWIRE3_J003335.04-425458.6	0.21277	SWIRE3_J003551.83-424442.1	0.07070
SWIRE3_J003339.84-430908.8	0.22149	SWIRE3_J003552.04-430205.0	0.18486
SWIRE3_J003343.91-432149.5	0.40215	SWIRE3_J003552.98-432142.4	0.39342
SWIRE3_J003348.84-430904.4	0.20033	SWIRE3_J003556.02-421810.9	0.24246
SWIRE3_J003351.10-424258.2	0.26489	SWIRE3_J003556.95-433947.0	0.42403
SWIRE3_J003355.92-424153.9	0.21902	SWIRE3_J003600.06-424555.6	0.54820
SWIRE3_J003400.08-430537.8	0.20725	SWIRE3_J003609.00-424433.8	0.18637
SWIRE3_J003403.95-425805.9	0.32737	SWIRE3_J003611.10-425004.1	0.33055
SWIRE3_J003404.81-431335.8	0.18986	SWIRE3_J003619.16-424839.2	0.20139
SWIRE3_J003404.90-430945.6	0.27894	SWIRE3_J003630.77-423814.6	0.05462
SWIRE3_J003408.19-431736.3	0.14801	SWIRE3_J003636.80-432152.6	0.15536
SWIRE3_J003410.81-424105.3	0.27872	SWIRE3_J003645.06-423419.9	0.32288
SWIRE3_J003410.96-430444.7	0.42139	SWIRE3_J003645.88-431028.3	0.30023
SWIRE3_J003413.83-425647.6	0.32816	SWIRE3_J003647.94-431037.1	0.29938
SWIRE3_J003415.22-430234.2	0.18821	SWIRE3_J003655.07-425404.1	0.27827
SWIRE3_J003415.87-430840.9	0.22201	SWIRE3_J003659.30-431824.1	0.22634
SWIRE3_J003419.26-430334.0	0.22040	SWIRE4_J003706.38-431442.3	0.66842
SWIRE3_J003421.99-425817.0	0.41943	SWIRE3_J003706.70-431836.0	0.01959
SWIRE3_J003422.08-430623.7	0.22014	SWIRE3_J003707.12-430302.7	0.22293
SWIRE3_J003426.01-434349.1	0.20469	SWIRE3_J003711.92-430711.4	0.22153
SWIRE3_J003428.82-425203.7	0.12161	SWIRE3_J003728.02-434143.2	0.20727
SWIRE3_J003430.97-425901.6	0.14762	SWIRE3_J003748.09-433353.8	0.30986

So long, and thanks for all the fish.

Douglas Adams